UNIVERSITÉ DE GRENOBLE

THÈSE

Pour obtenir le grade de

DOCTEUR DE L'UNIVERSITÉ DE GRENOBLE

Spécialité : **Matériaux, Mécanique, Génie civil, Electrochimie**

Arrêté ministériel : 7 août 2006

Présentée par

Murad S. AbuAisha

Thèse dirigée par **Benjamin Loret**

préparée au sein du **Laboratoire Sols, Solides, Structures – Risques**
dans **l'École Doctorale : Ingénierie – Matériaux Mécanique Énergétique Environnement Procédés Production**

Géothermie profonde: stimulation de la perméabilité par fracturation hydraulique dans un cadre thermo-poroélastique

Thèse soutenue publiquement le **28 Avril 2014**,
devant le jury composé de :

Mr Leonhard Ganzer
Professor, Technische Universität Clausthal, Allemagne, Rapporteur,
Mr Dashnor Hoxha
Professeur, Université d'Orléans, Rapporteur,
Mr Thomas Kohl
Professor, Karlsruher Institut für Technologie, Allemagne,
Mr Benjamin Loret
Professeur, Institut National Polytechnique, Grenoble, Directeur de thèse

Université Joseph Fourier / Université Pierre Mendès France / Université Stendhal / Université de Savoie / Grenoble INP

Abstract

The application of the Hydraulic Fracturing (HF) technology to exploit geothermal energy from Hot Dry Rocks (HDR) reservoirs is addressed. HF is achieved by extensively pumping geothermal fluids to already existing fractured HDR reservoirs of low permeability. High fluid pressures are expected to drive cracks to evolve and connect. The newly created burgeoning hydraulic conduits should supposedly enhance the permeability of the existing HDR reservoirs. The flow rate/pressure values at which geothermal fluids should be pumped, as well as the pumping schedule to initiate HF, depend primarily on the existing geostatic conditions (geostatic stresses, initial HDR pressure and temperature) as well as on HDR fracture properties (initial mean fracture length, mean fracture aperture, density and orientational distribution of fractures). While these components, in addition to their effects on borehole stability, are scrutinized in this research, focus is on the evolution during circulation processes of the fracture properties.

A fracturing model that is capable of tracking fracture evolution in all possible spatial orientations is used to obtain the time course of the anisotropic permeability tensor. This evolving property is integrated into a domestic finite element code which is developed to solve thermo–poroelastic BVPs: emphasis is laid on the efficiency of the doublet flow technique where a fluid gains thermal energy by circulating through the HDR reservoir from the injection well to the production well.

The spurious oscillations in the hyperbolic solutions of the approximated finite element approach that are commensal with the phenomenon of forced heat convection are healed/mitigated through several stabilization approaches.

Résumé

Ce travail concerne l'utilisation de la technique de Fracturation Hydraulique (FH) pour exploiter l'énergie géothermique des réservoirs profonds de roches sèches chaudes (HDR). La fracturation hydraulique est réalisée par injection de fluides géothermiques dans des réservoirs partiellement fracturés de faible perméabilité. Les fluides à haute pression sont destinés à faire évoluer les fissures et leur connectivité. Les valeurs de débit/pression auxquelles les fluides géothermiques doivent être pompés, ainsi que le calendrier de pompage pour initier la fracturation hydraulique, dépendent principalement des conditions géostatiques existantes (contraintes géostatiques, pression fluide et température initiales de l'HDR) ainsi que des propriétés des fissures de l'HDR (longueur, épaisseur, densité et distribution directionnelle initiales moyennes de fissures). Tous ces éléments, en sus de leurs effets sur la stabilité des forages, sont analysés dans cette recherche.

Des modèles de fracturation, qui sont capables de suivre l'évolution des fissures dans toutes les orientations spatiales possibles, sont utilisés pour obtenir le tenseur anisotrope de perméabilité. Ces modèles sont intégrés dans un code domestique d'éléments finis qui est développé pour résoudre des problèmes aux limites thermo-poroélastiques.

Pour supprimer/diminuer les oscillations qui accompagnent les solutions paraboliques et/ou hyperboliques lors de la convection forcée, plusieurs techniques de stabilisation ont dû être implémentées.

إلَيْكِ: إلَيْكِ يَا أُمِّي ...

إلَيْكِ يَا أُمِّي, يَا آيَتِي الْتِّي لمْ يَجْعَلَهَا اللهُ لَلْعَالَمِين

To you: To you my mother ...

..... You are the miracle that G–D only made to me

Acknowledgements

This PhD research was financially supported by a CNRS fellowship for a period of three years. I would like to express my deep feelings of gratitude to the members in the INP-G and CNRS for facilitating my coming to France and pursuing my PhD research. I feel totally indebted to many members in the laboratory 3S-R, especially Professor Desrues Jacques, for fostering an outstanding research environment and for welcoming me in the laboratory. I can not be any more grateful to my supervisor Professor Benjamin Loret for his tireless efforts and quick responses to my calls for assistance. I am also thankful to Professors Kohl, Ganzer, Hoxha and Plé for coming from different far places and for accepting to be members in the jury of the defense.

For their friendship and day–to–day support, I am acknowledged to Khadija, Khaled, Mukhles, Jadalhaq, Wasim, Hanaa, Elie, Mahmoud, Mohammed, Hashem, Sinan, Lekë, Mario, Hussain, Adel, Wael, Jamal, Dino, Benjamin, Jérôme, Rémi, Wafa, Widad and Denis. I apologize for those I could not remember, I thank them too.

I would like also to thank my parents and my brothers for their support, kindness and endless encouragement. Finally, I would like to acknowledge the thousands of individuals who have coded for the LaTeX project for free. It is due to their efforts that we can generate professionally typeset PDFs now.

Contents

List of Figures

List of Tables

Introduction

Objective, method and scope

The objective of this research is to develop an environment that describes permeability enhancement of geothermal systems in a Thermo–Hydro–Mechanical (THM) framework. The developed environment is to include mechanical ingredients, i.e. fracturing models, to describe Hydraulic Fracturing (HF), and a computational aspect to implement the HF process in thermo–poroelasticity.

A great deal of time is spent in studying thermo–poroelasticity on the mathematical and the finite element levels. The contribution from the available literature is highly valued and investigated. A domestic Fortran 90 finite element code is developed to simulate thermo–poroelasticity in single–porosity media subjected to temperature changes. Fracture and damage mechanics are employed to develop and modify fracturing models to describe HF. The fracturing models are integrated into our finite element code to study HF in a thermo–poroelastic framework.

Validation of the fracturing models is accounted for. Several stimulation and/or circulation tests at the geothermal reservoir of Soultz–Sous–Forêts are finally presented.

Strategy of the PhD research

Geothermal geomechanics and its applications on the Enhanced Geothermal Systems (EGS) is presented. Under the framework of thermodynamics, the mechanics of porous media subjected to thermal changes is precisely studied. The field equations attributed to thermo–poroelasticity with full coupling between the mechanical, the fluid diffusive and the thermal diffusive effects are presented. A full mathematical model to describe fluid-temperature transports in single–porosity deformable fractured zones is hence developed.

Using the Finite Element Method (FEM), this mathematical model was discretized in the space and time to get the matrix formulation that can be coded for to solve the thermo-poroelastic Transient Boundary Value Problems (TBVPs).

INTRODUCTION

Using Fortran 90, a Finite Element (FE) code capable of simulating plane strain and axisymmetric thermo-poroelastic TBVPs is developed. The FE code is used to simulate the thermal recovery from large–scale geothermal systems lying deep in the ground.

To enhance the performance and/or the efficiency of these geothermal systems, the process of HF is studied thoroughly. HF is achieved by extensively pumping geothermal fluids to already existing geothermal reservoirs of low permeability. High fluid pressures will drive cracks to evolve and connect, the new created burgeoning hydraulic conduits will supposedly enhance the permeability of the existing reservoir and hence the efficiency of heat extraction process.

To numerically simulate the process of HF, fracture and damage mechanics are employed to develop fracturing models capable of describing the directional fracture evolution. These fracturing models are tested against experimental data to ensure good results before applying them in the research.

The fracturing models are working following this scheme: a criterion to decide whether fracturing and hence damage, at the scale of Gauss' points and in any direction, takes place or not and a rule that provides the incremental length of the crack are presented. Knowing the new fracture radius, the change in fracture aperture is estimated based on analytical estimations and/or experimental data which relate aperture change to change of fracture radius. Using the new fracture aperture along with the fracture radius, the local velocity field is calculated by implementing Navier–Stokes equation for laminar flow between two parallel plates. The macroscopic velocity field is deduced by the directional averaging (sort of a homogenization approach) over the local velocities. A macroscopic anisotropic permeability tensor, that accurately describes the hydraulic connectivity of the hydraulically fractured medium, is then calculated by applying Darcy's law for laminar flow.

These fracturing models are integrated into the FE code that addresses thermo–poroelastic TBVPs: thermal recovery from Hot Dry Rock (HDR) reservoirs is upgraded by enhancing geothermal fluid circulation, i.e. increasing the reservoir permeability between injection and production wells by the process of HF. HF has been proven to enhance the efficiency of the thermal recovery from HDR reservoirs by 50%.

The problem of borehole stability associated with tensile and shear failure of the borehole case–shoe is also presented to ensure safe HF process of HDR reservoirs.

A fairly sufficient study on designing the Enhanced Geothermal Systems; in terms of size, impedance, efficiency and life time is outpointed. Chemical enhancement of EGS is also briefly addressed from several researchers who have been working on it recently. The effect of temperature change on geothermal fluids, Newtonian and Non-Newtonian, viscosity is neatly addressed.

The phenomenon of forced heat convection is highlighted with several approaches to heal/ mitigate the oscillations in the hyperbolic solutions of the approximated finite element approach.

The commonly used Streamline Upwind Petrov-Galerkin (SUPG) method fails to heal these oscillations at early times near the injection wells and at late times near the production wells. New approaches like the Subgrid Scale (SGS) and the Discontinuity Capturing Method (DCM) are worked and employed in our FE code to perfectly heal those numerical oscillations against which the SUPG schemes are inefficient.

Chapter 1

Geothermy and Enhanced Geothermal Systems (EGS): General view

1.1 Geothermal energy: Historical point of view

Geothermal energy (The adjective geothermal originates from the Greek roots geo, meaning earth, and thermos, meaning heat) is the thermal energy generated and stored in the Earth. Our planet self–generates this energy from the decaying of certain radioactive minerals and from the tectonic activities. This thermal energy is driven to the surface of the Earth due to a continuous conduction which is a natural result of an existing difference of *gradient* of temperature between the core and the surface of the planet (Turcotte and Schubert, [2002]).

Geothermal energy exploitation has been historically limited to certain areas on the planet where it was feasible and easy to use it, for instance areas near tectonic plates boundaries. Modern technologies, such as hydro–fracturing, have been employed to enhance the capability of extracting geothermal energy from any place on the planet, if cost effective though. Geothermal power is reliable, sustainable, and environmentally friendly; the greenhouse gases that could be released while extracting it, are much lower per unit energy produced than fossil fuels. Geothermal energy could be the salvation of humanity that suffers from global warming if it was widely deployed.

The estimated total thermal energy above mean surface temperature to a depth of 10 km is 1.3×10^{27} J, equivalent to burning 3.0×10^{17} barrels of oil. Since the global energy consumptions for all types of energy, is equivalent to use of about 100 million barrels of oil per day, the Earth's energy to a depth of 10 kilometers could theoretically supply all of mankind's energy needs for six million years (Lund, [2007]). It is quite obvious that the Earth's geothermal resources are

theoretically sufficient to supply humanity's energy needs, however, they cannot be all efficiently exploited. The efficiency here is more or less the economic efficiency; drilling to deep resources is not inexpensive, future needs for energy, future technologies and logistic interests could be the mean reasons driving the use of the geothermal power.

Hot springs have been used for bathing at least since Paleolithic times (Cataldi, [1993]). The first commercial use of geothermal power appeared in the first century AD, when Romans conquered *Aquae sulis*[1]and used hot springs there for public paths and heating. The world's oldest geothermal district heating system is in *Chaudes-Aigues* (hot waters in old French), France, and has been operating since the 14th century (Lund, [2007]).

The USA were the first to use geothermal energy to run an entire heating system in *Boise Idaho, Klamath Fallas, and Oregon* between 1892 and 1900. Geysers were also used to heat green houses in Iceland around 1900's and to heat homes in 1943 (Dickson and Fanelli, [2004]). The exploitation of geothermal energy became much common and accepted after the implementation of the heat pump in 1940's. *J. Donald Kroeker* was the first to heat a common–wealth building *Portland, Oregon* in 1946 by a commercial heat pump that he designed[2]. The idea of exploiting geothermal energy became widely accepted and started to grow slowly after the oil crisis in 1973. As of 2004, there are over a million geothermal heat pumps installed worldwide providing 12 GW of thermal capacity (Curtis et al., [2004]). Each year, about 80,000 units are installed in the USA and 27,000 in Sweden (Curtis et al., [2004]).

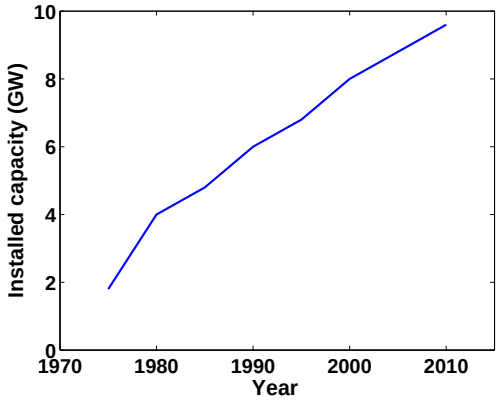

Figure 1.1: Total worldwide geothermal capacity from 1975 up to end of 2007 (Bertani,[2007]).

[1]Aquae Sulis was a small town in the Roman province of Britannia.

[2]Kroeker J. Donald, Chewning Ray C. (February 1948), A Heat Pump in an Office Building, ASHVE Transactions 54: 221-238.

1.2 Types of geothermal systems

1.2.1 Conventional geothermal systems

Traditional geothermal energy systems for effective electricity production can be potentially used only on less than 10 percent of Earth's surface. They rely on locating anomalies, section(1.1). They use a well to pump water out of the ground and pass it through a heat exchanger. A refrigerant cycle is then used to remove heat from the water. This refrigerant is compressed to make a hot gas that could be used to heat buildings (Lund, [2007]).

1.2.2 Enhanced geothermal systems

The vast majority of geothermal energy, within reach of available techniques, is in dry and non-permeable rock *Hot Dry Rock* (HDR) (Duchane and Brown, [2002]). *Enhanced Geothermal Systems* (EGS), unlike the conventional geothermal systems, do not require any certain location anomalies; engineers would rather enhance and/or create the geothermal recovery from this HDR through hydraulic stimulation, see figure (1.2).

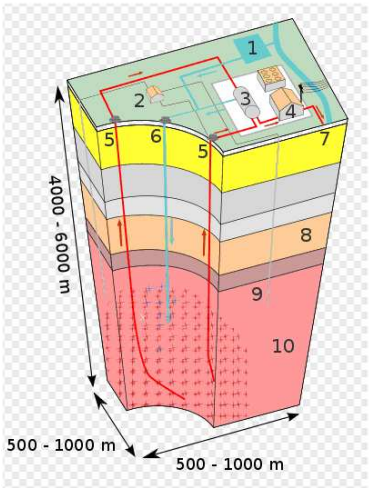

Figure 1.2: Enhanced geothermal system 1:Reservoir 2:Pump house 3:Heat exchanger 4:Turbine hall 5:Production well 6:Injection well 7:Hot water to district heating 8:Porous sediments 9:Observation well 10:Crystalline bedrock (Wikipedia EGS, 30/08/2011).

When the rock is not porous enough to allow efficient rates of flow, cold pressurized water is injected down the borehole. The injection increases the fluid pressure in the naturally fractured rock which incites shear events, enhancing the permeability of the fractured system. This

process is called hydro–shearing/fracturing.

Water travels through fractures in the rock, capturing the heat of the rock until it is forced out of a second borehole as very hot water, which is converted into electricity using either a steam turbine or a binary power plant system. All of the water, now cooled, is injected back into the ground to heat up again in a closed loop. Distinct from conventional geothermal systems, HDR / EGS may be feasible anywhere in the world depending on the economic limits of drilling depth. Good locations are over deep granite covered by a thick (3-5 km) layer of insulating sediments which slow heat loss. Most of HDR wells are expected to have a useful life of 20 to 30 years before the outflow temperature drops about 10 °C and the well becomes uneconomic. If left for 50 to 300 years the temperature will recover (Beardsmore, [2007]).

There are HDR and EGS systems currently being developed and tested in France, Australia, Japan, Germany, the U.S. and Switzerland. The largest EGS project in the world is a 25 megawatt demonstration plant currently being developed in the Cooper Basin, Australia. The Cooper Basin has the potential to generate 5,000-10,000 MW (Beardsmore, [2007]).

1.3 Types of geothermal resources

On average, the temperature of the Earth increases about 30 °C/km above the mean surface ambient temperature. Thus, assuming a conductive gradient, the temperature of the earth at 10 km would be over 300 °C. However, most geothermal exploration occurs where the gradient is higher and thus where drilling is shallower and less costly. These shallow depth geothermal resources occur due to (Wright, [1989]):

1. Intrusion of molten rock (magma) from depth, bringing up great quantities of heat.

2. High surface heat flow, due to a thin crust and high temperature gradient.

3. Ascent of groundwater that has circulated to depths of several kilometers and been heated due to the normal temperature gradient.

4. Insulation of deep rocks by thick formation of rocks like shale whose thermal conductivity is low (Thermal Blanketing).

5. Anomalous heating of shallow rock by decay of radioactive elements, perhaps augmented by thermal blanketing.

Geothermal resources are usually classified as shown in Table (1.1). Geothermal resources range from the mean annual ambient temperature of around 20 °C to over 300 °C. In general, resources above 150 °C are used for electric power generation, and resources below 150 °C are usually used in direct–use projects for heating and cooling (White and Williams, [1975]).

Table 1.1: Geothermal Resource Types (White and Williams, [1975]).

Resource Type	Temperature Range °C
Convective hydrothermal resources	
Vapor dominated	240°
Hot-water dominated	20 to 350° +
Other hydrothermal resources	
Sedimentary basin	20 to 150°
Geo–pressured	90 to 200°
Radiogenic	30 to 150°
Hot rock resources	
Solidified (Hot Dry Rock)	90 to 650°
Part still molten (magma)	> 650°

1.3.1 Vapor dominated systems

Produce steam from boiling of deep waters in low permeability rocks. These reservoirs are few in number, with The Geysers in Northern California, *Larderello* in Italy and *Matsukawa* in Japan being ones where the steam is exploited to produce electric energy (White et al., [1971]).

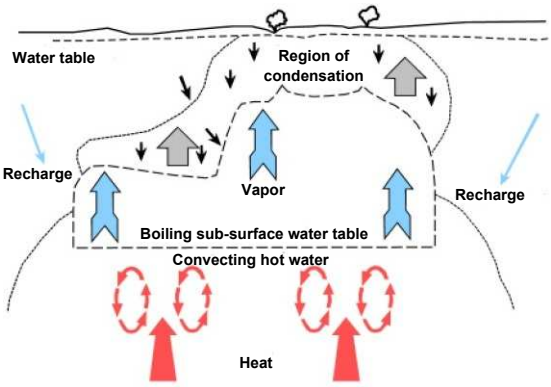

Figure 1.3: Vapor dominated geothermal system edited from (White et al., [1971]).

1.3.2 Water dominated systems

These systems are generated from water circulating deep in permeable rocks that are heated by a convecting source and later lifted up by buoyancy. These systems include an up–flow zone

at the center of each convection cell, an outflow zone of heated water moving laterally away from the center of the system, and a down–flow zone where recharge is taking place. Surface manifestations could include hot springs, Geysers, chemically altered rocks, or sometimes a blind source with no surface manifestation (White et al., [1971]).

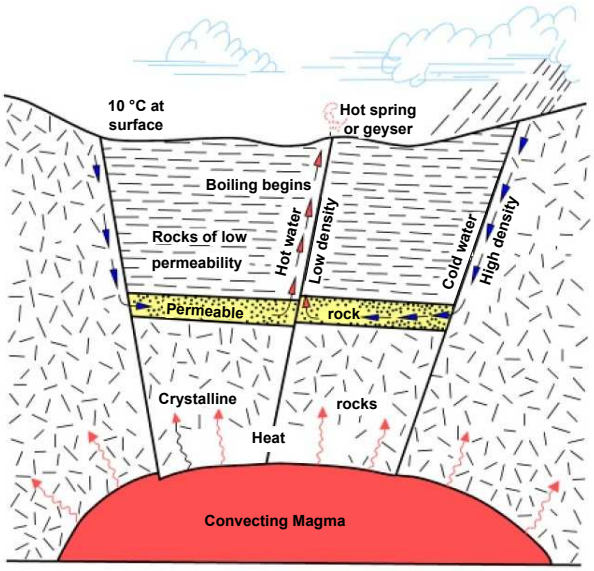

Figure 1.4: Hot water dominated geothermal system edited from (White et al., [1971]).

1.3.3 Sedimentary basins

Produce higher temperature resources than the surrounding formations due to their low thermal conductivity "geothermal gradients $> 30°C/km$". These basins generally extend over large areas and are typical of the Madison Formations of North Dakota, South Dakota, Montana and Wyoming area of the northern United States and the Pannonian Basin of central Europe where it has been used extensively in Hungary (Anderson and Lund, [1979]).

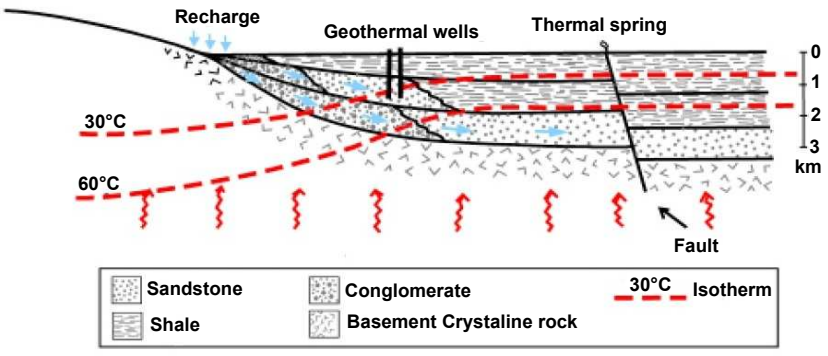

Figure 1.5: Sedimentary basin geothermal resource edited from (Anderson and Lund, [1979]).

1.3.4 Geo–pressured resources

These resources, figure (1.6), occur as result of water circulating in permeable sedimentary rocks which are buried deep in the earth crust. These deeply circulating fluids are heated by natural/*enhanced*[1] geothermal gradients and tightly confined by the surrounding impermeable rocks holding pressure much larger than the hydrostatic. These waters are target for drilling not only for geothermal power but also for the dissolved *methane*. The Texas and Louisiana Gulf Coast in the United States has been tested for the geothermal energy, however, due to the great depths of several kilometers they have not proved economic (Bebout et al., [1978]).

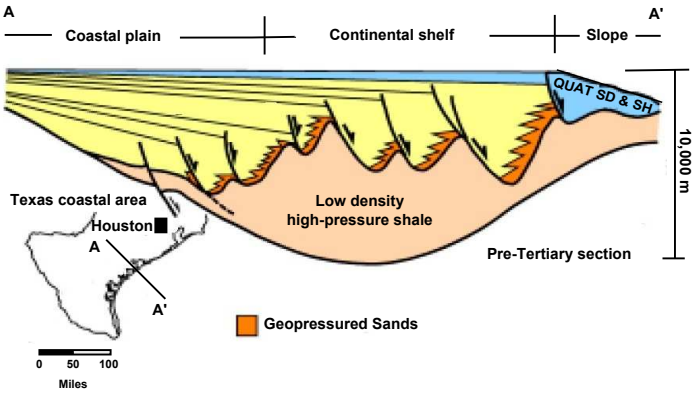

Figure 1.6: Geopressured geothermal system edited from (Bebout et al., [1978]).

1.3.5 Radiogenic resources

Found where granitic intrusions are near surface heating up the local groundwater from the decay of radioactive thorium, potassium and uranium. This localized heating increases the normal geothermal gradient providing hot water at economical drilling depths. This type of resource occurs along the eastern United States, but has not been developed commercially.

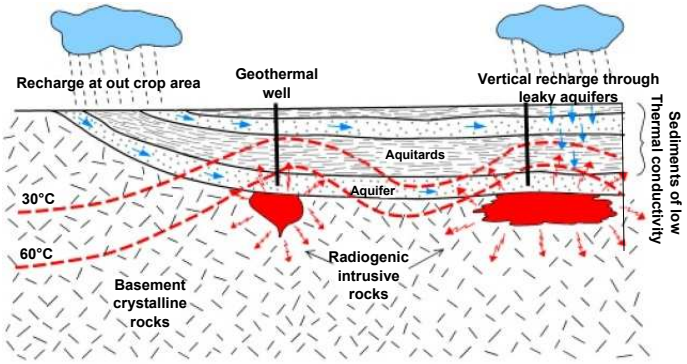

Figure 1.7: Radiogenic geothermal system edited from (Anderson and Lund, [1979]).

[1] By a convective source like magma.

1.3.6 Hot Dry Rock (HDR) resources

These resources represent heat trapped in quite deep rocks (up to 10 km). At such depths geothermal energy cannot be extracted economically, besides these rocks contain few pores or fractures and thus very low or no permeability.

In order to extract the heat, experimental projects have artificially fractured the rock by hydraulic pressure, followed by circulating cold water down one well to extract the heat from the rocks and then producing from a second well in a closed system. Early experimental projects were undertaken at Fenton Hill (Valdes Caldera) in northern New Mexico and on Cornwall in southwest England, however, both of these projects have been abandoned due to lack of funds and poor results. Projects are currently underway in Soultz-sous-Forêts in the Rhine Graben on the French-German border, in Switzerland at Basel and Zürich, in Germany at Bad Urach, several locations in Japan, and in the Cooper Basin of Australia (Tenzer, [2001]).

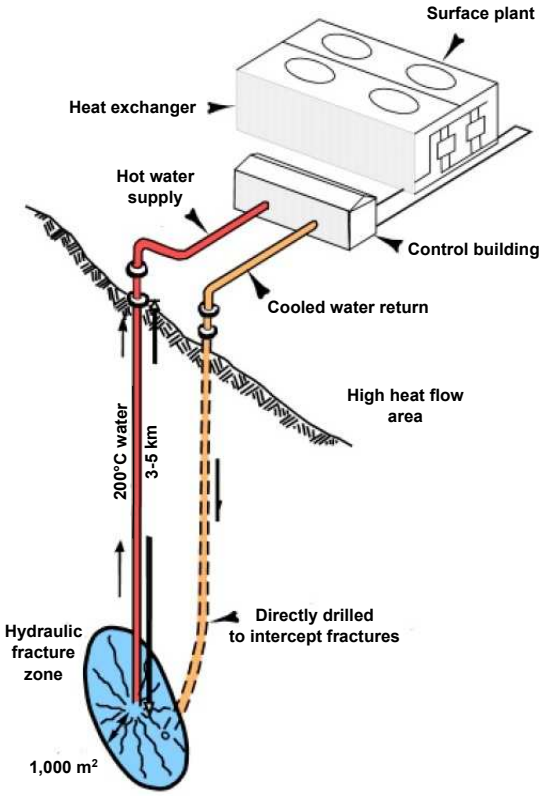

Figure 1.8: Hot Dry Rock (HDR) exploitation edited from (Lund, [2007]).

1.3.7 Molten rock or magma resources

A heat exchanger constructed on the surface of the lava flow recovered steam resulting from boiling of downward percolation water from the surface. These resources have been drilled in Hawaii experimentally to extract heat energy directly from molten rock. It has been used successfully at Heimaey in Iceland (one of the Westmann Islands) after the 1973 eruption.

1.4 Utilization of geothermal energy

1.4.1 Electric power generation

Geothermal energy is generated by using the hot steam which turns a turbine which is, in its turn, designed to generate electricity. Vapor dominated resources figures (1.3) and (1.9) can be used directly. However, water dominated resources need a pre–step in which pressure is reduced to generate the steam, figure (1.10).

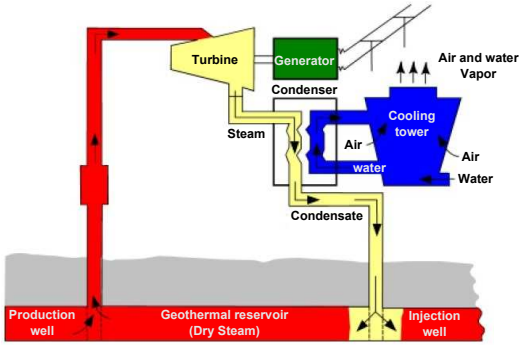

Figure 1.9: Steam plant using a vapor or dry steam dominated geothermal resource edited from (Lund, [2007]).

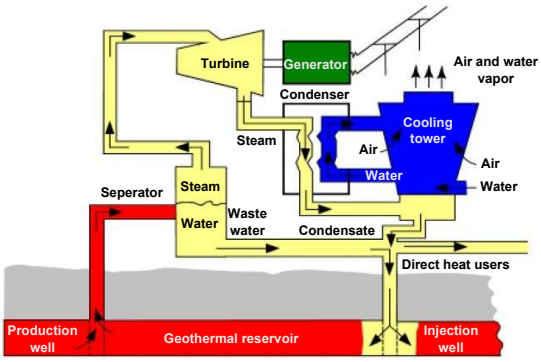

Figure 1.10: Flash steam plant using a water-dominated geothermal resource with a separator to produce steam edited from (Lund, [2007]).

When exploiting geothermal resources with low temperature < 150 °C, the use of a binary

cycle called *Rankine cycle* that contains low–boiling organic fluid is necessary to generate the vapor required to run the turbine, figure (1.11). Later a cooling tower is used to condense the vapor leaving the turbine and thus increasing the efficiency of the system by creating a considerable drop in the temperature of the vapor.

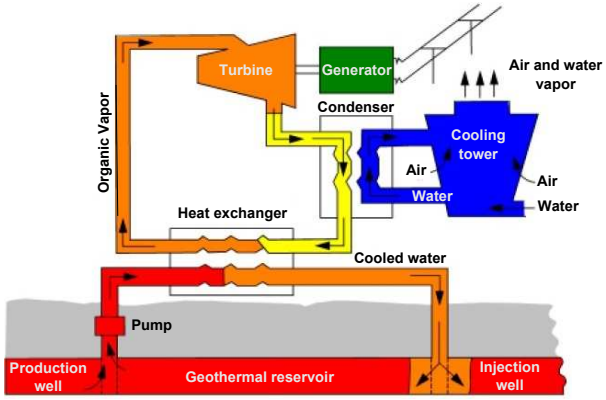

Figure 1.11: Binary power or organic Rankine cycle plant using a low temperature geothermal resource and a secondary fluid of a low boiling-point hydrocarbon edited from (Lund, [2007]).

1.4.2 Direct utilization

Direct use of geothermal energy is widespread and could be located in very far and isolated areas. This renders the estimation of the global direct utilization a tremendous task, however, the main utilization categories are:

1. Swimming, bathing and balneology.
2. Space heating and cooling including district energy systems.
3. Agricultural applications such as greenhouse and soil heating.
4. Aquaculture application such as pond and raceway water heating.
5. Industrial applications such as mineral extraction, food and grain drying.

Direct utilization of geothermal energy includes geothermal resources which give low to intermediate temperature. These low to intermediate temperature resources are feasible and exist in at least 80 countries at economic depths (Lund, [2007]). The direct utilization projects range from individual scales of homes and greenhouses heating to large scales operations such as minerals extraction.

Geothermal waters are oxygen free and care must be payed to prevent oxygen from penetrating them. Dissolved gases and minerals such as *Arsenic* and *Hydrogen Sulfide* must be removed or isolated since they are harmful to humans and plants. On the other hand, carbon dioxide which often occurs in geothermal waters can be extracted and used to enhance growth in greenhouses.

1.5 Environmental considerations

Although geothermal resources are considered renewable and green, there are several environmental impacts, that are usually mitigated, which must be considered during utilization. These include emission of harmful gases, noise pollution, water use and quality, land use, impact on natural phenomena, and induced seismicity (Kagel et al., [2005]).

1.5.1 Emissions

These are normally direct results of using vapor power plants with cooling towers as they produce water steam emission. Depending on the reservoir type, these vapor emissions include: carbon dioxide, sulfur dioxide, nitrous oxides, hydrogen sulfide along with particulate matter. Table (1.2) shows a small comparison of emitted gases (kg/MWh) between a coal-fired plant and a geothermal power plant.

Table 1.2: Comparison of emitted gases (kg/MWh) between a coal-fired plant and a geothermal power plant (Lund, [2007]).

Name of the emitted gas	Amount released from a coal–fired plant	Amount released from a geothermal power plant
Carbon dioxide	994	40
Sulfur dioxide	4.71	0.16
Nitrogen oxides	1.95	0
Hydrogen sulfide	0	0.08
Other particulate matters	1.01	0

Hydrogen sulfide is routinely treated at geothermal power plants and converted to elemental sulfur. Binary (air–cooled) power plants and direct-use projects normally do not produce any pollutants, as the water is injected back into the ground after use without exposing it to the atmosphere.

1.5.2 Noise

The majority of the noise produced at a power plant or direct-use site is during the well drilling operation which normally shuts down at night. The noise from a power plant is not considered an issue of concern as it is extremely low, unless you are next to or inside the plant. Most of the noise comes from cooling fans and the rotating turbines (Lund, [2007]).

1.5.3 Water use

The amount of freshwater used to cool a geothermal power plant is estimated to 20 liters per MWh (binary power plants use no water), compared to 1,370 liters of freshwater needed by a coal-fired plant. An oil plant uses about 15% less and nuclear about 25% more than the coal plant. The only use of water is to cool the plant and the only discharge of it is to change the fluid during the cyclation. Water is normally reinjected into the aquifer without mixing with the shallow groundwater.

At the Geysers facility in northern California, 42 million liters of treated wastewater from *Santa Rosa* are pumped daily for injection into the geothermal reservoir. This reduces surface water pollution in the community and increases the production of the geothermal field. A similar project supplies waste water from the Clear Lake area on the northeast side of the Geysers. These projects have increased the capacity of the field by over 100 MW (Lund, [2007]).

1.5.4 Land use

Generally the power plants of geothermal energy can be located near recreational areas with very limited visual impacts; they are designed to blend quite well with the surrounding. A typical geothermal power plant uses 404 m^2 of land per GWh compared to a coal facility that uses 3,632 m^2 per GWh and a wind farm that uses 1,335 m^2 per GWh (Lund, [2007]). Seismicity and land subsidence are the main impacts that should be considered when designing a geothermal power plant. However, they can be mitigated by reinjecting the used water back into the aquifer. Utilizing geothermal resources eliminates the mining, processing and transporting required for electricity generation from fossil fuel and nuclear resources (Lund, [2007]).

1.5.5 Impact on natural phenomena, wildlife and vegetation

As was stated in (1.5.1), geothermal water contains dangerous gases that could be very harmful to humans, animals and plants. Geothermal power plants are to be located far away from wildlife and vegetation. Designers and operators are especially sensitive about preserving manifestations considered sacred to indigenous people. Any site considered for a geothermal power plant must

be reviewed and considered for the impact on wildlife and vegetation. Direct use projects are usually small and thus have no significant impact on natural features.

1.5.6 Induced seismicity

Seismicity has become the term that accompanies the geothermal energy; seismic events have been observed in a number of operating geothermal fields and EGS projects.

1.6 Induced seismicity

Seismic activities have been observed around geothermal resources for the last 30 years in so many countries worlwide. Such countries include Indonesia, the Philippines, South America, New Zealand, Switzerland at Basel (2009) and Saint–Gall (2013), The Geysers and Coso geothermal in California fields have a long history of geothermal production and a range of induced seismicity.

Actually, thousands of earthquakes have been observed annually, yet these earthquakes are micro-earthquakes (MEQ's) and not felt by people. In worst recorded cases they could have reached magnitudes of 4 range on Richter scale. The induced seismicity may be entirely of very low magnitudes, or may be a short–lived transient phenomenon. In the majority of the dozens of operating hydrothermal fields around the world, there is no evidence whatsoever of any induced seismicity causing significant damage to the surrounding community.

There are several mechanisms that could be deployed to understand the occurrences of such seismic activities in the geothermal facilities:

1. Pore pressure increase: Increased fluid pressure can reduce stresses keeping the faults from failing and thereby facilitate seismic slip in the presence of an unbalanced stress field. In such cases, the seismicity is driven by the local stress field, but triggered on an existing fracture by the pore-pressure increase. In many cases, the pore pressure required to shear favorably oriented joints can be very low, and vast numbers of microseismic events occur as the pressure migrates away from the well bore in a preferred direction associated with the direction of maximum principal stress.

   In a geothermal field, one obvious mechanism is fluid injection. Point injection from wells can locally increase pore pressure and possibly account for high seismicity around injection wells. If the rock is of very low permeability (not many open fractures) then it may be

necessary to inject fluids at higher pressures. At higher pressures, fluid injection can exceed the rock strength creating new fractures in the rock, i.e hydro-fracturing the rock.

2. Temperature changes: Fluids interacting with hot rock can cause contraction of fracture surfaces in a process known as thermoelastic strain. As with effective stress, the slight opening of the fracture reduces static friction and triggers slip along a fracture that is already near failure in a regional stress field. Alternatively, cool fluids interacting with hot rock can create fractures and seismicity directly related to thermal contraction.

3. Volume change due to fluid withdrawal/injection: As fluid is produced (or also injected) from an underground resource, the reservoir rock may compact or be stressed. These volume changes cause a perturbation in local stresses which are already close to the failure state (geothermal systems are typically located within faulted regions under high states of stress). This situation can lead to seismic slip within or around the reservoir. A similar phenomenon occurs where solid material is removed underground, such as in mines, leading to *Rock Bursts*[1] as the surrounding rock adjusts to the newly created void.

4. Chemical alteration of fracture surfaces: Injecting non-native fluids into the formation (or allowing fluids to flow into the reservoir due to extraction) may cause geochemical alteration of fracture surfaces, thus reducing or increasing the coefficient of friction on the surface. In the case of reduced friction, MEQs (smaller events) would be more likely to occur. It has been supposed that if seismic barriers evolve and asperities form, resulting in increased friction, events larger than MEQs may become more common.

There is also another point that concerns the researchers of geothermal energy about seismic activities. Actually the employment of hydro–fracturing aims at enhancing the permeability of the HDR. However, this enhancement is targeted to a definite size, i.e. the radius of the enhancement is not to exceed a certain distance beyond the injection well (usually a few hundred meters). It is that to extract the maximum heat from a given volume of rock one does not want to have any *fast paths* that would short circuit the water, thus not allowing the injected water to heat to the desired temperature. Ideally, one wants a large matrix of many small fractures to give the maximum surface area for heating the injected water.

Seismic events, though dangerous, are one of the few methods in which permeability enhancement is monitored. If larger events were to be avoided, small events with magnitudes up

[1] A rock burst is a spontaneous violent fracture of rock that can occur in deep mines. The opening of a mine shaft relieves neighboring rocks of tremendous pressure which can literally cause the rock to explode as it attempts to re–establish equilibrium.

to 2 for geothermal sources with radii 100 m or less, could be of great help. However, events of magnitude 2 near certain projects have raised residents concern for both damage from single events and their cumulative effects. Some residents believe that the induced seismicity may cause structural damage similar to that caused by larger natural earthquakes. There is also fear that the small events may be an indication of larger events to follow. A related concern is that not enough resources have been invested in trying to answer some of the questions associated with larger induced events.

The Geothermal Implementing Agreement under the International Energy Agency (IEA) initiated an international collaboration in induced seismicity in 2004. The purpose of this collaboration is stated in the "Environmental Impacts of Geothermal Development, Sub Task D, and Seismic Risk from Fluid Injection into Enhanced Geothermal Systems Geothermal Implementing Agreement (IEA/GIA)" as follows:

Participants will pursue a collaborative effort to address an issue of significant concern to the acceptance of geothermal energy in general but EGS in particular. The issue is the occurrence of seismic events in conjunction with EGS reservoir development or subsequent extraction of heat from underground. These events have been large enough to be felt by populations living in the vicinity of current geothermal development sites. The objective is to investigate these events to obtain a better understanding of why they occur so that they can either be avoided or mitigated. Understanding requires considerable effort to assess and generate an appropriate source parameter model, testing of the model, and then calculating the source parameters in relation to the hydraulic injection history, stress field and the geological background. An interaction between stress modeling, rock mechanics and source parameter calculation is essential. Once the mechanism of the events is understood, the injection process, the creation of an engineered geothermal reservoir, or the extraction of heat over a prolonged period may need to be modified to reduce or eliminate the occurrence of large events.

Following this agreement, the U.S department of energy, Geothermal Technology office has held 3 international workshops, between 2009 and 2010, in which 17 countries have participated. An initial induced seismicity protocol was developed for operators of geothermal fields to follow. Specific protocols for different areas will supplement the general protocol depending on potential for seismicity and proximity to local communities. These activities are continuing in addressing research needs and refining protocols for induced seismicity.

1. GEOTHERMY AND ENHANCED GEOTHERMAL SYSTEMS (EGS): GENERAL VIEW

In final words, the exploitation of geothermal power and electricity generation has increased over the past 30 years by about 15% annually, yet dropped to 3% annually the last 10 years (1990 to 2000) due to an economic declination in the far east and the low price of competing fuels. Direct utilization of geothermal energy has remained fairly steady over the 30 year period at 10% growth annually. Only ten countries reported electrical production and/or direct utilization from geothermal energy at the beginning of this 30 year period. Yet, by the end of this period ($\tilde{2}000$), 72 countries reported utilizing geothermal energy. This is over a seven-time increase in participating countries. At least another 10 countries are actively exploring for geothermal resources and should be on–line by now (Lund, [2007]).

1.7 Relevant studies

These remarks were collected at the beginning of my PhD thesis as I was trying to have a general view about this field of research. These studies may sound difficult for those who are not so deep in the field. However, I have chosen to keep them for those individuals who may find them interesting as comprehensive and auxiliary notes.

- (Cheng et al., [2001]) studied the heat extraction from a fracture embedded in a geothermal reservoir. It is a very simple approach as the authors assumed only thermal effects. They assumed constant aperture width and rigid rock body, they also assumed that there would be no leakage through the walls of the fracture nor would the pore pressure change. The authors considered the following approaches:

    1. Heat transport equation in the fracture, the effects of longitudinal dispersion as well as heat storage were examined.
    2. Heat conduction in the rock body, which was tested for both one and two dimensional effects then both cases were compared.
    3. Integral solution using Green's function has been applied, leading to completely eliminating the outer geometry of the reservoir.

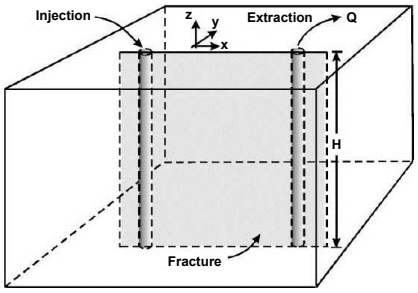

(a) Idealized view of heat extraction from a hot dry rock reservoir.

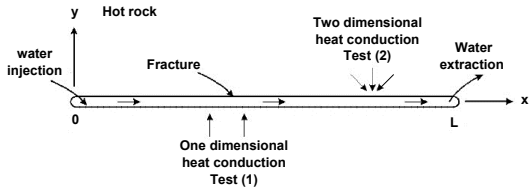

(b) Solution domain of the mathematical problem.

Figure 1.12: Idealized view of heat extraction from a hot dry rock (left) with the mathematical solution domain (right).

This work has proven that:

1. The heat storage and the heat dispersion effects are not usually important due to dominant advective transport in the fracture fluid flow.
2. Two-dimensional heat conduction can significantly alter the prediction of heat extraction temperature and the reservoir life.

3. While modeling of heat conduction in geothermal reservoir, the use of correct reservoir geometry could be important in predicting the life of the HDR reservoir.
4. Improvements like modeling the reservoir elasticity, thermoelasticity, and poroelasticity, leading to a fracture fluid pressure, temperature, and reservoir compliance need fracture aperture–width relations to be established.

- (Ghassemi et al., [2008]) investigated the poroelastic and thermoelastic effects of cold-water injection in an enhanced geothermal system (EGS) by considering flow in a pre–existing fracture in a hot rock matrix that could be permeable or impermeable. Assuming plane fracture geometry, expressions were derived for changes in fracture aperture caused by cooling and fluid leak-off into the matrix.

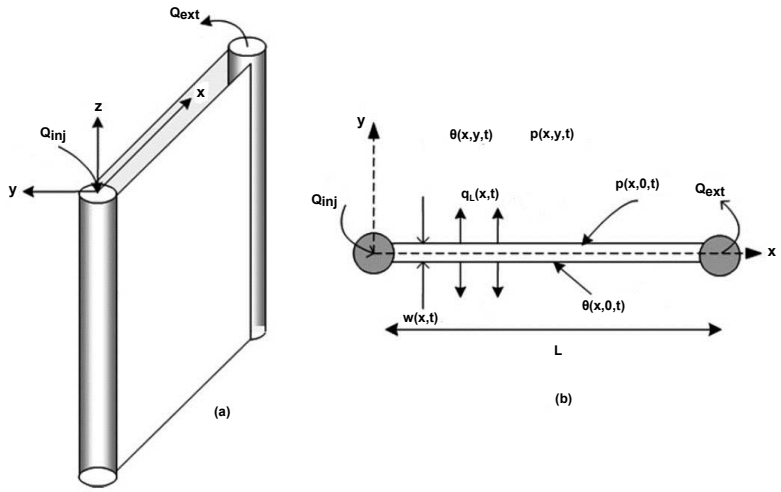

Figure 1.13: Side (a) and top (b) view of the system being modeled. The reservoir is assumed to extend from the top to the bottom of the system. The vertical fracture intersects the entire reservoir and extends between the injection well on the left and the production well on the right.

The authors considered the following approaches:

1. The reservoir is assumed to be horizontal and of constant thickness, confined at the top and the bottom by rigid, impermeable and thermally insulated formations.
2. The fracture is modeled as a vertical plane of uniform width that intersects the entire reservoir thickness.
3. Solution geometry is 2-dimensional.
4. Rock displacement parallel to the fracture is neglected.
5. Deformation of the rock mass is not significant to affect the pore pressure.

This work came out with the following results:

First, the poroelastic effects:

1. Although fluid loss from the fracture into the matrix reduces the pressure in the crack, the poroelastic stress associated with fluid leak-off tends to reduce the aperture and increase the pressure in the fracture (sort of self–pressurization).
2. High rock stiffness and low fluid diffusivity cause the poroelastic contraction of the fracture aperture to slowly develop in time.
3. Maximum reduction of the aperture occurs at the injection point (due to self–pressurization created by extensive leak–off) and becomes negligible at the extraction point.

Second, the thermoelastic effects:

1. Thermally induced stress increases the fracture aperture near the injection point, and as result, the fluid pressure at this point is dramatically reduced.
2. Thermoelastic effects are particularly dominant near the inlet compared to those of poroelasticity, yet pronounced everywhere along the fracture for large times.

- (Bai and Abousleiman, [1997]) discussed the general conditions where the coupling should be maintained and where a partial or full decoupling technique may be applied[1]. Three cases have been addressed by the authors:

  1. For a stiff material or for a material subjected to relatively small load and insignificant fluid flow, the effects of elastic deformation and thermal convection may be neglected. Thus, the system of field equations describing thermo–poroelasticity sums into two equations, namely; the equation of the *balance of mass* with the mechanical part disregarded, and the equation of the *balance of energy* with the mechanical part, the pore fluid part, as well as convectional effect disregarded.
  2. For a stiff material or for a material subjected to relatively small load, and with negligible influence of thermal expansion or contraction on the rate of change of fluid flow. The system of field equations describing thermo–poroelasticity sums into two equations, namely; the equation of the *balance of mass* with the mechanical and the thermal parts disregarded, and the equation of the *balance of energy* with the mechanical and the pore fluid parts disregarded.
  3. For less significant influence of the rate of change of the elastic volumetric deformation on those of both fluid flow and thermal transport, and negligible thermal convection, the system of field equations describing thermo–poroelasticity sums into three equations, namely; the equation of the *balance of momentum*, the equation of the *balance*

[1] Coupling or decoupling here concerns whether to or not to consider the mechanical and fluid diffusive effects in the equation of balance of energy in the frame work of Thermo–poroelasticity, see chapter (2).

of mass with the mechanical part disregarded, and the equation of the *balance of energy* with the mechanical part, the pore fluid part, as well as convectional effect disregarded.

Generally, Thermoelastic effects are manifest in cases like; the storage of high-level nuclear waste in dry rock masses, the contaminated site remediation through hot air stripping, and rock fracturing using non–liquid–type heat sources. Meanwhile the poroelastic effects are manifest in cases like; the consolidation in fluid-saturated porous materials, the fault dislocation due to fluid withdrawal, and borehole stability in oil/gas production, all in the isothermal environment. The results have shown that:

1. The development of a fully coupled thermo–hydro–mechanical approach is, sometimes, necessary to minimize the potential errors while modelling the behavior of poroelastic media under non–isothermal conditions.
2. However, the full coupling may not be feasible if the engineering–oriented analytical solutions are desired.
3. Simplifications, such as using partial decoupling, should be attempted when the influence of each coupling term is determined and the omission of such a term is justified on a physical and analytical ground.

- (Zhou et al., [2009]) provided a three dimensional partially coupled thermo–poroelastic model to investigate the poroelastic and thermoelastic effects of cold water injection into EGS.

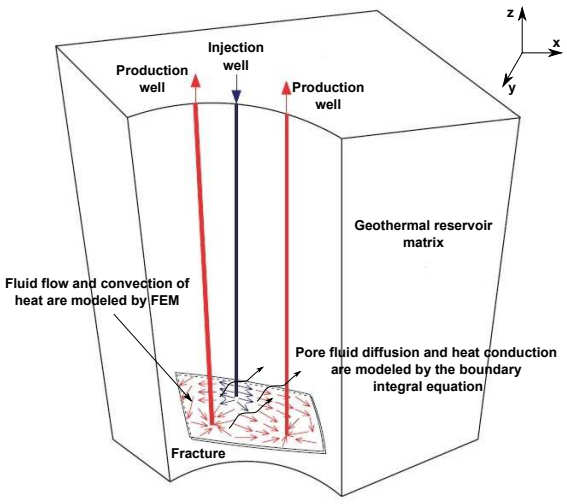

Figure 1.14: Fluid circulation in a geothermal reservoir.

The lubrication fluid flow and the convective heat transfer in the fracture are modeled by finite element method, while the pore fluid diffusion and heat conductive transfer into the reservoir matrix are assumed to be three-dimensional and modeled by the boundary integral equation method without the need to discretize the reservoir. The finite element method and the boundary element method are coupled and share the same mesh on the fracture plane.

The application of the model has shown that:

First, the poroelastic effects:

1. The fluid pressures near the injection well are much larger than those near the extraction wells.
2. The variations of the fluid flow field and the fluid pressure field in the fracture with time may be neglected since the fluid leak off rate (which depends on the difference of the fracture pressure and matrix pore pressure and the permeability of the reservoir matrix) is small compared with the injection rate.
3. The pore pressures dissipate from the fracture surface to the far field with the elapse of the time. A significantly large rock volume experiences pore pressure increases of as much as 1MPa.
4. As pressure in the fracture decreases toward the extraction wells with time, so does the induced total stresses σ_{xx} and σ_{yy}.
5. All poroelastic total stresses σ_{xx}, σ_{yy}, and σ_{zz} are compressive. They are larger around the injection well than those around the extraction wells, which results from the larger fluid pressures in the fracture around the injection well and correspondingly the larger fluid leak off rates from the fracture into the reservoir formation.
6. The total stress components σ_{xx} and σ_{yy} are larger than σ_{zz}, but their values are in the same order of magnitude.
7. The compressive total stresses in the reservoir increase and the front of the stresses resulting from the fluid leak off moves into the reservoir with time.
8. The effective stresses from the fluid leak off are tensile, which enhance rock failure potential around the injection zone and contributes to permeability increase and seismicity.

Second, the thermoelastic effects:

1. With the elapse of the time, the low temperature area spreads from the injection well to the extraction well and the temperature of the extracted fluid decreases. The cooling spreads faster toward the extraction well that is closer.

2. Fracture cooling will induce tensile σ_{xx} and σ_{yy} in the rock.
3. The distributions of σ_{xx} and σ_{yy} at the fracture are similar to the distribution of the temperature.
4. Both σ_{xx} and σ_{yy} are larger near the injection well than their values near the extraction well since the cooling effect on the rock around the injection is more pronounced.
5. The tensile σ_{zz} from the cold water injection would tend to increase fracture aperture and induce new fractures.
6. Values of σ_{zz} are in order of magnitude larger than the σ_{xx} and σ_{yy}.
7. The induced compressive and tensile stresses can contribute to rock failure in shear and tension, resulting in increased seismicity.

- (Ghassemi and Zhou, [2011]) provided a three-dimensional partially coupled numerical model that couples fracture aperture variation to the pressure in the fracture, and that considers the impact of the coupled thermo–poroelastic processes and the feedback between them, when injecting cold water into an arbitrary shaped fracture in geothermal reservoirs, see figure(1.14). The fluid flow and the convective heat transfer in the fracture are modeled by the finite element method, while the three-dimensional pore fluid diffusion and heat conduction in the rock matrix are modeled by the boundary integral equation method without discretizing the reservoir domain. The work has shown that:

  1. Both fracture pressure and aperture are influenced by the poroelastic effect which governs the fracture response during the early injection stage.
  2. The thermoelastic stress becomes dominant after a long time of fluid injection.
  3. When the initial fracture aperture is small enough to generate a relatively large fracture pressure in comparison to the initial reservoir pressure, a large amount of fluid leaks off into the matrix. This significantly decreases the fracture aperture and pressure compared to the case without fluid leak off.
  4. However, as cooling increases, the leak off influence becomes less important with the elapse of time. After a long time of injection, the fracture aperture significantly increases mainly in response to the thermoelastic effects.
  5. As different points on the fracture plane can experience different cooling and pressurization histories, they undergo different stresses and thus display different aperture variations.

There have also been some works which put a great spot of light on the permeability changes, the damage of the rock matrix and the induced seismicity while extracting heat. Some of them are mentioned below for their importance.

- (Lee and Ghassemi, [2010]) A fully–coupled thermo–poro-mechanical finite element model is developed with damage mechanics and stress dependent permeability. The damage model used corresponds to the brittle rock failure behavior with crack initiation, micro–void growth and permanent increase prior to failure. In order to capture the full effects of rock cooling by injection in the presence of higher fluxes caused by rock degradation and permeability enhancement, the model considers both convective and conductive heat transport in the porous medium. Numerical simulations are presented to verify the model and to illustrate the role of various mechanisms in rock fracture and distributed damage evolution.

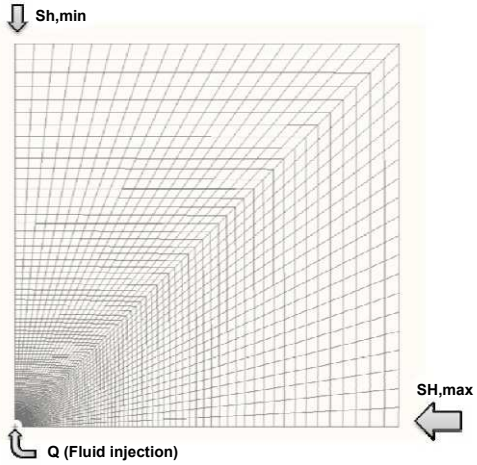

Figure 1.15: Mesh used in simulation; SH, max represents maximum far field stress and Sh, min is for minimum far field stress. Injection rate is Q.

The authors adopted the following approaches:

1. The continuum damage mechanics approach where the strain-stress behavior of a rock can be divided into an elastic phase and a damage phase.
2. In the elastic phase there is no damage in the rock, whereas the rock begins to fail by crack initiation and void growth when the stress conditions reach the failure level, i.e. they satisfy some failure criterion.
3. Damage is measured by using a dimensionless parameter which is related to the initial modulus of elasticity and elastic strain as well as the residual compressive/tensile strengths of the material.
4. The progress of damage is traced using Mohr–Coulomb failure criterion.
5. The rock permeability model used, which employs the effective stresses, considers altered permeability in the elastic and damage phases.

Their work has demonstrated the following points:

1. The effective stresses are mitigated in the damaged phase as result of the reduction of rock modulus and increased permeability.
2. As result, a discontinuous pore pressure field is developed that impacts the total stress distributions around the wellbore.
3. Concentrations of the effective stresses are observed at the interface between the damaged phase and the intact rock. This stress concentration is caused by fluid invasion and leads to damage propagation into the reservoir.

- (Lee and Ghassemi, [2011]) A three–dimensional fully–coupled thermo–poro–mechanical finite element model with damage mechanics is presented. The model considers stress-dependent permeability and convective heat transport in the thermo–poroelastic formulation. Locations of potential induced–seismicity caused by injection are also calculated. The authors have adopted the same approaches as in (Lee and Ghassemi, [2010]).

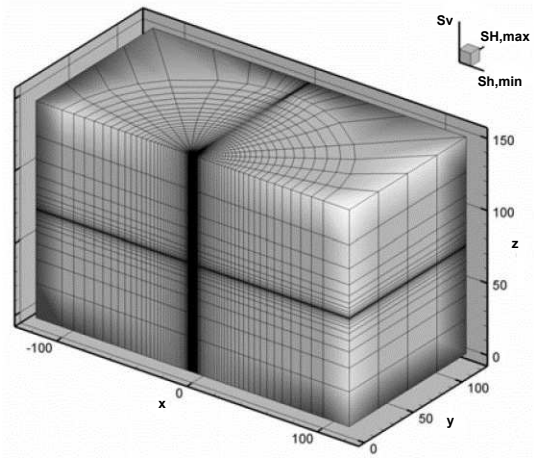

Figure 1.16: Mesh used in simulation; SH, max represents maximum horizontal stress, Sh, min is the minimum horizontal stress, and Sv is vertical stress.

Three different far–field stress regimes were presented by the authors:

1. Strike-slip: (SH, max = 30 MPa, Sh, min = 10 MPa, Sv = 20 MPa), horizontal far-field stress as the minimum *in situ* stress. Numerical results have shown that:
   - Fluid injection causes both effective tangential and effective axial stresses to become tensile.
   - Damage and fractures propagate vertically and horizontally in this case where the minimum stress is horizontal.

  - The effective axial stress caused by fluid injection is the main contributor to tensile failure across the wellbore, (Sh, min as minimum).

2. Thrust ($SH, max = 30$ MPa, $Sh, min = 20$ MPa, $Sv = 10$ MPa), vertical far field stress as the minimum *in situ* stress. Numerical results have shown that:
   - Injection induced damage and fractured area propagate horizontally.
   - The effective axial stress is not significant and the wellbore hoop stress serves to propagate the damage.
   - A higher injection pressure is needed to generate the fractured plane in the homogeneous rock case when Sv is the minimum *in situ* stress rather than Sh, min.
3. Normal faulting regime ($SH, max = 20$ MPa, $Sh, min = 10$ MPa, $Sv = 30$ MPa), the vertical far field stress as the maximum *in situ* stress. Numerical results have shown that:
   - A stronger tendency for the induced damage and fractured zone to propagate vertically.
   - The effective axial stress caused by fluid injection is the main contributor to tensile failure across the wellbore, (Sh, min as minimum).

Number of authors developed the theory of (McTigue, [1986]) to include the states of inhomogeneous *in situ* stresses, see for instance (Detournay and Cheng, [1988]), (Abousleiman and Ekbote, [2005]) and (Abousleiman and Nguyen, [2009]). Others addressed the dual–porosity, see for instance (Abousleiman et al., [1999]). The work of (Abousleiman et al., [1999]) is to be presented:

- (Abousleiman et al., [1999]) The dual-porosity poroelastic behavior of an inclined wellbore subjected to an inhomogeneous *in situ* state of stress, under generalized plane strain conditions is the subject of this study. The finite element formulations are presented and solutions compared to the single porosity cases are shown.
  Anisotropic materials properties and non–homogeneous *in situ* stress conditions generally render the problems of thermo–poroelasticity three-dimensional. In certain conditions it is possible to develop two dimensional algorithms to solve these problems yet material anisotropy and three–dimensional *in situ* stress boundary conditions are admitted by considering the Generalized Plane Strain (GPS) method.

  Results have shown that:

  1. The scenarios of wellbore injection or pumping are frequently assumed by a two–dimensional plane strain setting due to the large axial length to diameter ratios.

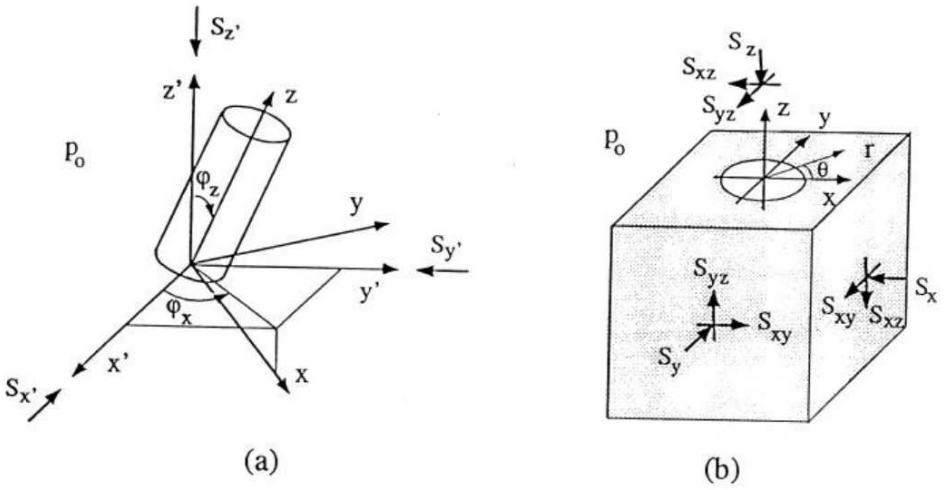

Figure 1.17: Coordinate system for an inclined wellbore.

2. The plane strain approach may not be appropriate since the wellbore axis may not be aligned with one of the principal *in situ* stresses. In addition, the shear stresses along the wellbore axis which are not incorporated in the plane strain situation do influence the wellbore stability.
3. The generalized plane strain method can eliminate these deficiencies without sacrificing the simplicity of the plane strain method, while maintaining the full terms of the three-dimensional stress components.
4. The generalized plane strain approach is suitable for the fractured non-homogeneous media.
5. Preliminary studies identify the fracture spacing, an index of the fracture density, as the influential parameter which controls the magnitudes and distributions of the coupled pore pressure and rock deformation, in particular within the near–well regions.
6. Future parametric investigations may include discrete features of the fracture network, such as orientations, distributions and connectivities.

Chapter 2

Equations for thermo–poroelasticity, fracture propagation and permeability evolution

This chapter provides a brief description of the theory of fluid–saturated thermo–poroelastic media. The constitutive equations used to describe such media are illustrated and substituted in the general conservation laws, to get the field equations that shall be used to solve for the Initial Boundary Value Problems (IBVPs) of thermo–poroelasticity. A brief representation of fracture and damage mechanics is also outpointed. A fracturing model which includes a criterion to decide whether fracturing, in any direction, takes place or not and a rule that provides the incremental length of the crack are presented. Knowing the new fracture radius, the change in fracture aperture is estimated based on experimental data which relate aperture change to change of fracture radius. Using the new fracture aperture along with the fracture radius, the local velocity field is calculated by implementing Navier-Stokes equation for laminar flow between two parallel plates. The macroscopic velocity field is deduced by a directional averaging over the local velocities. An anisotropic permeability tensor, that accurately describes the hydraulic connectivity of the fractured medium, is then calculated by applying Darcy's law for laminar flow. Finally, the fracturing model is modified by accounting for crack aperture reduction, and validation of the model against experimental data is highlighted.

2.1 The theory of fluid-saturated, porous, thermoelastic media

A porous medium is a solid (generally called *matrix*) which is permeated by interconnected voids that could be filled by fluid or gas. Both the solid matrix and the pore space are assumed to be continuous such that they form two interpenetrating continua like a *sponge*. Any porous

medium whose solid matrix is elastic and whose fluid is barotropic is called a *poroelastic* medium; a poroelastic medium is characterized by its permeability, porosity and the properties of its constituents fluid and solid.
The concept of the poroelastic medium has first appeared in the works of *Karl von Terzaghi, 1883-1963* the father of soil mechanics. Yet it was later interpreted generally (independent of its nature and application) in the works of *Maurice Anthony Biot, 1905-1985*. Between 1935-1957, *Biot* developed the theory of dynamic poroelasticity also called (Biot's theory). For his theory of *Linear Poroelasticity* Biot has employed the following equations:

- Equations of *linear elasticity* for the solid matrix.
- *Navier-Stokes* equation for the viscous fluid.
- *Darcy's law* for the flow of fluid through the porous matrix.

The linear theory of fluid–saturated porous thermoelastic medium was developed by (McTigue, [1986]). This theory stands for the compressibility and thermal expansion of both the fluid and the solid constituents. However, the model of *McTigue* is fully linearized and it neglects a lot of phenomena that could be of a vital importance in so many applications. For example, it assumes a homogeneous single–porosity material with a small *Péclet number* so that the convection of heat could be neglected. Considering that in geothermal energy extraction the existence of fracture porosity as well as an increasing permeability is crucial to efficient production, the assumptions of McTigue render the theory of thermo–poroelasticity with some limitations.

Generally the problem to be described is an open system which consists of several phases. It is evident that at the *macroscopic* scale each phase acts separately from others. However, the summation over all phases gives the mixture equations of the system.

2.1.1 Constitutive equations used in thermo–poroelasticity

Constitutive equations are simply relations of two kinetic quantities describing the behavior of materials under different external effects. Some constitutive equations are phenomenological others are derived from stem physical principles. All the constitutive equations of thermo–poroelasticity in this chapter are to be presented for homogeneous single–porosity media.

2.1.1.1 Mixture stress equation

According to (McTigue, [1986]) the mixture stress constitutive equation is expressed as:

$$\sigma_{ij} = 2G\,\varepsilon_{ij} + \frac{2G\nu}{1-2\nu}\,\varepsilon_{kk}\,\delta_{ij} - \kappa\,p\,\delta_{ij} - K\,\alpha_s^{'}\,\theta\,\delta_{ij}, \tag{2.1}$$

where σ_{ij} is the total stress tensor (compressive stresses have negative sign), ε_{ij} is the infinitesimal strain tensor, G is the shear modulus, ν is the drained Poisson's ratio, K is the drained bulk modulus, κ is effective stress (Biot's) coefficient equation (2.2) where $K_s^{'}$ is the first solid constituent bulk modulus:

$$\kappa = \frac{K_s^{'} - K}{K_s^{'}}, \tag{2.2}$$

p is the fluid pore pressure, $\alpha_s^{'}$ is the first cubical thermal expansion coefficient for the solid, and θ is the change of temperature $(T - T_0)$, where T_0 is the reference temperature of the mixture.

By manipulating equation (2.1), the infinitesimal strain tensor ε_{ij} takes the form:

$$\varepsilon_{ij} = \frac{1}{2G}\left[\sigma_{ij} - \frac{\nu}{1+\nu}\,\sigma_{kk}\,\delta_{ij}\right] + \frac{\kappa}{3K}\,p\,\delta_{ij} + \frac{\alpha_s^{'}}{3}\,\theta\,\delta_{ij} \tag{2.3}$$

It is worth mentioning the trace of the infinitesimal strain tensor ε_{kk}:

$$\varepsilon_{kk} = \frac{\sigma_{kk}}{3K} + \frac{\kappa p}{K} + \alpha_s^{'}\,\theta, \tag{2.4}$$

where $K = 2G(1+\nu)/3(1-2\nu)$, and in terms of the elastic modulus E, $K = E/3(1-2\nu)$ and $G = E/2(1+\nu)$.

The infinitesimal shear strain tensor is expressed as:

$$\varepsilon_{ij} = \frac{\sigma_{ij}}{2G}, \quad i \neq j \tag{2.5}$$

2.1.1.2 Change in mixture fluid content equation

According to (McTigue, [1986]) the change in mixture fluid content constitutive equation can be expressed as:

$$\zeta = \frac{1}{3}\left(\frac{1}{K} - \frac{1}{K_s^{'}}\right)(\sigma_{kk} + \frac{3}{B}\,p) - \phi_0(\alpha_f - \alpha_s^{''})\,\theta, \tag{2.6}$$

where ζ is the change in the fluid content, $\alpha_s^{''}$ is the second cubical thermal expansion coefficient for the solid, B is the pore pressure (Skempton's) coefficient equation (2.7) where $K_s^{''}$ is the second solid constituent bulk modulus:

$$\frac{1}{B} = 1 + \phi_0\frac{K(1 - K_f/K_s^{''})}{K_f(1 - K/K_s^{'})}, \tag{2.7}$$

ϕ_0 is the reference porosity of the mixture. In terms of the trace of infinitesimal strain tensor, equation (2.6) can be written as in (Lee and Ghassemi, [2010]):

$$\zeta = \kappa\,\varepsilon_{kk} + p\left(\frac{-\kappa^2}{K} + \frac{\kappa}{BK}\right) - \theta\left[\kappa\,\alpha_s^{'} + \phi_0(\alpha_f - \alpha_s^{''})\right] \tag{2.8}$$

Assuming that $K_s^{'} = K_s^{''} = K_s$ leads to the definition of Biot's modulus M, such that:

$$\frac{1}{M} = \frac{\kappa - \phi_0}{K_s} + \frac{\phi_0}{K_f}, \tag{2.9}$$

and thus equation (2.8) takes the form (Abousleiman and Ekbote, [2005]):

$$p = M\left[\zeta - \kappa\,\varepsilon_{kk} + \theta\left(\kappa\,\alpha_s^{'} + \phi_0(\alpha_f - \alpha_s^{''})\right)\right] \tag{2.10}$$

The difference between the bulk moduli $K_s^{'}$ and $K_s^{''}$ is usually ascribed to the presence of unconnected porosity. Meanwhile, the difference in the expansion coefficients $\alpha_s^{'}$ and $\alpha_s^{''}$ maybe viewed as reflecting a difference between the thermal response of the bulk drained porous medium and that of solid constituents alone. $\alpha_s^{''}$ may be considered equal to $\alpha_s^{'}$ (henceforth denoted by α_s) if the change in temperature is not expected to affect the reference porosity ϕ_0.

2.1.1.3 Darcy's equation

The constitutive equation of Darcy (2.11) relates the apparent flux of fluid to pressure gradient and is used to describe the diffusion of fluid in the porous medium.

$$\boldsymbol{q}_f = \phi_0(\boldsymbol{v}_f - \boldsymbol{v}_s) = -\frac{\boldsymbol{k}}{\mu}.(\boldsymbol{\nabla} p - \rho_f\,\boldsymbol{g}), \tag{2.11}$$

where $\boldsymbol{q}_f$ is the apparent volumetric flux of the fluid relative to the solid skeleton (m/s), $\boldsymbol{v}_f$ is the fluid velocity (m/s), $\boldsymbol{v}_s$ is the solid velocity (m/s), $\boldsymbol{k}$ is the permeability tensor of the mixture (m^2), μ is the dynamic fluid viscosity (Pa.s), ρ_f is the intrinsic fluid density (kg/m^3), and $\boldsymbol{g} = g\,\boldsymbol{e_3}$, g is the gravitational acceleration (m/s^2) and $\boldsymbol{e_3}$ is the descending vertical direction.

2.1.2 Field equations

Field equations are general equations which describe the equilibrium of a medium. Mathematically, these equations are partial differential equations. They are obtained by substituting the constitutive equations in general conservation laws.

The modeling of single–porosity Thermo-Hydro-Mechanical (THM) couplings will assume a homogeneous *continuum* mixture framework. For the model to be general, it would assume an open system where the surroundings could contribute to the balance of the field equations.

2.1.2.1 Equation of balance of momentum of the mixture

The equation of *balance of momentum* also called the *equilibrium equation of elasticity* is derived based on Newton's law of motion which states that: in an initial frame of reference, the material rate of change of the linear momentum of a body is equal to the resultant applied forces.

$$\boldsymbol{\nabla.\sigma} + \boldsymbol{F} = \boldsymbol{0}, \quad \text{or}, \quad \frac{\partial \sigma_{ij}}{\partial x_j} + F_i = 0, \quad i = 1,\, 2,\, 3 \tag{2.12}$$

F_i is the vector of the body forces. By applying this principle in equation (2.1) one obtains:

$$G\,\frac{\partial^2 u_i}{\partial x_j \partial x_j} + \left(K + \frac{G}{3}\right)\,\frac{\partial}{\partial x_i}\,\frac{\partial u_j}{\partial x_j} - \kappa\,\frac{\partial p}{\partial x_i} - K\,\alpha_s^{'}\,\frac{\partial \theta}{\partial x_i} + F_i = 0, \quad i = 1,\, 2,\, 3 \tag{2.13}$$

That is to say three equations of balance of momentum which will result in two possibilities:

1. Whether one gets the displacement components directly by the Finite Element Method (FEM),
2. or one finds the strain components first, then integrates to get the displacement components.

Considering the symmetric strain tensor, 6 strain components are recognized. However, there are always three displacement components: to find a single solution for displacement components, the components of strain tensor cannot be arbitrary. They have to satisfy a *compatibility condition*. In case of plane strain this condition is expressed as:

$$2\frac{\partial^2 \varepsilon_{xy}}{\partial x \partial y} = \frac{\partial^2 \varepsilon_{xx}}{\partial y^2} + \frac{\partial^2 \varepsilon_{yy}}{\partial x^2}, \tag{2.14}$$

where:

$$\begin{aligned} \varepsilon_{xx}(x,y) &= \frac{\partial u_x}{\partial x} \\ \varepsilon_{yy}(x,y) &= \frac{\partial u_y}{\partial y} \\ \varepsilon_{xy}(x,y) &= \frac{1}{2}(\frac{\partial u_x}{\partial y} + \frac{\partial u_y}{\partial x}) \end{aligned} \tag{2.15}$$

2.1.2.2 Equation of balance of mass of the mixture

The equation of *balance of mass* accounts for materials entering or leaving the system. The linearized fluid mass balance equation according (McTigue, [1986]) is given by:

$$\frac{\partial \zeta}{\partial t} + \nabla.\boldsymbol{q}_f = 0 \tag{2.16}$$

By applying this principle to equations (2.8) and (2.11) and by assuming that $K_s^{'} = K_s^{''} = K_s$, it is found that (Abousleiman and Ekbote, [2005]):

$$\nabla.\left(-\frac{\boldsymbol{k}}{\mu}.\boldsymbol{\nabla} p + \frac{\boldsymbol{k}}{\mu}.\rho_f\,\boldsymbol{g}\right) + \kappa\,\frac{\partial}{\partial t}\left(\frac{\partial u_i}{\partial x_i}\right) + \left(\frac{\kappa-\phi_0}{K_s} + \frac{\phi_0}{K_f}\right)\frac{\partial p}{\partial t} = \frac{\partial \theta}{\partial t}\left[\phi_0\,\alpha_f + (\kappa-\phi_0)\alpha_s^{'}\right] \tag{2.17}$$

2.1.2.3 Equation of balance of energy of the mixture

The equation of *balance of energy* comes from the *law of energy conservation* where heat fluxes are replaced by their values given by the law of heat conduction or *Fourier's law*. Assuming an equilibrated temperature field, the equation of balance of energy takes the following form[1] (McTigue, [1986]):

$$\rho c_v\,\frac{\partial \theta}{\partial t} + \rho_f c_{vf}\,q_{f,i}(\boldsymbol{x},t)\frac{\partial \theta}{\partial x_i} + T_0\left[-\left(\phi_0\alpha_f + (\kappa-\phi_0)\alpha_s^{'}\right)\frac{\partial p}{\partial t} + K\,\alpha_s^{'}\,\frac{\partial^2 u_i}{\partial t\partial x_i}\right] - \chi\,\frac{\partial^2\theta}{\partial x_i\partial x_i} = 0, \tag{2.18}$$

where $\rho_f c_{vf}$ is the fluid volumetric heat capacity (J/m^3 °C), ρc_v and χ (W/m °C) are the effective volumetric heat capacity and conductivity of the mixture, $q_{f,i}(\boldsymbol{x},t)$ is the volumetric fluid discharge (m/s), and T_0 is the reference temperature. Several authors including (McTigue, [1986]) and (Bai et Abousleiman, [1997]) have noted that the mechanical and fluid diffusion terms are, in most cases, of very minor effects on the solution of the thermo–poroelastic BVPs. Thus the third term of equation (2.18) can be neglected[2].

$$\underbrace{\frac{\partial \theta}{\partial t}}_{\text{Heat storage}} + \underbrace{\frac{\rho_f c_{vf}}{\rho c_v}\,q_{f,i}(\boldsymbol{x},t)\frac{\partial \theta}{\partial x_i}}_{\text{Heat convection}} - \underbrace{\psi\,\frac{\partial^2\theta}{\partial x_i\partial x_i}}_{\text{Heat conduction}} = 0, \tag{2.19}$$

where ψ is the effective thermal diffusivity of the mixture expressed as $\psi = \chi/\rho c_v$ (m^2/s). Equation (2.19) shows clearly that the convection of heat mitigates the rate in which it is lost by conduction. In the linearized mixture theory, the effective conductivity and heat capacity can be related to the constituent properties:

$$\chi = (1-\phi_0)\chi_s + \phi_0\,\chi_f \tag{2.20}$$

$$\rho c_v = (1-\phi_0)\rho_s c_{vs} + \phi_0\,\rho_f c_{vf} \tag{2.21}$$

The subscripts s and f refer to the solid and fluid constituents respectively.

[1] The influence of pore fluid pressure on the enthalpy of the system is neglected as proven insignificant.

[2] If the convective term is also to be neglected, in cases of small pore fluid velocity for instance, the equation of balance of energy can be decoupled from the system of equations and solved alone, see equation (2.19).

2.1.2.4 The equation of stress diffusion

This equation is derived by manipulating the constitutive equations in the foregoing to reach a form which can be solved by well-known methods (McTigue, [1986]). This approach is an extension of the work of (Rice and Cleary, [1976]).

$$\begin{aligned}\left(\frac{\partial}{\partial t}-c\nabla^2\right)\left(\sigma_{kk}+\frac{3}{B}p\right) &= c\frac{4G(1+\nu)}{3(1-\nu)}\alpha_s^{'}\nabla^2\theta \\ &+ \frac{2GB(1+\nu)(1+\nu_u)}{3(\nu_u-\nu)}\phi_0(\alpha_f-\alpha_s^{''})\frac{\partial\theta}{\partial t},\end{aligned} \tag{2.22}$$

where the hydraulic diffusivity c (m^2/s) is given by (Mc Tigue, [1986]):

$$c=\frac{k}{\mu}\frac{2G(1-\nu)}{(1-2\nu)}\left[\frac{B^2(1+\nu_u)^2(1-2\nu)}{9(1-\nu_u)(\nu_u-\nu)}\right] \tag{2.23}$$

The undrained Poisson's ratio is given by:

$$\nu_u=\frac{3\nu+B(1-2\nu)(1-K/K_s^{'})}{3-B(1-2\nu)(1-K/K_s^{'})} \tag{2.24}$$

Following equation (2.22), it is obvious that the quantity $(\sigma_{kk}+\frac{3}{B}p)$ is integrated in a diffusion equation that depends on spatial and temporal effects of the temperature field.

Equation (2.22) is derived without invoking the equation of balance of energy. Consequently, this equation is general and it could be used for many theories with or without considering the convection of heat.

If equation (2.19) is to be considered without the convective term, the temperature field is decoupled and thus solved for alone. The temperature field is henceforth substituted in the diffusion equation (2.22) to get the term $(\sigma_{kk}+\frac{3}{B}p)$ which is then used to solve for the pressure field, equation (2.17).

2.1.3 Time scale of Thermo–poroelastic IBVPs

There are two distinct time scales associated with the problems of thermo-poroelasticity; one for each of the operating diffusive mechanisms. The first time scale is associated with the diffusive heat transfer and is given by $t_\theta = L^2/\psi$. In general, the thermal properties used in this expression should be weighted average quantities based on the volume fraction of the pores, see equations (2.20) and (2.21).

The second time scale is associated with diffusive flow of the pore fluid and is given by $t_p = L^2/C_c$, C_c is the consolidation coefficient (m^2/s) and is defined as $C_c = k\,(\lambda+2G)/\gamma_f$, k is the hydraulic conductivity of the medium (m/s), γ_f is the specific weight of the pore fluid

($\mathrm{N/m^3}$) and $\lambda \,\&\, G$ are Lamé's elastic constants ($\mathrm{N/m^2}$). In both cases L is a typical length of the BVP considered (m).

2.2 Fracture mechanics and damage

A brief description of the failure theory and fracture mechanics is to be presented in this section. A commonly used approach which combines the physical (at microscopic scale) and the phenomenological (at macroscopic scale) conceptions of fracturing is outlined. This approach will be employed to calculate an anisotropic damage tensor which precisely describes the material state under loading. Though damage is well defined mathematically through out this chapter, it shall not be used further in this research while doing the simulations. We hope that future studies will integrate this model in definite frameworks where it will be significantly utilized.

The *theory of failure* is the science of predicting the conditions under which solid materials fail under the action of external loads. Depending on certain conditions like the rate of loading and/or the stress state, this theory states that the failure of materials can be either *brittle* or *ductile*.

The damage of a specific material means the loss of the material capability to hold loads. This failure can be tested in different scales from *microscopic* to *macroscopic*.

- Microscopic failure is expressed in terms of crack propagation and initiation. Henceforth, all the failure criteria are related to microscopic fracturing.
- Macroscopic failure is defined in terms of load carrying capacity or energy storage capacity. The macroscopic failure models can be expressed in terms of macroscopic effects like stress or strain or macroscopic property like *stiffness* or the coefficient of thermal expansion.

Generally there are five levels to consider the damage of a specific material; the material behavior at one level is considered as a collective of its behavior at a sub–level. A damage model should be consistent at each level. These levels are summarized as below:

1. The structural element scale.
2. The macroscopic scale where macroscopic stresses and strains are defined.
3. The mesoscale which is represented typically by a void.
4. The microscale.

5. The atomic scale.

All these criteria, to be considered, render the development of a perfect damage model a quite tremendous task. One should choose a model such that it includes as many levels as possible and such that it is consistent at each level. To go on with describing damage, a brief discussion of fracture mechanics is to be presented below.

2.2.1 Fracture mechanics

Fracture mechanics is the field of mechanics which studies the initiation and evolution of cracks. It relates the theories of *elasticity* or *plasticity*, in terms of stress and strain, to the microscopic crystallographic defects of materials to predict the macroscopic behavior.

2.2.1.1 Linear Elastic Fracture Mechanics (LEFM)

Linear elastic fracture mechanics was first developed by *A. A. Griffith*, see (Griffith, [1921]), to explain the failure of brittle materials. Figure (2.1) shows an edge crack embedded in a semi–infinite plate subjected to a loading state.

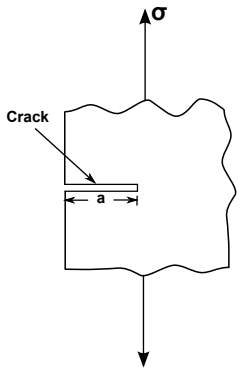

Figure 2.1: An edge crack of length a in a semi–infinite plate.

Considering the model of figure (2.1), Griffith found that:

$$\sigma_f \sqrt{a} = \text{Constant}, \tag{2.25}$$

where σ_f is the stress at the crack's tip (at the initiation of the crack propagation, fracturing stress). By solving the elasticity problem of a finite crack in an elastic plate, Griffith also found that:

$$\text{Constant} = \sqrt{\frac{2\,E\,\gamma}{\pi}}, \tag{2.26}$$

where E is the Young's modulus of the material (Pa) and γ is the surface energy density (J/m^2) of the material. For this simple case of a thin rectangular plate with a crack perpendicular to the load, Griffith's theory becomes:

$$G = \frac{\pi\,\sigma^2\,a}{E}, \tag{2.27}$$

where G is the strain energy release rate or the rate at which energy is absorbed by growth of the crack (J/m^2). The strain energy release at the threshold of crack propagation is defined using the fracturing stress σ_f as:

$$G_c = \frac{\pi\,\sigma_f^2\,a}{E} \tag{2.28}$$

If for any case $G \geq G_c$ the crack will begin to propagate.

The work of Griffith was quite sufficient to describe the evolution of cracks in brittle materials. However, later *G. R. Irwin* found that the work of Griffith not able to represent the evolution of cracks in the ductile materials. In ductile materials a plastic zone is developed at the tip of the crack and it increases as the applied load increases. Thus there is a part of the energy dissipated during this plastic loading. Irwin divided the fracturing energy into two parts (Irwin, [1957]):

1. The stored elastic strain energy which is released as the crack grows (driving force of the fracture).
2. The dissipated energy which provides the resistance to fracture.

$$\text{Following that:} \qquad G = 2\gamma + G_p, \tag{2.29}$$

where γ is the surface energy and G_p is the plastic energy dissipation per unit area of crack growth (J/m^2). Irwin's energy criterion can be written as:

$$\sigma\,\sqrt{a} = \sqrt{\frac{E\,G}{\pi}}, \quad \text{or,} \quad K_I = \sigma\,\sqrt{a\,\pi} \tag{2.30}$$

$$\begin{aligned} K_c &= \sqrt{E\,G_c}, \quad \text{for plane strain} \\ K_c &= \sqrt{\frac{E\,G_c}{1-\nu^2}}, \quad \text{for plane stress} \end{aligned} \tag{2.31}$$

K_I is the stress intensity factor (Pa.m$^{0.5}$), K_c is the crack toughness (Pa.m$^{0.5}$) and ν is the Poisson's ratio. Cracks start to propagate when $K_I \geq K_c$.

Depending on the way of loading the material, there are several modes to express the intensity factor, see figure (2.2):

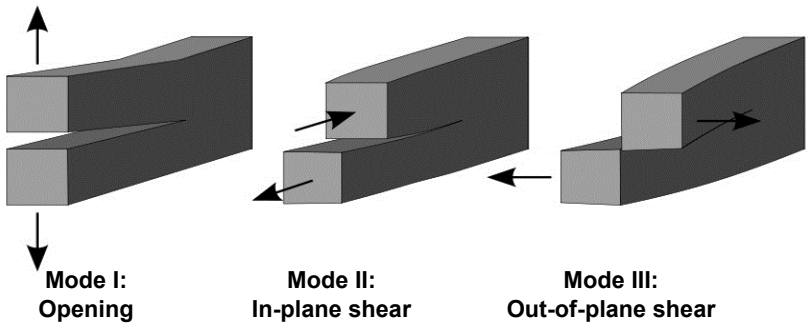

Figure 2.2: The three modes of fracturing.

1. Mode I crack, (K_I): Opening mode (a tensile stress normal to the plane of the crack).
2. Mode II crack, (K_{II}): Sliding mode (a shear stress acting parallel to the plane of the crack and perpendicular to the crack front).
3. Mode III crack, (K_{III}): Tearing mode (a shear stress acting parallel to the plane of the crack and parallel to the crack front).

Note that the expression for K_I in equation (2.30) shall be different for geometries other than the center–cracked infinite plate discussed by Irwin and Griffith.

2.2.1.2 Elastic–plastic fracture mechanics (EPFM)

A lot of materials show non–linearities or inelastic behavior under considerable loads: at such states the adoption of the LEFM may not hold correct. For cases when the plastic zone reaches a size of the same order of magnitude as the crack, or when the plastic zone shape changes as the applied load increases, the work of Irwin does not stand correct and Elastic Plastic Fracture Mechanics (EPFM) is to be considered.

EPFM is not to be presented in this thesis and all models are to be simulated under the framework of LEFM.

2.2.2 Evolution of damage and damage tensor

Let us consider a body which initially represents a continuum without defects at state (1). The body is later loaded and cracks are initiated, state (2). A vector of displacement $\boldsymbol{u}$ that tracks all the points from state (1) to state (2) can connect the two states. $\boldsymbol{b} = \boldsymbol{u}^+ - \boldsymbol{u}^-$ is the jump[1] of the field $\boldsymbol{u}$ crossing a definite surface S. If $\boldsymbol{n}$ is a unit vector normal to S, then $b_i\, n_j$ is a

[1]Note that $||\boldsymbol{b}|| = 2\,||\boldsymbol{u}^+||$ is the distance between the sides of the crack at a given point. The vector $\boldsymbol{b}$ has the same direction as the unit vector $\boldsymbol{n}$ normal to the crack face at the same point where $||\boldsymbol{b}||$ is calculated.

second order tensor that corresponds to the defect at each point $M \in S$. The geometry of such a defect as a whole is defined by a field concentrated on S as:

$$\boldsymbol{D} = \boldsymbol{b}\,\boldsymbol{n}\,\delta S \tag{2.32}$$

For many defects equation (2.32) goes like:

$$\boldsymbol{D} = \sum_k \boldsymbol{b}_k\,\boldsymbol{n}_k\,\delta S_k \tag{2.33}$$

$\boldsymbol{D}$ is a singular tensor field that describes isolated defects. This field should be spread over an elementary volume Ω to reach the continuum model (*space averaging*). Let us consider a point M at the center of an elementary volume Ω: the equivalent continuum tensor $(\boldsymbol{D})_\Omega$ at point M is obtained by an integration reduced to the sum of several integrals over the parts $S_k(\Omega)$ of the discontinuity surface S_k contained in Ω.

$$(\boldsymbol{D})_\Omega = \frac{1}{\Omega}\sum_k \int_{S_k(\Omega)} \boldsymbol{b}_k\,\boldsymbol{n}_k\,dS_k, \tag{2.34}$$

$(\,.\,)_\Omega$ means averaging over a representative volume Ω. Since $\boldsymbol{b}$ and $\boldsymbol{n}$ have the same direction, the field $\boldsymbol{b}$ can be written as $\boldsymbol{b} = \beta\boldsymbol{n}$ where β is the distance between the sides of the crack at a given point ($\beta = ||\boldsymbol{b}||$). Equation (2.34) is now expressed as:

$$(\boldsymbol{D})_\Omega = \frac{1}{\Omega}\sum_k \int_{S_k(\Omega)} \beta_k\,\boldsymbol{n}_k\,\boldsymbol{n}_k\,dS_k \tag{2.35}$$

As far as linear elastic properties are considered (i.e. elastic changes of state (2)), the history of transition from state (1) to state (2) is irrelevant. Only crack field geometry of state (2) is of importance.

Most of the damage models assume that the damage simply alters the elasticity of the material. A natural common step is to assume that the free–energy density (W) is a function of the relevant state variables, generally, the strain and the damage (Atkinson, [1991]):

$$W = W(\boldsymbol{\varepsilon}, \boldsymbol{D}) \tag{2.36}$$

For small deformations, W is a quadratic in the strains and a quadratic dependence on $\boldsymbol{D}$ is also assumed. The stress is then derived from the free–energy density as common:

$$\boldsymbol{\sigma} = \frac{\partial W}{\partial \boldsymbol{\varepsilon}} \tag{2.37}$$

According to the models proposed in (Lubarda et al., [1994]), (Souley et al., [2001]) and (Shao et al., [2005]), the tensile stress (T) on a given crack is assumed to be proportional to the applied deviatoric stress normal to the surface of the crack such that:

$$T = F\ \boldsymbol{n}^T.\boldsymbol{\sigma^d}.\boldsymbol{n}, \tag{2.38}$$

where $\boldsymbol{\sigma^d}$ is the applied deviatoric stress tensor $\boldsymbol{\sigma^d} = \boldsymbol{\sigma} - (\mathrm{tr}\,\boldsymbol{\sigma}/3)\,\boldsymbol{\delta}$, $\boldsymbol{n}$ is a unit vector normal to the crack surface and F is the proportionality factor between the local tensile stress and the applied deviatoric stress. The proportionality factor F is given by (Atkinson, [1991], p. 201):

$$F = f\left[\frac{d}{\boldsymbol{a}.\boldsymbol{n}\sqrt{1-\dfrac{\boldsymbol{a}.\boldsymbol{n}}{d_1}}}\right], \tag{2.39}$$

where d is the size of the tensile region, f is a constant, d_1 is the distance between the neighboring cracks in the initial configuration, and $\boldsymbol{a} = a\,\boldsymbol{n}$ is the crack vector of magnitude a proportional to the crack size.

If it is assumed that a is constant and related to the initial configuration, F is a linear function of d since the local tensile stress relieves as cracks propagate. This function plays a similar role as a hardening–softening function in plastic models.

By considering the compressive stress acting on the crack due to the hydrostatic component of the applied stress, the local driving normal traction acting on a crack is given by:

$$T = \frac{1}{3}\mathrm{tr}\,\boldsymbol{\sigma} + F\ \boldsymbol{n}^T.\boldsymbol{\sigma^d}.\boldsymbol{n} \tag{2.40}$$

2.3 A Directionally Distributed Fracture Model (DDFM) to describe damage and permeability enhancement

This section aims at defining a fracturing model that will be used to describe damage and permeability evolution of geomaterials under loading. Though anisotropic damage is fully presented mathematically, it will not be used later in the simulations.

The model adopted in this work to represent damage and permeability enhancement is the model proposed by (Shao et al., [2005]). The motivations behind using this model stem from the following facts:

1. It is a coupled constitutive model which takes into account the intrinsic permeability of the rocks.

2. The formulation of the model is based on experimental observations and main physical mechanisms included at the microcracks scale.

3. The model is suitable for compression–dominated and tensile–dominated cracks.

4. The model is expressed in the macroscopic scale and thus it can be easily implemented in engineering problems.

This model is based on a semi–empirical and engineering–oriented approach. It is a phenomenological model where the relevant micromechanical features are included. Hence, it gathers the characteristics of the micromechanical and phenomenological models. The dissipation of the stored strain energy is a prime result of damage and the plastic deformation due to dislocation can be neglected (still working in the frame of LEFM).

The following assumptions are, however, to be considered when opting this model:

1. The crack density remains small and the interaction between microcracks can be neglected before the onset of the coalescence of microcracks.

2. The initial behavior of materials is isotropic and anisotropy is induced by preferential growth of microcracks.

3. The model is limited to the mechanical behavior of brittle rocks before the macroscopic failure.

2.3.1 The DDFM for anisotropic damage

Consider a representative elementary volume (REV) Ω containing an arbitrary distribution of microcracks in space orientations and subjected to a uniform stress field on its boundary. A continuous crack density function, denoted by $\varpi(\boldsymbol{n})$ where $\boldsymbol{n}$ is a unit vector normal to the boundary of Ω, is introduced to represent the orientational distribution of such cracks.

The macroscopic free enthalpy can be obtained by the integration of crack contributions over all orientations defined on the surface of a unit sphere denoted by S. The elastic enthalpy of cracked material is written as, see appendix (A.1) for details:

$$\begin{aligned} W_c &= \frac{1}{2}\boldsymbol{\sigma}' : \boldsymbol{S}^0 : \boldsymbol{\sigma}' + \frac{h}{4\pi}\int_{S^+} \varpi(\boldsymbol{n})\left(1-\frac{\nu_0}{2}\right)(\boldsymbol{\sigma}'.\boldsymbol{n}).\langle \boldsymbol{n}.\boldsymbol{\sigma}'.\boldsymbol{n}\rangle\, \boldsymbol{n}\, dS \\ &+ \frac{h}{4\pi}\int_{S^-} \varpi(\boldsymbol{n})\left[(\boldsymbol{\sigma}'.\boldsymbol{\sigma}') : (\boldsymbol{n}\otimes\boldsymbol{n}) - \boldsymbol{\sigma}' : (\boldsymbol{n}\otimes\boldsymbol{n}\otimes\boldsymbol{n}\otimes\boldsymbol{n}) : \boldsymbol{\sigma}'\right] dS \end{aligned} \tag{2.41}$$

The surface S is decomposed into two complementary but non-overlapped subdomains. Respectively, the subdomain S^+ corresponds to the orientations of opening cracks and the subdomain S^- corresponds to the orientations of closing cracks.

$\boldsymbol{S}^0$ is the initial elastic compliance tensor of the undamaged material and $\boldsymbol{\sigma}'$ is the Cauchy effective stress tensor. The bracket $\langle\, \boldsymbol{n}.\boldsymbol{\sigma}'.\boldsymbol{n}\,\rangle$ defines the positive cone of the normal effective stress in the orientation $\boldsymbol{n}$. $\varpi(\boldsymbol{n})$ is the crack density in the orientation $\boldsymbol{n}$ and h is the elastic compliance of the cracks, defined respectively as:

$$\varpi(\boldsymbol{n}) = \frac{N\, r(\boldsymbol{n})^3}{\Omega}, \qquad h = \frac{16(1-\nu_0^2)}{3E_0(2-\nu_0)} \tag{2.42}$$

N and $r(\boldsymbol{n})$ are the number and the average radius of cracks in the orientation $\boldsymbol{n}$ respectively. E_0 and ν_0 are the drained Young's modulus and the Poisson's ratio of the undamaged material respectively.

Assuming isotropic distribution of microcracks in the initial material, the macroscopic damage tensor is defined as the relative variation of crack density in each orientation:

$$\boldsymbol{D} = \frac{1}{4\pi}\int_S \varpi(\boldsymbol{n})\,(\boldsymbol{n}\otimes\boldsymbol{n})\, dS = \frac{1}{4\pi}\int_S \frac{N}{\Omega}\,(r(\boldsymbol{n})^3 - r_0^3)\,(\boldsymbol{n}\otimes\boldsymbol{n})\, dS, \tag{2.43}$$

where r_0 is the average radius of initial microcracks, compare with equation (2.35). By integrating equation (2.41) analytically, the free–enthalpy is obtained as function of the damage tensor $\boldsymbol{D}$:

$$\begin{aligned} W_c &= \frac{1}{2}\boldsymbol{\sigma}' : \boldsymbol{S^0} : \boldsymbol{\sigma}' + a_1\,\mathrm{tr}(\boldsymbol{D})\,(\mathrm{tr}\boldsymbol{\sigma}')^2 + a_2\,\mathrm{tr}(\boldsymbol{\sigma}'.\boldsymbol{\sigma}'.\boldsymbol{D}) + a_3\,\mathrm{tr}(\boldsymbol{\sigma}')\,\mathrm{tr}(\boldsymbol{D}.\boldsymbol{\sigma}') \\ &+ a_4\,\mathrm{tr}(\boldsymbol{D})\,\mathrm{tr}(\boldsymbol{\sigma}'.\boldsymbol{\sigma}') \end{aligned} \tag{2.44}$$

The four parameters a_i depend on the elastic properties of intact material as follows:

$$a_1 = \frac{-c}{70}\,h, \quad a_2 = \frac{7+2c}{7}\,h, \quad a_3 = \frac{c}{7}\,h, \quad a_4 = \frac{-c}{35}\,h \tag{2.45}$$

The coefficient c is $c = -\nu_0$ for the case of opening cracks and $c = -2$ for the case of closing cracks. It is important to point out that the expression of the free–enthalpy given by (2.44) is valid only for two particular cases;

1. all the cracks are always opening or;
2. all the cracks are always closing.

The stress–strain relation of the damaged material is obtained by deriving the equation of strain energy (2.44):

$$\begin{aligned} \boldsymbol{\varepsilon} + \boldsymbol{\varepsilon}^r(\boldsymbol{D}) = \frac{\partial W_c(\boldsymbol{\sigma}',\,\boldsymbol{D})}{\partial \boldsymbol{\sigma}'} &= \frac{1+\nu_0}{E_0}\,\boldsymbol{\sigma}' - \frac{\nu_0}{E_0}(\mathrm{tr}\boldsymbol{\sigma}')\boldsymbol{\delta} + 2a_1(\mathrm{tr}\boldsymbol{D}\,\mathrm{tr}\boldsymbol{\sigma}')\boldsymbol{\delta} + a_2(\boldsymbol{\sigma}'.\boldsymbol{D} + \boldsymbol{D}.\boldsymbol{\sigma}') \\ &+ a_3[\mathrm{tr}(\boldsymbol{\sigma}'.\boldsymbol{D})\boldsymbol{\delta} + (\mathrm{tr}\boldsymbol{\sigma}')\boldsymbol{D}] + 2a_4(\mathrm{tr}\boldsymbol{D})\boldsymbol{\sigma}', \end{aligned} \tag{2.46}$$

where $\boldsymbol{\delta}$ is the Kronecker delta tensor, $\boldsymbol{\varepsilon}^r(\boldsymbol{D})$ is the damage–related inelastic strain tensor. This tensor is not related to plastic dislocation flow but rather associated with damage evolution[1] and thus the damage growth is the only dissipation mechanism in the material.

The constitutive equation (2.46) can be rewritten in the following form:

$$\boldsymbol{\varepsilon} + \boldsymbol{\varepsilon}^r(\boldsymbol{D}) = \frac{\partial W_c(\boldsymbol{\sigma}',\,\boldsymbol{D})}{\partial \boldsymbol{\sigma}'} = \boldsymbol{S}(\boldsymbol{D}) : \boldsymbol{\sigma}' \tag{2.47}$$

The elastic compliance tensor of the damaged material, $\boldsymbol{S}(\boldsymbol{D})$, is given by:

$$\begin{aligned} S_{ijkl}(\boldsymbol{D}) &= \frac{1+\nu_0}{2E_0}\,(\delta_{ik}\,\delta_{jl} + \delta_{il}\,\delta_{jk}) - \frac{\nu_0}{E_0}\delta_{ij}\,\delta_{kl} + 2a_1(\mathrm{tr}\boldsymbol{D})\delta_{ij}\,\delta_{kl} \\ &+ \frac{1}{2}a_2(\delta_{ik}D_{jl} + \delta_{il}D_{jk} + D_{ik}\delta_{jl} + D_{il}\delta_{jk}) + a_3(\delta_{ij}D_{kl} + D_{ij}\delta_{kl}) \\ &+ a_4(\mathrm{tr}\boldsymbol{D})(\delta_{ik}\,\delta_{jl} + \delta_{il}\,\delta_{jk}) \end{aligned} \tag{2.48}$$

[1] We are always working in the frame of LEFM. These permanent strains are direct result of the macroscopic volumetric dilatancy due to crack face mismatch and local grain-matrix interaction during crack growth.

2.3.2 A fracturing criterion for the DDFM

The damage evolution can be determined by a crack propagation criterion based on LEFM equations (2.49) and (2.50). This criterion uses a simple approach inspired from fracture mechanics, section (2.2.1). The growth of the idealized penny–shaped cracks is assumed similar. The propagation of each crack is calculated at each loading step using this criterion, and the damage tensor is then calculated using equation (2.43).

This model combines the two modes (I and II) of crack propagation and accounts for all possible fracture spatial orientations. For any group of cracks in a specific direction $\boldsymbol{n}$, the local stress normal to the crack surface acts as the confining pressure, meanwhile the local stress applied to the crack plane is the driving force for the crack propagation, see also equation (2.40). All the real cracks are imagined as penny–shaped cracks embedded in an infinite body and submitted to local effective stresses.

$$F(\boldsymbol{\sigma'},\, r,\, \boldsymbol{n}) = \sqrt{r}\left[\sigma_n^{'}\left(\frac{f_{c,t}}{f_{c,t}+\langle -\sigma_n^{'}\rangle}\right)^m + f(r)\,\tilde{q}(\boldsymbol{n})\right] - C_{rc} \leq 0 \tag{2.49}$$

$$\sigma_n^{'} = \boldsymbol{n}.\boldsymbol{\sigma'}.\boldsymbol{n}, \quad \boldsymbol{\sigma'^{d}} = \boldsymbol{\sigma'} - \left(\frac{\operatorname{tr}\boldsymbol{\sigma'}}{3}\right)\boldsymbol{\delta}, \quad \sigma_n^{'d} = \boldsymbol{n}.\boldsymbol{\sigma'^{d}}.\boldsymbol{n}, \quad \tilde{q}(\boldsymbol{n}) = 3\,\langle \sigma_n^{'d}\rangle \tag{2.50}$$

In these equations[1], $\sigma_n^{'}$ is the normal effective stress applied to the crack, and $\tilde{q}(\boldsymbol{n})$ is the normal projection of the deviatoric effective stress tensor. The bracket $\langle x\rangle$ denotes that $\langle x\rangle = (x + |x|)/2$. C_{rc} is a material parameter whose physical meaning is similar to the fracture toughness K_c, see appendix (B.1).

- The exponent m describes the non–linear dependence of crack propagation condition on the confining pressure. The ratio subjected to the power m tends to decrease announcing the stabilizing effect of a compressive normal stress[2].

- $f_{c,t}$ is either the uniaxial compression strength or the uniaxial tensile strength of the material. The choice of the controlling strength depends on the dominant fracturing mechanism; the compressive strength for compression–dominated cracks and the tensile strength for the tension–dominated cracks.

- $f(r)$ is a positive scalar valued function, see figure (2.3), which controls the kinetics of crack propagation and has a meaning similar to the function described in equation (2.39). The form of the function $f(r)$ is determined experimentally based on the deterioration of

[1] The mechanism of the model is illustrated later in this section after defining all the parameters of the model.
[2] We use negative sign for compressive stresses in our sign convention.

the elastic properties as damage evolves. However, $f(r)$ must satisfy two conditions (Shao et al., [2005]):

1. The function should decrease as the crack begins to propagate denouncing the relaxation of local tensile stresses as the cracks grow away from the zone of stress concentration. This effect insures the stable growth of cracks.
2. As the cracks start to coalesce the function reaches an asymptotic value. This effect marks the onset of damage localization and macroscopic failure.

For this model the function $f(r)$ takes the following form:

$$f(r) = \begin{cases} \eta \left(\frac{r_f}{r}\right), & r < r_f \\ \eta, & r \geq r_f \end{cases} \tag{2.51}$$

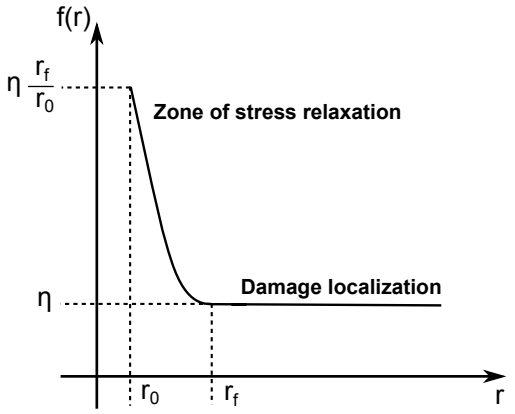

Figure 2.3: The definition of the function $f(r)$.

r_f denotes the critical crack radius for accelerated coalescence of microcracks, and η is a parameter of the model. The loading-unloading condition for crack propagation in the orientation $\boldsymbol{n}$ is defined according to the Kuhn-Tucker relations:

$$\dot{r} \geq 0, \quad F(\boldsymbol{\sigma}', r, \boldsymbol{n}) \leq 0, \quad \dot{r}\, F(\boldsymbol{\sigma}', r, \boldsymbol{n}) = 0 \tag{2.52}$$

When the continuum body is under compression–dominated stresses, material fails due to exceeding the limit of the compressive strength and $f_{c,t}$ is replaced by f_c such that:

$$f_c = \frac{C_{rc}}{\eta \sqrt{r_f}} \tag{2.53}$$

Otherwise, tensile–dominated stresses state is controlling and failure is happening due to exceeding the limit of tensile strength f_t such that:

$$f_t = \frac{C_{rc}}{(1+2\eta) \sqrt{r_f}} \tag{2.54}$$

Compression–dominated or tensile–dominated stresses state is determined by considering the active fracturing mode, that is to say:

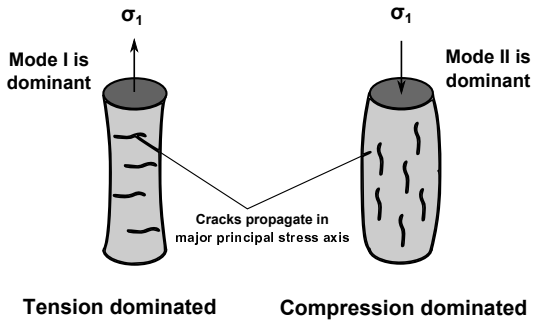

Figure 2.4: Cylindrical rock sample subjected to tensile dominated stresses left, and compressive dominated stresses right.

$f_c/f_t = (1+2\eta)/\eta$, this ratio ranges between 2 and 23 depending on the type of rocks, hence $\eta \in [\sim 0.05,\ \infty]$. For granite, $f_c/f_t \approx 16$.

To better understand this fracturing criterion, let us consider a vertical crack embedded in a cylindrical dry rock sample subjected to the stress state shown in figure (2.5). Compressive stresses are negative in the sign convention adopted all along this research. The driving stresses at the crack scale can be expressed as:

$$\sigma_n^{'} = \sigma_2, \quad \text{and} \quad \tilde{q}(\boldsymbol{n}) = \langle \sigma_2 - \sigma_1 \rangle \tag{2.55}$$

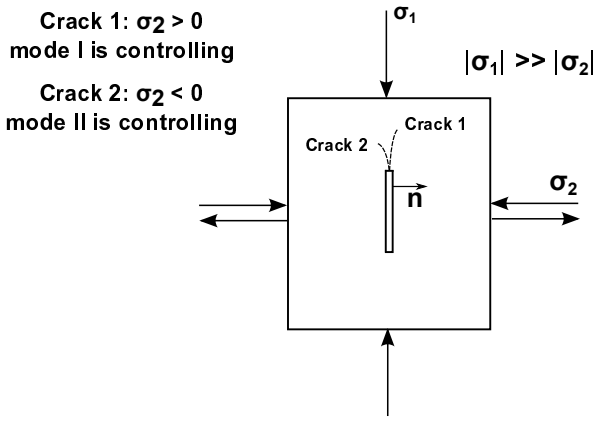

Figure 2.5: Vertical crack embedded in a cylindrical rock sample subjected to an arbitrary stress state, out–of–plane stress is equal to σ_2.

If σ_2 is compressive (negative), the factor $[f_c/(f_c+\langle -\sigma_n \rangle)]^m < 1$ and more emphasis is placed on the term $q(\boldsymbol{n})$ and mode II of fracturing is controlling the propagation of cracks. Controversially, if $\sigma_2 > 0$, the factor $[f_t/(f_t + \langle -\sigma_n \rangle)]^m = 1$ and the driving force $\sigma_n^{'}$ is as effective as the

term $q(\boldsymbol{n})$. At this point propagation of the crack happens quite fast and mode I is controlling the fracturing.
This particular case has been presented to illustrate the roles of the driving forces in the fracturing criterion. Other possibilities are to be worked the same way, and the model shall always stand for mode I and/or mode II of fracturing whichever is dominant.

The evolution of the average radius of a set of cracks in direction $\boldsymbol{n}$ as a function of the average crack radius, the normal effective stress and the deviatoric effective stress can be derived following equations (2.49) and (2.50). Though the evolution of crack radius is also derived mathematically for the unstable crack growth ($r \geq r_f$), it will not be used further in doing the simulations through out this research.

First, when $r < r_f$:

$$F = \sqrt{r}\,\sigma_n^{'}\left(\frac{f_{c,t}}{f_{c,t}+\langle-\sigma_n^{'}\rangle}\right)^m + 3\,\eta\left(\frac{r_f}{\sqrt{r}}\right)\langle\sigma_n^{'d}\rangle - C_{rc} = 0, \tag{2.56}$$

and,

$$\frac{\partial F}{\partial r} = \frac{1}{2\sqrt{r}}\,\sigma_n^{'}\left(\frac{f_{c,t}}{f_{c,t}+\langle-\sigma_n^{'}\rangle}\right)^m - \frac{3}{2}\,\eta\left(\frac{r_f}{\sqrt{r^3}}\right)\langle\sigma_n^{'d}\rangle \tag{2.57}$$

$$dr = -\frac{1}{\dfrac{\partial F}{\partial r}}\left[\Pi(r,\,\sigma_n^{'})\,(\boldsymbol{n}\otimes\boldsymbol{n}) + \Psi(r,\,\sigma_n^{'d})\left(\boldsymbol{n}\otimes\boldsymbol{n}-\frac{\boldsymbol{\delta}}{3}\right)\right] :\, d\boldsymbol{\sigma}^{'} \tag{2.58}$$

The functions $\Pi(r,\,\sigma_n^{'})$ and $\Psi(r,\,\sigma_n^{'d})$ can be defined as follows:

$$\Pi(r,\,\sigma_n^{'}) = \begin{cases} \sqrt{r}, & \text{if } \sigma_n^{'} > 0 \\ \sqrt{r}\,\sigma_n^{'}\dfrac{m\,f_{c,t}^m}{(f_{c,t}-\sigma_n^{'})^{m+1}} + \sqrt{r}\left(\dfrac{f_{c,t}}{f_{c,t}-\sigma_n^{'}}\right)^m, & \text{if } \sigma_n^{'} < 0 \\ 0, & \text{if } \sigma_n^{'} = 0 \end{cases} \tag{2.59}$$

$$\Psi(r,\,\sigma_n^{'d}) = \begin{cases} 3\,\eta\left(\dfrac{r_f}{\sqrt{r}}\right), & \text{if } \sigma_n^{'d} > 0 \\ 0, & \text{if } \sigma_n^{'d} \leq 0 \end{cases} \tag{2.60}$$

Second, when $r \geq r_f$:

$$F = \sqrt{r}\,\sigma_n^{'}\left(\frac{f_{c,t}}{f_{c,t}+\langle-\sigma_n^{'}\rangle}\right)^m + 3\,\eta\,\sqrt{r_f}\,\langle\sigma_n^{'d}\rangle - C_{rc} = 0, \tag{2.61}$$

and,

$$\frac{\partial F}{\partial r} = \frac{1}{2\sqrt{r}}\,\sigma_n^{'}\left(\frac{f_{c,t}}{f_{c,t}+\langle-\sigma_n^{'}\rangle}\right)^m \tag{2.62}$$

$$dr = -\frac{1}{\dfrac{\partial F}{\partial r}} \left[\Pi(r,\, \sigma_n^{'}) \, (\boldsymbol{n} \otimes \boldsymbol{n}) + \Psi(r,\, \sigma_n^{'d}) \left(\boldsymbol{n} \otimes \boldsymbol{n} - \frac{\boldsymbol{\delta}}{3} \right) \right] \, : \, d\boldsymbol{\sigma}^{'} \tag{2.63}$$

The functions $\Pi(r,\, \sigma_n^{'})$ and $\Psi(r,\, \sigma_n^{'d})$ can be defined as follows:

$$\Pi(r,\, \sigma_n^{'}) = \begin{cases} \sqrt{r}, & \text{if } \sigma_n^{'} > 0 \\ \sqrt{r}\, \sigma_n^{'} \, \dfrac{m\, f_{c,t}^{m}}{(f_{c,t} - \sigma_n^{'})^{m+1}} + \sqrt{r} \left(\dfrac{f_{c,t}}{f_{c,t} - \sigma_n^{'}} \right)^{m}, & \text{if } \sigma_n^{'} < 0 \\ 0, & \text{if } \sigma_n^{'} = 0 \end{cases} \tag{2.64}$$

$$\Psi(r,\, \sigma_n^{'d}) = \begin{cases} 3\, \eta \, \sqrt{r_f}, & \text{if } \sigma_n^{'d} > 0 \\ 0, & \text{if } \sigma_n^{'d} \leq 0 \end{cases} \tag{2.65}$$

The details regarding deriving all the aforementioned equations are mentioned in appendix (A.2)

2.3.3 The DDFM to estimate the permeability change

The following assumptions will be adopted while using the DDFM to calculate the change in the permeability of a porous matrix:

1. Cracks are regarded as small interconnected and/or dead–end channels embedded in a porous matrix.

2. At any loading step, a homogenization technique is adopted and the overall permeability tensor of the cracked medium, is thus, composed of two parts: the initial permeability tensor denoted as $\boldsymbol{k}_0$ due to the initial porosity, and the microcrack induced permeability tensor denoted by $\boldsymbol{k}_c$. The flow in the two voids happens in parallel and the total permeability tensor is hence $\boldsymbol{k} = \boldsymbol{k}_0 + \boldsymbol{k}_c$.

3. The average value of local pressure fluctuations at the crack scale are quite small and disregarded; uniform pressure is assumed at the crack scale and the macroscopic scale of the porous matrix.

4. The permeability tensor depends directly on the distribution of cracks which is determined using the crack propagation criterion section (2.3.2). As the distribution of cracks is orientation dependent, the permeability tensor is *anisotropic* in nature.

2. EQUATIONS FOR THERMO–POROELASTICITY, FRACTURE PROPAGATION AND PERMEABILITY EVOLUTION

Let us consider again a REV Ω of the total porous matrix which is submitted to a uniform pressure gradient on the boundaries. This REV can be assumed homogeneous and anisotropic at the same time. The flow in the porous medium obeys Darcy's law. The apparent fluid flow velocity $\boldsymbol{v}$ is related to the macroscopic pressure gradient $\boldsymbol{\nabla} p$ through the total permeability tensor $\boldsymbol{k}$ (m^2):

$$\boldsymbol{v} = -\frac{\boldsymbol{k}}{\mu}.\boldsymbol{\nabla} p = -\frac{\boldsymbol{k}_0 + \boldsymbol{k}_c}{\mu}.\boldsymbol{\nabla} p, \tag{2.66}$$

μ is the dynamic viscosity of the fluid (Pa.s).

Let us now assume a group of N microcracks with direction $\boldsymbol{n}$ and volume Ω_c embedded in the REV Ω. The crack permeability tensor is a function of the cracks orientation $\boldsymbol{n}$, the radius $r(\boldsymbol{n})$, the average aperture $w(\boldsymbol{n})$ and the number of cracks N. Inside a given crack of the orientation $\boldsymbol{n}$, it is assumed that fluid flow takes place only in the direction parallel to the crack plane, and can be described by the Navier–Stokes equation for laminar flow between two parallel plates. The local flow velocity, denoted by $\boldsymbol{v}^c(\boldsymbol{n})$, is thus expressed as follows:

$$\boldsymbol{v}^c(\boldsymbol{n}) = -\frac{\lambda}{12}\frac{1}{\mu} w(\boldsymbol{n})^2 (\boldsymbol{\delta} - \boldsymbol{n} \otimes \boldsymbol{n}).(\boldsymbol{\nabla} p)^c, \quad 0 \leq \lambda \leq 1 \tag{2.67}$$

where $(\boldsymbol{\nabla} p)^c$ denotes the local pressure gradient applied to the crack. The positive scalar λ, less than the unity here, intends to convey the idea that some parts of cracks are simply dead–ends and do not contribute to the flow, see figure (2.6). When $\lambda = 1$ the classical cubic law is recovered, λ will be assumed equal to 1 all along this research later on.

A problem here arises about how to relate the local pressure gradient $(\boldsymbol{\nabla} p)^c$ with the macroscopic pressure gradient $\boldsymbol{\nabla} p$. Generally, an appropriate localization law is to be used. However, using the assumption of neglecting the average value of all local pressure fluctuations, $(\boldsymbol{\nabla} p)^c$ can be assumed equal to $\boldsymbol{\nabla} p$.

The macroscopic fluid flow velocity $\boldsymbol{v}$ is obtained from the averaging of local velocity fields $\boldsymbol{v}^c$ over the crack volume Ω_c:

$$\boldsymbol{v} = -\frac{\boldsymbol{k}_0}{\mu}\boldsymbol{\nabla} p + \frac{1}{\Omega}\int_{\Omega^c} \boldsymbol{v}^c \, d\Omega^c \tag{2.68}$$

Linear elastic response is to be considered starting from state (2), see section (2.2.2). The crack volume occupied by the set of cracks in the orientation $\boldsymbol{n}$, $d\Omega^c(\boldsymbol{n})$, is calculated as:

$$d\Omega^c(\boldsymbol{n}) = N \, w(\boldsymbol{n}) \, \pi \, r(\boldsymbol{n})^2 \tag{2.69}$$

One should keep in mind that although all the cracks are contributing to macroscopic mechanical responses of a damaged rock, it is not the case for hydraulic flow. At the local scale, a certain number of cracks may be hydraulically isolated and do not contribute to the variation of macroscopic permeability of the rock. This phenomenon leads to the definition of the connectivity coefficient $R(r(\boldsymbol{n}))$ such that:

$$R(r(\boldsymbol{n})) = t_1 \left(\frac{r(\boldsymbol{n}) - r_0}{r_f - r_0} \right)^{t_2}, \quad 0 \leq R(\boldsymbol{n}) \leq t_1 \tag{2.70}$$

where t_1 and t_2 are constants to be determined. The value of this coefficient depends on the microstructure of the damaged material. The expression also indicates that the cracks which grow contribute initially, when $r(\boldsymbol{n}) = r_0$, to zero permeability. Nonetheless it also indicates that connectivity between cracks increases as the cracks grow in size which contributes to the crack permeability part $\boldsymbol{k}_c$.

The confusion between the roles of the coefficients $R(r(\boldsymbol{n}))$ and λ can be overstepped as follows: as the coefficient $R(r(\boldsymbol{n}))$ ensures that connectivity is necessary for a contribution in the permeability tensor, λ ensures that the average crack aperture used in calculating the flow and hence the permeability tensor is not to be overestimated due to dead–ends of cracks, see figure (2.6).

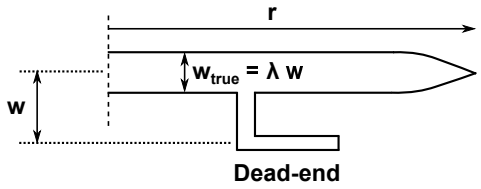

Figure 2.6: The role of the coefficient λ in calculating the correct average crack aperture available for fluid flow.

By substituting equation (2.69) in equation (2.68) and by adopting the method of space averaging to get the continuum response, it is found that:

$$\boldsymbol{v} = -\frac{\boldsymbol{k}_0}{\mu}.\boldsymbol{\nabla} p + \frac{N}{\Omega}\frac{1}{4\pi}\int_S R(\boldsymbol{n})\, \boldsymbol{v}^c(\boldsymbol{n})\, w(\boldsymbol{n})\, \pi\, r(\boldsymbol{n})^2\, dS \tag{2.71}$$

From equation (2.67):

$$\boldsymbol{v} = -\frac{\boldsymbol{k}_0}{\mu}.\boldsymbol{\nabla} p + \left[\left(-\frac{1}{\mu} \right) \frac{\lambda\pi}{12} \frac{N}{\Omega} \frac{1}{4\pi} \int_S R(\boldsymbol{n})\, w(\boldsymbol{n})^3\, r(\boldsymbol{n})^2\, (\boldsymbol{\delta} - \boldsymbol{n} \otimes \boldsymbol{n})\, dS \right] .\boldsymbol{\nabla} p \tag{2.72}$$

Comparing (2.72) with the macroscopic Darcy's law (2.66), the overall crack permeability tensor can be identified as follows:

$$\boldsymbol{k}_c = \frac{N}{\Omega}\frac{\lambda\pi}{12}\frac{1}{4\pi}\int_S R(\boldsymbol{n})\, w(\boldsymbol{n})^3\, r(\boldsymbol{n})^2\, (\boldsymbol{\delta} - \boldsymbol{n}\otimes\boldsymbol{n})\, dS \tag{2.73}$$

Microcracks are assumed to be penny–shaped and thus they are characterized by the radius r and the aperture w. These two variables can evolve independently. However, this is not the approach adopted here, the evolution of the radius r is investigated and the evolution of the aperture w is considered as a function of the evolution of the radius r, i.e. a relation $dw = h(dr)$ is to be found in order to proceed with using equation (2.73).

2.3.4 Integration over a unit sphere

The components of the damage and the crack permeability tensors are calculated by the integration over all the space orientations on the surface of a unit sphere. For the implementation of the model, the numerical integration procedure of directional integration is used.

In terms of the angles θ and ϕ, the unit vector $\boldsymbol{n}$ is written componentwise in the axes shown in figure (2.7):

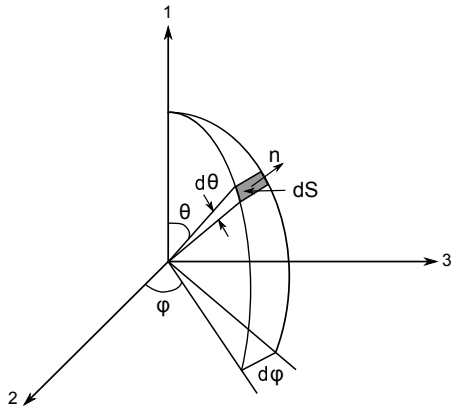

Figure 2.7: Angular parametrization of a unit sphere $\Omega = \Omega(\theta \in [0,\pi],\ \phi \in [0, 2\pi])$.

$$\boldsymbol{n} = \begin{bmatrix} \cos\theta \\ \sin\theta\ \cos\phi \\ \sin\theta\ \sin\phi \end{bmatrix} \tag{2.74}$$

The differential vector area $d\boldsymbol{S}$ is defined as:

$$d\boldsymbol{S} = \frac{\partial \boldsymbol{n}}{\partial\theta} \wedge \frac{\partial \boldsymbol{n}}{\partial\phi}\, d\theta\, d\phi = \boldsymbol{n}\sin\theta\, d\theta\, d\phi \tag{2.75}$$

$$d\Omega = |d\boldsymbol{S}| = \sin\theta\, d\theta\, d\phi \tag{2.76}$$

For any directional distribution $\mathfrak{D}(\boldsymbol{n})$, the weighted integration has the form:

$$\int_{\Omega} [...]\, \mathfrak{D}(\boldsymbol{n})\, d\Omega = \int_0^{2\pi} d\phi \int_0^{\pi} \mathfrak{D}(\theta, \phi) \sin\theta\, d\theta \tag{2.77}$$

For integration over a unit sphere, the weighting factor is given by:

$$\int_{\Omega} d\Omega = 4\pi \tag{2.78}$$

2.4 Developing the DDFM by considering the change of crack aperture

The model presented in section (2.3.2) accounts only for permeability enhancement due to crack evolution, and at a definite stress threshold when the criterion of propagation, equations (2.49) and (2.50), starts working. Actually, starting from the very instant of loading some cracks will either close, due to normal compressive stresses, or open and thus extend due to shear stresses (shear slippage), see figure (2.8).

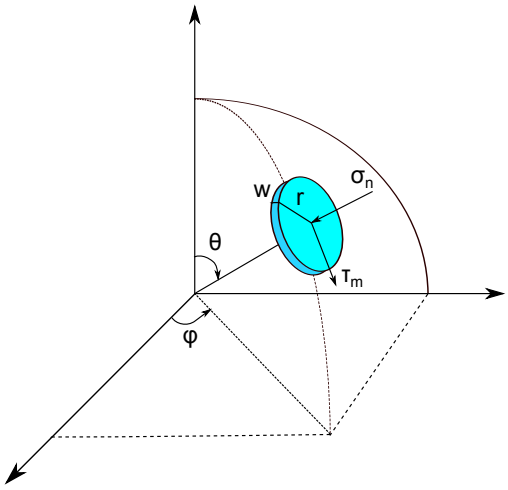

Figure 2.8: Penny-shaped crack with normal and shear stresses acting on it.

This section is divided into two parts; the first part provides a model to track the reduction of crack aperture (Barton's closure model) due to compressive driving forces before and while the fracturing criterion, equations (2.49) and (2.50), is active as the criterion never accounts for crack aperture reduction. The second part is consecrated to find a model that shall be able to track the increase of a crack aperture as a result of shear slipping (crack slipping model) before the onset of the fracturing criterion defined in equations (2.49) and (2.50). As soon as the fracturing criterion starts to work, the crack slipping model does not have to be applied as the shear effect is included in the deviatoric stress part $\tilde{q}(\boldsymbol{n})$. The crack slipping model, despite being provided mathematically, will not be used in doing the simulations of this research. It is therefore provided for future studies.

2.4.1 Barton's hyperbolic closure model for crack aperture reduction

To account for permeability loss due to compressive stresses and crack aperture reduction, Barton's hyperbolic normal closure model (Bandis et al., [1983]) has been adopted in this work. It is a two-parameter model that ensures a finite aperture at zero effective stress and stands only for normal compliance of fractures.

Given a normal stiffness coefficient k_{n0} at initial effective stress $\sigma_{n0}^{'}$ and maximum closure value w_0 for a joint, the available aperture w for a fluid motion at a given effective stress level $\sigma_n^{'}$ is derived as follows:

$$u \text{ (value of the closure)} = \frac{\langle -\sigma_n^{'} \rangle w_0}{w_0 k_{n0} + \langle -\sigma_n^{'} \rangle} \tag{2.79}$$

$$w = w_0 - u = w_0 \left(1 - \frac{\langle -\sigma_n^{'} \rangle}{w_0 k_{n0} + \langle -\sigma_n^{'} \rangle} \right) \tag{2.80}$$

This coupled approach is only valid for compressive stresses and it was tested against various *in situ* experiments performed in hard rocks in the framework of a nuclear waste storage research program. Predictive results were compared with those of other numerical approaches (Rejeb and Bruel, [2001]).

2.4.2 Crack aperture increase due to shear slippage before the onset of the fracturing criterion (crack slipping model)

If the effect of shearing stresses is to be considered before the onset of the fracturing criterion section (2.3.2), the following model is to be adopted[1]:

$$\tau_m^{'} = \left| \sigma_n^{'} \right| \tan(\phi) + c, \tag{2.81}$$

where c is the apparent cohesion, see figure (2.6). The evolution of Mohr–Coulomb yield surface can be obtained by changing c, ϕ or both. Apparent cohesion will be the changing parameter in this approach. Let us define the function $G(\boldsymbol{\sigma}^{'}, c)$ as follows:

$$G = \tau_m^{'} - \left| \sigma_n^{'} \right| \tan(\phi) - c \tag{2.82}$$

The first value of $\tau_m^{'}$ is the shear strength of the material, next values are to be calculated assuming that the cohesion c changes with $\sigma_n^{'}$:

[1]This model is based on the study of Kohl presented in (Kohl and Mégel, [2007]) with a lot of modifications considering Mohr-Coulomb criterion of failure.

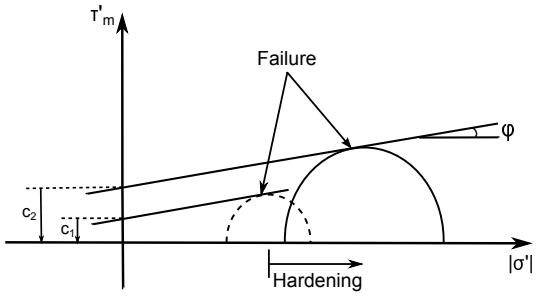

Figure 2.9: Sketch of Mohr-Coulomb criterion, the angle of the straight lines ϕ is "the angle of friction". The apparent cohesion is the changing parameter for hardening.

$$dG = \frac{\partial G}{\partial \boldsymbol{\sigma}'} : d\boldsymbol{\sigma}' + \frac{\partial G}{\partial c}\, dc \tag{2.83}$$

$$dG = \left[\frac{\partial G}{\partial \tau_m'}\frac{\partial \tau_m'}{\partial \boldsymbol{\sigma}'} + \frac{\partial G}{\partial \sigma_n'}\frac{\partial \sigma_n'}{\partial \boldsymbol{\sigma}'}\right] : d\boldsymbol{\sigma}' + \frac{\partial G}{\partial c}\, dc \tag{2.84}$$

$$\begin{aligned}
\frac{\partial G}{\partial c} &= -1 \\
\frac{\partial G}{\partial \tau_m'} &= 1 \\
\frac{\partial \tau_m'}{\partial \boldsymbol{\sigma}'} &= \frac{1}{2}(\boldsymbol{m}\otimes\boldsymbol{n} + \boldsymbol{n}\otimes\boldsymbol{m}) \\
\frac{\partial G}{\partial \sigma_n'} &= \operatorname{sgn}(\sigma_n')\tan(\phi) \\
\frac{\partial \sigma_n'}{\partial \boldsymbol{\sigma}'} &= \boldsymbol{n}\otimes\boldsymbol{n}
\end{aligned} \tag{2.85}$$

On the failure surface, $dG = 0$:

$$dc = -\frac{1}{\dfrac{\partial G}{\partial c}}\left[\frac{\partial G}{\partial \tau_m'}\frac{\partial \tau_m'}{\partial \boldsymbol{\sigma}'} + \frac{\partial G}{\partial \sigma_n'}\frac{\partial \sigma_n'}{\partial \boldsymbol{\sigma}'}\right] : d\boldsymbol{\sigma}' \tag{2.86}$$

$$dc = \left[\frac{1}{2}(\boldsymbol{m}\otimes\boldsymbol{n} + \boldsymbol{n}\otimes\boldsymbol{m}) + \operatorname{sgn}(\sigma_n')\tan(\phi)\,(\boldsymbol{n}\otimes\boldsymbol{n})\right] : d\boldsymbol{\sigma}' \tag{2.87}$$

Finally the dilatancy $U(\boldsymbol{n})$ due to shear slipping is given by:

$$U(\boldsymbol{n}) = \frac{w_0\,\tau_m'}{k_s}\tan(\phi_{dil}), \tag{2.88}$$

ϕ_{dil} is the dilatancy angle of the fracture and k_s is the fracture shear stiffness. To carry on with using this model, the following points should be accounted for:

1. Equation (2.87) gives the evolution of cohesion as a result of changing the state of the effective stress. For the model to be consistent a good convincing relation between cohesion change and aperture increase due to dilatation is to be found.

2. dc is to be calculated for all possible vectors $\boldsymbol{m}'s$ at the fracture plane and the most critical case is to be considered.

Dilatation is to be considered as long as the threshold of the fracturing criterion is not reached. As soon as the fracturing criterion becomes active the shear effect is included in the deviatoric stress part $\tilde{q}(\boldsymbol{n})$ of the model. Meanwhile, Barton's closure model remains active at any loading step as the fracturing criterion never accounts for crack aperture reduction.

Before the threshold of the fracturing criterion, see figure (2.10):

$$w = w_0 - u + U \ (U, \text{ crack opening due to dilatation (shear slippage)}) \tag{2.89}$$

When the fracturing criterion starts working:

$$w = w_0 - u + h(dr) \ (dw = h(dr), \text{ crack opening due to shearing } \tilde{q}(\boldsymbol{n})) \tag{2.90}$$

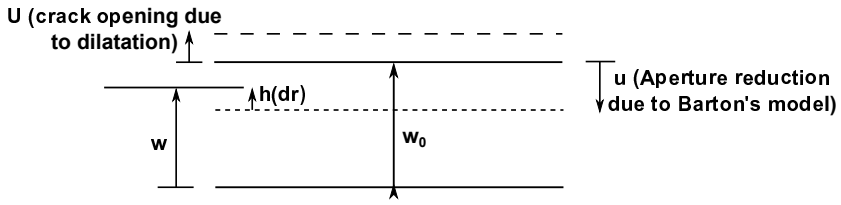

Figure 2.10: Sketch for a crack section illustrating contraction and dilatancy due to both compliance and shearing.

2.5 Application of the DDFM: Simulations and expectations

Anisotropic damage due to preferential growth and closure of microcracks subjected to non–hydrostatic stresses is the key mechanism for inelastic deformation, and leads to failure in most brittle rocks. Crack growth at microscopic scale is associated with changes in crack aperture which is the main reason for macroscopic volumetric dilatancy as well.

Failure of geomaterials is hence a direct result of microcracks coalescence and localization in a form of macrocraks. The main consequences of microcracks growth that have to be considered in the constitutive modeling are:

1. Non-linear stress-strain relations; microcracks surface dislocation and mismatch will cause a macroscopic dilatancy and permanent irreversible strains, see section (2.3.1).

2. Deterioration of elastic properties as the material gets weaker with the evolution of microcracks.

3. Induced anisotropy; the evolution of microcracks is not the same in all directions and the initial "isotropy" in mechanical and transport properties might be progressively modified.

4. Volumetric dilatancy as result of microcrack surfaces dislocation and mismatch.

5. Irreversible strains.

There is a clear relation between volumetric dilatancy and the increase in permeability in brittle rocks (Oda et al., [2002]). It is a common sense to have in mind that permeability will increase when the applied stress state induces damage expressed by microcrack opening and growth (Kranz et al., [1979]) and (Zoback and Byerlee, [1975]).

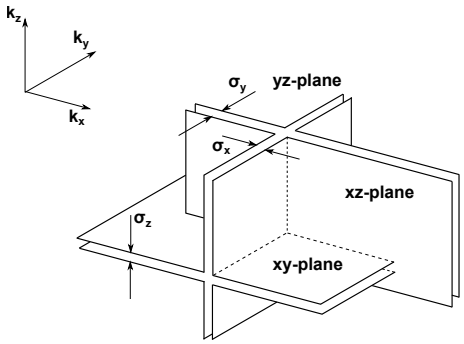

Figure 2.11: Conceptualization of anisotropic permeability occurring on three orthogonal fracture planes.

Preferential growth of microcracks will result in an anisotropic permeability tensor, see figure (2.11). The maximum permeability component is observed parallel to the axis of major stress. However, the anisotropy ratio of permeability between the axial and radial directions is quite small (maximum of about 2.5) according to (Schulze et al., [2001]).

Stress–strain curves for brittle rocks, under dominating compressive stresses, show four different regions (Souley et al., [2001]) and (Shao et al., [2005]), see figure (2.12):

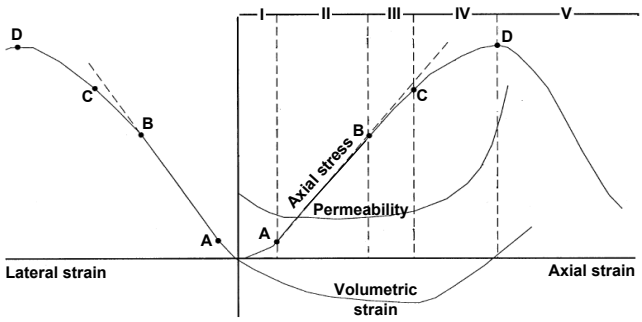

Figure 2.12: Deformation stages and corresponding permeability change of a rock specimen tested in compression, (Souley et al., [2001]).

- Region I: Closure of pre–existing microcracks.
- Region II: Elastic behavior zone.
- Region III: Stable growth of cracks.
- Region IV: Unstable growth of cracks.

Triaxial tests with permeability measurement have indicated that:

1. Permeability decreases in region I because of the closure of pre-existing microcracks.
2. Permeability remains constant in region II and at the beginning of the region of stable crack growth III.
3. Permeability increases as a function of the deviatoric stress at region IV announcing the onset of unstable crack growth. Permeability increases drastically in region V when cracks start to coalesce announcing the macroscopic failure of the sample.

2.5.1 Numerical simulations

The first part of this section applies the proposed model of directionally distributed fractures DDFM, section (2.3), to a typical brittle rock of *Lac du Bonnet* Granite. This rock has been widely studied in the context of Under Ground Research Laboratory (URL) in Canada for the studies of nuclear waste storage (Shao et al., [2005]).

The second part integrates Barton's closure model in the DDFM and compares the numerical results for the same type of rock.

2.5.1.1 DDFM without considering crack aperture reduction: Application to Lac du Bonnet rock sample

The model developed in section (2.3) is to be applied to a cylindrical sample of Lac du Bonnet granitic rock. The sample is subjected to different values of confining pressure P_c until it completely consolidates. When consolidation is done, the sample is loaded axially by a deviatoric stress $\Delta\sigma$ to create a non–hydrostatic stress state and to drive cracks to evolve, see figure (2.13).

The initial elastic parameters have been determined from the compression triaxial tests and the change in their values with confining pressure is very small (Shao et al., [2005]). Table (2.1) shows the values of all the parameters used in the simulation.

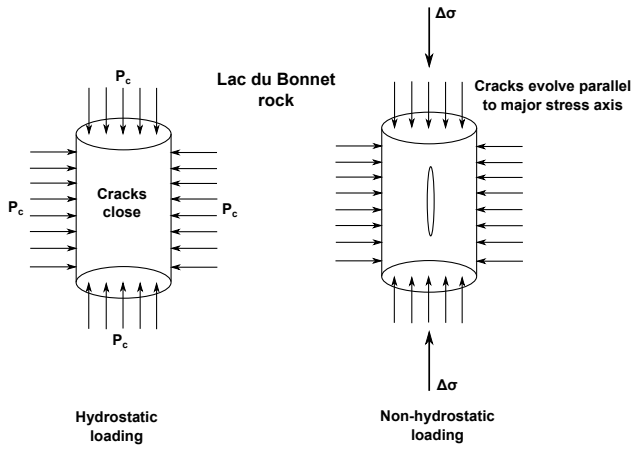

Figure 2.13: Hydrostatic and non-hydrostatic loadings of a cylindrical Lac du Bonnet rock sample.

Table 2.1: Parameters used in the simulations of DDFM on Lac du Bonnet granite, (Shao et al., [2005]).

	Parameter	Value
Elastic parameters	Elastic modulus E_0 (MPa)	68000
	Poisson's ratio ν_0	0.21
Damage parameters	Initial radius of cracks r_0 (mm)	3.0
	Final radius of cracks r_f (mm)	9.0
	Initial aperture of cracks w_0 (mm)	0.015
	Material toughness parameter	
	C_{rc} (MPa$\sqrt{\text{m}}$)	1.03
	f_c/f_t	18.7 ©
	Model parameter η	0.06
	Non–linearity parameter m	4
	Number of cracks N per	
	unit volume ($\Omega = 1$ m^3)	2×10^6 †
Hydraulic connectivity	t_1	0.0001 ‡
parameters	t_2	1.0
	λ	1.0

†: Crack density of a certain rock is estimated experimentally using x–ray tomography, see (Fabre et al., [1989]).
‡: The value of t_1 is determined after estimating the crack density such that permeability order of magnitude for a certain rock at the limit of accelerated crack coalescence $r = r_f$ is reached. For the parameters and rock described above, at failure $k \sim 10^{-17}$ m^2.
©: Using equations (2.53) and (2.54), the ratio f_c/f_t corresponds to $\eta = 0.06$.

In order to calculate the anisotropic permeability tensor using DDFM equation (2.73), a convincing relation between the evolution of an average crack radius δr and the corresponding average variation of its aperture δw is to be found.

Authors like (Klimczak et al., [2010]), (Takahashi and Watanabe, [1995]), (Papanastasiou

and Thiercelin, [1993]) and (Shao et al., [2005]) have related the normal increment of crack aperture to crack face mismatch and local grain matrix interaction during crack growth. Thus, the normal crack aperture increment is proportional to the average crack radius increment, that is to say:

$$\frac{\delta w}{\delta r} = \beta \tag{2.91}$$

β is the proportionality coefficient. (Klimczak et al., [2010]) have performed experiments on 15 types of rocks and have found that $\beta \in [0.0005, 0.5]$. Data were collected from several references to reach Table (2.2) shown below:

Table 2.2: Average crack radii and apertures relation.

Average crack radius, r (m)	Average crack aperture, w (m)	References
0.006	0,00003	Shao et al., [2005]
1.2	0,00045	Papanastasiou and Thiercelin, [1993]
25	0,000501	Bruel, [2002]
30	0,00018	Rejeb and Bruel, [2001]
40	0,00032	Kohl and Mégel, [2007]

A power-fitting curve, equation (2.92) and figure (2.14), with a correlation coefficient $R^2 = 0.67$ is used to represent the data shown in Table (2.2):

$$w(\text{m}) = 0.0002\, r^{0.2497}(\text{m}) \tag{2.92}$$

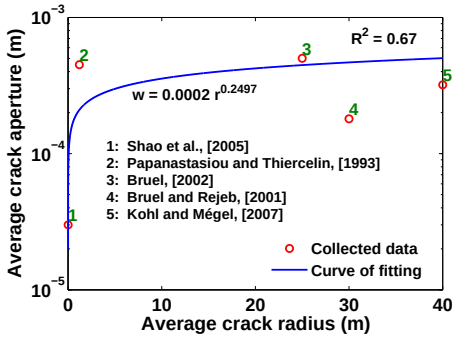

Figure 2.14: The relation between the crack average aperture w and its average radius r. Scattered data are collected from five references. A power fitting curve, equation (2.92), with $R^2 = 0.67$ is chosen to represent the data.

The derivative of equation (2.92) gives the slope β:

$$\beta(\mathrm{m/m}) = 5 \times 10^{-5} r^{-0.75}(\mathrm{m}) \tag{2.93}$$

β being function of r will render equation (2.91) non-linear. However, it is the only means in hand to control the flow in very long cracks.

The model was coded using Fortran 90, the initial permeability tensor $\boldsymbol{k}_0$ associated with pore connectivity is set to $\mathbf{0}$. Since no cracks are initially connected $r = r_0$, the initial crack permeability tensor $\boldsymbol{k}_c$ is also $\mathbf{0}$, see equations (2.70) and (2.73). The results obtained, as shown below, represent the permeability generated due to crack propagation only, i.e. $r > r_0$. The results demonstrate the following points:

1. Cracks are only evolving in the vicinity of the axial direction as the sample is loaded vertically with deviatoric stresses, see figure (2.15(b)).

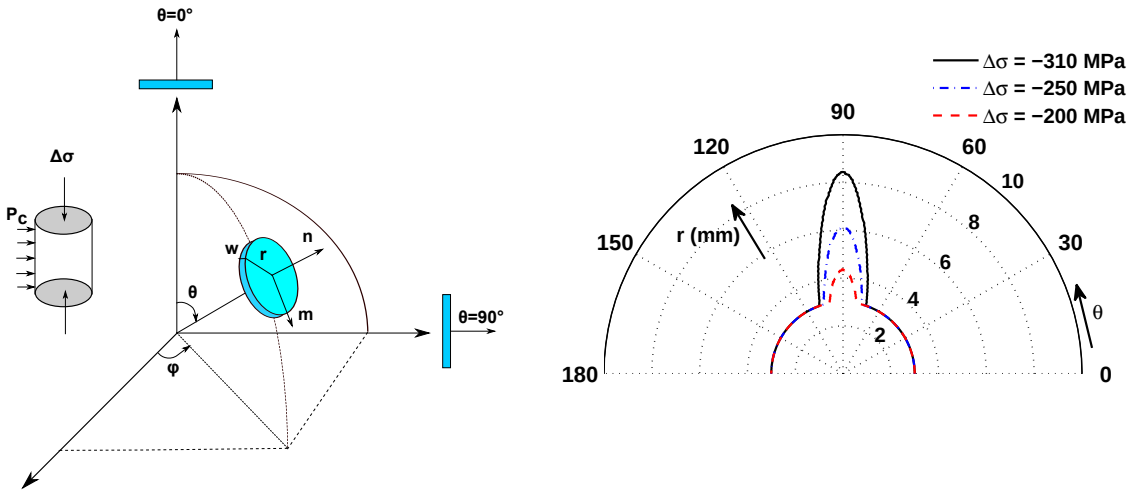

(a) $\theta - \phi$ position of a crack of radius $r(\boldsymbol{n})$ (b) Directional evolution of the radius of cracks

Figure 2.15: Directional evolution of cracks radii for three values of deviatoric stress in a vertical cross–section and for a confining pressure of 10 MPa.

2. The two curves of lateral permeabilities k_{22} and k_{33} coincide when dividing the circumference into 160 segments "segment=$2\pi/160$". This is a direct result of an axisymmetric loading state, see figure (2.16).

3. Permeability is increasing in the axial and lateral directions simultaneously as the DDFM stands for Mode I and Mode II of crack propagation. The DDFM is adopting the so called "wing crack" propagation, see (Simpson and Guéguen, [2001]).

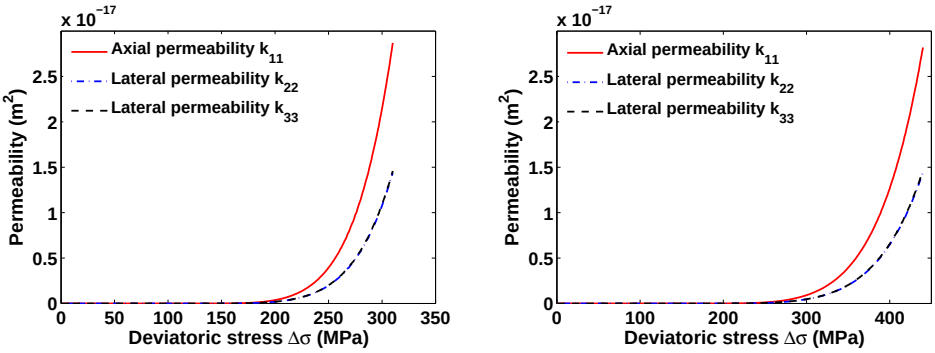

(a) Confining pressure $P_c = 10$ MPa (b) Confining pressure $P_c = 40$ MPa

Figure 2.16: Variation of permeability in the axial and radial directions during two triaxial compression tests on Lac du Bonnet granite.

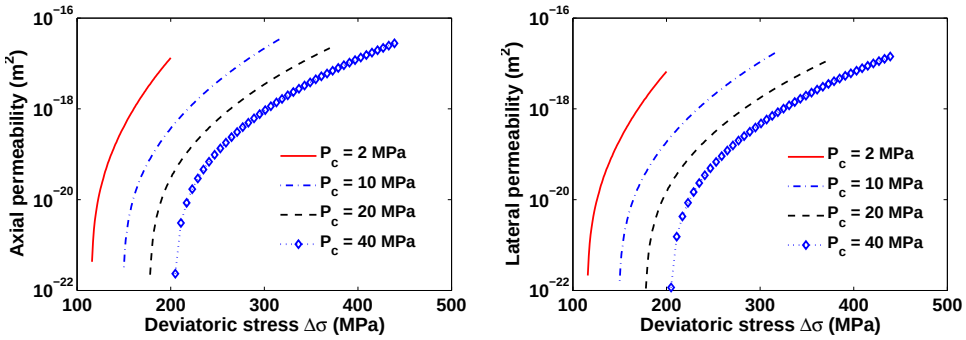

(a) Permeability in the axial direction (b) Permeability in the radial direction

Figure 2.17: Variation of permeability in the axial and radial directions during triaxial compression tests on Lac du Bonnet granite with 4 confining pressure values.

4. Increasing the confining pressure will shift the threshold of deviatoric stress before cracks start to evolve as well as the compression strength of the rocks, see figure (2.17).

5. This model accounts only for propagating cracks and does not stand at all for the reduction in permeability that results from crack aperture reduction due to normal effective compressive stresses.

2.5.1.2 Modifying the DDFM to stand for the reduction of crack aperture

To account for the reduction in permeability that results from the closure of cracks, Barton's hyperbolic closure model, equation (2.94), is to be integrated in our DDFM. The hyperbolic model is the most widely adopted model for a non–linear behavior of a fracture under normal stress (Bandis et al., [1983]), (Bruel, [2002]) and (Baghbanan and Jing, [2008]).

$$w = w_0 - u = w_0 \left(1 - \frac{-\sigma_n^{'}}{w_0 k_{n0} - \sigma_n^{'}}\right), \tag{2.94}$$

where w is the available aperture of the crack at the stress level $\sigma_n^{'}$, w_0 is the initial aperture of the crack/maximum closure of the crack and u is the value of the closure at the stress level $\sigma_n^{'}$. Barton's model is to be parameterized before application; the stiffness coefficient k_{n0} at the reference normal effective stress $\sigma_{n0}^{'}$ is to be determined. Determination of the exact value of the stiffness coefficient is an enormous task. The rocks are lying deep in the ground and physical properties of the cracks including average lengths, average apertures or orientations are always approximated.

(Bandis et al., [1983]) and (Bandis and Barton, [1985]) tried to find an empirical relation that links the stiffness coefficient to crack face properties and some empirical constants which depend on the cycles of loading. These empirical relations and the associated constants were valid in the tested samples and under the specific testing conditions. Care should be exercised when they are applied to general practical problems.

Let us write equation (2.94) in the following form:

$$\frac{u}{w_0} = \frac{\sigma_n^{'}/\sigma_{n0}^{'}}{(\sigma_n^{'}/\sigma_{n0}^{'}) + 1}, \tag{2.95}$$

where $-\sigma_{n0}^{'} = k_{n0}\, w_0$. The relative normal compliance C_n is defined as:

$$C_n = \frac{\partial(u/w_0)}{\partial(\sigma_n^{'}/\sigma_{n0}^{'})} = \frac{1}{(1 + \sigma_n^{'}/\sigma_{n0}^{'})^2} \tag{2.96}$$

Figure (2.18) shows that when the normalized stress ratio, $\sigma_n^{'}/\sigma_{n0}^{'}$, is large enough, the relative normal compliance becomes negligible, and the variation of the normalized normal closure reaches an asymptotic value of 1.

In this study as in (Baghbanan and Jing, [2008]), it is assumed that the minimum variation of u/w_0 is approximated when the normalized normal stress exceeds 9. Let us define the critical normal effective stress $\sigma_{nc}^{'}$ such that the normalized critical normal stress $\sigma_{nc}^{'}/\sigma_{n0}^{'}$ is equal to 10, at this point the normal compliance C_0 is negligible, see figure (2.18).

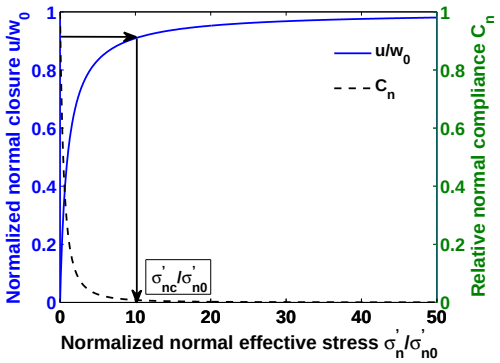

Figure 2.18: Variation of normalized normal closure u/w_0 and relative normalized compliance C_n versus normalized effective stress of cracks $\sigma_n^{'}/\sigma_{n0}^{'}$.

Unless the initial conditions are well known to estimate $\sigma_{n0}^{'}$ and to calculate the stiffness coefficient $k_{n0} = -\sigma_{n0}^{'}/w_0$, the initial stiffness coefficient k_{n0} can be calculated using the critical normal effective stress $\sigma_{nc}^{'} = 10\,\sigma_{n0}^{'}$ that causes almost the entire closure of cracks through the relation:

$$k_{n0} = \frac{-\sigma_{nc}^{'}}{10\,w_0} \tag{2.97}$$

It is worth noting here that $\sigma_{n0}^{'}$ has been replaced by $\sigma_{nc}^{'}$ while calculating the stiffness coefficient without problems as both of them stand for a boundary state. $\sigma_{n0}^{'}$ represents the boundary of no crack aperture reduction $w = w_0$, meanwhile $\sigma_{nc}^{'}$ represents the boundary of almost full closure of the crack $u/w_0 \to 1$.

(Zangerl et al., [2008]) collected experimental results from more than 29 references to reach a table that relates $\sigma_{nc}^{'}$, $\sigma_{n0}^{'}$ and the crack dimensions. The results of their article were used and distributed naturally to find a relation between $\sigma_{nc}^{'}$ and w_0. It was found that an average value of maximum aperture w_0, of 60 μ m, was distributed around a critical normal effective stress $\sigma_{nc}^{'}$ of 32 MPa.

(Baghbanan and Jing, [2008]) have also given a linear relation between $\sigma_{nc}^{'}$ and w_0:

$$-\sigma_{nc}^{'}\,(\text{MPa}) = 0.541 w_0\,(\mu\text{m}) + 2.51 \tag{2.98}$$

If the result of (Zangerl et al., [2008]) is to be substituted in equation (2.98), we obtain:

$$-\sigma_{nc}^{'}\,(\text{MPa}) = 0.541 \times 60\,(\mu\text{m}) + 2.51 = 34.97\,\text{MPa}, \tag{2.99}$$

which is not far from the value that (Zangerl et al., [2008]) have given of 32 MPa. The works of (Zangerl et al., [2008]) and (Baghbanan and Jing, [2008]) have made clear that the initial stiffness coefficient k_{n0} is related to the dimension of cracks via the critical normal effective stress $\sigma_{nc}^{'}$.

The works of (Zangerl et al., [2008]) and (Bandis et al., [1983]) have also illustrated that, with increasing the normal stress cracks become stiffer. Experimental results have also shown that with increasing hydraulic aperture, higher stresses should be applied to reach the maximum closure of cracks. Thus, it is almost impossible to get a comprehensive relation that describes the evolution of the stiffness coefficient of a crack while loading. In this research the stiffness coefficient will be assumed constant and equal to the initial stiffness coefficient, i.e. k_{n0}.

Let us now consider the cylindrical sample of the Lac du Bonnet granite which was hydrostatically loaded with a confining pressure of 10 MPa. The deviatoric stresses were later added in a mood that guarantees drained conditions. For this simulation $w_0 = 15$ μm, as in section (2.5.1.1), which gives by equation (2.98), $\sigma_{nc}^{'} = -11$ MPa and the initial stiffness is $k_{n0} = 74$ GPa by equation (2.97). The threshold of crack propagation is 150 MPa for a confining pressure of 10 MPa, see figure (2.17).
At a random vertical–section of the axisymmetrically loaded sample, figure (2.19) presents the directional distribution of the normal effective stress as well as the closing curve for all possible orientations of cracks at a deviatoric stress of -60 MPa.

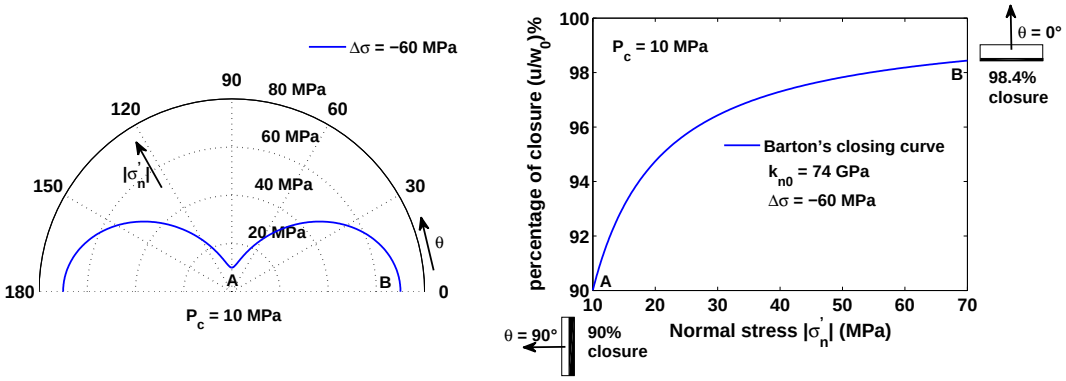

(a) Directional distribution of normal effective stress $\sigma_n^{'}$

(b) Barton's closure curve

Figure 2.19: Directional distribution of the normal effective stress and Barton's hyperbolic closure curve at a vertical cross–section and for a deviatoric stress $\Delta\sigma = -60$ MPa and confining pressure of 10 MPa. Point A represents a vertical crack closed by 90% due to the confining pressure ($\sigma_n^{'} = -10$ MPa at any time). Point B represents a horizontal crack that will continue to close while adding the deviatoric stresses ($\sigma_n^{'} \geq -10$ MPa at any time).

When the sample is fully consolidated by the confining pressure of 10 MPa, all cracks would have been closed by 90% in harmony, see $\Delta\sigma = 0$ MPa in figure (2.20(a)). Starting to apply the deviatoric stresses, unless the threshold of crack propagation is reached, cracks with orientations other than $\theta = 90°$ will continue to close preferentially with direction, see $\Delta\sigma = -60$ MPa in figure (2.20(a)).

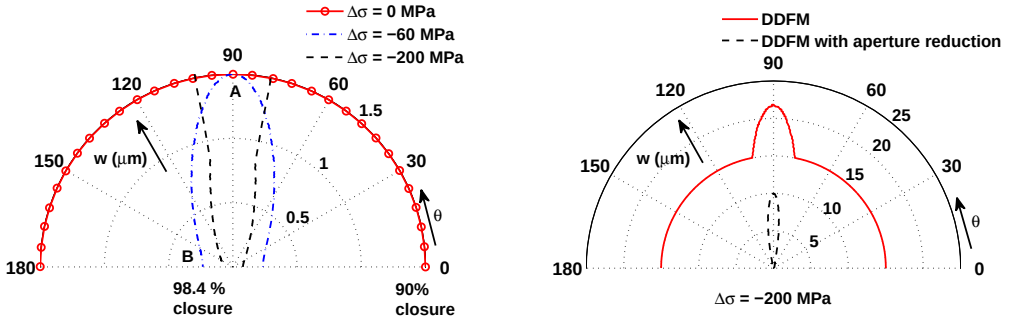

(a) DDFM with aperture reduction for different values of deviatoric stress. A & B are the crack orientations highlighted in figure (2.19)

(b) Comparison between the results of the DDFM "with and without aperture reduction" for a deviatoric stress of -200 MPa

Figure 2.20: Directional distribution of crack aperture for $w_0 = 15$ μm and for a confining pressure of 10 MPa.

When the threshold of crack propagation is reached ($\Delta\sigma \geq -150$ MPa), cracks start to evolve and the apertures start to increase significantly following equation (2.92), see $\Delta\sigma = -200$ MPa in figure (2.20(a)) and figure (2.20(b)).

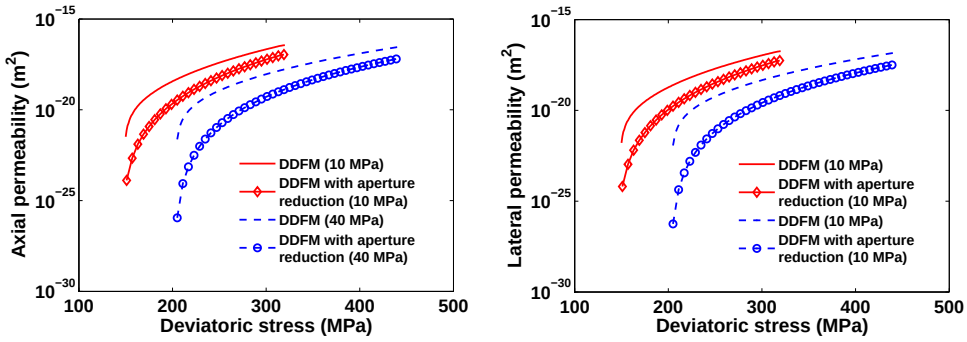

(a) Axial permeability

(b) Lateral permeability

Figure 2.21: Variation of permeability for confining pressures of 10 and 40 MPa with and without considering the closure of cracks, $k_{n0} = 74$ GPa.

From the previous graphs it is concluded that:

1. Cracks close simultaneously in all directions when the confining pressure is applied. In the previous results, 90% closure is achieved when the sample is totally consolidated by the confining pressure of 10 MPa.

2. When the deviatoric stresses are applied, cracks with orientations other than $\theta = 90°$ continue to close preferentially with direction, see the curve of $\Delta\sigma = -60$ MPa in figure (2.20(a)).

3. When the threshold of crack propagation is reached, cracks start to grow and average aperture starts to increase significantly, see the curve of $\Delta\sigma = -200$ MPa in figure (2.20(a)).

4. The difference in the components of permeability tensors, between the cases of considering or not considering crack aperture reduction, is significant at the beginning of crack propagation. However, this difference is compensated for as cracks start to evolve and average aperture to increase, see figure (2.21).

5. Since cracks evolve in the vicinity of the major stress axis, aperture reduction affects the lateral permeability in as much as it affects the axial permeability. The anisotropy ratio of permeability between the axial and radial directions remains quite small.

2.6 Validating the DDFM with aperture reduction using experimental data

(Souley et al., [2001]) have performed a large number of experiments on Lac du Bonnet Granite in a matter of estimating its *in situ* hydraulic properties. Those tests were part of the tunnel sealing experiment at the 420 m level of Canada's Underground Research Laboratory (URL). The experimental data were collected and correlated with the numerical response given by the DDFM with aperture reduction, see figure (2.22) shown below.

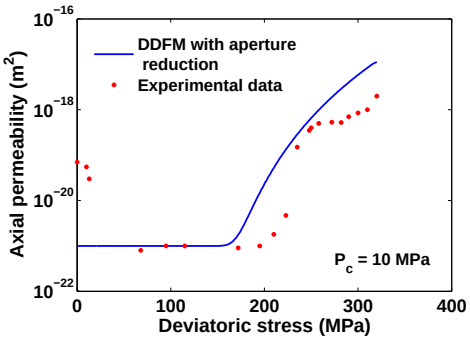

Figure 2.22: Correlating the DDFM with aperture reduction with the experimental data given by (Souley et al., [2001]), $C_{rc} = 1.03$ MPa$\sqrt{\text{m}}$.

Following figure (2.22), it is seen that the parameters which were used in Table (2.1) underestimate the threshold of cracks propagation, weaker rock obviously. To overcome this shortage, the value of material toughness C_{rc} was changed such that the numerical response would simulate

the threshold of crack propagation. A value of 1.26 MPa$\sqrt{\text{m}}$ was chosen for material toughness C_{rc}. The numerical response of the DDFM with aperture reduction correlates satisfyingly the experimental data as shown in figure (2.23).

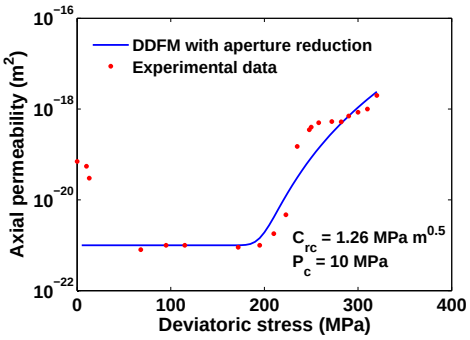

Figure 2.23: Correlating the DDFM with aperture reduction with the experimental data given by (Souley et al., [2001]), $C_{rc} = 1.26$ MPa$\sqrt{\text{m}}$.

Chapter 3

Finite element formulation for thermo–poroelastic IBVPs: Focus on fluid compressibility

The finite element method (FEM) is used to relate the primary unknowns to the boundary conditions and the body forces through a discretizing technique. The unknowns are discretized over space and equations are then solved to force the residual to vanish. The partial differential equations are reduced to either a system of linear or non–linear equations (in steady state problems), or a system of semi–discrete ordinary differential equations (in transient problems).

This chapter is to be divided into three parts:

- Presenting the finite element formulation for the transient thermo–poroelastic problems introduced in chapter (2).
- Testing the capability of ABAQUS[1] to simulate thermo-hydro-mechanical IBVPs.
- Finally developing and validating a domestic Fortran 90 Finite Element (FE) code which was modified by (Gelet, [2012]). The numerical results of the FE code are compared with the ABAQUS response and analytical solutions for one–dimensional and two–dimensional thermo–poroelastic IBVPs.

3.1 From mathematics to the finite element formulation

The brief summary below is based on the work of (Hughes, [2000]) and proceeds in three steps:

[1]ABAQUS is a suite of software applications for finite element analysis and computer–aided engineering, originally released in 1978.

3. FINITE ELEMENT FORMULATION FOR THERMO–POROELASTIC IBVPS: FOCUS ON FLUID COMPRESSIBILITY

1. The variational or weak formulation of the problem is first obtained from the partial differential equations.

2. A discretizing method is used to discretize the weak formulation in space.

3. Within a generic element, a system of algebraic equations is finally developed.

The set of solutions for our problem is presumed to be a vector space which means that all the classical algebraic operations can be conducted like for vectors of ordinary geometry.

Let the function $u(x)$ be the sought solution and f a smooth scalar function defined in the segment $\Omega =]0,1[$. The strong form if the BVP to be considered includes the partial differential equations and the boundary conditions:

$$(\mathrm{S}) \quad \begin{cases} \dfrac{\partial^2 u}{\partial x^2} + f & = 0, \quad \text{on }]0,1[\\ u(1) & = g \\ -\dfrac{\partial u(0)}{\partial x} & = h \end{cases} \tag{3.1}$$

(1) The strong formulation (S) of the BVP is multiplied by the variation w and is integrated by part over the domain Ω to get the variational or weak formulation (V).

$$(\mathrm{V}) \quad \int_0^1 \frac{\partial w}{\partial x}\frac{\partial u}{\partial x}\,dx = \int_0^1 w\,f\,dx + w(0)\,h \tag{3.2}$$

The variation w or sometimes called the weighting function is required to satisfy the homogeneous counter–part of the g-boundary, $w(1) = 0$, and to have square-integrable derivatives. The boundary conditions are either known parts of the solution (Dirichlet boundary conditions) or derivatives of the solution at the boundary (Neumann boundary conditions). Equation (3.2) is indicating that enforcing a vector to be equal to zero in the space is equivalent to enforcing every projection of this vector to be equal to zero as well. This has the physical interpretation of the virtual work.

(2) The weak formulation is to be discretized in space. Within a generic element e, the discretization of the trial solution u^h and the variation w^h is done based on a spatial discretization corresponding to a characteristic length h. The trial solution u^h has a known part g^h and unknown part v^h, such that:

$$u^h = v^h + g^h, \tag{3.3}$$

Assuming, along the Galerkin's discretizing procedure, that the function v^h belongs to the same collection of the variations w^h, it henceforth satisfies that $v^h(1) = 0$. The function g^h goes with the definition $g^h(1) = g$. Gathering all the known parts of the discretized weak formulation at the right hand side leads to Galerkin's formulation (G) of the problem.

$$\text{(G)} \quad \int_0^1 \frac{\partial w^h}{\partial x} \frac{\partial v^h}{\partial x}\, dx = \int_0^1 w^h\, f^h\, dx - \int_0^1 \frac{\partial w^h}{\partial x} \frac{\partial g^h}{\partial x}\, dx + w^h(0)\, h \tag{3.4}$$

If the functions v^h do not belong to the collection of variations w^h, the method is called Petrov-Galerkin method.

(3) The last step includes writing (G) in a coupled system of algebraic equations (the matrix problem). This can be done by writing w^h and v^h in terms of basis functions. Let w^h and v^h consist of all the linear combinations of given functions N_A and N_B over the closure $\bar{\Omega} = [0, 1]$ of Ω, where A, $B = 1, 2, 3, \ldots, n$. Thus, there exist constants c_A's and d_B's such that:

$$w^h = \sum_{A=1}^{n} c_A\, N_A \quad \text{and} \quad v^h = \sum_{B=1}^{n} d_B\, N_B \tag{3.5}$$

N_X's are referred to as shape, basis or interpolation functions. Each shape function N_X should satisfy:

$$N_X(1) = 0, \quad X = 1, 2, 3, \ldots, n \tag{3.6}$$

An $n+1$ shape function N_{n+1} is defined such that $N_{n+1}(1) = 1$ and g^h is hence given by:

$$g^h = g\, N_{n+1} \quad \text{and thus} \quad g^h(1) = g \tag{3.7}$$

Now (G) is written as:

$$\begin{aligned} \sum_A^n c_A \sum_B^n \int_0^1 \frac{\partial N_A}{\partial x} \frac{\partial N_B}{\partial x}\, d_B\, dx \;&=\; \sum_A^n c_A \int_0^1 N_A\, f^h + \sum_A^n c_A\, [N_A(0)\, h] \\ &-\; \sum_A^n c_A \int_0^1 \frac{\partial N_A}{\partial x} \frac{\partial N_{n+1}}{\partial x}\, g\, dx \end{aligned} \tag{3.8}$$

Since the c_A's are arbitrary constants, equation (3.8) provides a set of n equations, namely for $A = 1, 2, 3, \ldots, n$.

$$\sum_B^n \int_0^1 \frac{\partial N_A}{\partial x} \frac{\partial N_B}{\partial x}\, d_B\, dx = \int_0^1 N_A\, f^h + [N_A(0)\, h] - \int_0^1 \frac{\partial N_A}{\partial x} \frac{\partial N_{n+1}}{\partial x}\, g\, dx \tag{3.9}$$

All quantities appearing in equation (3.9) are known except for the d_B's. Concisely, this relation can be expressed as:

$$\sum_{B}^{n} \boldsymbol{K}_{AB}\, \boldsymbol{d}_B = \boldsymbol{F}_A, \quad A = 1,\, 2,\, 3,\, \ldots,\, n \tag{3.10}$$

Adopting the matrix notation, the matrix formulation (M) of the problem is reached:

$$\text{(M)} \;\; \boldsymbol{K}\,\boldsymbol{X} = \boldsymbol{F}, \tag{3.11}$$

where $\boldsymbol{K}$ is the stiffness matrix (for elasticity problems), componentwise:

$$\boldsymbol{K} = [\boldsymbol{K}_{AB}] = \begin{bmatrix} \boldsymbol{K}_{11} & \boldsymbol{K}_{12} & \ldots & \boldsymbol{K}_{1n} \\ \boldsymbol{K}_{21} & \boldsymbol{K}_{22} & \ldots & \boldsymbol{K}_{2n} \\ . & . & & . \\ . & . & & . \\ . & . & & . \\ \boldsymbol{K}_{n1} & \boldsymbol{K}_{n2} & \ldots & \boldsymbol{K}_{nn} \end{bmatrix} \tag{3.12}$$

$\boldsymbol{F}$ is termed the force vector (in elasticity problems) and is equal to the right hand side of equation (3.9):

$$\boldsymbol{F} = [\boldsymbol{F}_A] = \begin{bmatrix} \boldsymbol{F}_1 \\ \boldsymbol{F}_2 \\ . \\ . \\ . \\ \boldsymbol{F}_n \end{bmatrix} \tag{3.13}$$

$\boldsymbol{X}$ is the overall/global displacement vector given by:

$$\boldsymbol{X} = [\boldsymbol{d}_B] = \begin{bmatrix} \boldsymbol{d}_1 \\ \boldsymbol{d}_2 \\ . \\ . \\ . \\ \boldsymbol{d}_n \end{bmatrix} \tag{3.14}$$

The following remarks are to be stated:

1. The previous brief illustration describes generally the Finite Element Method (FEM) of a one–dimensional problem, the mathematics are viewed from a global point of view.

2. The solution of (G) through the discretization process is only an approximate solution of (V). The Dirichlet boundary conditions are exactly met but the Neumann boundary conditions may not be accurately satisfied. The accuracy of this approximate solution also depends on the choice of shape functions and the number n.

3. The matrix $\boldsymbol{K}$ is symmetric due to the symmetry of the partial differential operator and due to the use of Galerkin's method, i.e the same shape functions for the variations and the trial solutions.

4. Following schematically the steps until the matrix solution is reached, the scheme adopted involves two equivalent steps and an approximate step:

$$(\mathrm{S}) \Leftrightarrow (\mathrm{V}) \approx (\mathrm{G}) \Leftrightarrow (\mathrm{M}) \tag{3.15}$$

The only approximation made was by solving (V) through (G). However, in practice the data f, g and h as well as the domain Ω may need to be approximated.

3.2 Finite element method for thermo-poroelasticity

In this research the BVPs of thermo-poroelasticity are transient problems and thus the FEM will result in a system of semi-discrete ordinary differential equations. The constitutive model has been presented in chapter (2). The weak and the matrix formulations are to be presented below.

3.2.1 The weak formulations

In a space of dimension n_{sd}, there are $n_{sd}+2$ partial differential/field equations to be satisfied at each node:

- The balance of momentum of the mixture, equation (2.13).
- The balance of mass of the pore fluid, equation (2.17).
- The balance of energy of the mixture, equation (2.19).

Note that single porosity and local thermal equilibrium are assumed at any time. The weak formulations are obtained by multiplying the three field equations, written in a rate form for compatibility, by the variations $\delta\dot{\boldsymbol{u}}$, $\delta\dot{p}$ and $\delta\dot{\theta}$. The weak and the matrix formulations are to be presented for anisotropic thermo–poroelasticity for generalization.

3.2.1.1 The weak formulation of the balance of momentum of the mixture

Following equation (2.12), the equation of balance of momentum in a rate form is expressed as (the convention of summing over the mute indices is adopted all along this research):

$$\frac{\partial \dot{\sigma}_{ij}}{\partial x_j} + \dot{F}_i = 0, \quad i = 1,\, 2,\, 3 \tag{3.16}$$

Multiplying equation (3.16) by the variation $\delta\dot{u}_i$ and integrating over the body gives:

$$\int_V \delta\dot{u}_i \, \frac{\partial \dot{\sigma}_{ij}}{\partial x_j} + \delta\dot{u}_i \, \dot{F}_i \, dV = 0 \tag{3.17}$$

Integrating equation (3.17) by parts:

$$\int_{\partial V} \delta\dot{u}_i \, \dot{\sigma}_{ij} \, n_j \, ds - \int_V \frac{\partial(\delta\dot{u}_i)}{\partial x_j} \, \dot{\sigma}_{ij} \, dV + \int_V \delta\dot{u}_i \, \dot{F}_i \, dV = 0 \tag{3.18}$$

The rate of change of surface traction $\dot{t}_i$ can be expressed as:

$$\dot{t}_i = \dot{\sigma}_{ij} \, n_j, \tag{3.19}$$

where n_j is the unit outward vector normal to the boundary ∂V. Substituting for equation (3.19) in equation (3.18) yields:

$$\begin{aligned} \int_V \frac{\partial(\delta\dot{u}_i)}{\partial x_j} \left[D_{ijkl} \, \dot{\varepsilon}_{kl} - \kappa_{ij} \, \dot{p} - K_{ijkl} \, \alpha'_{skl} \, \dot{\theta} \right] dV - \int_{\partial V} \delta\dot{u}_i \, \dot{t}_i \, ds \\ - \int_V \delta\dot{u}_i \, \dot{F}_i \, dV = 0 \end{aligned} \tag{3.20}$$

Here, K_{ijkl} is the anisotropic drained elastic modulus tensor. Assuming micro–homogeneity and micro–isotropy, the anisotropic Biot's coefficient tensor κ_{ij} is expressed as in (Kanj and Abousleiman, [2005]):

$$\kappa_{ij} = \delta_{ij} - \frac{K_{ijkk}}{3K_s} \tag{3.21}$$

3.2.1.2 The weak formulation of the balance of mass of the pore fluid

Following equation (2.17), the equation of balance of mass takes the form:

$$\frac{\dot{p}}{M} = \frac{\partial}{\partial x_i} \left(\frac{k_{ij}}{\mu} \frac{\partial p}{\partial x_j} - \frac{k_{ij}}{\mu} \rho_f g_j \right) - \kappa_{ij} \frac{\partial^2 u_i}{\partial t \partial x_j} + \dot{\theta} \left[\kappa_{ij} \, \alpha'_{sij} + \phi_0 (\alpha_f - \alpha''_{skk}) \right] \tag{3.22}$$

For a matter of convenience, let us note:

$$\omega = \kappa_{ij} \alpha'_{sij} + \phi_0 (\alpha_f - \alpha''_{skk}) \tag{3.23}$$

Thus, ω is the pore fluid thermic parameter which relates the pore pressure variation to the change in the temperature. Assuming micro–homogeneity and micro–isotropy, Biot's modulus M for anisotropic thermo–poroelasticity is expressed as in (Kanj and Abousleiman, [2005]):

$$M = \frac{K_s}{\left(1 - \frac{K_{iijj}}{9K_s}\right) - \phi_0 \left(1 - \frac{K_s}{K_f}\right)} \tag{3.24}$$

Multiplying equation (3.22) by the weighting function $\delta\dot{p}$ and integrating over the body gives:

$$\int_V \delta\dot{p}\,\frac{\partial}{\partial x_i}\left(\frac{k_{ij}}{\mu}\frac{\partial p}{\partial x_j}-\frac{k_{ij}}{\mu}\,\rho_f g_j\right)dV+\int_V -\delta\dot{p}\,\kappa_{ij}\,\dot{\varepsilon}_{ij}\,dV+\int_V \delta\dot{p}\;\omega\,\dot{\theta}\,dV=\int_V \delta\dot{p}\,\frac{\dot{p}}{M}\,dV \tag{3.25}$$

Let us define the pore fluid flux vector $\boldsymbol{Q}$ (without accounting for the gravity term) as:

$$Q_i=-\frac{k_{ij}}{\mu}\,\frac{\partial p}{\partial x_j} \tag{3.26}$$

Substituting for equation (3.26) in equation (3.25) and integrating by parts yields:

$$\begin{aligned}\int_V \frac{\partial(\delta\dot{p})}{\partial x_i}\,\frac{k_{ij}}{\mu}\,\frac{\partial p}{\partial x_j}\,dV+\int_V \delta\dot{p}\,\kappa_{ij}\,\dot{\varepsilon}_{ij}\,dV+\int_V \delta\dot{p}\,\frac{\dot{p}}{M}\,dV\\ -\int_V \delta\dot{p}\,\omega\,\dot{\theta}\,dV+\int_{\partial V}\delta\dot{p}\,Q_i\,n_i\,ds-\int_V \frac{\partial(\delta\dot{p})}{\partial x_i}\,\frac{k_{ij}}{\mu}\,\rho_f g_j\,dV=0\end{aligned} \tag{3.27}$$

The normal pore fluid flux is defined as: $Q_n=Q_i\,n_i=-k_{ij}/\mu\,(\partial p/\partial x_j)\,n_i$.

3.2.1.3 The weak formulation of the balance of energy of the mixture

Following equation (2.19), the equation of balance of energy takes the form:

$$-\rho c_v\,\frac{\partial\theta}{\partial t}-\rho_f c_{vf}\,q_{f,i}\frac{\partial\theta}{\partial x_i}+\frac{\partial}{\partial x_i}(\chi_{ij}\,\frac{\partial\theta}{\partial x_j})=0 \tag{3.28}$$

χ_{ij} is the anisotropic thermal conductivity tensor of the mixture, ρc_v is the reference[1] volumetric heat capacity of the mixture. Multiplying equation (3.28) by the weighting function $\delta\dot{\theta}$ and integrating over the body gives:

$$\int_V -\rho c_v\,\delta\dot{\theta}\,\frac{\partial\theta}{\partial t}\,dV+\int_V -\rho_f c_{vf}\,\delta\dot{\theta}\,q_{f,i}\,\frac{\partial\theta}{\partial x_i}\,dV+\int_V \delta\dot{\theta}\,\frac{\partial}{\partial x_i}(\chi_{ij}\,\frac{\partial\theta}{\partial x_j})\,dV=0 \tag{3.29}$$

Based on the law of heat conduction/ Fourier's law, let us define the heat flux vector $\boldsymbol{H}$ such that:

$$H_i=-\chi_{ij}\,\frac{\partial\theta}{\partial x_j} \tag{3.30}$$

Substituting for equation (3.30) in equation (3.29) and integrating by parts yields:

$$\begin{aligned}\int_V -\rho c_v\,\delta\dot{\theta}\,\frac{\partial\theta}{\partial t}\,dV+\int_V -\rho_f c_{vf}\,\delta\dot{\theta}\,q_{f,i}\,\frac{\partial\theta}{\partial x_i}\,dV+\int_{\partial V}-\delta\dot{\theta}\,H_i\,n_i\,ds\\ +\int_V -\frac{\partial(\delta\dot{\theta})}{\partial x_i}\,\chi_{ij}\,\frac{\partial\theta}{\partial x_j}\,dV=0\end{aligned} \tag{3.31}$$

[1]The value of the volumetric heat capacity at a given point can also change depending on the thermo–poroelastic conditions at that point.

The normal heat flux H_n is defined such that: $H_n = H_i\, n_i = -\chi_{ij}(\partial\theta/\partial x_j)\, n_i$.

With some manipulation equations (3.20), (3.27) and (3.31) can be written in a form that follows equation (3.2):

$$\begin{aligned}
\int_V \boldsymbol{\nabla}(\delta\dot{\boldsymbol{u}}) : \dot{\boldsymbol{\sigma}}\, dV \quad &- \quad \int_V \delta\dot{\boldsymbol{u}} \,.\, \dot{\boldsymbol{F}}\, dV \quad = \quad \int_{\partial V} \delta\dot{\boldsymbol{u}} \,.\, \dot{\boldsymbol{\sigma}} \,.\, \boldsymbol{n}\, ds \\
\int_V \boldsymbol{\nabla}(\delta\dot{p}) \,.\, \left(\boldsymbol{Q} - \frac{\boldsymbol{k}}{\mu}\rho_f \boldsymbol{g}\right) dV \quad &- \quad \int_V \delta\dot{p}\, \dot{F}_p\, dV \quad = \quad \int_{\partial V} \delta\dot{p}\; \boldsymbol{Q} \,.\, \boldsymbol{n}\, ds \\
\int_V \boldsymbol{\nabla}(\delta\dot{\theta}) \,.\, \boldsymbol{H}\, dV \quad &- \quad \int_V \delta\dot{\theta}\, \dot{F}_\theta\, dV \quad = \quad \int_{\partial V} \delta\dot{\theta}\, \boldsymbol{H} \,.\, \boldsymbol{n}\, ds
\end{aligned} \tag{3.32}$$

The functions $\dot{F}_p$ and $\dot{F}_\theta$, equation (3.32), are called the thermo–poroelastic functions. They depend on the poroelastic and thermoelastic properties of the mixture as well as on the solution, i.e. pressure, temperature and their gradients.

$$\begin{aligned}
\dot{F}_p = \dot{\zeta} \quad &= \quad \kappa_{ij}\, \dot{\varepsilon}_{ij} - \omega\, \dot{\theta} + \frac{\dot{P}}{M} \\
\dot{F}_\theta \quad &= \quad \rho c_v\, \dot{\theta} + \rho_f c_{vf}\, q_{f,i}\, \frac{\partial\theta}{\partial x_i}
\end{aligned} \tag{3.33}$$

3.2.2 Discretization and Galerkin's method

Galerkin's procedure is adopted and the same interpolation functions are used to discretize the primary unknowns as well as the variations[1]. The unknowns are interpolated within the generic element e in terms of the nodal values of the displacement vector $\boldsymbol{u}$, pressure p and temperature θ through the interpolation functions $\boldsymbol{N_u}$, $\boldsymbol{N_p}$ and $\boldsymbol{N_\theta}$.

$$\begin{aligned}
&\dot{\boldsymbol{u}} = \boldsymbol{N_u}\, \dot{\boldsymbol{u}}^e, \qquad &&\delta\dot{\boldsymbol{u}} = \boldsymbol{N_u}\, \delta\dot{\boldsymbol{u}}^e, \qquad &&\boldsymbol{\varepsilon}(\delta\dot{\boldsymbol{u}}) = \boldsymbol{B_u}\, \delta\dot{\boldsymbol{u}}^e, \\
&\dot{\boldsymbol{p}} = \boldsymbol{N_p}\, \dot{\boldsymbol{p}}^e, \qquad &&\delta\dot{\boldsymbol{p}} = \boldsymbol{N_p}\, \delta\dot{\boldsymbol{p}}^e, \qquad &&\boldsymbol{\nabla}(\delta\dot{p}) = \boldsymbol{B_p}\, \delta\dot{\boldsymbol{p}}^e, \\
&\dot{\boldsymbol{\theta}} = \boldsymbol{N_\theta}\, \dot{\boldsymbol{\theta}}^e, \qquad &&\delta\dot{\boldsymbol{\theta}} = \boldsymbol{N_\theta}\, \delta\dot{\boldsymbol{\theta}}^e, \qquad &&\boldsymbol{\nabla}(\delta\dot{\theta}) = \boldsymbol{B_\theta}\, \delta\dot{\boldsymbol{\theta}}^e,
\end{aligned} \tag{3.34}$$

The same interpolation functions have been chosen for the primary variables, that is to say:

$$\boldsymbol{N_u} = \boldsymbol{N_p} = \boldsymbol{N_\theta}, \quad \text{and} \quad \boldsymbol{B_p} = \boldsymbol{B_\theta}, \tag{3.35}$$

where,

$$\boldsymbol{B_p} = \boldsymbol{\nabla N_p}, \quad \text{and} \quad \boldsymbol{B_\theta} = \boldsymbol{\nabla N_\theta} \tag{3.36}$$

[1] Convection terms need a special treatment, chapter (6).

This approach is satisfactory in hydro-mechanics, however it is to be tested when the thermal effects are considered (Gelet, [2012]).

Two-dimensional four-node isoparametric elements (Q4) are used to represent the spatial discretization of the IBVPs. Each shape function is associated with a given node; it is equal to one at this node and to zero at the other nodes. The shape functions of a parent four-node bilinear quadrilateral element are shown in figure (3.1):

$$
\begin{aligned}
N^1 &= \tfrac{1}{4}(1-\zeta)(1-\eta)\\
N^2 &= \tfrac{1}{4}(1+\zeta)(1-\eta)\\
N^3 &= \tfrac{1}{4}(1+\zeta)(1+\eta)\\
N^4 &= \tfrac{1}{4}(1-\zeta)(1+\eta)
\end{aligned}
$$

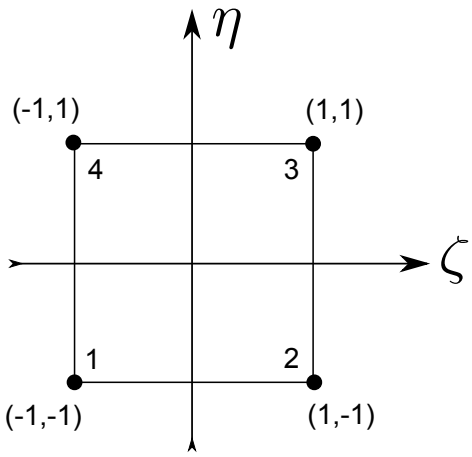

Figure 3.1: Shape functions for a four-node bilinear quadrilateral parent element (Q4). Nodal points are labeled in ascending order in counter-clockwise direction.

3.2.3 The matrix formulation of the semi-discrete equations

To get the matrix formulation from the weak variational semi-discrete system, equation (3.32), the contributions of all generic elements (N^{el}) are to be considered. The two steps (G) and (M) are gathered here for clearer and more concise illustration.

3.2.3.1 The matrix formulation of the balance of momentum of the mixture

The matrix formulation is obtained by substituting the definitions (3.34) into the equation (3.20):

$$
\begin{aligned}
&\sum_{e=1}^{N^{el}} \int_{V^e} (\boldsymbol{B_u}\boldsymbol{\delta}\dot{\boldsymbol{u}}^e)^T\, \boldsymbol{D}\, \boldsymbol{B_u}\dot{\boldsymbol{u}}^e - (\boldsymbol{B_u}\boldsymbol{\delta}\dot{\boldsymbol{u}}^e)^T\, \boldsymbol{\kappa}\, \boldsymbol{N_p}\, \dot{\boldsymbol{p}}^e - (\boldsymbol{B_u}\boldsymbol{\delta}\dot{\boldsymbol{u}}^e)^T\, \boldsymbol{K}\, \boldsymbol{\alpha}_s^{'}\, \boldsymbol{N_\theta}\, \dot{\boldsymbol{\theta}}^e\, dV^e \\
-\ &\sum_{e=1}^{N^{el}} \int_{\partial V^e} (\boldsymbol{N_u}\boldsymbol{\delta}\dot{\boldsymbol{u}}^e)^T\, \dot{\boldsymbol{t}}^e\, ds^e - \sum_{e=1}^{N^{el}} \int_{V^e} (\boldsymbol{N_u}\boldsymbol{\delta}\dot{\boldsymbol{u}}^e)^T\, \dot{\boldsymbol{F}}^e\, dV^e = \boldsymbol{0}
\end{aligned}
\tag{3.37}
$$

By writing equation (3.37) using the matrix form, it is found that:

$$\sum_{e=1}^{N^{el}} \begin{bmatrix} \boldsymbol{\delta \dot{u}}^e & \boldsymbol{\delta \dot{p}}^e & \boldsymbol{\delta \dot{\theta}}^e \end{bmatrix}^T \left(\int_{V^e} \begin{bmatrix} \boldsymbol{B_u^T\, D\, B_u} & \boldsymbol{-B_u^T\, \kappa\, N_p} & \boldsymbol{-B_u^T\, K\, \alpha_s' N_\theta} \\ - - - & - - - & - - - \\ - - - & - - - & - - - \end{bmatrix} \begin{bmatrix} \boldsymbol{\dot{u}}^e \\ \boldsymbol{\dot{p}}^e \\ \boldsymbol{\dot{\theta}}^e \end{bmatrix} dV^e \right)$$
$$+ \sum_{e=1}^{N^{el}} \begin{bmatrix} \boldsymbol{\delta \dot{u}}^e & \boldsymbol{\delta \dot{p}}^e & \boldsymbol{\delta \dot{\theta}}^e \end{bmatrix}^T \left(\int_{\partial V^e} \begin{bmatrix} \boldsymbol{-N_u^T\, \dot{t}}^e \\ - - - \\ - - - \end{bmatrix} ds^e + \int_{V^e} \begin{bmatrix} \boldsymbol{-N_u^T\, \dot{F}}^e \\ - - - \\ - - - \end{bmatrix} dV^e \right) = \begin{bmatrix} \mathbf{0} \\ - - - \\ - - - \end{bmatrix} \tag{3.38}$$

3.2.3.2 The matrix formulation of the balance of mass of the pore fluid

The matrix formulation is obtained by substituting the definitions (3.34) into the equation (3.27):

$$\begin{aligned} &\sum_{e=1}^{N^{el}} \int_{V^e} (\boldsymbol{B_p\, \delta \dot{p}}^e)^T \frac{\boldsymbol{k}}{\mu}\, \boldsymbol{B_p\, p^e}\, dV^e \quad + \quad \sum_{e=1}^{N^{el}} \int_{V^e} (\boldsymbol{N_p\, \delta \dot{p}}^e)^T\, \boldsymbol{\kappa\, B_u\, \dot{u}}^e\, dV^e \\ + &\sum_{e=1}^{N^{el}} \int_{V^e} (\boldsymbol{N_p\, \delta \dot{p}}^e)^T \frac{\boldsymbol{N_p\, \dot{p}}^e}{M}\, dV^e \quad - \quad \sum_{e=1}^{N^{el}} \int_{V^e} (\boldsymbol{N_p\, \delta \dot{p}}^e)^T\, \boldsymbol{N_\theta}\, \omega\, \boldsymbol{\dot{\theta}}^e\, dV^e \\ + &\sum_{e=1}^{N^{el}} \int_{\partial V^e} (\boldsymbol{N_p\, \delta \dot{p}}^e)^T\, Q_n\, ds^e \quad - \quad \sum_{e=1}^{N^{el}} \int_{V^e} (\boldsymbol{B_p\, \delta \dot{p}}^e)^T \frac{\boldsymbol{k}}{\mu}\, \rho_f\, \boldsymbol{g}\, dV^e = \mathbf{0} \end{aligned} \tag{3.39}$$

By writing equation (3.39) using the matrix form, it is concluded that:

$$\sum_{e=1}^{N^{el}} \begin{bmatrix} \boldsymbol{\delta \dot{u}}^e & \boldsymbol{\delta \dot{p}}^e & \boldsymbol{\delta \dot{\theta}}^e \end{bmatrix}^T \left(\int_{V^e} \begin{bmatrix} - - - & - - - & - - - \\ - - - & \boldsymbol{B_p^T \frac{k}{\mu} B_p} & - - - \\ - - - & - - - & - - - \end{bmatrix} \begin{bmatrix} \boldsymbol{u}^e \\ \boldsymbol{p}^e \\ \boldsymbol{\theta}^e \end{bmatrix} dV^e \right.$$
$$\left. + \int_{V^e} \begin{bmatrix} - - - & - - - & - - - \\ \boldsymbol{N_p^T\, \kappa\, B_u} & \boldsymbol{\frac{N_p^T N_p}{M}} & \boldsymbol{-N_p^T\, N_\theta\, \omega} \\ - - - & - - - & - - - \end{bmatrix} \begin{bmatrix} \boldsymbol{\dot{u}}^e \\ \boldsymbol{\dot{p}}^e \\ \boldsymbol{\dot{\theta}}^e \end{bmatrix} dV^e \right)$$
$$+ \sum_{e=1}^{N^{el}} \begin{bmatrix} \boldsymbol{\delta \dot{u}}^e & \boldsymbol{\delta \dot{p}}^e & \boldsymbol{\delta \dot{\theta}}^e \end{bmatrix}^T \left(\int_{\partial V^e} \begin{bmatrix} - - - \\ \boldsymbol{N_p^T}\, Q_n \\ - - - \end{bmatrix} ds^e + \int_{V^e} \begin{bmatrix} - - - \\ \boldsymbol{-B_p^T \frac{k}{\mu} \rho_f g} \\ - - - \end{bmatrix} dV^e \right) = \begin{bmatrix} - - - \\ \mathbf{0} \\ - - - \end{bmatrix} \tag{3.40}$$

3.2.3.3 The matrix formulation of the balance of energy of the mixture

The matrix formulation is obtained by substituting the definitions (3.34) into the equation (3.31):

$$\begin{aligned}
&\sum_{e=1}^{N^{el}} \int_{V^e} -\rho c_v \, (\boldsymbol{N_\theta}\, \boldsymbol{\delta\dot{\theta}}^e)^T \, \boldsymbol{N_\theta}\, \boldsymbol{\dot{\theta}}^e \, dV^e \quad + \quad \sum_{e=1}^{N^{el}} \int_{V^e} -\rho_f c_{vf} \, (\boldsymbol{N_\theta}\, \boldsymbol{\delta\dot{\theta}}^e)^T \, \boldsymbol{q}_f \, \boldsymbol{B_\theta}\, \boldsymbol{\theta}^e \, dV^e \\
+ &\sum_{e=1}^{N^{el}} \int_{\partial V^e} -(\boldsymbol{N_\theta}\, \boldsymbol{\delta\dot{\theta}}^e)^T \, H_n \, ds^e \quad + \quad \sum_{e=1}^{N^{el}} \int_{V^e} -(\boldsymbol{B_\theta}\, \boldsymbol{\delta\dot{\theta}}^e)^T \, \boldsymbol{\chi}\, \boldsymbol{B_\theta}\, \boldsymbol{\theta}^e \, dV^e = \boldsymbol{0}
\end{aligned} \tag{3.41}$$

By writing equation (3.41) using the matrix form, one finds:

$$\begin{aligned}
&\sum_{e=1}^{N^{el}} \begin{bmatrix} \boldsymbol{\delta\dot{u}}^e & \boldsymbol{\delta\dot{p}}^e & \boldsymbol{\delta\dot{\theta}}^e \end{bmatrix}^T \left(\int_{V^e} \begin{bmatrix} - & - & - \\ - & - & - \\ - & - & -\rho c_v \, \boldsymbol{N_\theta^T}\, \boldsymbol{N_\theta} \end{bmatrix} \begin{bmatrix} \boldsymbol{\dot{u}}^e \\ \boldsymbol{\dot{p}}^e \\ \boldsymbol{\dot{\theta}}^e \end{bmatrix} dV^e \right. \\
&\qquad \left. + \int_{V^e} \begin{bmatrix} - & - & - \\ - & - & - \\ - & - & -\rho_f c_{vf} \, \boldsymbol{N_\theta^T}\, \boldsymbol{q}_f \, \boldsymbol{B_\theta} - \boldsymbol{B_\theta^T}\, \boldsymbol{\chi}\, \boldsymbol{B_\theta} \end{bmatrix} \begin{bmatrix} \boldsymbol{u}^e \\ \boldsymbol{p}^e \\ \boldsymbol{\theta}^e \end{bmatrix} dV^e \right) \\
+ &\sum_{e=1}^{N^{el}} \begin{bmatrix} \boldsymbol{\delta\dot{u}}^e & \boldsymbol{\delta\dot{p}}^e & \boldsymbol{\delta\dot{\theta}}^e \end{bmatrix}^T \int_{\partial V^e} \begin{bmatrix} - & - & - \\ - & - & - \\ -\boldsymbol{N_\theta^T}\, H_n \end{bmatrix} ds^e = \begin{bmatrix} - & - & - \\ - & - & - \\ \boldsymbol{0} \end{bmatrix}
\end{aligned} \tag{3.42}$$

Assembling equations (3.38), (3.40), and (3.42):

$$\begin{aligned}
&\sum_{e=1}^{N^{el}} \begin{bmatrix} \boldsymbol{\delta\dot{u}}^e & \boldsymbol{\delta\dot{p}}^e & \boldsymbol{\delta\dot{\theta}}^e \end{bmatrix}^T \left(\int_{V^e} \begin{bmatrix} \boldsymbol{B_u^T}\, \boldsymbol{D}\, \boldsymbol{B_u} & -\boldsymbol{B_u^T}\, \boldsymbol{\kappa}\, \boldsymbol{N_p} & -\boldsymbol{B_u^T}\, \boldsymbol{K}\, \boldsymbol{\alpha}_s' \, \boldsymbol{N_\theta} \\ \boldsymbol{N_p^T}\, \boldsymbol{\kappa}\, \boldsymbol{B_u} & \dfrac{\boldsymbol{N_p^T}\, \boldsymbol{N_p}}{M} & -\boldsymbol{N_p^T}\, \boldsymbol{N_\theta}\, \omega \\ \boldsymbol{0} & \boldsymbol{0} & -\rho c_v \, \boldsymbol{N_\theta^T}\, \boldsymbol{N_\theta} \end{bmatrix} \begin{bmatrix} \boldsymbol{\dot{u}}^e \\ \boldsymbol{\dot{p}}^e \\ \boldsymbol{\dot{\theta}}^e \end{bmatrix} dV^e \right. \\
&\qquad \left. + \int_{V^e} \begin{bmatrix} \boldsymbol{0} & \boldsymbol{0} & \boldsymbol{0} \\ \boldsymbol{0} & \boldsymbol{B_p^T}\, \dfrac{\boldsymbol{k}}{\mu}\, \boldsymbol{B_p} & \boldsymbol{0} \\ \boldsymbol{0} & \boldsymbol{0} & -\boldsymbol{B_\theta^T}\, \boldsymbol{\chi}\, \boldsymbol{B_\theta} \end{bmatrix} \begin{bmatrix} \boldsymbol{u}^e \\ \boldsymbol{p}^e \\ \boldsymbol{\theta}^e \end{bmatrix} dV^e \right) \\
+ &\sum_{e=1}^{N^{el}} \begin{bmatrix} \boldsymbol{\delta\dot{u}}^e & \boldsymbol{\delta\dot{p}}^e & \boldsymbol{\delta\dot{\theta}}^e \end{bmatrix}^T \int_{V^e} \begin{bmatrix} \boldsymbol{0} & \boldsymbol{0} & \boldsymbol{0} \\ \boldsymbol{0} & \boldsymbol{0} & \boldsymbol{0} \\ \boldsymbol{0} & \boldsymbol{0} & -\rho_f c_{vf} \, \boldsymbol{N_\theta^T}\, \boldsymbol{q}_f \, \boldsymbol{B_\theta} \end{bmatrix} \begin{bmatrix} \boldsymbol{u}^e \\ \boldsymbol{p}^e \\ \boldsymbol{\theta}^e \end{bmatrix} dV^e \\
= &\sum_{e=1}^{N^{el}} \begin{bmatrix} \boldsymbol{\delta\dot{u}}^e & \boldsymbol{\delta\dot{p}}^e & \boldsymbol{\delta\dot{\theta}}^e \end{bmatrix}^T \left(\int_{\partial V^e} \begin{bmatrix} \boldsymbol{N_u^T}\, \boldsymbol{\dot{t}}^e \\ -\boldsymbol{N_p^T}\, Q_n \\ \boldsymbol{N_\theta^T}\, H_n \end{bmatrix} ds^e + \int_{V^e} \begin{bmatrix} \boldsymbol{N_u^T}\, \boldsymbol{\dot{F}}^e \\ \boldsymbol{B_p^T}\, \dfrac{\boldsymbol{k}}{\mu}\, \rho_f \boldsymbol{g} \\ \boldsymbol{0} \end{bmatrix} dV^e \right)
\end{aligned} \tag{3.43}$$

For any arbitrary variations $\delta\dot{\boldsymbol{u}}$, $\delta\dot{p}$ and $\delta\dot{\theta}$, the system (3.43) sums to:

$$\sum_{e=1}^{N^{el}} \left[\mathbb{D}^e \left(\frac{d}{dt} \mathbb{X}^e \right) + \mathbb{K}^e \, \mathbb{X}^e + \mathbb{C}^e \, \mathbb{X}^e - \mathbb{F}^e \right] = \mathbb{O}, \tag{3.44}$$

where,

- $\mathbb{X}^e$ is the vector of the nodal unknowns $\{\boldsymbol{u}, p \text{ and } \theta\}$.
- $\mathbb{D}^e$ is the element diffusion matrix.
- $\mathbb{K}^e$ is the element stiffness matrix.
- $\mathbb{C}^e$ is the element convection matrix.
- $\mathbb{F}^e$ is the vector of generic element contributions. These contributions include the body forces and the surface/ boundary loading terms.

3.2.4 Time marching scheme for solving the equations: The predictor multi-corrector method

Boundary value problems that concern fluid saturated mixtures with non-linear terms and constituents that are in thermal equilibrium, are either parabolic (like in diffusion problems) or hyperbolic (like in pure convection). The predictor multi-corrector method is to be used to solve our linearized semi-discrete system, equation (3.44), over the time.

The overall system of equations may be written in the following format:

$$\mathbb{D}\,\mathbb{V} + \mathbb{K}\,\mathbb{X} + \mathbb{C}\,\mathbb{X} = \mathbb{F} \tag{3.45}$$

The matrices $\mathbb{D}$, $\mathbb{K}$ and $\mathbb{C}$ are the global diffusion, stiffness and convection matrices respectively. The vectors $\mathbb{X}$ and $\mathbb{F}$ are the global solution and the global load vectors respectively, $\mathbb{V}$ is the time derivative of $\mathbb{X}$.

This system can also be written in terms of the global load vector $\mathbb{F}$ as the difference between the global surface load vector and the global internal load vectors:

$$\mathbb{R} = \underbrace{\mathbb{F}^{\mathrm{TE}}(\mathbb{X}, \mathbb{V}) + \mathbb{F}^{\mathrm{conv}}(\mathbb{X}, \mathbb{V})}_{\text{Internal forces}} - \underbrace{\mathbb{F}^{\mathrm{surf}}(\mathbb{S}, \mathbb{V})}_{\text{Surface forces}} = \mathbb{O}, \tag{3.46}$$

$\mathbb{F}^{\mathrm{TE}}$, $\mathbb{F}^{\mathrm{conv}}$ and $\mathbb{F}^{\mathrm{surf}}$ represent the contributions from the thermoelastic, the convective and the surface effects respectively. $\mathbb{S}$ represents the collective surface loading and $\mathbb{R}$ stands for the

residual of the system.

The aim is to find the vector of the unknowns $\mathbb{X}$ by rendering the residual $\mathbb{R}$ equal to $\mathbb{O}$. Starting from the initial situation the solution $\mathbb{X}_0$ is known, going from step n to step $n+1$ requires moving through the time by an interval $\Delta t = t_{n+1} - t_n$. The predictor multi-corrector method, described below, is to be used to find the solution $\mathbb{X}_{n+1}$ at the time step $n+1$.

The predictor multi-corrector method is an iterative procedure used to solve transient BVPs. The predictor multi–corrector method proceeds in two steps. First, the prediction step calculates an initial rough approximation of the desired quantity. Second, the corrector step refines the initial approximation. Typically this method uses an explicit method for the predictor step and an implicit method for the corrector step. Implicit here means that it uses the previous approximate solution for the correction.

The system of equations (3.45) is to be integrated over a *Generalized trapezoidal method*[1] defined by a scalar $\alpha \in]0,1]$. Within a time interval of $\Delta t = t_{n+1} - t_n$, the approximate solution is assumed to be found at an iteration $i+1$. A new concept of explicit/implicit operator split is introduced; this means that we choose to make some terms of the system (3.45) explicit or implicit. The time integration procedure will use the predictor multi–corrector scheme with an explicit/implicit operator split. Implicit/explicit terms means that such terms contribute/do not contribute to the calculation of the effective diffusion matrix. Following equation (3.46), the vector of the internal body forces is always implicit and the vector of the surface loads is always explicit, meanwhile the vector of the convective forces can be either implicit or explicit.

1. If the convective forces are implicit the residual $\mathbb{R}$ at iteration $i+1$ can be written as:

$$\mathbb{R}^{i+1}_{n+\alpha} = \mathbb{F}^{\mathrm{TE}}(\mathbb{X}^{i+1}_{n+\alpha}, \mathbb{V}^{i+1}_{n+\alpha}) + \mathbb{F}^{\mathrm{conv}}(\mathbb{X}^{i+1}_{n+\alpha}, \mathbb{V}^{i+1}_{n+\alpha}) - \mathbb{F}^{\mathrm{surf}}(\mathbb{S}^{i}_{n+\alpha}, \mathbb{X}^{i}_{n+\alpha}) \tag{3.47}$$

Note that at the step $n+1$ the above relation is forced to be equal to $\mathbb{O}$ at the time $t_{n+\alpha} = t_n + \alpha\,\Delta t$ with $\Delta t = t_{n+1} - t_n$. This leads us to the following definition, for any $\mathbb{Z} = \mathbb{X},\ \mathbb{V}$ or $\mathbb{S}$:

$$\mathbb{Z}^{i+1}_{n+\alpha} = (1-\alpha)\,\mathbb{Z}_n + \alpha\,\mathbb{Z}^{i+1}_{n+1} \tag{3.48}$$

[1] See (Hughes, [2000]) for more details.

The iterative process (with i being the iteration number) proceeds as follows:

$$\begin{aligned}
&\text{Initialization} \quad : \quad \begin{cases} \mathbb{X}^0_{n+1} = \mathbb{X}_n + (1-\alpha)\,\Delta t\,\mathbb{V}_n \\ \mathbb{V}^0_{n+1} = \mathbb{V}_n \end{cases} \\
&\text{for } \; i \geq 0 \qquad : \quad \begin{cases} \mathbb{X}^{i+1}_{n+1} &= \mathbb{X}_n + \Delta t\,\mathbb{V}^{i+1}_{n+\alpha} = \mathbb{X}^0_{n+1} + \alpha\,\Delta t\,\mathbb{V}^{i+1}_{n+1} \\ &= \tilde{\mathbb{X}}^i_{n+1} + \alpha\,\Delta t\,\Delta\mathbb{V} \\ \mathbb{V}^{i+1}_{n+1} &= \mathbb{V}^i_{n+1} + \Delta\mathbb{V} \end{cases}
\end{aligned} \tag{3.49}$$

The *predictor value* $\tilde{\mathbb{X}}^i_{n+1}$ is given by:

$$\text{where } i \geq 0 \quad , \quad \tilde{\mathbb{X}}^i_{n+1} = \mathbb{X}^0_{n+1} + \alpha\,\Delta t\,\mathbb{V}^i_{n+1} \quad \text{and} \quad (= \mathbb{X}^i_{n+1} \quad \text{for} \quad i > 0) \tag{3.50}$$

By inserting the time-integrator (3.49) in the equation (3.47):

$$\begin{aligned}
\mathbb{R}^{i+1}_{n+\alpha} &= -\mathbb{F}^{\text{surf}}(\mathbb{S}^i_{n+\alpha}, \mathbb{X}^i_{n+\alpha}) + \mathbb{F}^{\text{TE+conv}}\Big((1-\alpha)\,\mathbb{X}_n + \alpha\,\mathbb{X}^{n+1}_{i+1}, (1-\alpha)\,\mathbb{V}_n + \alpha\,\mathbb{V}^{n+1}_{i+1}\Big) \\
&= -\mathbb{F}^{\text{surf}}(\mathbb{S}^i_{n+\alpha}, \mathbb{X}^i_{n+\alpha}) \\
&+ \mathbb{F}^{\text{TE+conv}}\Big((1-\alpha)\,\mathbb{X}_n + \alpha\,\tilde{\mathbb{X}}^i_{n+1} + \alpha^2\,\Delta t\,\Delta\mathbb{V}, (1-\alpha)\,\mathbb{V}_n + \alpha\,(\mathbb{V}^i_{n+1} + \Delta\mathbb{V})\Big)
\end{aligned} \tag{3.51}$$

The notation $\mathbb{F}^{\text{TE+conv}} = \mathbb{F}^{\text{TE}} + \mathbb{F}^{\text{conv}}$ is adopted since the vectors of internal forces and convective forces are implicit. By expanding equation (3.51) to the second terms using *Taylor series*:

$$\begin{aligned}
\mathbb{R}^{i+1}_{n+\alpha} &\approx -\mathbb{F}^{\text{surf}}(\mathbb{S}^i_{n+\alpha}, \mathbb{X}^i_{n+\alpha}) \\
&+ \mathbb{F}^{\text{TE+conv}}\Big((1-\alpha)\,\mathbb{X}_n + \alpha\,\tilde{\mathbb{X}}^i_{n+1}, (1-\alpha)\,\mathbb{V}_n + \alpha\,\mathbb{V}^i_{n+1}\Big) \\
&+ \left(\frac{\partial\mathbb{F}^{\text{TE+conv}}}{\partial\mathbb{X}}\right)\Big((1-\alpha)\,\mathbb{X}_n + \alpha\,\tilde{\mathbb{X}}^i_{n+1}, (1-\alpha)\,\mathbb{V}_n + \alpha\,\mathbb{V}^i_{n+1}\Big)\,\alpha^2\Delta t\,\Delta\mathbb{V} \\
&+ \left(\frac{\partial\mathbb{F}^{\text{TE+conv}}}{\partial\mathbb{V}}\right)\Big((1-\alpha)\,\mathbb{X}_n + \alpha\,\tilde{\mathbb{X}}^i_{n+1}, (1-\alpha)\,\mathbb{V}_n + \alpha\,\mathbb{V}^i_{n+1}\Big)\,\alpha\Delta\mathbb{V} \\
&\approx -\mathbb{F}^{\text{surf}}(\mathbb{S}^i_{n+\alpha}, \mathbb{X}^i_{n+\alpha}) + \mathbb{F}^{\text{TE+conv}}\Big(\tilde{\mathbb{X}}^i_{n+\alpha}, \mathbb{V}^i_{n+\alpha}\Big) + \Big((\mathbb{K}+\mathbb{C})\,\alpha\Delta t + \mathbb{D}\Big)\,\alpha\Delta\mathbb{V},
\end{aligned} \tag{3.52}$$

where:

$$\mathbb{D} = \left(\frac{\partial\mathbb{F}^{\text{TE+conv}}}{\partial\mathbb{V}}\right)\Big(\tilde{\mathbb{X}}^i_{n+\alpha}\Big) \qquad \text{and} \qquad \mathbb{K}+\mathbb{C} = \left(\frac{\partial\mathbb{F}^{\text{TE+conv}}}{\partial\mathbb{X}}\right)\Big(\tilde{\mathbb{X}}^i_{n+\alpha}\Big) \tag{3.53}$$

By defining $\mathbb{C}^* = \mathbb{D} + (\mathbb{K}+\mathbb{C})\,\alpha\Delta t$ the *effective convection–diffusion matrix*, equation (3.52) can be expressed as:

$$\mathbb{R}^{i+1}_{n+\alpha} \approx \mathbb{R}^i_{n+\alpha} + \mathbb{C}^*\,\alpha\Delta\mathbb{V} \tag{3.54}$$

The residual $\mathbb{R}^{i+1}_{n+\alpha}$ is forced to $\mathbb{O}$ and equation (3.54) is solved at each iteration to get the *Newton direction* $\Delta\mathbb{V}$. Note that the derivatives of the vectors $\mathbb{F}^{\text{TE+conv}}$ do not depend on the rate vector $\mathbb{V}$.

2. If the convective forces are explicit, the residual $\mathbb{R}$ at iteration $i+1$ can now be written as:

$$\mathbb{R}^{i+1}_{n+\alpha} = \mathbb{F}^{\text{TE}}(\mathbb{X}^{i+1}_{n+\alpha}, \mathbb{V}^{i+1}_{n+\alpha}) + \mathbb{F}^{\text{conv}}(\mathbb{X}^{i}_{n+\alpha}, \mathbb{V}^{i}_{n+\alpha}) - \mathbb{F}^{\text{surf}}(\mathbb{S}^{i}_{n+\alpha}, \mathbb{X}^{i}_{n+\alpha}), \tag{3.55}$$

The notation $-\mathbb{F}^{\text{surf+conv}} = -\mathbb{F}^{\text{surf}} + \mathbb{F}^{\text{conv}}$ is introduced since the vector of convective forces as well as the vector of surface forces are explicit. Equation (3.55) is linearized to get the following expression:

$$\begin{aligned} \mathbb{R}^{i+1}_{n+\alpha} &\approx -\mathbb{F}^{\text{surf+conv}}(\mathbb{S}^{i}_{n+\alpha}, \mathbb{X}^{i}_{n+\alpha}, \mathbb{V}^{i}_{n+\alpha}) + \mathbb{F}^{\text{TE}}(\tilde{\mathbb{X}}^{i}_{n+\alpha}, \mathbb{V}^{i}_{n+\alpha}) - (\mathbb{K}\,\alpha\Delta t + \mathbb{D})\,\alpha\Delta\mathbb{V} \\ &\approx \mathbb{R}^{i}_{n+\alpha} + \mathbb{C}^{*} \alpha\Delta\mathbb{V} \end{aligned} \tag{3.56}$$

The effective diffusion matrix $\mathbb{C}^*$ is now defined by $\mathbb{C}^* = \mathbb{D} + \mathbb{K}\,\alpha\Delta t$. The residual $\mathbb{R}^{i+1}_{n+\alpha}$ is forced to $\mathbb{O}$ and equation $(3.56)_2$ is solved at each iteration to get the Newton direction $\Delta\mathbb{V}$.

The algorithm for the predictor multi–corrector method at step $n+1$ can be expressed in the following manner:

1. Initialization

$$i = 0 \quad : \quad \begin{cases} \mathbb{X}^{0}_{n+1} = \mathbb{X}_n + (1-\alpha)\Delta t\, \mathbb{V}_n \\ \mathbb{V}^{0}_{n+1} = \mathbb{V}_n \end{cases}$$

2. Getting Newton direction

$$\mathbb{C}^*\,(\alpha\,\Delta\mathbb{V}) = \mathbb{R}^{i}_{n+\alpha}$$

3. Correction

$$i \geq 0 \quad : \quad \begin{cases} \tilde{\mathbb{X}}^{i}_{n+1} = \mathbb{X}^{0}_{n+1} + \alpha\,\Delta t\,\mathbb{V}^{i}_{n+1} \\ \mathbb{X}^{i+1}_{n+1} = \tilde{\mathbb{X}}^{i}_{n+1} + \alpha\,\Delta t\,\Delta\mathbb{V} \\ \mathbb{V}^{i+1}_{n+1} = \mathbb{V}^{i}_{n+1} + \Delta\mathbb{V} \end{cases}$$

4. If the iterative change in the solution vector $\mathbb{X}$ and/or in the residual $\mathbb{R}$ is smaller than a given tolerance then go to 5
   Else $i = i + 1$ and go to 2

5. End

More information about convergence and accuracy can be found in (Hughes, [2000]). This time marching scheme will be used all along this PhD research to solve the thermo–poroelastic IBVPs. It will be tested against the numerical simulations given by ABAQUS in section (3.4.1) for one dimensional IBVP, and against the analytical solution for two-dimensional IBVP in section (3.4.2).

3.3 Simulation of thermo-poroelasticity using ABAQUS

This section presents the ABAQUS simulation of a one-dimensional transient BVP of a saturated rock column subjected to thermal loading while consolidating. The ABAQUS numerical results are correlated to the analytical solution given by (Selvadurai and Suvorov, [2009]) for the same IBVP. A study on the effects of some hydraulic and thermal parameters on the thermo-poro-mechanical behavior is also presented.

Consider a column of rock of height L and width B which is initially saturated and heated to a uniform temperature change θ_0 without allowing any heat or fluid fluxes. This uniform pre–heating without allowing any fluid or heat dissipation at the boundaries caused trapped fluid to build up a uniform initial pressure value of p_0^-. The column is then suddenly loaded with a surcharge of value σ_0 while allowing fluid and heat to dissipate through only the upper surface of the column $x_2 = 0$, heat and fluid fluxes at $x_2 = L$ are set to zero at any time. Lateral displacement is prevented and the only displacement component allowed for is in the direction of x_2. Follow figure (3.2) shown below.

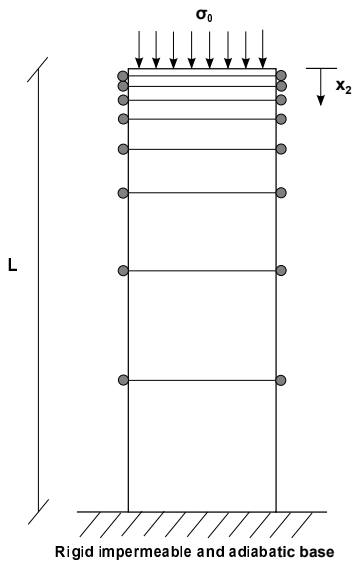

Figure 3.2: Schematic diagram of the one-dimensional problem to be solved.

Initial conditions at time $t = 0^-$ (just before applying the surcharge and allowing for heat and fluid dissipation at the top) are expressed as:

$$\begin{aligned} \theta(x_2,\, t = 0^-) &= \theta_0 \\ p(x_2,\, t = 0^-) &= p_0^- \end{aligned} \tag{3.57}$$

The pore fluid built up pressure p_0^- is uniform which necessarily means that gravity effect is not considered.

The boundary conditions for $t > 0$ are:

$$\begin{array}{lll} p(x_2 = 0,\, t) = 0 & ; & \dfrac{\partial p}{\partial x_2}\big|_{(x_2=L,\,t)} = 0 \\ \theta(x_2 = 0,\, t) = 0 & ; & \dfrac{\partial \theta}{\partial x_2}\big|_{(x_2=L,\,t)} = 0 \\ \sigma_{22}(x_2 = 0,\, t) = \sigma_0 & ; & \sigma_{12}(x_2 = 0,\, t) = 0 \end{array} \qquad (3.58)$$

$$u_2(x_2 = L,\, t) = 0$$

Applying the boundary and initial conditions to the main field equations of thermo-poro–elasticity, while considering that solid grains are incompressible ($\kappa = 1$) and while neglecting the poroelastic and the convective terms in the energy equation, (Selvadurai and Suvorov, [2009]) have presented the following analytical solution:

$$\theta(x_2, t) = \theta_0 \sum_{m=1,3,5\ldots} \frac{4}{m\pi}\, \sin(\frac{m\pi}{2L} x_2)\, \exp(-\tau_m^2\, t)\ , \quad \tau_m^2 = \frac{m^2\pi^2}{4L^2}\frac{\chi}{\rho c_v} \qquad (3.59)$$

The ratio $\chi/\rho c_v$ is the thermal diffusivity ψ.

$$p(x_2, t) = \sum_{m=1,3,5\ldots} C_m\, \sin(\frac{m\pi}{2L} x_2)\, \exp(-\omega_m^2\, t) + \sum_{m=1,3,5\ldots} A_m\, \sin(\frac{m\pi}{2L} x_2)\, \exp(-\tau_m^2\, t), \qquad (3.60)$$

while,

$$A_m = \frac{\left(\dfrac{K}{K + 4G/3}\,\alpha_s - n\alpha_f - (1-n)\alpha_s\right)\dfrac{4\theta_0\tau_m^2}{m\pi}}{\dfrac{k_{22}}{\gamma_f}\dfrac{m^2\pi^2}{4L^2} - \left(\dfrac{1}{K + 4G/3} + \dfrac{n}{k_f}\right)\tau_m^2}, \qquad (3.61)$$

$$C_m = p_0^+ \frac{4}{m\pi} - A_m, \qquad (3.62)$$

and,

$$\begin{aligned} p_0^+ &= \Delta p_\sigma + p_0^- \\ &= \frac{-\sigma_0}{1 + (K + 4G/3)\dfrac{n}{K_f}} + \frac{\theta_0[n\alpha_f + (1-n)\alpha_s](K + 4G/3) - K\,\alpha_s\theta_0}{1 + (K + 4G/3)\dfrac{n}{K_f}} \end{aligned} \qquad (3.63)$$

Δp_σ is the abrupt increase in the pore pressure as result of applying the surcharge σ_0 at $t = 0^+$ while allowing heat and fluid to dissipate at $x_2 = 0$, γ_f is the unit weight of water.

$$\omega_m^2 = \frac{m^2\pi^2}{4L^2} \frac{k_{22}\left(K + \frac{4}{3}G\right)}{\gamma_f\left(1 + \frac{n}{K_f}\left(K + \frac{4}{3}G\right)\right)} \tag{3.64}$$

K and G are the bulk and shear moduli of the geomaterial under drained conditions, α_s and α_f are the solid and the fluid volumetric thermal expansion coefficients respectively, k_{22} is the medium hydraulic conductivity in the direction x_2 and K_f is the fluid bulk modulus.

$$\begin{aligned} u_2(x_2,t) = \frac{1}{K+4G/3} \Bigg[& -K\,3\alpha_s\theta_0 \sum_{m=1,3,5\ldots} \frac{8L^2}{m^2\pi^2} \cos(\frac{m\pi}{2L}x_2)\, \exp(-\tau_m^2\, t) \\ & - \sum_{m=1,3,5\ldots} C_m \frac{2L}{m\pi} \cos(\frac{m\pi}{2L}x_2)\, \exp(-\omega_m^2\, t) \\ & - \sum_{m=1,3,5\ldots} A_m \frac{2L}{m\pi} \cos(\frac{m\pi}{2L}x_2)\, \exp(-\tau_m^2\, t) \\ & + (y-L)\sigma_0 \Bigg] \end{aligned} \tag{3.65}$$

The constant of integration y is found by requiring the displacement to be equal to zero at $x_2 = L$ for any time t.

3.3.1 Results obtained using ABAQUS

ABAQUS^{TM} version 6.11-1 has been used to simulate the above mentioned one-dimensional thermo-poroelastic problem. When simulating by ABAQUS, one must keep the following important notes in mind:

- The geostatic step is not needed as the sample is initially in equilibrium under the thermal loading.
- Checking the time scales of the BVP, section (2.1.3), is of tremendous importance to estimate the time required for full analysis.
- Since energy equation is decoupled from mechanical and fluid diffusion effects, the problem could have been solved in two parts. A heat transfer problem (a) was first simulated, the file was saved and then used to solve the second problem of consolidation (b).
- The same mesh and numbering system should be adopted in the two parts of the problem. The best mesh choice has been noticed to be a one-dimensional mesh of ratio ~ 3 between the largest and the smallest elements. 100 elements were sufficient to get very accurate results for a column of 10 m height.

- 8-node plane strain quadrilateral elements (Q8) with reduced integration have been used to solve both parts of heat transfer and consolidation, i.e. displacement, pore pressure and temperature fields are discretized using Q8 elements.

- Fixed time interval transient analyses have been used to simulate the two parts of the problem. According to the instructions of the manual (section 6.8.1), using transient analyses in a mesh of second–order elements may lead to diverging results. This can be overstepped by considering the following criteria for increment size:

  - $\Delta t > \dfrac{\rho c_v}{6\chi}\,(\Delta l)^2$, for the heat transfer part and,
  - $\Delta t > \dfrac{\gamma_f}{6E\,k_{22}}\left(1-\dfrac{E}{K_s}\right)(\Delta l)^2$, for the consolidation part

  Δl is the largest element size of the mesh, K_s is the bulk modulus of solid grains and E is the drained elastic modulus. The above relations are derived from the integration procedure used in ABAQUS, it introduces a relationship between the minimum usable time increment and the element size. Unless a maximum allowable time increment is specified, generally, there is no upper limit on the time increment size (The integration procedure used is unconditionally stable, at least of linear problems). If smaller time increments are required, a finer mesh is to be used in regions where changes occur rapidly.

- When simulating the thermo-poroelastic problems with transient analyses, it is highly recommended to set the default load variation with time to "Ramp linearly over step". This will give more accurate results.

- When filling the material properties, namely, the logarithmic bulk modulus ϑ, one must follow equation (3.66) shown below. This equation is a linearization of the expression given by the manual (section 21.3.1) provided that P_t, the material tensile strength, is sufficiently large.

$$K = \frac{1+e_0}{\vartheta}\,P_t \tag{3.66}$$

  e_0 is the initial void ratio and K is the bulk modulus of the sample. The best assumption for P_t is to start with $P_t \sim (100-150)\,p$, where p is the largest expected value of the pore pressure.

- Table (3.1) shows the time analysis that has been considered to solve the 1–dimensional column IBVP:

Table 3.1: Time discretization considered to simulate the 1-dimensional problem by ABAQUS.

Step number	Period of the step (days)	Increment size (s)	Number of increments
1	1	1000	87
2	10	1500	519
3	100	5000	1556
4	365	10000	2290
5	700	30000	965
6	1400	70000	864

Let us now define the problem more concisely as follows: it is a one-dimensional column of height $L = 10$ m occupying the domain $0 \leq x_2 \leq L$ with a base width $B = 3$ m. The column is initially $(t = 0^-)$ at elevated temperature θ_0=100 °C and non–zero built up pressure p_0^-. The load σ_0 of 10 MPa is applied at $(t = 0^+)$ while allowing heat and fluid to dissipate through the surface $x_2 = 0$. The hydraulic and thermal properties given in Table (3.2) are used to simulate the problem.

Table 3.2: Properties of the sample material "Typically rock".

Property	Value
Porosity n	0.25
Young's modulus E	60×10^9 (Pa)
Poisson's ratio ν	0.3
Unit weight of water γ_f	9800 (N/m^3)
Medium hydraulic conductivity k	2.94×10^{-12} (m/s)
Effective thermal conductivity χ	4 (W/m°C)
Effective heat capacity ρc_v	2465000 (J/m^3 °C)
Volumetric thermal expansion of solid phase α_s	2.49×10^{-5} (1/°C)
Volumetric thermal expansion of liquid α_f	0 or 4.2×10^{-4} (1/°C)
Fluid bulk modulus K_f	∞ or 2.2×10^9 (Pa)

Let us define the vertical displacement at the top of the rock column ($x_2 = 0$) due to pre–heating from 0 to 100 °C by u_{20}^-. To stand for the effect of certain parameters, particularly "α_f and K_f", on the thermo-poroelastic behavior of the rock column, four cases as shown in Table (3.3) shall be considered. p_0^- and u_{20}^- for any case are calculated directly by implementing equations (3.63) and (3.65) respectively. The effect of the linear thermal expansion α_f and fluid bulk modulus K_f on the thermo–poroelastic behavior of the problem is of tremendous significance. Explanations for these effects are to be given later in this section.

Table 3.3: Pore pressure (uniform) and vertical displacement (at $x_2 = 0$) initially built up as result of pre–heating the column from 0 to 100 °C.

Case definition		p_0^- (MPa)	u_{20}^- (mm)
(1) α_f=0,	K_f=∞	26.30	18.54
(2) α_f=0,	K_f=2.2×10^9 Pa	2.950	14.55
(3) α_f=4.2×10^{-4} /°C,	K_f=2.2×10^9 Pa	85.91	24.79
(4) α_f=4.2×10^{-4} /°C,	K_f=∞	830.0	121.8

ABAQUS numerical response is to be tested against the analytical solution of (Selvadurai and Suvorov, [2009]). In the figures presented below, the analytical solution is shown with a solid line meanwhile ABAQUS response is shown with scattered markers.

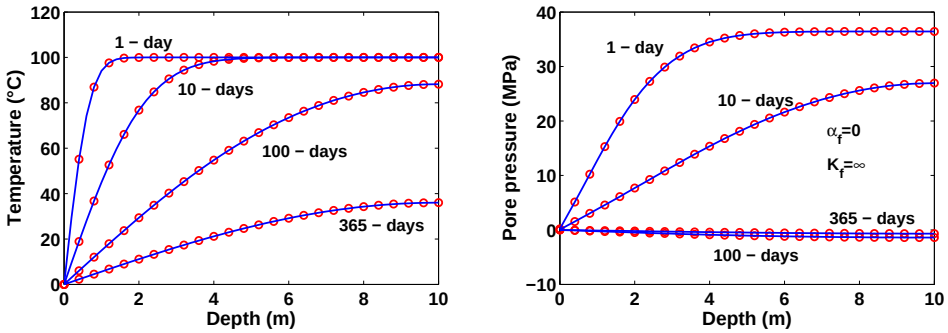

(a) Distribution of temperature

(b) Distribution of pore pressure

Figure 3.3: Temperature and pore pressure distributions within a one–dimensional element subjected to temperature change from 100 to 0 °C and compressive load 10 MPa, with subsequent heat and fluid dissipation through its upper surface only.

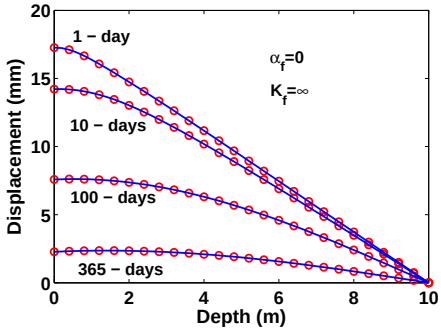

Figure 3.4: Vertical displacement distribution within a one-dimensional element subjected to temperature change from 100 to 0 °C and compressive load 10 MPa, with subsequent heat and fluid dissipation through its upper surface only. Note that $u_{20}^- = 18.54$ mm.

As fluid and heat start to dissipate from the column upper surface, the column starts to cool down. Consequently, pore pressure and vertical displacement built up fields begin to decrease significantly. Figures (3.5), (3.6) and (3.7) show the pore pressure and vertical displacement

time profiles for the cases defined in Table (3.3).

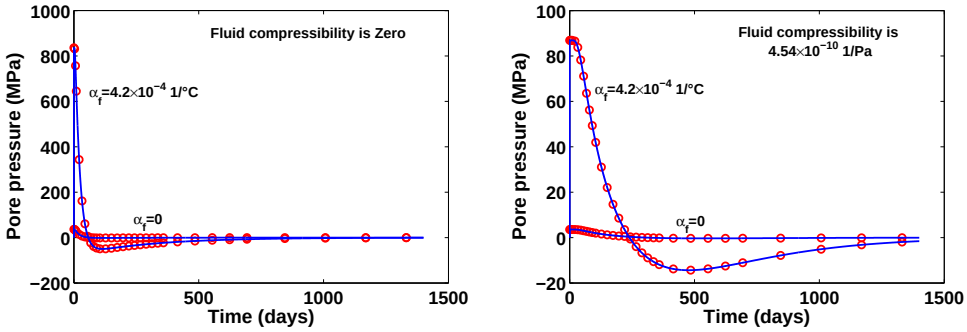

(a) Zero fluid compressibility (b) Fluid compressibility is 4.54×10^{-10} 1/Pa

Figure 3.5: Pore pressure time profiles at ($x_2 = 10$ m) without and with considering the compressibility of pore fluid.

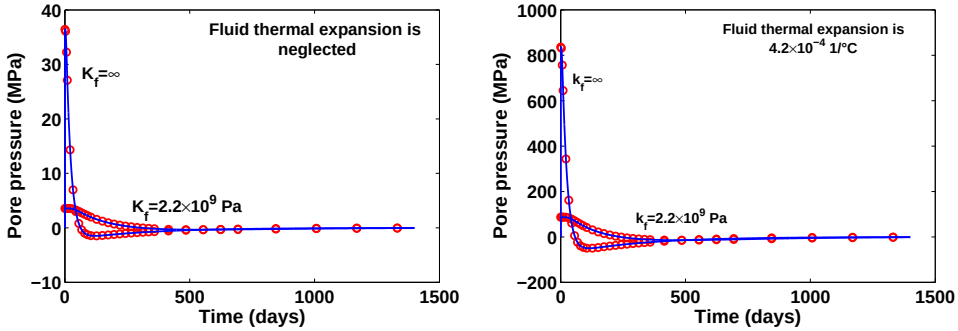

(a) Zero thermal expansion (b) Fluid thermal expansion is 4.2×10^{-4} 1/°C

Figure 3.6: Pore pressure time profiles at ($x_2 = 10$ m) without and with considering the thermal expansion of pore fluid.

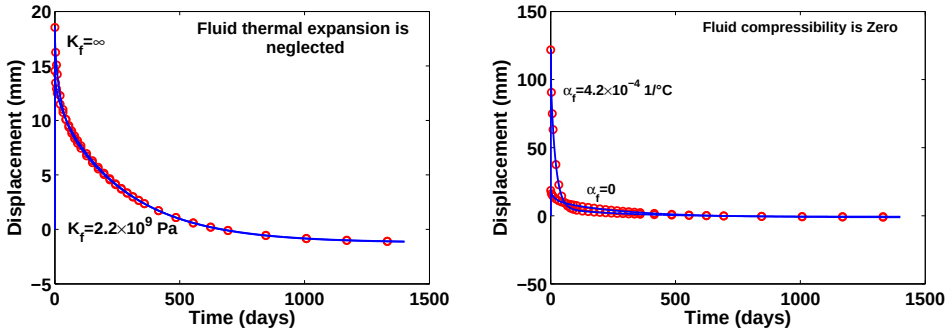

(a) Zero thermal expansion (b) Zero fluid compressibility

Figure 3.7: Vertical displacement time profiles at ($x_2 = 0$ m).

From the graphs previously shown, the following points are concluded:

- Thermo–poroelastic simulations are very sensitive to hydraulic and thermal parameters considered for both phases, solid and fluid.
- The pore pressure p_0^- and the vertical displacement u_{20}^- generated during the heating phase (a) can be qualitatively explained by the following physical arguments:
  1. the higher the thermal expansion coefficient of the fluid phase, the higher the fluid volume would likely to increase;
  2. since the pore fluid is not free to move out of the solid skeleton, this will increase pore pressure and vertical displacement fields tremendously;
  3. the increase in pore pressure and vertical displacement fields, is still somehow, reduced by the mechanical compressibility of the fluid. These effects provide some explanation to the values of pore pressure and vertical displacement shown in Table (3.3).
- Pore pressure gets expectedly smaller for larger values of fluid compressibility.
- Compressible fluids are less likely to be affected by thermal loadings than incompressible fluids.
- For this problem, the higher the values of linear thermal expansion coefficients of the fluid phase, the higher will be the values of pore fluid pressure[1].

3.3.2 Comparing the effect of heat transfer to the abrupt change caused by the sudden application of the surcharge σ_0

This part is aimed at comparing the effect of 100 °C temperature change through the sample to the effect of the 10 MPa applied surcharge. The sample is left to totally consolidate on a temperature field of θ =100 °C and then, when consolidation is done, the boundary temperature at $x_2 = 0$ is set to zero. Figure (3.8) shows the history of loading for this study.
Four cases were considered, numerical responses shown below are obtained by ABAQUS:

- Fluid with zero compressibility and neglected thermal expansion, figure (3.9(a)).
- Fluid with compressibility 4.54×10^{-10} 1/Pa and neglected thermal expansion, figure (3.9(b)).
- Fluid with zero compressibility and linear thermal expansion 4.2×10^{-4} 1/°C, figure (3.10(a)).

[1]This cannot be generalized as the BVP simulated here is highly constrained, see the foregoing notes.

- Fluid with compressibility 4.54×10^{-10} 1/Pa and linear thermal expansion 4.2×10^{-4} 1/°C, figure (3.10(b)).

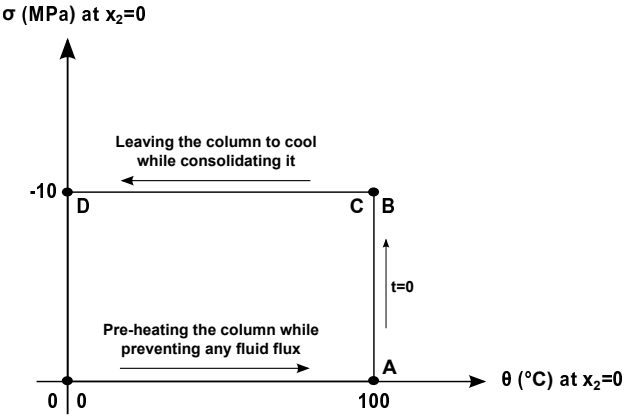

Figure 3.8: History of loading for this study can be summarized as follows: A- The sample has been heated from zero to 100 °C without allowing any fluid seepage which has led the pore pressure to build up an initial value p_0^-. B- At time $t = 0^+$, a load of 10 MPa is applied at the top of the column allowing it to consolidate while preventing any heat dissipation through the surface $x_2 = 0$ m. C- After consolidation is totally done, zero temperature is imposed at the surface $x_2 = 0$ allowing heat transfer to take place and sample to consolidate again until temperature change over all the column vanishes "D".

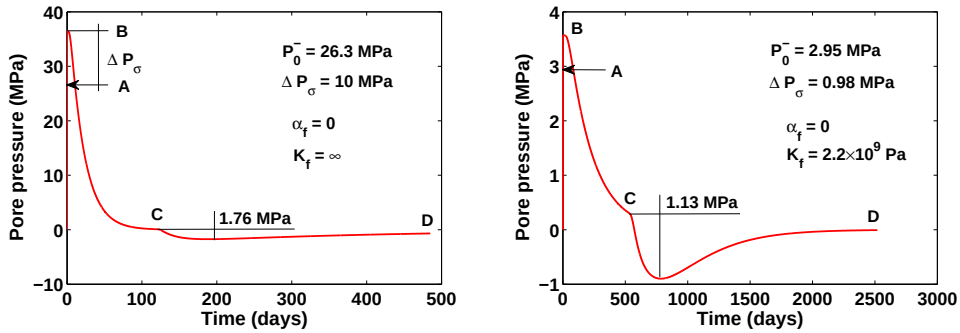

(a) Zero fluid compressibility (b) Fluid compressibility is 4.54×10^{-10} 1/Pa

Figure 3.9: Pore pressure time profiles at ($x_2 = 10$ m), fluid thermal expansion is neglected.

The negative values of pore pressure in figure (3.9) indicate fluid suction. This can be explained as follows; since cooling starts after the built up pressure p_0^- vanishes, the fluid dissipation at the upper surface which is driven by the applied surcharge σ_0 and the contraction resulting from cooling, requires fluid to be sucked from the column so that the column remains saturated while consolidating again by cooling, see figure (3.11). The effect of suction is more evident in the cases when the fluid thermal expansion is considered. The ratio α_f/α_s is equal to 16.9 which means that fluid is contracting 17 times larger than the solid skeleton while cooling. This also causes pore fluid to be sucked to fill the formed gaps in order to guarantee a fully saturated medium.

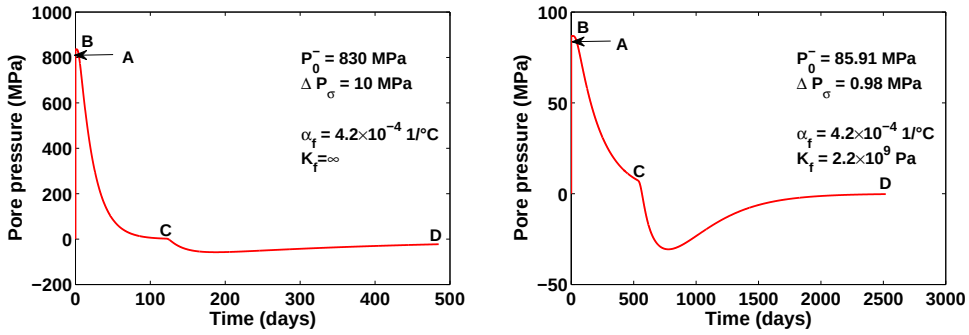

(a) Zero fluid compressibility (b) Fluid compressibility is 4.54×10^{-10} 1/Pa

Figure 3.10: Pore pressure time profiles at ($x_2 = 10$ m), fluid thermal expansion is 4.2×10^{-4} 1/°C.

The fourth case, when considering both fluid compressibility and thermal expansion, tends to be the most realistic and it imitates the field state. To further go into the details of this case; this work gives the graphs of the effective axial stress σ'_{22} and axial strain ε_{22} at the bottom of the column $x_2 = 10$ m.

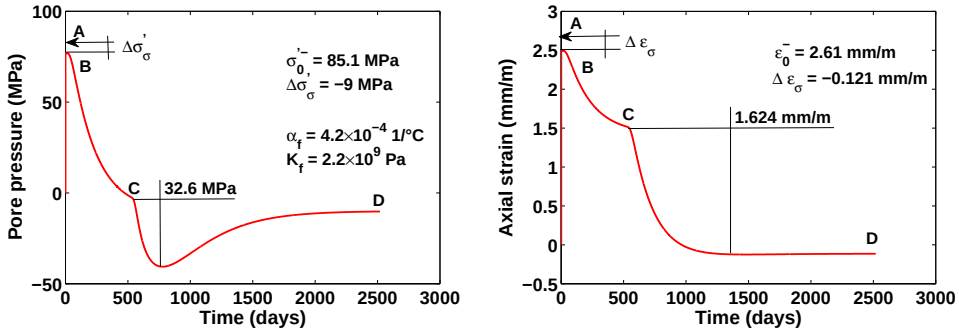

(a) Effective axial stress profile (b) Axial strain profile

Figure 3.11: Axial stress and strain time profiles at ($x_2 = 10$ m), fluid thermal expansion and compressibility are 4.2×10^{-4} 1/°C and 4.54×10^{-10} 1/Pa respectively.

σ'^{-}_0 and ε_0^- are the initial axial effective stress and strain at x_2=10 m which have been built up as result of heating the column from zero to 100 °C. $\Delta\sigma'_\sigma$ and $\Delta\varepsilon_\sigma$ are the abrupt changes of axial effective stress and strain when the surcharge of 10 MPa is suddenly applied.

The effect of 100 °C temperature change through the sample to the effect of the 10 MPa suddenly applied surcharge σ_0, can be conceived by dividing the maximum change caused by heat transfer to the maximum abrupt change caused the consolidating surcharge. For example following figure (3.9(a)), $\Delta p_\theta / \Delta p_\sigma = 1.76/10 = 0.176$. Table (3.4) summarizes the results of the comparison for all the possible combinations of α_f and K_f:

Table 3.4: Comparison between the effect of heat transfer to the effect of consolidation.

Case definition		$\Delta p_\theta/\Delta p_\sigma$	$\Delta\sigma'_{22\theta}/\Delta\sigma'_{22\sigma}$	$\Delta\varepsilon_{22\theta}/\Delta\varepsilon_{22\sigma}$
α_f=0,	K_f=∞	0.176	0.176	13.4
α_f=0,	K_f=2.2 $\times$ 10^9 1/Pa	1.15	0.115	13.4
α_f=4.2 $\times$ 10^{-4} 1/°C,	K_f=2.2 $\times$ 10^9 1/Pa	36.2	3.62	13.4
α_f=4.2 $\times$ 10^{-4} 1/°C,	K_f=∞	5.76	5.76	13.4

Following Table (3.4), one concludes:

1. The effect of heat transfer to that of the sudden surcharge on the pore pressure p "$\Delta p_\theta/\Delta p_\sigma$" is significantly affected by the thermal expansion of pore fluid. It also increases tremendously when assuming compressible fluid.

2. The previous result holds correct for the axial stress σ'_{22}, and is equal to that of the pore pressure "$\Delta p_\theta/\Delta p_\sigma = \Delta\sigma'_{22\theta}/\Delta\sigma'_{22\sigma}$", unless the fluid is assumed compressible.

3. Changing α_f and K_f does not affect the ratio $\Delta\varepsilon_{22\theta}/\Delta\varepsilon_{22\sigma}$. This is a unique result for this problem as it is highly constrained $\varepsilon_{kk} = \varepsilon_{22}$. The axial strain of the homogeneous field does not depend on α_f nor K_f, see equation (3.75).

3.3.3 Verifying the homogeneous parts of the numerical solution with the analytical solution

In this section the numerical results of pore pressure field due to pre–heating, as well as the axial strain field at the end of consolidation and heat transfer are verified by the analytical solutions of thermo–poroelasticity, section (2.2.1).

3.3.3.1 Verifying pore pressure increase due to the thermal loading only

The sample has been initially at 0 °C, then it is homogeneously heated to 100 °C while fluid is trapped. After sufficient time, a homogeneous state of thermal loading is finally achieved. Lateral strains (in directions 1 and 3) are restricted to zero, total axial stress (in direction 2) is also zero since the surcharge at the top is not yet applied.

Starting with equation (2.4), one can write:

$$\varepsilon_{22} = \frac{2\sigma_{11}}{3K} + \frac{\kappa p}{K} + \alpha_s\theta \tag{3.67}$$

Using equation (2.3):

$$\varepsilon_{11} = \frac{1}{2G}\left(\sigma_{11} - \frac{2\nu\sigma_{11}}{1+\nu}\right) + \frac{\kappa}{3K}p + \frac{\alpha_s}{3}\theta = 0 \tag{3.68}$$

$\varepsilon_{11} = 0$, thus equation (3.68) becomes:

$$\sigma_{11} = \frac{E}{\nu - 1}\left(\frac{\kappa}{3K}p + \frac{\alpha_s}{3}\theta\right) \tag{3.69}$$

Substituting equation (3.69) in equation (3.67) while noting that $3K = E/(1-2\nu)$ yields:

$$\varepsilon_{22} = \varepsilon_{kk} = \frac{1+\nu}{3(1-\nu)}\left(\frac{p\kappa}{K} + \alpha_s\theta\right) \tag{3.70}$$

Using equation (2.10), the pore pressure p is written in the form:

$$p\left(\frac{1}{M} + \frac{\kappa^2(1+\nu)}{3K(1-\nu)}\right) = \theta\left(\frac{-\kappa(1+\nu)\alpha_s}{3(1-\nu)} + \alpha_s(\kappa - \phi_0) + \alpha_f\phi_0\right) \tag{3.71}$$

Considering the values mentioned in Table (3.2) for the case $\alpha_f = 0$ and $K_f = \infty$, the pore pressure is easily calculated $p = 26.34$ MPa. This value is identical to the value obtained numerically by ABAQUS[1].

3.3.3.2 Verifying the homogeneous field of the axial strain at the end of consolidation and heat transfer

When the homogeneous field of the axial strain is reached, the axial stress (in direction 2) is equal to -10 MPa and the change in the pore pressure p vanishes.
Following equation (2.3), one writes:

$$\varepsilon_{22} = \frac{1}{2G}\left(\sigma_{22} - \frac{\nu\sigma_{kk}}{1+\nu}\right) + \frac{\alpha_s}{3}\theta \tag{3.72}$$

Considering equation (2.4) gives:

$$\varepsilon_{22} = \frac{\sigma_{kk}}{3K} + \alpha_s\theta, \tag{3.73}$$

and:

$$\sigma_{kk} = 3K(\varepsilon_{22} - \alpha_s\theta) \tag{3.74}$$

Substituting equation (3.74) in equation (3.72) while noting that $3K = E/(1-2\nu)$ yields:

$$\varepsilon_{22}\left(1 + \frac{\nu}{1-2\nu}\right) = \frac{\sigma_{22}(1+\nu)}{E} + \alpha_s\theta\left(\frac{\nu}{1-2\nu} + \frac{1}{3}\right) \tag{3.75}$$

Considering the values mentioned in Table (3.2) and that $\theta = 0$ °C, the axial strain is calculated $\varepsilon_{22} = -0.124$ mm/m, which is identical to the value obtained numerically by ABAQUS[2].

[1] See for instance figure (3.9(a)) and Table (3.3).
[2] See for instance figure (3.11(b)).

3.4 Validation of the Fortran 90 finite element code

Though the numerical solution that was given by ABAQUS was quite satisfying, ABAQUS is not going to be used later in doing the simulations of this study. Actually, the version of ABAQUS used in doing the simulations of section (3.3) can not implement a fully coupled thermo–hydro–mechanical BVP. As was stated, the heat transfer part was simulated alone by solving a mere heat transfer problem and the results were uploaded to the poro–elastic part.

To avoid any mistakes resulting from dividing the thermo–poroelastic simulations, and to have our own domestic code where a specific and advanced developed model of damage and permeability enhancement can be integrated, a developed Fortran 90 FE code which was modified by (Gelet, [2012]) and in turn modified by me is to be used to obtain the sought numerical responses.

The aim of this section is to validate the initial version of the FE code by comparing the analytical results with the numerical simulations shown by the FE code. Two transient conduction problems are to be studied, namely:

1. The aforementioned one–dimensional problem presented by (Selvadurai and Suvorov, [2009]). Since the authors neglect the mechanical and hydraulic contributions to the energy equation, we will also disregard them to provide a valid comparison. However, it should be outpointed here that the FE code may/may not stand, depending on the user's desire, for full coupling in the energy equation and that convection of heat is also partially treated.

2. A two–dimensional wellbore stability problem which is presented in the study of (He and Jin, [2010]). The authors neglect the mechanical and hydraulic contributions to the energy equation as well as part of the mechanical contribution, namely the term $(\partial^2 u_i/\partial t \partial x)$, to the equation of balance of mass to get the analytical solution of the BVP. In our FE code we can stand for full decoupling of hydraulic and mechanical effects in the energy equation, nonetheless full coupling is always ensured in the equation of balance of mass. Consequently, the FE code thermal response is expected to match that of the analytical solution of (He and Jin, [2010]), meanwhile some differences are expected in pore pressure response between the FE code results and the analytical solution.

3.4.1 One–dimensional application

The analytical solution offered by (Selvadurai and Suvorov, [2009]) stands only for incompressible grains $\kappa = 1$. The Fortran 90 FE code cannot simulate thermo–poroelastic problems with

incompressible grains, incompressible fluid, or neglected thermal expansions; that will result in a division by zero. Thus, the quite accurate results of ABAQUS will be used as a reference instead of the analytical solution. The thermal and hydraulic properties shown in Table (3.5) were used to simulate the problem.

Table 3.5: Properties of the sample material "Typically rock".

Property	Value
Porosity n	0.25
Young's modulus E	38×10^9 (Pa)
Poisson's ratio ν	0.3
Unit weight of water γ_f	9800 (N/m^3)
Medium hydraulic conductivity k	2.94×10^{-12} (m/s)
Effective thermal conductivity χ	4 (W/m°C)
Effective heat capacity ρc_v	2465000 (J/m^3 °C)
Volumetric thermal expansion of solid phase α_s	2.49×10^{-5} (1/°C)
Volumetric thermal expansion of liquid α_f	4.2×10^{-4} (1/°C)
Fluid bulk modulus K_f	2.2×10^9 (Pa)
Solid bulk modulus K_s	37.0×10^9 (Pa)

The same boundary and initial conditions, as in section (3.3), are adopted here. The only addition is that solid grains are assumed compressible with solid constituent bulk modulus of $K_s = 37.0 \times 10^9$ Pa. The reference solution is obtained for 700 days by simulating the transient BVP using ABAQUS following the same scheme as in Table (3.1).

To simulate this problem using our FE code, the following approach is used:

- A one–dimensional mesh of 30 elements refined at the top of the column with ratio 10 between the largest and the smallest elements is considered.
- The time scheme used in the FE code is designed to calculate and to plot time–logarithmic results. First time step starts at second 1, just after verifying the geostatic step, and continues to increase logarithmically until it reaches a maximum value (is set here to be 1,000,000 s). After the maximum value is reached, the next time step is calculated as the previous time plus the maximum value, see figure (3.12).
- Hydraulic and mechanical contributions to the equation of energy are disregarded as our version of ABAQUS can not simulate fully coupled thermo–poroelstic response.

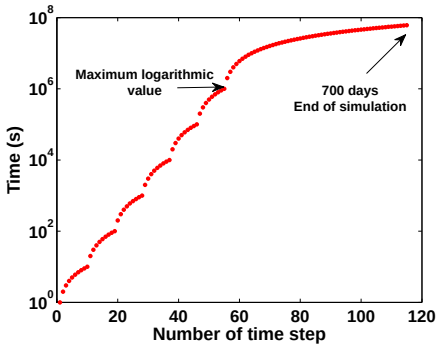

Figure 3.12: Time scheme used in the domestic FE code to solve the thermo–poroelastic IBVPs. First time step starts at second 1 and continues to increase logarithmically till a specific maximum value. After the maximum value is reached, time steps are to increase linearly by a slope equal to the maximum value.

- Unlike the Q8 elements used for discretization by ABAQUS, our FE code uses 4–node bilinear quadrilateral elements to discretize the space of all the unknowns, see section (3.2.2).
- This transient BVP is also simulated in two steps by the FE code:
  1. The sample was sealed at all boundaries to prevent fluid fluxes and then heated from 0 to 100 °C. This has led the pore pressure to build up an initial value p_0^- equal to 94.6 MPa,
  2. the surcharge σ_0 is then applied as the sealing at the top is removed to allow the column to consolidate through a temperature change from 100 to 0 °C

Numerical response of the FE code and ABAQUS results were in good agreement, see figures (3.13) and (3.14):

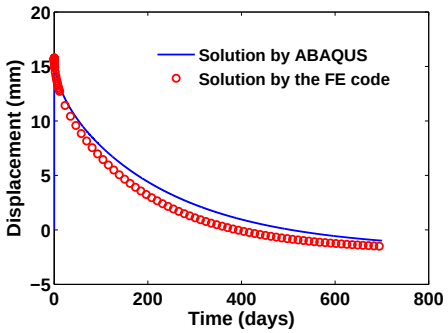

Figure 3.13: Vertical displacement time profile at ($x_2 = 0$ m), comparison between numerical response of the FE code and ABAQUS simulation.

The small differences between the FE code response and ABAQUS results in the vertical displacement and temperature profiles are most likely attributed to the facts that; much smoother

refinement is adopted in doing the ABAQUS simulation (100 elements), and the Q8 elements may describe the thermo–hydromechanical behavior better than the Q4 elements used in our FE code.

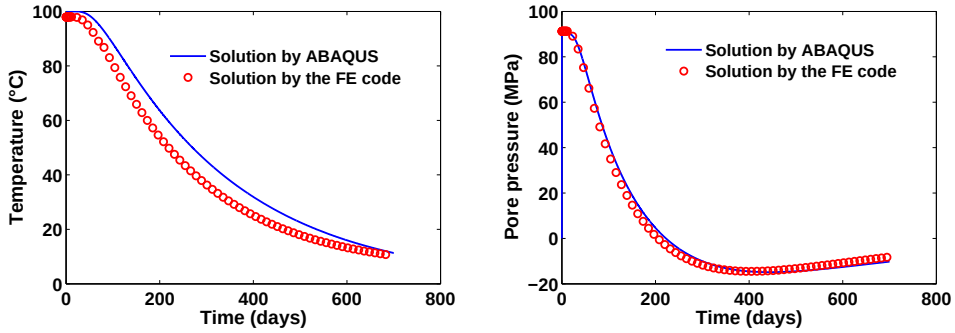

(a) Temperature profile

(b) Pore pressure profile

Figure 3.14: Temperature and pore pressure time profiles at (x_2 = 10 m), comparison between numerical response of the FE code and ABAQUS simulation.

3.4.2 Two–dimensional application

To further verify the simulation capacities of the domestic FE code, this section uses the code to simulate a 2–dimensional wellbore stability BVP. Wellbore stability problems are often encountered when drilling in high permeability formations where the analyses of thermal stresses are of importance see for instance (Abousleiman and Ekbote, [2005]), (Abousleiman and Nguyen, [2009]) and (He and Jin, [2010]). Wellbore stability will be addressed in details in section (4.6).

3.4.2.1 Model description

The model used in this study is the same as the model implemented in (He and Jin, [2010]). This model describes a torsionless axisymmetric transient BVP of a wellbore drilled in an infinite porous rock formation, see figure (3.15).

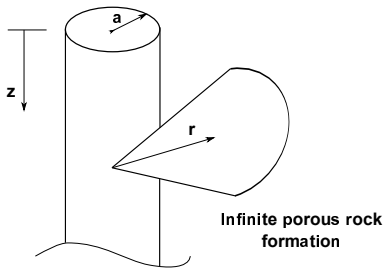

Figure 3.15: Cylindrical hole in an infinite fluid saturated porous rock formation.

Only a quarter of the model has been discretized taking advantage of the rotational symmetry. 4-node isoparametric quadrilateral elements (Q4) have been used to solve for displacement, pressure and temperature. Spatial discretization (FEM mesh) of 756 elements is shown in figure (3.16).

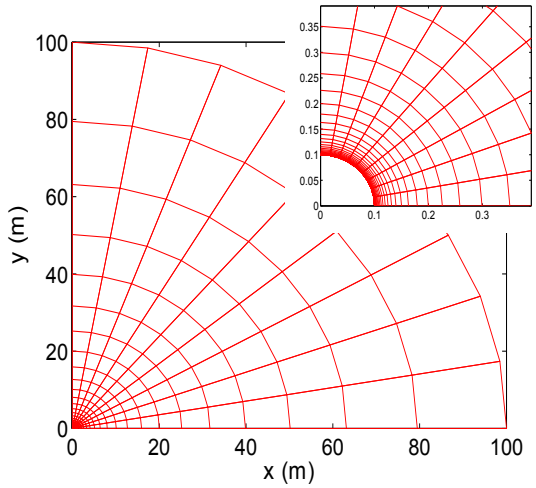

Figure 3.16: Spatial discretization of the model geometry.

3.4.2.2 The analytical solutions of the BVP

Short time single–porosity solutions for pressure and temperature are obtained using Laplace's transformation and its asymptotic properties (He and Jin, [2010]). To get these analytical solutions, authors have neglected the hydraulic and mechanical contributions to the energy equation as well as the a part of the mechanical contribution, namely the term $(\partial^2 u_i/\partial t \partial x)$, to the equation of balance of mass. All the boundary conditions are applied on the model such that only torsionless axisymmetric BVP is achieved.

- ***Temperature field***

Only conduction of heat is considered, the following initial and boundary conditions are applied:

$$\begin{array}{lll} \theta(r,t)|_{t=0} & = 0, & a \leq r < \infty \\ \theta(r,t)|_{r=a} & = \theta_a\, H(t), & t > 0 \\ \theta(r,t)|_{r\to\infty} & = 0, & t > 0 \end{array} \tag{3.76}$$

θ_a is a constant "the temperature of the solid applied at the boundary $r = a$" and $H(t)$ is the Heaviside step function. The analytical solution is given by (He and Jin, [2010]):

$$\theta(r,t) = \theta_a \sqrt{\frac{a}{r}}\, \mathrm{erfc}\left(\frac{r-a}{2\sqrt{\psi t}}\right), \tag{3.77}$$

where ψ is the thermal diffusivity given by $\psi = \chi/\rho\, c_v$, χ being the thermal conductivity, ρ is the density and c_v is the heat capacity of the saturated porous medium at constant volume.

- ***Pore pressure field***

The term $\partial^2 u_i/\partial t \partial x$ is disregarded from the equation of balance of mass. The following boundary and initial conditions are applied:

$$\begin{array}{lll} p(r,t)|_{t=0} & = 0, & a \leq r < \infty \\ p(r,t)|_{r=a} & = p_a\, H(t), & t > 0 \\ p(r,t)|_{r\to\infty} & = 0, & t > 0 \end{array} \tag{3.78}$$

p_a is the fluid pore pressure applied at the boundary $r = a$. By substituting for the temperature field using equation (3.77) in the equation of balance of mass, the analytical solution is given by (He and Jin, [2010]):

$$p(r,t) = \left\{ p_a + \frac{c'\theta_a\psi}{(c-\psi)} \right\} \sqrt{\frac{a}{r}}\, \mathrm{erfc}\left(\frac{r-a}{2\sqrt{ct}}\right) - \frac{c'\theta_a\psi}{(c-\psi)} \sqrt{\frac{a}{r}}\, \mathrm{erfc}\left(\frac{r-a}{2\sqrt{\psi t}}\right), \tag{3.79}$$

where c is the hydraulic diffusivity coefficient of the porous medium equation (2.23), and c' is given by:

$$c' = \frac{1}{S}\left[\frac{2(1-2\nu)}{3(1-\nu)}\,\kappa\alpha_s^{'} + \phi_0(\alpha_f - \alpha_s^{''})\right], \tag{3.80}$$

$$S = \frac{\kappa}{BK}\left(1 - \frac{4\eta B}{3}\right) \quad \text{and} \quad \eta = \frac{1-2\nu}{2(1-\nu)}\,\kappa, \tag{3.81}$$

where κ is the Biot's coefficient, $\alpha_s^{'}$ and $\alpha_s^{''}$ are the first and the second solid volumetric thermal expansion coefficients respectively. ϕ_0 is the reference porosity, B is the Skempton's coefficient equation (2.7) and K is the drained bulk modulus.

Table (3.6) lists the thermal properties of the solid and the fluid phases and Table (3.7) lists the poroelastic parameters of the fluid saturated porous medium..

Table 3.6: Thermal parameters for the fluid and the solid phases.

Property	Solid	Fluid
Effective thermal conductivity (W/m°C)	χ_s=2.4	χ_f=0.6
Density (kg/m^3)	ρ_s=2600	$\rho_f = 1000$
Specific heat at constant volume (J/Kg°C)	c_{vs}=920	$c_{vf} = 4200$
Volumetric thermal expansion coefficients (1/°C)	$\alpha_s^{''} = \alpha_s^{'}$=$3.3 \times 10^{-5}$	α_f=3.0×10^{-4}

Table 3.7: Poroelastic parameters for the fluid saturated porous medium.

Property	value
Shear modulus (GPa)	G=6.8
Poisson's ratio (drained)	ν=0.18
Bulk modulus (drained) (GPa)	K=8.4
Biot-Willis coefficient	κ=0.74
Skempton's coefficient	B=0.5
Reference porosity	ϕ_0=0.4
Hydraulic diffusivity (m^2/s)	$c = 1.4 \times 10^{-3}$

3.4.2.3 Calculations and results

Considering the fact that the analytical solutions were obtained by the asymptotic short time inverse of the equations written in the Laplace's s domain, all the numerical simulations were performed in a non–dimensional time interval $\tilde{t} \leq 0.3$: for the values defined in Table (3.6), this limits the simulation time to $t \leq 0.3\, a^2/\psi$.

If quantities of θ_a, p_a and a are given the values 100 °C, 25 MPa and 10 cm respectively, the numerical simulations using the FE code can be performed. In the graphs shown below, the solid lines represent the short time single–porosity analytical solution, equations (3.77) and (3.79).

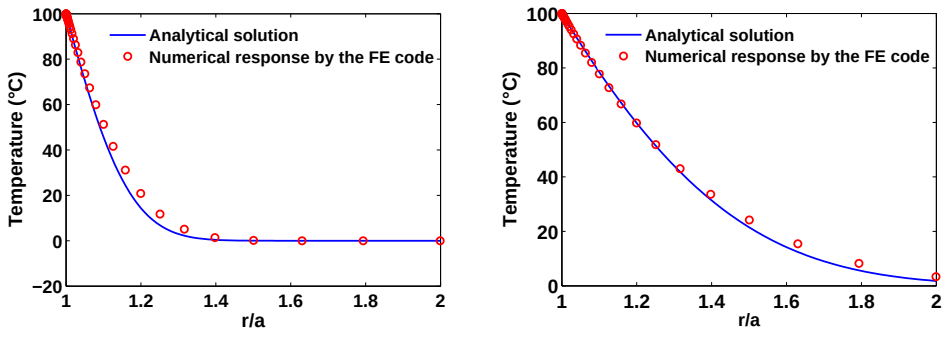

(a) Radial distribution $\tilde{t}$=0.01 (b) Radial distribution $\tilde{t}$=0.1

Figure 3.17: Temperature distribution along the radial direction.

The following notes are concluded:

1. The radial distributions of temperature, numerical and analytical, are in good agreement.
2. The difference between the analytical solution and the numerical response in figure (3.18) comes from the fact that, the term $\partial^2 u_i/\partial t \partial x$ has been disregarded from the equation

of balance of mass so that the analytical solution might be reached. The FE code is only valid for coupled pore pressure which is more realistic and maintain the constitutive hydro–mechanical coupling.

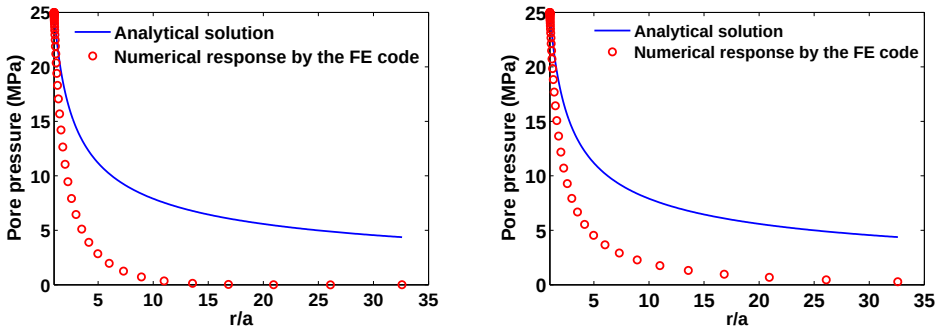

(a) Radial distribution $\tilde{t}$=0.01 (b) Radial distribution $\tilde{t}$=0.25

Figure 3.18: Pore pressure distribution along the radial direction.

3. Unlike the radial distribution of temperature, the radial distribution of pore pressure for the short–time solution does not change too much in the interval $\tilde{t} \leq 0.3$. It seems that the pore fluid diffusion happens much faster than the thermal diffusion. By checking the time scales of the diffusive heat transfer $t_\theta = L^2/\psi$ and the diffusive flow of pore fluid in the porous medium $t_p = L^2/C_c$, it is found that:

$$\frac{t_\theta}{t_p} \approx 2600 \tag{3.82}$$

It means that the diffusion of pore fluid is about 2600 times faster than the diffusion of heat in the medium. This is an expected result when simulating thermal recovery from Hot Dry Rock (HDR) reservoirs. The diffusion of pore fluid happens much faster than the conductive diffusion of heat. However, if the convection of heat is considered in the simulations, the diffusion of heat is to be enhanced several orders of magnitudes. Nonetheless in all cases, whether by convection or conduction, the diffusion of pore fluid remains faster than the diffusion of heat in most of the HDR reservoir implementations.

Chapter 4

Simulations of heat extraction from natural and enhanced HDR reservoirs by hydraulic fracturing

Geothermal reservoirs/ Hot–Dry–Rocks (HDR) are, nowadays, correctly simulated by assuming dual–porosity Local Thermal Non-Equilibrium (LTNE), where heat transport as well as hydraulic diffusion in each phase along with heat and fluid exchanges between phases are precisely described. The works of (Gelet et al., [2012]) have clarified that the assumption of dual–porosity LTNE is inevitable to get precise description of a geothermal reservoir. The convection of heat is dominant in the fissure fluid phase, meanwhile the conduction of heat is controlling in the pore fluid phase.

Dual–porosity LTNE is not covered in this thesis as we hope that we would provide an initial insight into the process of Hydraulic Fracturing in single–porosity Local Thermal Equilibrium (LTE). This insight can be used later as a basis for more sophisticated studies.

This chapter proceeds as follows; the simulations of heat and fluid transports at the geothermal reservoir of Soultz–Sous–Forêts without considering permeability stimulation by Hydraulic Fracturing (HF) are first presented. The process of HF is then discussed and a fracturing model which is based on mode I of fracturing and capable of tracking directional fracture evolution is developed. By implementing the fracturing model into our FE code, the hydraulic enhancement/stimulation of the geothermal reservoir of Soultz–Sous–Forêts is presented. Finally, the problem of borehole stability associated with tensile and shear failure of the borehole case-shoe is presented to ensure safe HF process of HDR reservoirs.

4.1 Preliminary results: The natural geothermal reservoir of Soultz–Sous–Forêts

Several HDR projects were initiated around the globe; Fenton Hill (USA) starting in 1973, Rosemanowes (England) in 1977 and Hijiori (Japan) in 1989. Several Enhanced Geothermal Systems (EGS) were later established for instance; projects at Soultz–Sous–Forêts (France), Coso (USA) and Habanero (Australia).

The HDR project at Soultz–Sous–Forêts, figure (4.1), is chosen to perform the preliminary simulations of the Thermo–Hydro–Mechanical research of this thesis. This HDR reservoir was artificially stimulated by hydraulic and/or chemical approaches (Evans et al., [2009]). Cold water is injected from the well (GPK1) and left to travel through the geothermal reservoir before it is retrieved via the production well (GPK2). Hot water is then passed through a heat exchanger where it is exploited and thus cooled. Cold water is re-injected through (GPK1) for the subsequent circulation.

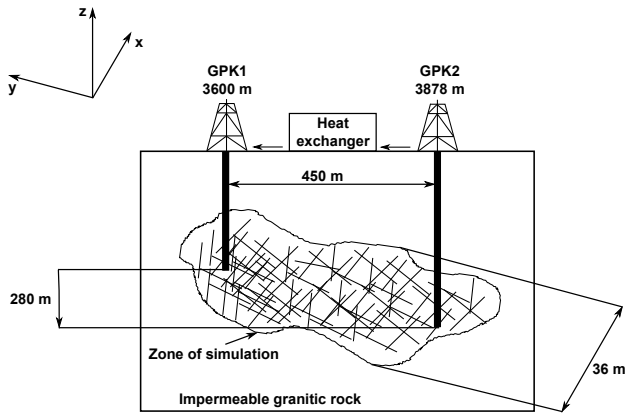

Figure 4.1: Modeling of the geothermal reservoir at Soultz–Sous–Forêts, figure is not to scale.

To imitate the conditions of the natural reservoir, simulations will be first performed assuming low permeability and therefore a brief description on temperature, pressure and stress distributions is obtained. The fracturing model will be then integrated to account for permeability enhancement. Convection of heat is to be treated a priori using the SUPG method, chapter (6).

4.1.1 Material properties

The material properties of Soultz–Sous–Forêts reservoir are shown in Table (4.1). The time scales associated with this particular BVP, for a length $L = 450$ m, were calculated as shown in section (2.3.1):

- for thermal diffusion, $t_\theta = 8482.5$ years,

- for hydraulic diffusion, $t_p = 1.6$ days.

Table 4.1: Material properties of Soultz–Sous–Forêts reservoir, (Evans et al., [2009]). *The permeability value is used as in (Taron and Elsworth, [2009]).

Property	Value
Drained Young's modulus E	54×10^9 † (Pa)
Drained Poisson's ratio ν	0.25
Bulk modulus of solid grains K_s	50×10^9(Pa)
Bulk modulus of fluid K_f	2.2×10^9 (Pa)
Dynamic viscosity of the fluid μ	3×10^{-4} (Pa.s)
Porosity ϕ	0.1003
Permeability* k_0	6.8×10^{-15} (m^2)
Solid thermal conductivity χ_s	2.49 (W/m°C)
Fluid thermal conductivity χ_f	0.6 (W/m°C)
Solid heat capacity at constant volume c_{vs}	1000 (J/kg °C)
Fluid heat capacity at constant volume c_{vf}	4200 (J/kg °C)
Density of solid ρ_s	2910.2 (kg/m^3)
Unit weight of water γ_f	9800 (N/m^3)
Volumetric thermal expansion of the solid α_s	7.5×10^{-6} (1/°C)
Volumetric thermal expansion of the fluid α_f	1×10^{-3} (1/°C)

†: Actually this value is quite large, obviously a very strong rock is encountered during the operations of Soultz–Sous–Forêts reservoir.

4.1.2 Geometry and FEM mesh

The dimensions of the reservoir to be simulated at Soultz–Sous–Forêts are 450 m × 36 m × 750 m in x, y and z (the vertical direction) respectively. This reservoir is composed of several fractured zones that extend over the 750 m height (Evans et al., [2009], p. 75). Only one fractured zone is to be simulated in this simple plane strain approach.

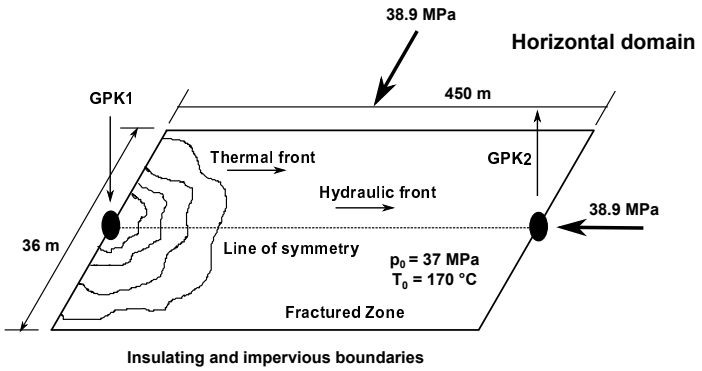

Figure 4.2: Initial conditions and geometric layout of a fractured zone at Soultz–Sous–Forêts.

The values of *in situ* stresses were calculated as shown in (Evans et al., [2009], p. 38–39) for $z = 3.7$ km. *In situ* stresses are identical in x and y directions for this depth, however anisotropic *in situ* stress states will be considered later. The initial pressure p_0 and the initial temperature T_0 also correspond to a typical depth of 3.7 km.

A temperature of $T = 80$ °C is applied at the injection well, the temperature at the outlet production well, 450 m away, is sought. All the other boundaries are thermally insulated, i.e. no thermal fluxes are permitted with the surroundings.
Injection and production pressures are fixed to $p_0 + 1$ MPa and $p_0 - 1$ MPa respectively, other boundaries are hydraulically insulated from the surroundings.
The mechanical boundary conditions are defined by the geostatic stresses applied at the upper and right boundaries. The lower boundary is constrained in y-direction, meanwhile the left boundary is constrained in x-direction (roller displacement), see figure (4.3).

These stresses are applied at $t = 0^-$ and allowed to equilibrate with the initial pore pressure of 37 MPa and the initial temperature of 170 °C. With a Biot's coefficient of $\kappa = 0.28$, the application of -28.54 MPa effective stresses over the geologic time gives an *in situ* permeability of 6.8×10^{-15} m^2. This value of the *in situ* permeability is just an assumption, chosen as in (Taron and Elsworth, [2009]). It is to be enhanced later by HF to reach the *in situ* permeability of the enhanced geothermal reservoir of Soultz–Sous–Forêts ($\sim 10^{-11}$ m^2).

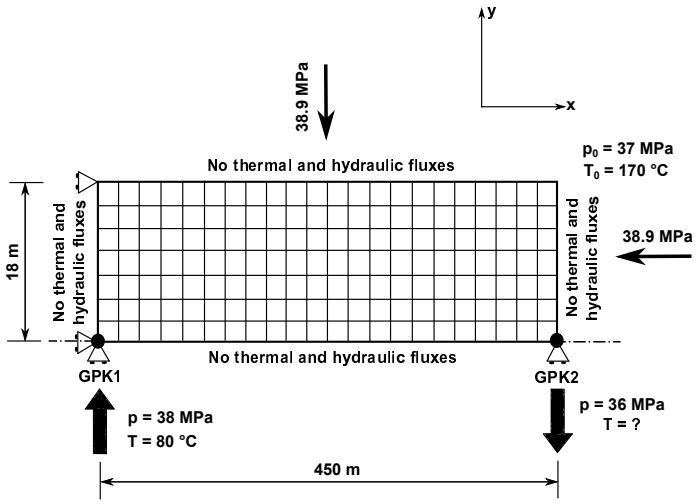

Figure 4.3: Modeling of a circulation test at Soultz–Sous–Forêts. Figure is not to scale.

Only the upper right quarter of the horizontal domain, figure (4.2), is discretized due to symmetry. Several FEM meshes were tested. The BVP is proven to be mesh independent. The

choice of the meshing scheme controls only the smoothness of the output contours. A FEM mesh of 300 elements, 10 elements in y-direction and 30 elements in x-direction, has been chosen so that smooth output contours may be obtained, see figure (4.3).

4.1.3 Simulations and expectations

The transient BVP discussed above is to be simulated using our domestic FE code. A brief discussion on the mesh definition and Péclet number is needed to explain the rule and significance of heat convection.

4.1.3.1 Mesh definition and Péclet number

The mesh is composed of 300 elements of size $h_x \times h_y = 15$ m $\times$ 1.8 m. The simulations are preliminarily preformed to get an impression about the pattern of fluid diffusion that corresponds to our IBVP, figure (4.4). Note that this fluid diffusion pattern will not change all along the simulations owing to extremely fast hydraulic diffusion of 1.6 days, see section (4.1.1).

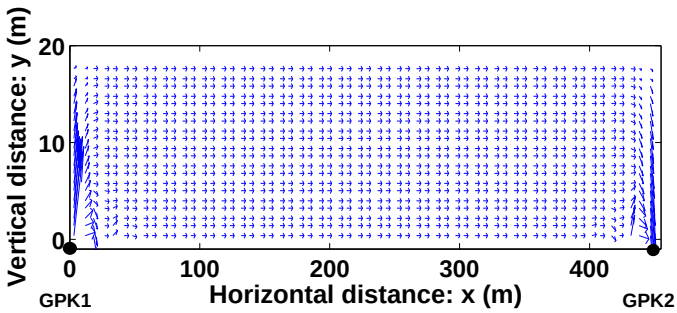

Figure 4.4: Scaled fluid velocity vectors for a steady state of injection pressure $p_0 + 1$ MPa at well GPK1 and extraction pressure $p_0 - 1$ MPa at GPK2. The velocity field is not homogeneous at the neighbors of the wells, however, the average velocity of the formation fluid is about $||\boldsymbol{v}|| = v_x = 9.46 \times 10^{-7}$ m/s since $v_y \approx 0$.

Grid Péclet number ($\mathrm{Pe_g}$) is hence calculated with an average fluid velocity of $||\boldsymbol{v}|| = 9.46 \times 10^{-7}$ m/s and thermal diffusivity $\psi = \chi/\rho c_v = 7.56 \times 10^{-7}$ m^2/s, see table (4.1).

$$\mathrm{Pe_g} = \frac{h_x \, ||\boldsymbol{v}||}{2\psi} = 9.38 \tag{4.1}$$

A Péclet number greater than 1 indicates that fluid is carrying heat faster than it is being diffused and thus the convection of heat is significant. The time required for thermal diffusion with heat convection is to be reduced several orders of magnitude less than the value presented in section (4.1.1):

$$t_{\mathrm{conv}} = \frac{L\,(= 450\,\mathrm{m})}{||\boldsymbol{v}||} = 15 \quad \text{years} \tag{4.2}$$

The profiles of temperature and pressure, along the symmetry line $y = 0$ m, at different times are shown in figure (4.5).

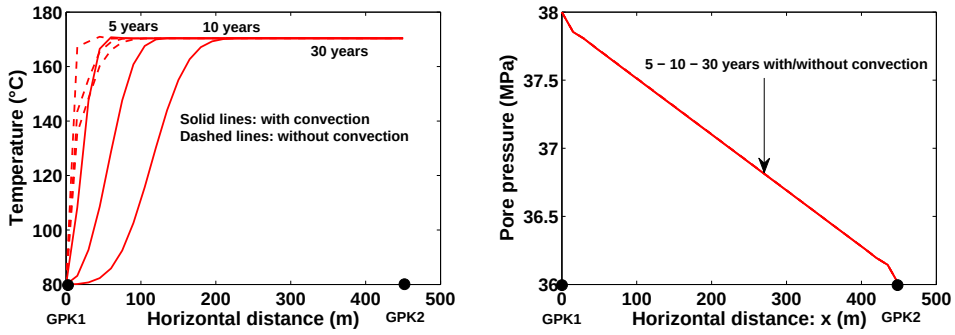

(a) Temperature profiles (b) Pore pressure profiles

Figure 4.5: Temperature and pore pressure profiles at $y = 0$ m. Hydraulic diffusion is very fast, meanwhile, heat front propagates faster, as expected, when convection of heat is accounted for.

Although the value of the permeability chosen is quite small, convection of heat is significant and plays an important role in facilitating the propagation of the heat wave, see figure (4.5(a)) and equation (4.2). The profiles of pore pressures are almost linear and do not show any palpable changes. This is due to the fact that the hydraulic diffusion time is about 1.6 days, and these changes can not be seen in these quite long–time simulations.

4.1.3.2 Contours of mixture temperature and effective stresses

The contours of mixture temperature at different times are shown in figure (4.6).

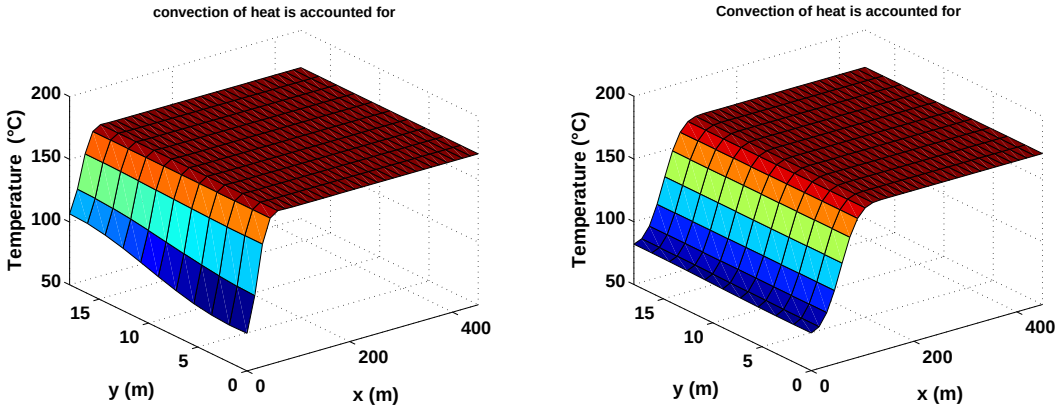

(a) Temperature contour at year 5 (b) Temperature contour at year 15

Figure 4.6: Contours of the mixture temperature at two times when convection of heat is considered in the simulations.

The reservoir is cooled quickly in y-direction, this is a due to the fact that fluid spreads all over the volume in this direction, see figure (4.4). This feature creates large hydraulic gradients in the neighbors of the injection well and can contribute to maintain the cracks open in spite of the shrinkage caused by rock cooling.

The contours of effective stresses in x, y and z-directions and for the simulations when the convection of heat is accounted for/not considered, are presented in figures (4.7), (4.8), (4.9), (4.10), (4.11) and (4.12).

First: for the longitudinal effective stress $\sigma_x^{'}$

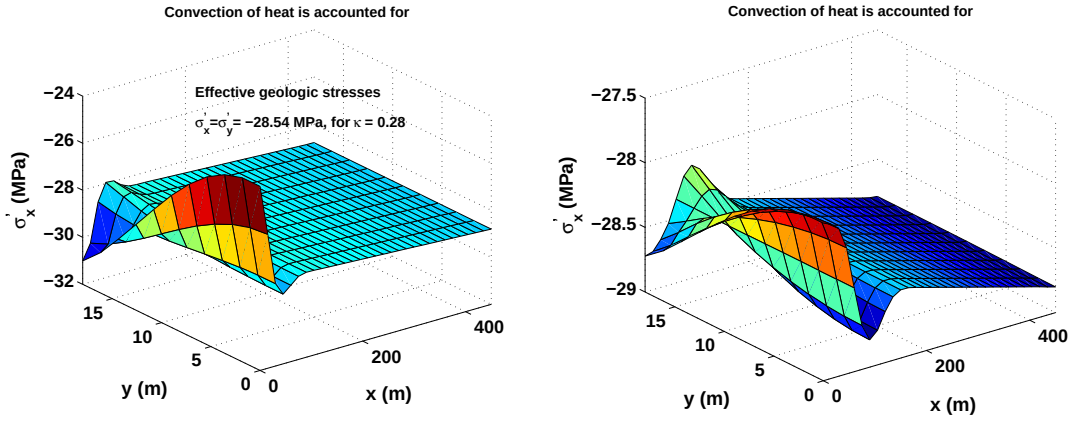

(a) Contour of $\sigma_x^{'}$ at year 5

(b) Contour of $\sigma_x^{'}$ at year 15

Figure 4.7: Contours of longitudinal effective stress $\sigma_x^{'}$ at two times when convection of heat is considered in the simulations.

1. At the injection well GPK1, i.e. $x = 0$ m and $y = 0$ m, the cold water injected causes rocks to contract and thus compressive stresses are mitigated.

2. Considering that the ratio $\alpha_f/\alpha_s \approx 133$, fluid will contract during cooling much more than the solid. This differential contraction between the two phases will cause pore pressure to be sucked to fill the gaps formed and to reach the assumption of full saturation. However, this reduction in the pore pressure is only a few kPa and it is not noticeable on the pressure curves, figure (4.5(b)) for instance. Obviously the permeability of the medium is sufficiently large and the moving fluid needs not to be strongly sucked to fill the gaps.

3. Being the shorter path 18 m/450 m, fluid starts to spread over the available volume in y-direction. Thus the created high fluid gradients, near the line of symmetry $x = 0$ m,

cause stresses to decrease leading micro–cracks to open if rock toughness is reached, See figure (4.7(a)).

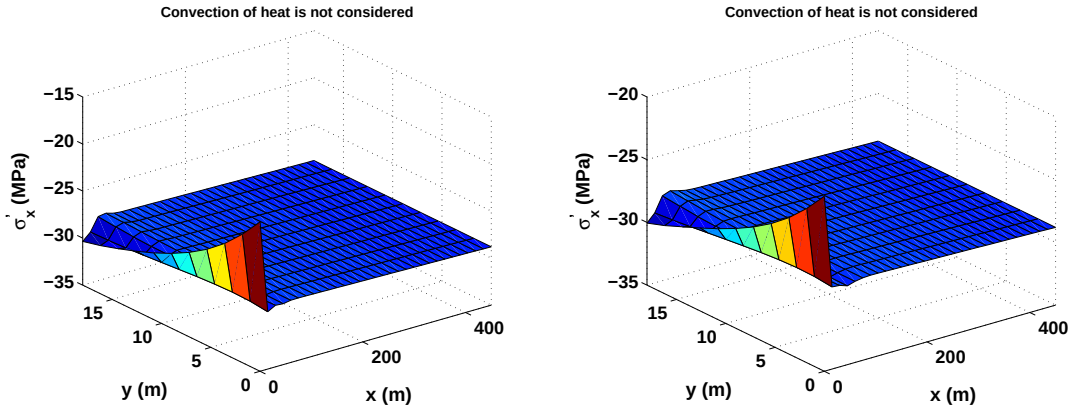

(a) Contour of $\sigma_x^{'}$ at year 5

(b) Contour of $\sigma_x^{'}$ at year 15

Figure 4.8: Contours of longitudinal effective stress $\sigma_x^{'}$ at two times when convection of heat is NOT considered in the simulations.

4. At the neighbors of the injection well and as the heat front moves away, the rock relaxes and the generated fluid fluxes dissipate taking stresses back to the equilibrium state, compare figures (4.7(a)) and (4.7(b)), figures (4.9(a)) and (4.9(b)).

Second: for the transversal effective stress $\sigma_y^{'}$

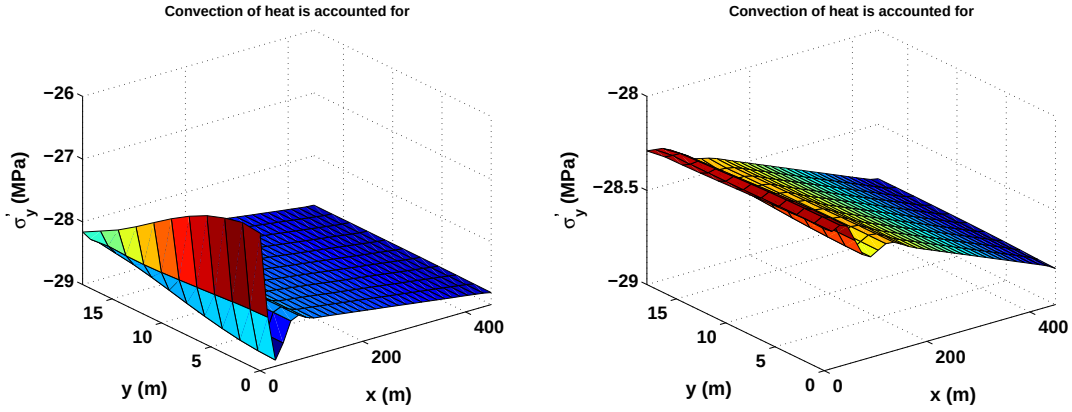

(a) Contour of $\sigma_y^{'}$ at year 5

(b) Contour of $\sigma_y^{'}$ at year 15

Figure 4.9: Contours of transversal effective stress $\sigma_y^{'}$ at two times when convection of heat is considered in the simulations.

5. Far from the injection well, the fluid fluxes are not that significant and the rock cools down for a gradient of 0.6 °C/m, see figure (4.6(b)). This behavior does not change the effective stresses from the state of equilibrium, $\sigma_y^{'} = \sigma_x^{'} = -28.76$ MPa, so much.

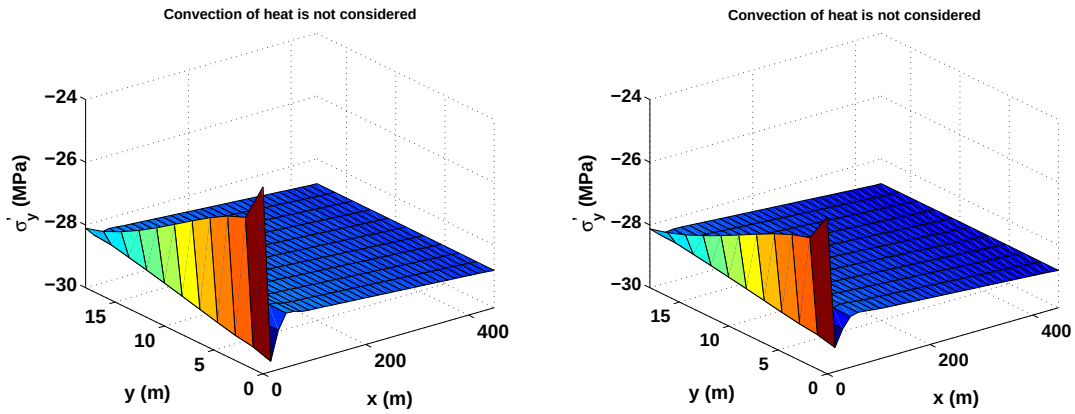

(a) Contour of $\sigma_y^{'}$ at year 5

(b) Contour of $\sigma_y^{'}$ at year 15

Figure 4.10: Contours of transversal effective stress $\sigma_y^{'}$ at two times when convection of heat is NOT considered in the simulations.

Third: for the out–of–plane effective stress $\sigma_z^{'}$

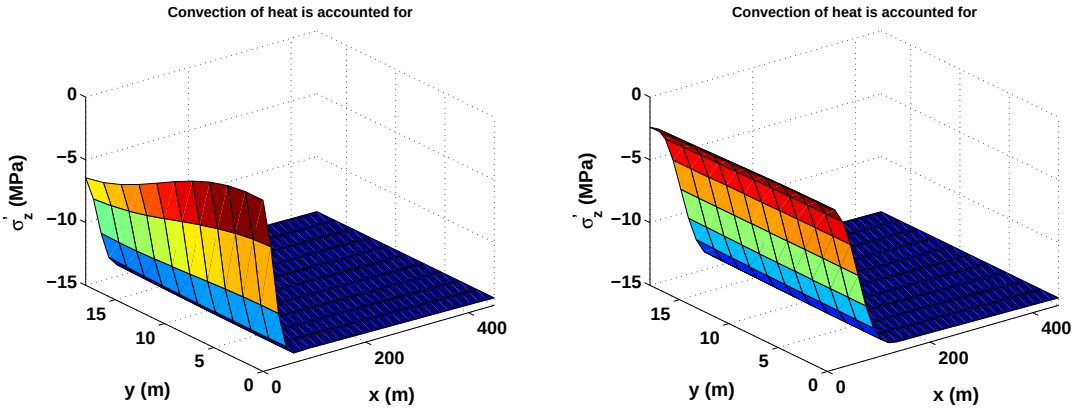

(a) Contour of $\sigma_z^{'}$ at year 5

(b) Contour of $\sigma_z^{'}$ at year 15

Figure 4.11: Contours of out–of–plane effective stress $\sigma_z^{'}$ at two times when convection of heat is considered in the simulations.

6. The out–of–plane effective stress, figures (4.11) and (4.12), is calculated based on the assumption $\varepsilon_z = 0$ which yields $\sigma_z^{'} = \nu(\sigma_x^{'} + \sigma_y^{'})$.

7. In all the above mentioned cases, the assumption of neglecting the convection of heat is ut-

terly non–realistic, section (4.1.3.1). This erroneous assumption leads to tremendous delay in the heat front. However, following figures (4.8) and (4.10), it is seen that convection of heat does not affect stresses that are mainly developed as result of the hydraulic gradients. This is due to the fact that the diffusion of fluid is very fast and the field of fluid velocity is almost homogeneous at the times considered in these simulations, see figures (4.7) and (4.9) and compare them with figures (4.8) and (4.10) near the injection well.

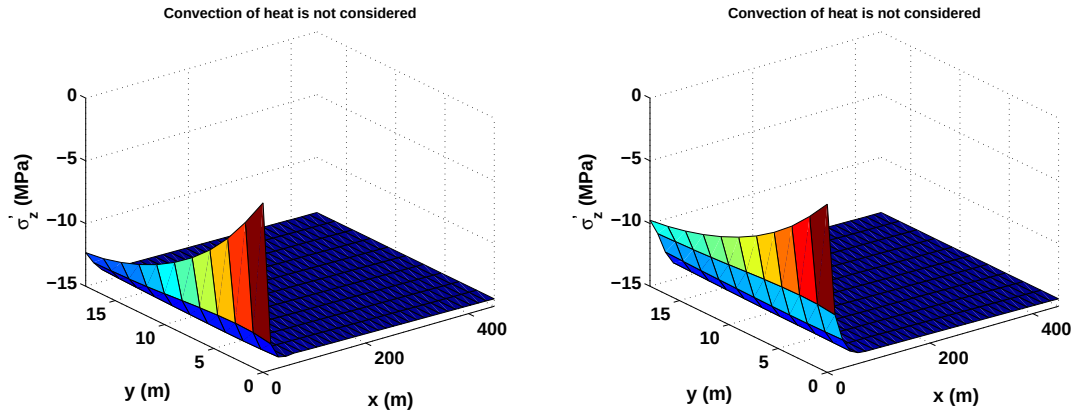

(a) Contour of $\sigma_z^{'}$ at year 5

(b) Contour of $\sigma_z^{'}$ at year 15

Figure 4.12: Contours of out–of–plane effective stress $\sigma_z^{'}$ at two times when convection of heat is NOT considered in the simulations.

4.2 An insight into the process of Hydraulic Fracturing (HF)

Hydraulic Fracturing (HF) is the process of causing fractures within a rock layer to propagate by using pressurized fluid. Normally the process of HF is suppressed by the confining pressure coming from the surrounding strata. This is particularly the case when describing mode I of fracturing where fracture walls are supposed to move away from each other. HF is practically done by reducing the effective stress by pumping pressurized fluid to a point where the minimum principal stress becomes tensile and exceeds the tensile strength of the rock layer.

Consider a vertical borehole, as shown in figure (4.13), if the pressure inside the fracture is assumed equal to the pressure in the borehole, and if the tensile limit is exceeded in the direction of the smallest principal stress σ_h, the vertical fracture will propagate perpendicular to this direction.

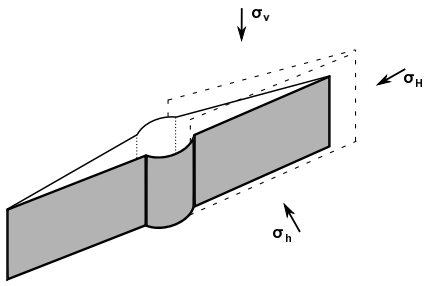

Figure 4.13: Vertical fracture around a vertical well. Two symmetric fracture wings develop perpendicularly to the direction of least principal stress.

Hydraulic fracturing has been commercially used to stimulate production techniques in low permeability reservoirs in the field of petroleum engineering since the early fifties. Such techniques involve pumping huge amounts of fluid and *proppants*[1] thus creating large permeability conduits filled with proppants.
A massive hydraulic fracturing job (MHF) may exceed one thousand cubic meters of fluid and one million kilograms of proppants. If these induced fractures are not filled with solid materials they will close when the fluid pressure drops (Fjaer et al., [2008]).

4.2.1 Lost circulation

Lost circulation is a common phenomenon in the process of HF where an unintentional fracturing may occur during drilling operations, or when the casing mud of a borehole is lost into an

[1] A proppant is a material that will keep an induced hydraulic fracture open, during or following a fracturing treatment, while the fracking fluid itself varies in composition depending on the type of fracturing used, and can be gel, foam or slickwater-based.

existing fracture. Lost circulation will lead to a serious drop of the hydraulic support in the wellbore. If the pressure in the wellbore drops below the pore pressure in the formation, and if the formation is sufficiently permeable, formation fluid will start penetrating into the wellbore in an uncontrolled manner causing, in worst cases, a blowout[1].
This is mainly an operational problem; partly because mud is expensive, or because there is a definite amount of the mud that can be loaded to the rig of the borehole. This problem is usually solved by keeping the weight of mud sufficient considering the following two criteria:

1. The limit of wellbore pressure for fracture initiation and growth in non-fractured formations,

2. and the fracture reopening pressure in naturally fractured formations, see (Fjaer et al., [2008], p. 319) for more details.

In recent applications of HF for extracting natural gas from shales, engineers started to use cement casing in stead of the mud, see figure (4.14). Cement is much stronger than the mud and hence a much smaller amount is needed which at the end turns to be more cost-effective.

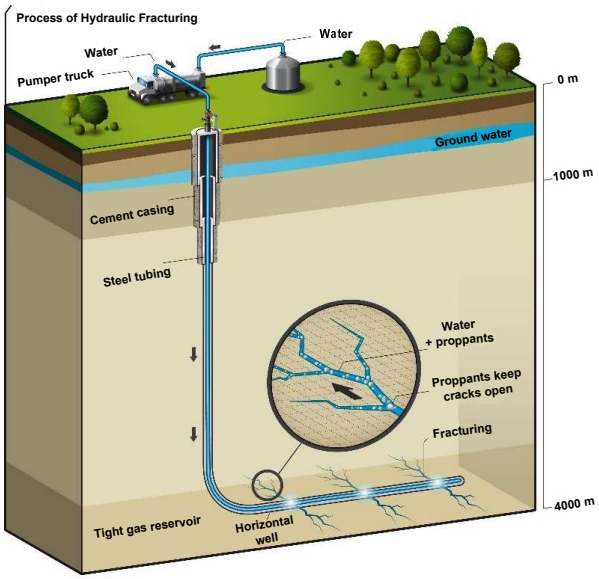

Figure 4.14: A schematic graph summarizing the process of extracting natural gas by using the technique of HF, reproduced from wikipedia.

While the main industrial use of HF is in arousing production from oil and gas wells, HF has several applications today that include:

1. Stimulation of groundwater wells.

[1]A blowout is the uncontrolled release of geothermal fluids from a borehole after pressure control systems have failed.

2. Disposal of waste by injection into deep rock formations.

3. As a method to measure *in situ* stresses in rock formations.

4. Extracting heat to produce electricity in Enhanced Geothermal Systems (EGS).

4.2.2 Tensile failure in HF

In the framework of LEFM fracturing is related to tensile failure, i.e. material fails when traction exceeds the tensile strength T_c assuming pure mode I of fracturing. The tensile fracturing condition should then read:

$$\sigma > T_c \tag{4.3}$$

For porous materials the total stress should be replaced by the effective stress and the condition will be (compressive stresses have negative sign):

$$\sigma + p_f > T_c, \tag{4.4}$$

where p_f is the pressure in the pores. Note that the coefficient of effective stress (Biot's coefficient) is equal to 1 here, since fracturing is a state of failure for the rock. In other words, the thermo–poroelastic relations involve Biot's effective stress but the failure condition involves Terzaghi's effective stress, see (Atkinson, [1991], p. 244) and (Fjaer et al., [2008], p. 371).

To consider the criterion in equation (4.4) in more details, let us assume that we have a plug of porous and permeable material, this plug is subjected to external stress σ. The pressure in the pores p_f can be changed, see figure (4.15).

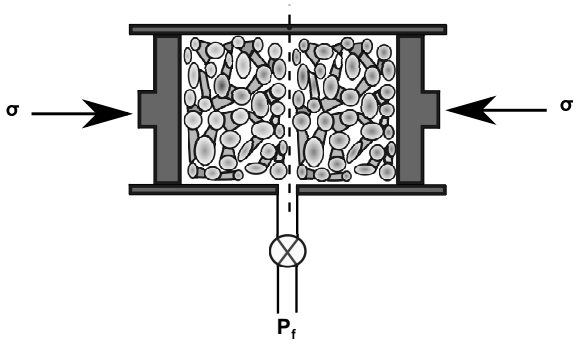

Figure 4.15: Hydraulic fracturing of a porous and permeable rock, (Fjaer et al., [2008]).

Let us consider that the grains are glued to each other and that the plug is also glued to the piston. Along the dashed line the bonds are yet broken thus forming a closed fracture. The stress needed to open the fracture is given by:

$$\sigma + p_f > 0 \tag{4.5}$$

Now let us assume that the two sides of the fracture are covered by impermeable films and that the fluid pressure p_f is injected between these films, the condition for opening the fracture still reads as in equation (4.5). The pore pressure in the plug (assuming a random value) does not play any role as long as it remains less than σ and p_f.

If the bonding between the grains forming the crack is to be considered, then additional hurdle is to be overcome which is the tensile strength of such a bond. The condition for fracturing will be again like in equation (4.4):

$$\sigma + p_f > T_c, \tag{4.6}$$

where p_f is the pressure in the fracture or in the pores forming the fracture. Generally, equation (4.6) represents the general criterion of splitting a material in tension, while equation (4.5) represents the criterion for reopening of an existing fracture.

4.2.2.1 Initiation of fractures and breakdown of formation

The basics of borehole failure in tension[1] (HF) are to be outpointed here. For a more complete and advanced presentation, the reader is advised to check (Fjaer et al., [2008], chapter 4). To illustrate the concept of fracture initiation let us consider the following situation: a vertical borehole penetrating some rock formulation with far field stresses such that $-\sigma_v > -\sigma_H > -\sigma_h$, the rock formulation is assumed homogeneous and isotropic. As the borehole pressure p_w increases the effective tangential stress σ'_θ will correspondingly decrease, see figure (4.16).

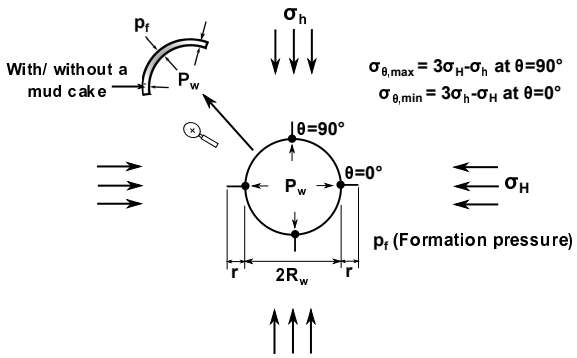

Figure 4.16: Vertical wellbore with vertical cracks. Wellbore wall can/can not be aligned with a mud cake.

[1]The failure of boreholes in shear is to be addressed later, section (4.6), as it is not likely to happen when HF is achieved, i.e. for high values of borehole casing shoe pressure p_w (Fjaer et al., [2008], p. 155).

The condition for HF initiation becomes:

$$\sigma_\theta + p_f = T_c, \tag{4.7}$$

where p_f is the formation pressure. In the presence of a mud cake, the borehole pressure required to create the hydraulic fracturing in the direction of σ_H is expressed as in equation (4.8):

$$p_w^f = -\left[(3\sigma_h - \sigma_H) + p_f - T_c\right] \tag{4.8}$$

Equation (4.8) is only valid when the walls of the borehole are perfectly impermeable. In the absence of a mud cake and if the pressurization rate was slow enough to ensure steady state conditions during pumping, the pressure required to create hydraulic fracturing is given by (Fjaer et al., [2008], p. 374):

$$p_w^f = -\left[(1-\nu)(3\sigma_h - \sigma_H) + (1-2\nu)p_f - (1-\nu)T_c\right] \tag{4.9}$$

Note that even in the absence of a mud cake, full fluid pressure continuity, i.e. $p_w = p_f$, cannot be assumed. Equations (4.8) and (4.9) are based on experimental observations and should imitate the field situation (Fjaer et al., [2008]).

Equation (4.8) represents the upper limit for the pressure needed to start the fracturing (fast pressurization), meanwhile equation (4.9) represents the lower limit for HF pressure (slow pressurization).

The pressure response in a borehole can be expressed as shown in figure (4.17).

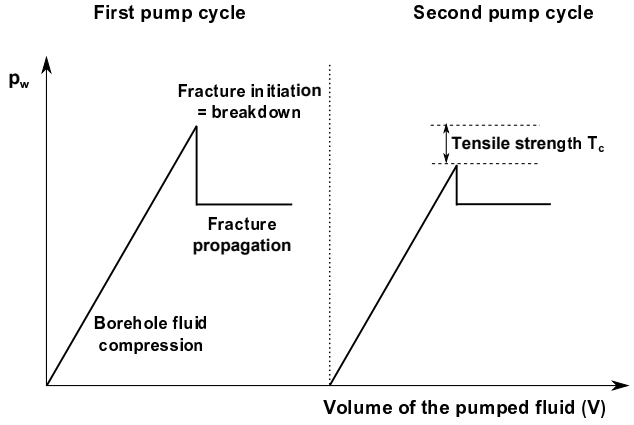

Figure 4.17: Borehole pressure response during hydraulic fracturing of a vertical borehole, two pressure cycles are defined. Figure is not to scale.

The first linear part of the curve represents the elastic deformation of borehole and the formation around it, this is a direct result of increasing the pressure and thus reducing the effective stress. The peak of the curve represents the point where the effective tensile stresses produced exceed the strength of the rock and thus fracturing begins at this point. The instantaneous drop of pressure at this point indicates accelerating growth of fractures where the volume of the fractures is growing at much higher rate than the rate at which fluid is pumped. Finally, a steady state is reached and stable fracture growth is achieved.

The second curve in figure (4.17) represents the second cycle of pumping where the only resistance that hinders the initiation of fractures is the stress concentration, since the tensile strength has already vanished as the fracture already exists.

Rock formations which have permeability less than 10^{-18} m^2 are considered totally impermeable. Boreholes drilled in such formations are considered lined with a mud cake and the upper limit of fracture initiation, equation (4.8), would apply. Rocks with permeability above this value are considered fully permeable and the lower limit of fracture initiation, equation (4.9), applies (Fjaer et al., [2008]).

4.2.2.2 Fracture size and shape

The study of fracture geometry started with the assumption of line crack embedded in an infinite elastic plane, (Griffith, [1921]) and (Irwin, [1957]). The effect of fluid pressure can then be integrated along with the possibility of leak off. The equation of balance of mass can be solved to get an expression for the fracture length, width and height.

The model used to describe fracture geometry in this research is the classical two–dimensional (Kristianovitch–Geertsma–de Klerk) KGD model, figure (4.18). The KGD model assumes strain to be confined to the horizontal plane which is quite the case when doing plane–strain analysis.

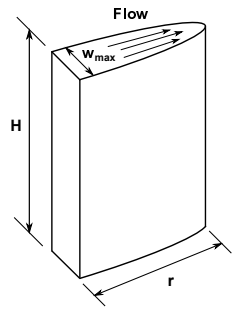

Figure 4.18: Illustration of the fracture shape for the KGD model.

The following two assumptions are to be accounted for when using the KGD model:

1. The fracture height is constant in time and independent of the fracture length.

2. The net pressure at the fracture tip is zero.

These two assumptions are merely simplifications since the hydraulic fractures evolve mainly in the vertical direction following σ_v, and consequently horizontally following σ_H. Net pressure at the fracture tip can not be zero since this pressure is required to overcome the tip resistance and make the fracture propagate (Savitski and Detournay, [2002]).

Assuming an elliptical shape of the fracture cross section, the average fracture width w can be found using the following expression, see (Savitski and Detournay, [2002]):

$$w = \frac{\pi(1-\nu^2) r\, p_e}{E}, \tag{4.10}$$

where r is the fracture half length, see figure(4.18), E is the drained Young's modulus, ν is the drained Poisson's ratio and p_e is the net fracture pressure (Terzaghi's effective stress acting on the fracture walls). The net fracture pressure depends on the flow resistance in the fracture, on the fluid fluxes to the surrounding and thus on fluid viscosity and injection rate. Equation (4.10) has been also suggested by (Atkinson, [1991], p. 245).

4.2.2.3 Thermal effects on hydraulic fracturing

Thermally induced fracturing is a phenomenon observed while injecting cold water into very hot rock layer. Rock matrix shrinks and thus reduces the compressive geologic stresses that confine the borehole. Let us follow equation (4.11) which describes the mechanical behavior of a saturated porous medium subjected to temperature change θ:

$$\boldsymbol{\sigma} + \kappa\, p\, \boldsymbol{\delta} = \boldsymbol{E} : (\boldsymbol{\varepsilon} - \boldsymbol{\varepsilon^{\theta}}), \tag{4.11}$$

$\boldsymbol{E}$ is the elasticity tensor and $\boldsymbol{\varepsilon^{\theta}}$ is the thermal strain tensor defined as $\varepsilon^{\theta}_{ij} = (\alpha_s/3)\,\theta\,\delta_{ij}$, α_s is the cubical thermal expansion coefficient. If the porous medium was sufficiently permeable to a point the diffusion of fluid happens much faster than the diffusion of heat (the common case when simulating real EGS reservoirs), the term $\kappa\, p\, \boldsymbol{\delta}$ could be assumed constant while cooling.

Thus, while cooling θ becomes negative and negative mechanical strains ($\boldsymbol{\varepsilon}$) are needed in equation (4.11) to keep the equilibrium condition $\boldsymbol{\nabla}.\boldsymbol{\sigma} = \boldsymbol{0}$. Negative mechanical strains (contraction) develop positive tensile stresses, imagine some degree of restrain at the boundaries, which in turn means reduction of the confining compressive geologic stresses.

(Fjaer et al., [2008], p. 388) has given the analytical expression for thermal stresses resulting from cooling a cylindrical zone of arbitrary radius d and arbitrary height h around a borehole.

For the situation ($d/h \to \infty$), i.e. when the cooling front moves considerably in the cylindrical zone, the temperature change θ becomes uniform around the borehole and the expression for the thermal stresses reads:

$$\sigma_r(\theta) = \sigma_\theta(\theta) = -\frac{E}{3(1-\nu)}\alpha_s\,\theta \tag{4.12}$$

If the temperature field is to be decoupled from the mechanical and hydraulic effects while assuming isotropy, equation (4.12) can be integrated in equations (4.8) and (4.9) to give the borehole pressures at failure in presence and in absence of mud cake as:

$$\text{With a mud cake:}\quad p_w^f = -\left[(3\sigma_h - \sigma_H) + p_f - \frac{E\,\alpha_s\,\theta}{3(1-\nu)} - T_c\right] \tag{4.13}$$

$$\text{Without a mud cake:}\quad p_w^f = -\left[(1-\nu)(3\sigma_h - \sigma_H) + (1-2\nu)p_f - \frac{E\,\alpha_s\,\theta}{3} - (1-\nu)T_c\right] \tag{4.14}$$

Note that the pressurization of impermeable media (permeability $< 10^{-18}$ m^2) is equivalent to the presence of a mud cake. Meanwhile all porous media with permeability $> 10^{-18}$ m^2 are assumed permeable and the limit for pressurization without a mud cake shall apply.

For typical sandstone values ($E = 5$ GPa, $\nu = 0.3$, $\alpha_s = 4.5 \times 10^{-5}$ 1/°C), equation (4.12) gives a stress change of -0.1 MPa/°C. From the correspondence between thermoelasticity and poroelasticity:

$$\kappa\,(1-2\nu)\,\Delta p \Longleftrightarrow -\frac{E\,\alpha_s\,\theta}{3} \tag{4.15}$$

For a typical injection test the change of temperature θ is up to -80 °C (cooling) which is equivalent to fluid pressure change of 15 MPa ($\kappa = 1$). This indicates that the cooling effects taking place at the beginning of an injection test can be equivalent to large pressurizing values.

The effect of temperature change on the fracture aperture, equation (4.10), must be also considered. Actually, tensile stresses developed by cooling could help reducing the confining stresses and consequently help opening the fractures. This will be addressed in more details in section (4.3.1).

Summing up the foregoing strategies, HF technique in EGS can be summarized following figure (4.19). As the injection of cold water begins, the geostatic stresses start to decrease. Temperature change (cooling) helps mitigating the compressive geostatic stresses as well. If pressurization and cooling continue to a point where effective stresses become tensile and exceed the tensile strength of the rock material, fracturing happens.

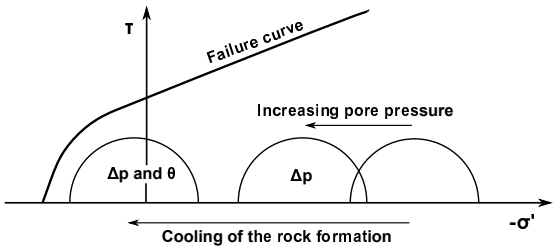

Figure 4.19: Mohr circles and failure line: the effect of increasing pore pressure and decreasing temperature on HF.

4.3 Development of the Hydraulic Fracturing Model (HFM)

This section is devoted to develop the initial version of the Hydraulic Fracturing Model (HFM) that will be used to simulate HF of geothermal systems. The section proceeds as follows; the mathematics of the model is firstly presented, a single point test is addressed with sufficient study on the model parameters, finally a scheme for integrating the HFM in our FE code is highlighted.

4.3.1 From continuum mechanics to fracture mechanics

Let us assume a vertical borehole as shown in figure (4.20), with a group of cracks of average radius r and arbitrary direction $\boldsymbol{n}$ in the horizontal plane (x, y). σ_v is the out–of–plane burden stress.

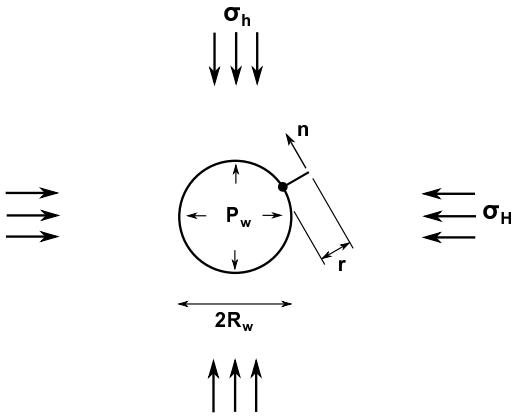

Figure 4.20: Vertical borehole with vertical fracture of average radius r and arbitrary direction $\boldsymbol{n}$.

The radius of the borehole R_w is assumed very small compared to the dimensions of the BVP considered, besides the ratio $r/R_w \to 0$. Actually, one should keep in mind that LEFM does not consider crack nucleation and we must start with already existing cracks though quite small.

If the borehole pressure is gradually increased to a point where the effective stress $\sigma_n^{'}$ (at the crack tip) becomes tensile and exceeds the limit of material tensile strength, the group of cracks starts propagating and consequently the average aperture of cracks increases.

The following model, equation (4.16), has been suggested to track the evolution of average radius r of a group of cracks in direction $\boldsymbol{n}$:

$$F(\sigma_n^{'}, r) = f(r)\,\sigma_n^{'}\sqrt{\pi r} - K_{Ic}, \tag{4.16}$$

where K_{Ic} is the material toughness for mode I of fracturing. The normal effective stress applied to the crack ($\sigma_n^{'}$) is expressed as:

$$\sigma_n^{'} = \boldsymbol{n}.\boldsymbol{\sigma}^{'}.\boldsymbol{n} \tag{4.17}$$

$f(r)$ has the same definition as illustrated in section (2.3.2) and is given by:

$$f(r) = \begin{cases} \eta\left(\frac{r_f}{r}\right), & r < r_f \\ \eta, & r \geq r_f \end{cases} \tag{4.18}$$

r_f denotes the critical crack radius for unstable coalescence of cracks. The function $f(r)$ in equation (4.18) has been chosen such that a stable crack growth is assured. A stable crack growth requires that additional tensile stresses to be added so that cracks may continue to propagate, in other words, $dG/dr < 0$ where G is the strain energy release rate (rate with respect to crack length and not time). For mode I of fracturing, the energy release rate G_I for plane strain problems is given by (Atkinson, [1991], p. 7):

$$G_I = \frac{K_I^2\,(1-\nu^2)}{E} \tag{4.19}$$

K_I is the stress intensity factor for mode I of fracturing. Following equation (4.16), $K_I = f(r)\,\sigma_n^{'}\sqrt{\pi r}$, the product $f(r)\,\sqrt{r}$ must be decreasing and thus a stable crack growth is achieved. When $r \geq r_f$ the product $f(r)\,\sqrt{r}$ is no longer decreasing and unstable crack growth is obtained. The latter case is not to be addressed in this research, more details about unstable crack growth can be found in (Atkinson, [1991], chapter 4).

The continuum mechanics approach, equations (4.8), (4.9), (4.13) or (4.14), has been presented such that the hydraulic fracturing model equation (4.16) can be parameterized. η, the model parameter, is to be determined such that the fracturing will begin at a borehole pressure p_w^f corresponding to one of the cases demonstrated in equations (4.8), (4.9), (4.13) or (4.14)

whichever applies.

The derivation of the incremental propagation dr of a group of cracks of average radius r and arbitrary direction $\boldsymbol{n}$ resulting from an increment of effective stress $d\sigma_n^{'}$ can be obtained following equations (4.16) and (4.18):

$$dF = \frac{\partial F}{\partial r}\, dr + \frac{\partial F}{\partial \boldsymbol{\sigma}^{'}} \,:\, d\boldsymbol{\sigma}^{'}, \tag{4.20}$$

which leads to:

$$dF = \frac{\partial F}{\partial r}\, dr + \left[\frac{\partial F}{\partial \sigma_n^{'}} \frac{\partial \sigma_n^{'}}{\partial \boldsymbol{\sigma}^{'}}\right] \,:\, d\boldsymbol{\sigma}^{'}, \tag{4.21}$$

thus, at the onset of fracturing ($dF = 0$):

$$dr = -\frac{1}{\dfrac{\partial F}{\partial r}} \left[\frac{\partial F}{\partial \sigma_n^{'}} \frac{\partial \sigma_n^{'}}{\partial \boldsymbol{\sigma}^{'}}\right] \,:\, d\boldsymbol{\sigma}^{'} \tag{4.22}$$

When $r < r_f$:

$$F = \eta \sqrt{\pi}\, \sigma_n^{'} \left(\frac{r_f}{\sqrt{r}}\right) - K_{Ic} = 0 \tag{4.23}$$

$$\frac{\partial F}{\partial r} = -\frac{1}{2}\, \eta \sqrt{\pi}\, \sigma_n^{'} \left(\frac{r_f}{\sqrt{r^3}}\right) \tag{4.24}$$

$$\frac{\partial F}{\partial \sigma_n^{'}} = \eta \sqrt{\pi} \left(\frac{r_f}{\sqrt{r}}\right) \tag{4.25}$$

$$\frac{\partial \sigma_n^{'}}{\partial \boldsymbol{\sigma}^{'}} = \boldsymbol{n} \otimes \boldsymbol{n} \tag{4.26}$$

The average crack aperture is now calculated following equation (4.10) suggested by (Savitski and Detournay, [2002]) and (Atkinson, [1991], p. 245):

$$w = \frac{\pi(1-\nu^2)\, r\, \sigma_n^{'}}{E} \tag{4.27}$$

The overall crack permeability tensor can be identified, see section (2.3.3), as follows:

$$\boldsymbol{k}_c = \frac{N}{\Omega} \frac{\lambda}{48} \int_S R(\boldsymbol{n})\, w(\boldsymbol{n})^3\, r(\boldsymbol{n})^2\, (\boldsymbol{\delta} - \boldsymbol{n} \otimes \boldsymbol{n})\, dS \tag{4.28}$$

The implementation of equation (4.28) requires that our KGD crack model, figure (4.18), to be replaced by a penny–shaped crack which shares the same cross–sectional properties (w and r) in a plane that contains $\boldsymbol{n}$.

4.3.2 Testing and calibrating the HFM at a Gauss' point

The purpose of this part is to test the Hydraulic Fracturing Model HFM, equations (4.16) and (4.18). Let us assume that we have a parallelepiped sample of Lac du Bonnet Granite. The rock sample is drilled at the middle where pressurized fluid is permitted to flow. While allowing drainage, the sample is subjected to the stress state shown in figure (4.21).

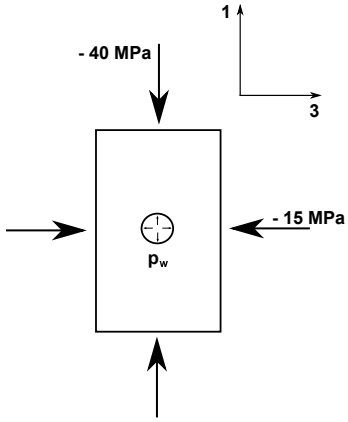

Figure 4.21: parallelepiped sample of Lac du Bonnet granite subjected to the stress state shown and drilled at the middle where fluid is pumped, out of plane stress is equal to -10 MPa.

Table (4.2) shows the values of all the parameters used in the simulations.

Table 4.2: Parameters used in testing the HF model (HFM). References: 1.(Shao et al., [2005]) and 2.(Atkinson, [1991], p. 245).

	Parameter	Value	Reference
Elastic parameters	Elastic modulus E_0 (MPa)	68000	1
	Poisson's ratio ν_0	0.21	1
Damage parameters	Initial radius of cracks r_0 (mm)	3.0	1
	Final radius of cracks r_f (mm)	9.0	1
	Initial aperture of cracks w_0 (mm)	$0.001^{\ddagger}$	Calculated
	or w_0 (mm)	0.015	1
	Material tensile strength T_c (MPa)	8.3	2
	Material toughness parameter K_{Ic} (MPa$\sqrt{\text{m}}$)	1.87	2
	Model parameter η	$1.6^{\dagger}$	Parameterized
	Number of cracks N per unit volume ($\Omega = 1$ m^3)	2×10^6	1
Hydraulic connectivity parameters	t_1	0.0001	1
	t_2	1.0	1
	Initial permeability k_0 (m^2)	10^{-21}	1

The value of the initial and final crack radii, r_0 and r_f, correspond to a sample tested at the laboratory scale. Larger values, in the order of cm's, will be used in subsequent studies when

simulating large scale geothermal reservoirs.

Note that the parallelepiped sample is subjected to a 3–dimensional non–axisymmetric loading state. Actually, the HFM model developed previously can be used for 2–dimensional or 3–dimensional problems. The definition of the direction $\boldsymbol{n}$ as well as the discretization of equation (4.28) control the dimensions of calculations.

The initial fracture aperture[‡] w_0 is calculated using equation (4.27) by replacing $\sigma_n^{'}$ by the tensile strength of the rock $T_c = 8.3$ MPa with $r = r_0$:

$$w_0 = \frac{\pi\,(1 - 0.21^2) \times 3 \times 10^{-3} \times 8.3 \times 10^6}{68 \times 10^9} = 1 \times 10^{-6}\ \text{m} \tag{4.29}$$

The sample is initially almost impermeable ($k_0 = 10^{-21}$ m^2). Since drainage is allowed in the aforementioned study figure (4.21), initial formation pressure p_f before pumping the fluid is zero. Thus, the value of pore pressure required to start the hydraulic fracturing is calculated based on equation (4.8):

$$p_w^f = -\Big[(3 \times -15 \times 10^6 + 40 \times 10^6) - 0.0 - 8.3\Big] \approx 14\ \text{MPa} \tag{4.30}$$

The value of the model parameter[†] η has been determined such that the fractures will start propagating at $p_w^f = 14$ MPa.

This problem has been simulated following two approaches:

1. The incremental change in the fracture aperture Δw due to increments of dr and $d\sigma_n^{'}$ is estimated using equation (4.27) or,
2. the incremental change Δw is calculated using the study presented in section (2.5.1.1).

The choice between the two approaches will depend on the results of simulations. In either case, the study presented in section (2.5.1.1) for permeability evolution of Lac du Bonnet granite during compression loading will be used as a guiding reference.

4.3.2.1 Δw is calculated using equation (4.27)

The evolution of axial and lateral permeability components (k_{11} and k_{33}) due to pumping fluid is shown in figure (4.22).

The general shape of the curve in figure (4.22) sounds fine, most of changes occur in the short interval $p_w \in [15, 23]$ MPa. This is due to the fact that only mode I of fracturing is considered.

As soon as the criterion for hydraulic fracturing is achieved r goes to r_f almost instantaneously[1] in the direction of maximum principal stress (direction 1).

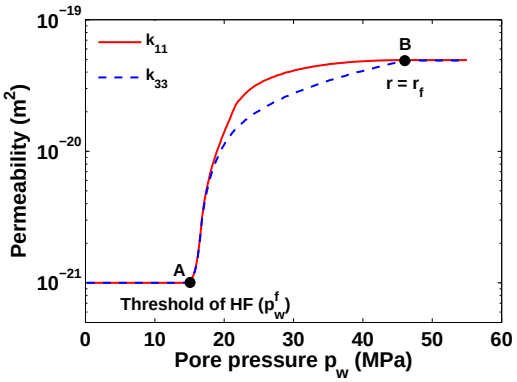

Figure 4.22: Variation of permeability in the axial and lateral directions during pumping water in a parallelepiped Lac du Bonnet granite sample with a stress state as shown in figure (4.21). Δw is calculated using equation (4.27). As the rock sample resembles a single point, the pumping pressure p_w is equal to the pore pressure.

Using equation (4.27) seems to underestimate the values of the permeability tensor components considerably. In fact, the values of the permeability tensor components at point B ($k_{11} = k_{33} = 4.9 \times 10^{-20}$ m^2) are not anyhow close to the values ($\sim 10^{-17}$ m^2) obtained for the same rock when destroyed in compression, figure (2.17). It is conceivable that fracturing should happen much faster when only mode I for tensile fracturing is considered. Nevertheless, the permeability of the damaged rock (whether in tension or in compression) should not differ so much when considering the order of magnitude.

The aforementioned point can be explained following the fact that; permeability is attributed to spatial connected conduits which will be reached whether the sample is damaged in compression or in tension.

Hence, the first approach, equation (4.27), will not be used any longer in performing HF simulations in this research. The second approach is to try the relations $w(r)$ that were derived in section (2.5.1.1).

[1]Fracturing is a steady state problem. If time–related vocabulary is used, it shall refer to the energy release rate with respect to the crack length and not time. In other words, for small changes in the controlling variable, there will be considerable changes in the fracture radius. The controlling variable in this single point study is the injection pressure p_w.

4.3.2.2 Δw is calculated using section (2.5.1.1)

Simulations are performed while assuming that the normal increment of crack aperture Δw is related to the increment of average crack radius Δr.

Like in figure (4.22) most of the change in the permeability tensor components (k_{11} and k_{33}) take place within the interval $p_w \in [15, 24]$ MPa, see figure (4.23). The propagation of cracks in direction 1 is very fast and the component k_{11} almost reaches its ultimate value at point C. Again, this is due to the fact that only mode I of fracturing is considered.

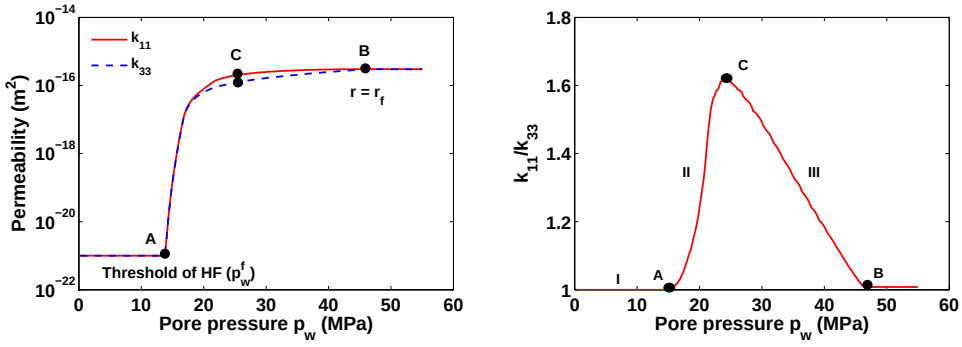

(a) (b)

Figure 4.23: (a) Variation of permeability in the axial and lateral directions during pumping water in a parallelepiped Lac du Bonnet granite sample with a stress state as shown in figure (4.21), Δw is calculated using section (2.5.1.1). (b) Variation of the ratio k_{11}/k_{33} with the pumping/pore pressure.

Figure (4.24(b)) shows the directional evolution of the crack radius at the vertical plane $\phi = 90°$ and at a pumping pressure $p_w = 24$ MPa.

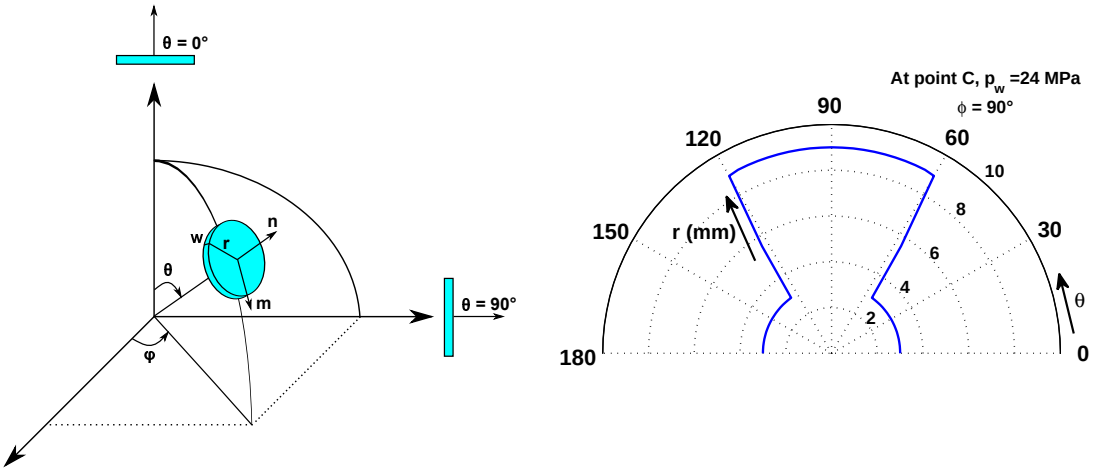

(a) $\theta - \phi$ position of a crack of radius $r(\boldsymbol{n})$ (b) Directional evolution of the radius of cracks

Figure 4.24: Directional evolution of cracks radii at point C, $p_w = 24$ MPa.

The ratio k_{11}/k_{33} increases significantly and almost instantly in region II, see figure (4.23(b)). This is due to the preferential growth of cracks in the direction of maximum principal compressive stress -40 MPa. At point C most of the cracks contributing to the component k_{11} are connected ($r = r_f$). However, cracks in other orientations continue to grow slowly contributing to the component k_{33}. In region III, k_{33} continues to increase slowly and thus the ratio k_{11}/k_{33} decreases consequently.

At point B all the cracks, in all orientations, get connected ($r = r_f$) leading to an isotropic state where $k_{11} = k_{33}$, see figure (4.25).

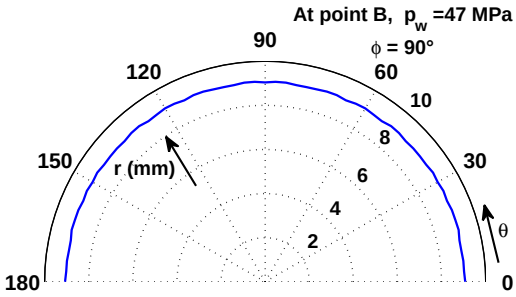

Figure 4.25: Directional evolution of cracks radii at point B, $p_w = 47$ MPa.

The isotropic permeability tensor obtained at the macroscopic failure of the sample ($r = r_f$) can be illustrated by knowing the value of the critical effective normal stress (σ'_{nc}) needed to drive r to r_f at any direction $\boldsymbol{n}$. Following equation (4.16):

$$\sigma'_{nc} = \lim_{r \to r_f} \frac{K_{Ic}}{f(r)\sqrt{\pi r}} = \frac{K_{Ic}}{\eta \sqrt{\pi r_f}} = 6.54 \text{ MPa}, \tag{4.31}$$

As soon as p_w is increased to a point the effective normal stress becomes equal to σ'_{nc} in all directions, r becomes equal to r_f and correspondingly the average aperture w reaches its ultimate value in all directions as well. At this point the sample fails at the macroscopic scale and this research does not model post failure behavior. Figure (4.26) shows the directional variation of the normal effective stress σ'_n at point B of curve (4.23(a)) and at a pumping pressure value of $p_w = 47$ MPa.

It is seen from figure (4.26) that, on cracks which are not aligned with the minor principal compressive stress, the effective normal stress σ'_n may exceed the critical effective normal stress σ'_{nc}. However as this research does not stand for unstable growth of cracks, any further change in the permeability is not to be studied.

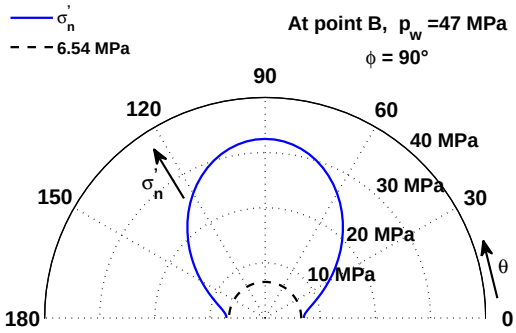

Figure 4.26: Directional variation of normal effective stress ($\sigma_n^{'} = \boldsymbol{n}.\boldsymbol{\sigma}^{'}.\boldsymbol{n}$) at point B, $p_w = 47$ MPa.

Summing up all the foregoing, it is concluded that:

1. Point A represents the threshold of hydraulic fracturing where the pore pressure reduces the confining stresses to a point the effective stresses become tensile and exceed the limit of material tensile strength at the tips of the cracks pointing toward the maximum principal stress -40 MPa.

2. Cracks propagate faster in the axial direction (direction 1) following the axis of maximum principal stress.

3. The difference between the axial permeability component k_{11} and the lateral permeability component k_{33} is maximum at the region of accelerated crack propagation, region II in figure (4.23(a)). However, this difference is coped for while the material enters the region of macroscopic failure.

4. Point B represents the stage where all microcracks coalesce ($r = r_f$) forming macroscopic fractures. After point B, permeability change is out of scope of this research.

5. The magnitudes of the permeability tensor components at point B are $k_{11} = k_{33} = 2.8 \times 10^{-16}$ m^2. These values are almost equal to the values obtained for the same rock when driving it to fail under compressive stresses, see for instance figure (2.17).

4.3.3 The role of the model parameter η

The model parameter η that appears in equations (4.16) and (4.18) should be determined experimentally based on the deterioration of the elastic properties of the rock considered as damage evolves, section (2.3.2). If η is equal to one, the classical Griffith fracturing model is retrieved.

In the study presented in the previous section (4.3.2), the value of the HF pressure was determined using the continuum approach equation (4.8) and was found to be 14 MPa. Let us

work equations (4.16) and (4.18) to get the model parameter η as a function of average crack radius at the threshold of crack propagation $F = 0$:

$$\eta = \frac{\sqrt{r}\, K_{Ic}}{\sqrt{\pi}\, r_f\, \sigma_n^{'}} \tag{4.32}$$

Following figure (4.21), the first group of cracks to start propagating are those oriented in the direction of maximum principal stress -40 MPa with direction $\boldsymbol{n}$ pointing to the out of plane minimum principal stress -10 MPa. The normal effective stress acting on such a group at the threshold of HF is $\sigma_n^{'} = -10$ MPa $+ 14$ MPa $= 4$ MPa. If this normal effective stress is substituted in equation (4.32), the model parameter to start HF at a pressure of 14 MPa is known, compare with the value in Table (4.2):

$$\eta = \frac{\sqrt{r_0}\, K_{Ic}}{\sqrt{\pi}\, r_f\, \sigma_n^{'}} = \frac{\sqrt{3 \times 10^{-3}} \times 1.87 \times 10^6}{\sqrt{\pi} \times 9 \times 10^{-3} \times 4 \times 10^6} = 1.6 \tag{4.33}$$

Actually for the rock sample presented in section (4.3.2), the radii of initial cracks are assumed normally distributed around $r_0 = 3$ mm. In such a case, larger cracks will give larger model parameter η if substituted in equation (4.32) for the same effective normal stress. They will also start propagating at lower pressure in case of using the same model parameter calculated for $r = r_0 = 3$ mm ($\eta = 1.6$ in the previous case).
Figure (4.27(a)) shows the plot of the equation (4.32) for the parameters values shown in Table (4.2). Meanwhile Figure (4.27(b)) shows the plot of the function $f(r)$ for 4 different values of the model parameter η and for $r_f = 9$ mm.

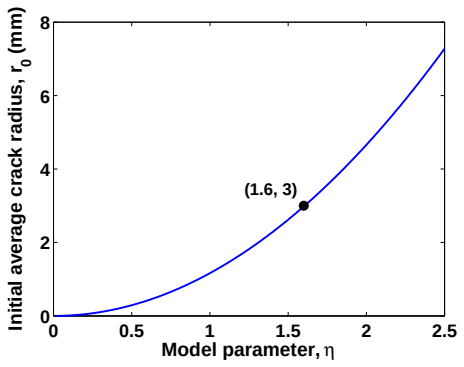

(a) Average initial crack radius as a function of η at the threshold of crack propagation $F = 0$, equation (4.32). See Table (4.2) for parameters values

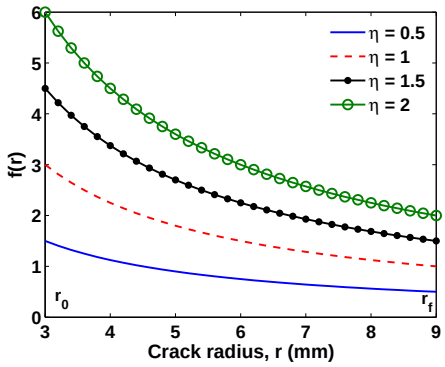

(b) The curves of $f(r)$, equation (4.18), for different values of η. r_0 and r_f are as indicated in Table (4.2)

Figure 4.27: Study of the model parameter η effects on crack propagation and stability of crack growth.

Figure (4.27) shows that: larger η is needed to start larger crack propagation if other parameters of equation (4.32) are kept constant. Regardless of the value of η, the definition of the scalar valued function $f(r)$, equation (4.18), makes the function decrease as the crack propagates, see figure (4.27(b)). However, the smaller the value of η, the smoother the slope of $f(r)$ especially for small propagations of cracks, which necessarily means stabler growth. Stabler growth means that crack will propagate slower for the same parameters and stress conditions. For instance the curve of $\eta = 0.5$, in figure (4.27(b)), reaches the asymptotic state almost at $r = 6$ mm meanwhile other curves continue to reduce considerably even at the state $r = r_f$.

Indeed, the value of the pore fluid pressure p_w^f at the threshold of HF, as a function of the model parameter η, can be determined following the stress state of figure (4.21) and equation (4.32):

$$p_w^f = \frac{\sqrt{r}\, K_{Ic}}{\eta \sqrt{\pi}\, r_f} - \underbrace{(-10 \times 10^6)}_{\text{minimum principal stress (Pa)}} \tag{4.34}$$

Using the parameters presented in Table (4.2) and values for η in the range [0.01, 2.5], equation (4.34) can be represented as shown in figure (4.28):

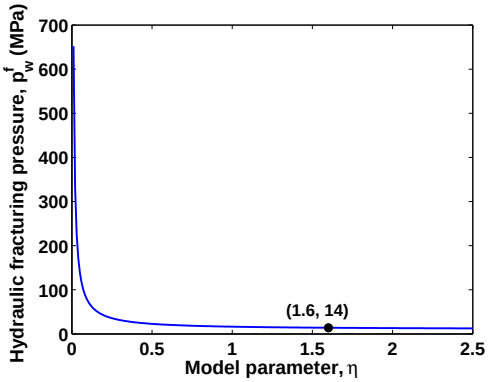

Figure 4.28: Effect of the model parameter η on the HF pressure, equation (4.34). Parameters values are used as in Table (4.2).

Figure (4.28) shows that the larger the model parameter, the smaller the value of pore fluid pressure needed to start the process of HF if other parameters are kept constant. Since larger crack radius requires larger values of η to start HF, see figure (4.27(a)), a smaller pore fluid pressure is needed to cause longer cracks to propagate by figure (4.28). This phenomenon is also proved by previous researches, see for instance (Atkinson, [1991], p. 244).

Figure (4.29) shows the simulations of the test presented in section (4.3.2) for four values of the model parameter η. The following points are finally concluded:

1. The four curves reach the ultimate order of magnitude for permeability $\sim 10^{-16}$ m^2, as it depends on values of r_0, r_f, crack density and the relation used to calculate the change in crack aperture.

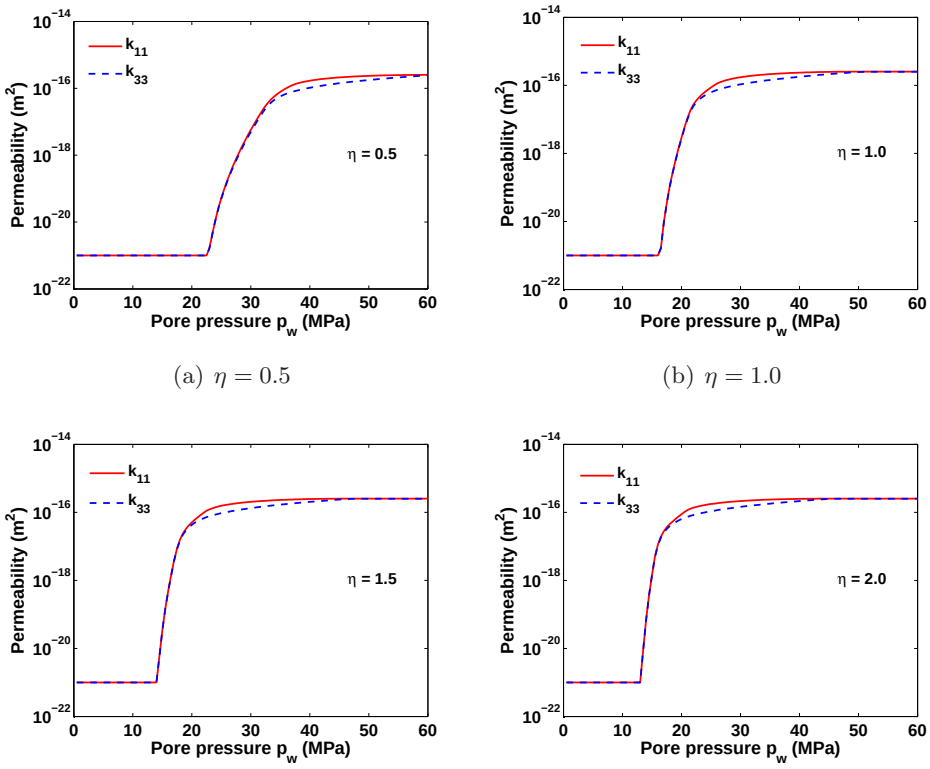

(a) $\eta = 0.5$ (b) $\eta = 1.0$

(c) $\eta = 1.5$ (d) $\eta = 2.0$

Figure 4.29: Variation of permeability in the axial and lateral directions during pumping water in a parallelepiped Lac du Bonnet granite sample with a stress state as shown in figure (4.21) and for different values of the model parameter η.

2. Reducing the value of the model parameter η means less damaged material and stabler growth of cracks, see figure (4.27(b)).

3. Less damaged material indicates smaller cracks and therefore an increased value of pore fluid pressure to start the process of HF.

4.4 Integrating the Hydraulic Fracturing Model (HFM) in the FEM

This section seeks to integrate the HFM which was presented in section (4.3) into the Fortran 90 FE code. Actually our FE code accounts only for plane strain and/or axi–symmetric isotropic

thermo–poro–elasticity. Under the framework of LEFM full anisotropy needs to be implemented at the scale of microcracks in order to calculate the macroscopic strain tensor, equation (2.47).

4.4.1 Anisotropy and Voigt's notation

Real materials can not be isotropic and in some cases, like in composite materials, the differences in properties in different directions are huge, and thus can not be neglected and full isotropy is not to be assumed. Within the frame work of LEFM, the relationship between stress and strain is given by *Hooke's law 1975*. Hooke's law uses a fourth–order stiffness tensor C_{ijkl} and describes the stress–strain relationship for anisotropic elastic material as follows:

$$\sigma_{ij} = C_{ijkl}\,\varepsilon_{kl} \tag{4.35}$$

The stiffness tensor C_{ijkl} consists of 81 components. However, accounting for the symmetries of the stress and strain tensors, Voigt's notation enables us to rewrite it considering only 36 components:

$$\sigma_i = C_{ij}\,\varepsilon_j \Rightarrow \begin{bmatrix}\sigma_{xx}\\ \sigma_{yy}\\ \sigma_{zz}\\ \sigma_{yz}\\ \sigma_{zx}\\ \sigma_{xy}\end{bmatrix} = \begin{bmatrix}C_{11} & C_{12} & C_{13} & C_{14} & C_{15} & C_{16}\\ C_{21} & C_{22} & C_{23} & C_{24} & C_{25} & C_{26}\\ C_{31} & C_{32} & C_{33} & C_{34} & C_{35} & C_{36}\\ C_{41} & C_{42} & C_{43} & C_{44} & C_{45} & C_{46}\\ C_{51} & C_{52} & C_{53} & C_{54} & C_{55} & C_{66}\\ C_{61} & C_{62} & C_{63} & C_{64} & C_{65} & C_{66}\end{bmatrix} \begin{bmatrix}\varepsilon_{xx}\\ \varepsilon_{yy}\\ \varepsilon_{zz}\\ \gamma_{yz}\\ \gamma_{zx}\\ \gamma_{xy}\end{bmatrix} \tag{4.36}$$

The stress and the strain tensors are introduced through pseudo–vectors of length 6:

$$\boldsymbol{\varepsilon} = \begin{bmatrix}\varepsilon_{xx} & \varepsilon_{xy} & \varepsilon_{xz}\\ \varepsilon_{yx} & \varepsilon_{yy} & \varepsilon_{yz}\\ \varepsilon_{zx} & \varepsilon_{zy} & \varepsilon_{zz}\end{bmatrix} \Rightarrow \quad \boldsymbol{\varepsilon^T} = \begin{bmatrix}\varepsilon_{xx} & \varepsilon_{yy} & \varepsilon_{zz} & \gamma_{yz} & \gamma_{zx} & \gamma_{xy}\end{bmatrix}, \tag{4.37}$$

and,

$$\boldsymbol{\sigma} = \begin{bmatrix}\sigma_{xx} & \sigma_{xy} & \sigma_{xz}\\ \sigma_{yx} & \sigma_{yy} & \sigma_{yz}\\ \sigma_{zx} & \sigma_{zy} & \sigma_{zz}\end{bmatrix} \Rightarrow \quad \boldsymbol{\sigma^T} = \begin{bmatrix}\sigma_{xx} & \sigma_{yy} & \sigma_{zz} & \sigma_{yz} & \sigma_{zx} & \sigma_{xy}\end{bmatrix}, \tag{4.38}$$

with the shear strains defined as:

$$\gamma_{yz} = 2\varepsilon_{yz}, \qquad \gamma_{xz} = 2\varepsilon_{xz}, \quad \text{and} \quad \gamma_{xy} = 2\varepsilon_{xy} \tag{4.39}$$

Conservative materials possess a strain energy density function and as a result, the stiffness and compliance tensors are symmetric. Therefore, only 21 stiffness and compliance components are actually independent in the generalized Hooke's law, equation (4.36).

4.4.1.1 Hooke's law for anisotropic plane strain linear elasticity

For plane strain anisotropic elasticity equations (4.37) and (4.38) simplify to:

$$\boldsymbol{\varepsilon} = \begin{bmatrix} \varepsilon_{xx} & \varepsilon_{xy} & 0 \\ \varepsilon_{yx} & \varepsilon_{yy} & 0 \\ 0 & 0 & 0 \end{bmatrix} \Rightarrow \quad \boldsymbol{\varepsilon^T} = \begin{bmatrix} \varepsilon_{xx} & \varepsilon_{yy} & 2\varepsilon_{xy} & 0 \end{bmatrix}, \tag{4.40}$$

and,

$$\boldsymbol{\sigma} = \begin{bmatrix} \sigma_{xx} & \sigma_{xy} & 0 \\ \sigma_{yx} & \sigma_{yy} & 0 \\ 0 & 0 & \sigma_{zz} \end{bmatrix} \Rightarrow \quad \boldsymbol{\sigma^T} = \begin{bmatrix} \sigma_{xx} & \sigma_{yy} & \sigma_{xy} & \sigma_{zz} \end{bmatrix} \tag{4.41}$$

Hooke's law, equation (4.36) becomes:

$$\begin{bmatrix} \sigma_{xx} \\ \sigma_{yy} \\ \sigma_{xy} \\ \sigma_{zz} \end{bmatrix} = \begin{bmatrix} C_{11} & C_{12} & C_{16} & 0 \\ C_{21} & C_{22} & C_{26} & 0 \\ C_{61} & C_{62} & C_{66} & 0 \\ C_{31} & C_{32} & C_{36} & 0 \end{bmatrix} \begin{bmatrix} \varepsilon_{xx} \\ \varepsilon_{yy} \\ 2\varepsilon_{xy} \\ 0 \end{bmatrix} \tag{4.42}$$

The strain pseudo–vector is related to the displacement vector through:

$$\begin{bmatrix} \varepsilon_{xx} \\ \\ \varepsilon_{yy} \\ \\ 2\varepsilon_{xy} \end{bmatrix} = \begin{bmatrix} \dfrac{\partial u_x}{\partial x} \\ \\ \dfrac{\partial u_y}{\partial y} \\ \\ \dfrac{\partial u_x}{\partial y} + \dfrac{\partial u_y}{\partial x} \end{bmatrix} \tag{4.43}$$

4.4.1.2 Hooke's law for anisotropic axisymmetric linear elasticity

For an axisymmetric analysis, all the displacement components are to be expressed in the cylindrical coordinates (r, θ, z) instead of the Cartesian coordinates (x, y, z). The main hypothesis of axisymmetry is that; all functions under consideration are to be independent of the rotation θ. In addition, the circumferential displacement u_θ is assumed equal to zero, $u_\theta = 0$. Noting that $\varepsilon_{\theta\theta} = u_r/r$ is generally not zero, the strain pseudo–vector in an axisymmetric analysis is related to the displacement vector through:

$$\begin{bmatrix} \varepsilon_{rr} \\ \\ \varepsilon_{zz} \\ \\ 2\varepsilon_{rz} \\ \\ \varepsilon_{\theta\theta} \end{bmatrix} = \begin{bmatrix} \dfrac{\partial u_r}{\partial r} \\ \\ \dfrac{\partial u_z}{\partial z} \\ \\ \dfrac{\partial u_r}{\partial z} + \dfrac{\partial u_z}{\partial r} \\ \\ \dfrac{u_r}{r} \end{bmatrix}, \tag{4.44}$$

thus, equations (4.40) and (4.41) for an axisymmetric analysis become:

$$\boldsymbol{\varepsilon} = \begin{bmatrix} \varepsilon_{rr} & \varepsilon_{rz} & 0 \\ \varepsilon_{zr} & \varepsilon_{zz} & 0 \\ 0 & 0 & \varepsilon_{\theta\theta} \end{bmatrix} \Rightarrow \quad \boldsymbol{\varepsilon^T} = \begin{bmatrix} \varepsilon_{rr} & \varepsilon_{zz} & 2\varepsilon_{rz} & \varepsilon_{\theta\theta} \end{bmatrix}, \tag{4.45}$$

and,

$$\boldsymbol{\sigma} = \begin{bmatrix} \sigma_{rr} & \sigma_{rz} & 0 \\ \sigma_{zr} & \sigma_{zz} & 0 \\ 0 & 0 & \sigma_{\theta\theta} \end{bmatrix} \Rightarrow \quad \boldsymbol{\sigma^T} = \begin{bmatrix} \sigma_{rr} & \sigma_{zz} & \sigma_{rz} & \sigma_{\theta\theta} \end{bmatrix} \tag{4.46}$$

Hooke's law, equation (4.36), for an axisymmetric linear elasticity is expressed in the following form:

$$\begin{bmatrix} \sigma_{rr} \\ \sigma_{zz} \\ \sigma_{rz} \\ \sigma_{\theta\theta} \end{bmatrix} = \begin{bmatrix} C_{11} & C_{12} & C_{16} & C_{13} \\ C_{21} & C_{22} & C_{26} & C_{23} \\ C_{61} & C_{62} & C_{66} & C_{63} \\ C_{31} & C_{32} & C_{36} & C_{33} \end{bmatrix} \begin{bmatrix} \varepsilon_{rr} \\ \varepsilon_{zz} \\ 2\varepsilon_{rz} \\ \varepsilon_{\theta\theta} \end{bmatrix} \tag{4.47}$$

4.4.2 Updating the Fortran 90 FE code for micro–scale anisotropy

To be able to track the evolution of micro–anisotropies over the failure surface expressed in equation (4.16), the stress should be calculated at each spatial position and each time discretization.

Each Gauss' point will be seen as a vertical borehole with a negligible diameter compared to the dimensions of the BVP simulated. The temperature change, formation pressure and effective stresses at each borehole (Gauss' point) are calculated using the balance equations of thermo–poroelasticity, see figure (4.30).

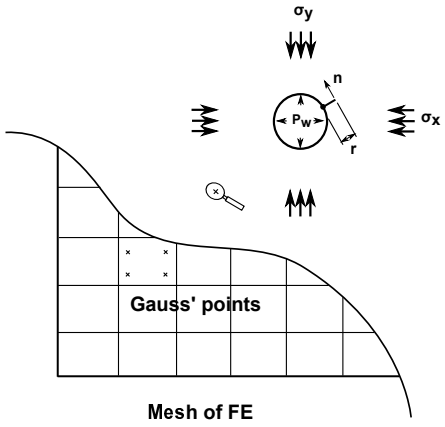

Figure 4.30: Schematic diagram which represents integrating the HFM into the FEM.

For the time discretization Δt, if the increment of effective stress is known at a definite Gauss' point, the evolution of cracks dr around this Gauss' point can be tracked as in section (4.3.1). The flow chart shown below is based on the time integration scheme of section (3.2.4),

and follows the same logarithm as in the available version of the FE code. It is only devoted to the researchers who may adjust the logarithm of the code.

- The matrix STRGS(LKS, 4) to store stress tensor is initialized. LKS is a counter for storing stress tensor, and the number 4 accounts for the 4 components of the stress tensor (in plane strain problems).
- The matrix STRGP(LKP, 4) to store permeability tensors is initialized. LKP is a counter for storing permeability tensor, and the number 4 accounts for the 4 components of the permeability tensor.
- Initial stress state, $\boldsymbol{\sigma^0}$, is stored in STRGS for LKS=1.
- Initial permeability tensor $\boldsymbol{k^0}$ is stored in STRGP for LKP=1.
- Considering the boundary and initial conditions, the Left–Hand–Side (LHS) is formed and factorized.
- (A) Beginning of the solution phase:

  1. Time is discretized and Δt for the step $n+1$ is calculated.
  2. Solving by the predictor multi–corrector method, Degrees of Freedom (DOF's) for the time step $n+1$, i.e. $\mathbb{X}^0_{n+1}$ are initialized for $i=0$.
  3. Stresses are calculated based on $\mathbb{X}^0_{n+1}$, i.e. $\boldsymbol{\sigma^0_{n+1}}$ is known.
  4. $\boldsymbol{\sigma^0_{n+1}}$ is stored in STRGS for LKS=LKS+1.
  5. The incremental stress change $\boldsymbol{\Delta\sigma^0_{n+1}}$ due to the thermo–poroelastic changes is calculated such as: $\boldsymbol{\Delta\sigma^0_{n+1}}$ =STRGS(LKS, 4)-STRGS(LKS-1, 4).
  6. Using $\boldsymbol{\sigma^0_{n+1}}$ and $\boldsymbol{\Delta\sigma^0_{n+1}}$ the permeability tensor $\boldsymbol{k^0_{n+1}}$ is calculated.
  7. $\boldsymbol{k^0_{n+1}}$ is stored in STRGP for LKP=LKP+1.
  8. Beginning of predictor multi–corrector method:

     8.1. $i=0$

     8.2. If $i=0$, first iteration in the predictor multi–corrector loop:

     - The Right–Hand–Side (RHS) matrix is formed using $\mathbb{X}^i_{n+1}$.
     - The formulation of the LHS matrix and the RHS matrix is solved to get the residual $\mathbb{R}^i_{n+\alpha}$ (it is equal to zero here).
     - The system $\mathbb{C}^*(\alpha\,\Delta\mathbb{V}) = \mathbb{R}^i_{n+\alpha}$ is solved to get $\Delta\mathbb{V}$.

     Else:

- If full Newton-Raphson method is implemented, $\mathbb{C}^*$ is updated using $\mathbb{X}^i_{n+1}$.
- The LHS matrix is updated and factorized using $\mathbb{X}^i_{n+1}$.
- The RHS matrix is formed using $\mathbb{X}^i_{n+1}$.
- The formulation of the LHS matrix and the RHS matrix is solved to get the residual $\mathbb{R}^i_{n+\alpha}$.
- The system $\mathbb{C}^*(\alpha\,\Delta\mathbb{V}) = \mathbb{R}^i_{n+\alpha}$ is solved to get $\Delta\mathbb{V}$.

Correctors are applied to get $\mathbb{X}^{i+1}_{n+1}$.

Stresses are calculated based on $\mathbb{X}^{i+1}_{n+1}$, i.e. $\boldsymbol{\sigma^{i+1}_{n+1}}$ is known.

$\boldsymbol{\sigma^{i+1}_{n+1}}$ is stored in STRGS for LKS=LKS+1.

The incremental stress change $\boldsymbol{\Delta\sigma^{i+1}_{n+1}}$ is calculated such as: $\boldsymbol{\Delta\sigma^{i+1}_{n+1}}$ =STRGS(LKS, 4)-STRGS(LKS-1, 4).

Using $\boldsymbol{\sigma^{i+1}_{n+1}}$ and $\boldsymbol{\Delta\sigma^{i+1}_{n+1}}$ the permeability tensor $\boldsymbol{k^{i+1}_{n+1}}$ is calculated.

$\boldsymbol{k^{i+1}_{n+1}}$ is stored in STRGP for LKP=LKP+1.

Convergence Test:

- If convergence is reached go to (A).
- Else, $i = i + 1$, go to 8.2.

- End

4.5 Hydraulic enhancement/stimulation: Geothermal reservoir of Soultz–Sous–Forêts

The geothermal reservoir presented in section (4.1) is to be hydraulically enhanced using the HFM and fluid circulation tests are to be simulated. Poroelastic and thermoelastic material properties are exactly as shown in Table (4.1) based on the study of (Evans et al., [2009]). Material properties for the process of HF are shown in Table (4.3).

Table 4.3: Parameters used in the application of HFM. References: 1.(Shao et al., [2005]), 2.(Atkinson, [1991], p. 245), 3.(Evans et al., [2009]) and 4.(Taron and Elsworth, [2009]).

	Parameter	Value	Reference
Elastic parameters	Elastic modulus E_0 (MPa)	54000	3
	Poisson's ratio ν_0	0.25	3
Damage parameters	Initial radius of cracks r_0 (cm)	15.0	3
	Final radius of cracks r_f (cm)	55.0	3
	Initial aperture of cracks w_0 (cm)	3.111×10^{-3}	Section (2.5.1.1)
	Material tensile strength T_c (MPa)	8.3	2
	Material toughness parameter K_{Ic} (MPa$\sqrt{\text{m}}$)	1.87	2
	Model parameter η	0.04	Parameterized
	Number of cracks N per unit volume ($\Omega = 1$ m^3)	2×10^6	1
Hydraulic connectivity parameters	t_1	0.0001	1
	t_2	1.0	1
	Initial permeability k_0 (m^2)	6.8×10^{-15}	4

The initial crack radius r_0 is determined based on the study of (Evans et al., [2009], p. 35) assuming homogeneous orientational distribution of cracks in the space. The final crack radius r_f is equal to [3-4] times r_0, the initial aperture w_0 is calculated based on the study presented in section (2.5.1.1). This combination of crack dimensional properties will give permeability components with maximum magnitude order around 10^{-11} m^2 as shown in (Evans et al., [2009], p. 79) for the enhanced reservoir.

The reservoir is initially fully permeable ($k_0 > 10^{-18}$ m^2), the excess formation pressure needed to start the HF for a temperature change of $\theta = -90$ °C is calculated using equation (4.14):

$$p_w^f = -\Big[(1-0.25)\times(2\times -38.9\times 10^6) + (1-2\times 0.25)\times 37\times 10^6 - 54000\times 10^6 \times 2.5\times 10^{-6}\times -90 - (1-0.25)\times 8.3\times 10^6\Big] = 33.93 \text{ MPa} \tag{4.48}$$

The casing shoe pressure at the injection well GPK1 should be around $(37 + 33.93 = 71)$ MPa to start the hydraulic fracturing. This magnitude is close to the values (around 65 MPa) implemented at Soultz–Sous–Forêts to start HF and to measure the minimum geologic stress at a depth of 3.7 km, (Evans et al., [2009], p. 50). The model parameter η is now determined by knowing the threshold of HF, chosen as $p_w^f = 65$ MPa. Figure (4.31) shows the FEM mesh of the upper right horizontal quarter of the reservoir to be simulated along with the initial and boundary conditions. The FEM mesh is composed of 300 Q4 elements, 10 elements in y-direction and 30 elements in x-direction.

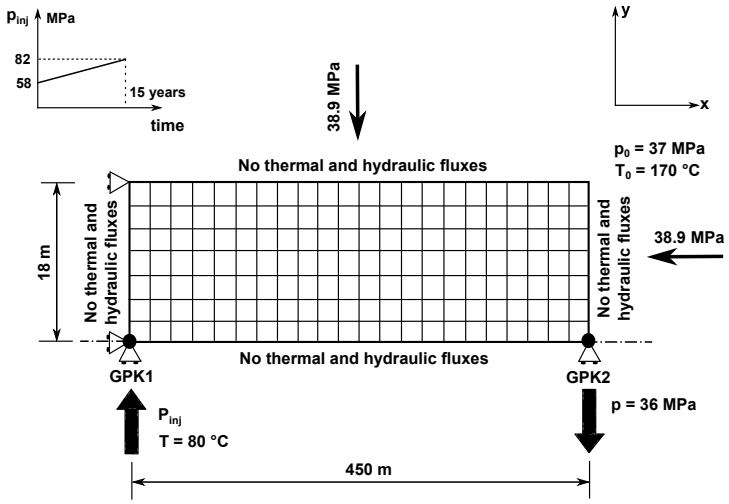

Figure 4.31: Modeling of HF process at Soultz–Sous–Forêts. Figure is not to scale.

Injection pressure is increasing at GPK1 linearly; pumping starts with 58 MPa and terminates, after 15 years, with 82 MPa. All other boundary and initial conditions are as illustrated in section (4.1). The curves of the simulations for time periods of 1, 5, 10 and 15 years with and without standing for HF are shown in the coming discussion.

The high fluid gradients near the injection well traveling mainly in y–direction cause fast cooling and bring cracks to propagate and thus permeability to increase in this direction, figures (4.32) and (4.38(a)). Since the reservoir is constrained in x and y directions due to roller displacement, near the injection well $y = x = 0$ m, cooling creates tensile stresses which mitigate geologic stresses and contribute to crack propagation in these directions, see figure (4.36). In the case when HF is utilized the distribution of effective stress is much more irregular following the preferential cooling derived by the new paths created by the HF, see figures (4.36(a)) and (4.36(c)) and compare with figures (4.34) and (4.38(a)). Formation fluid prefers to travel following the regions of high hydraulic fluxes carrying heat front right with it by convection. Thus, thermal stresses are noticed in the regions of high fluid velocity and/or enhanced permeability, again see figures (4.36(a)) and (4.36(c)) and compare with figures (4.34) and (4.38(a)).

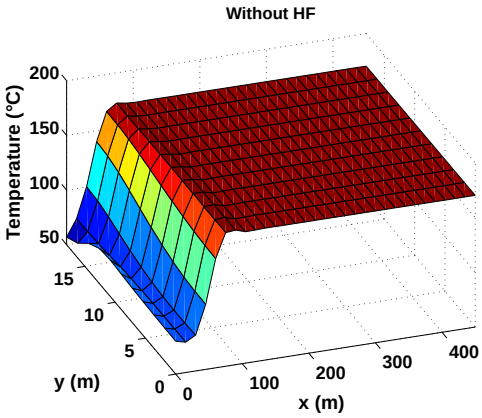

(a) Temperature contour at year 1 without HF

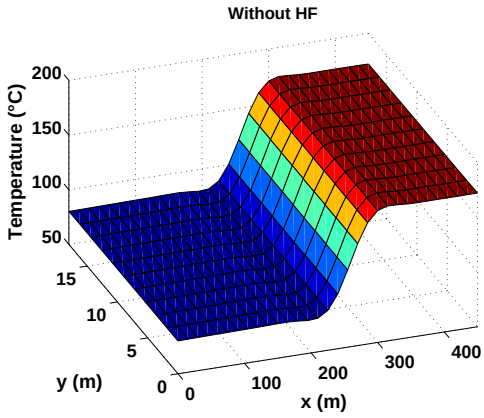

(b) Temperature contour at year 5 without HF

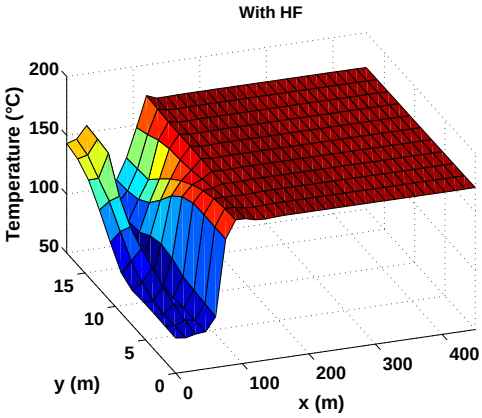

(c) Temperature contour at year 1 with HF

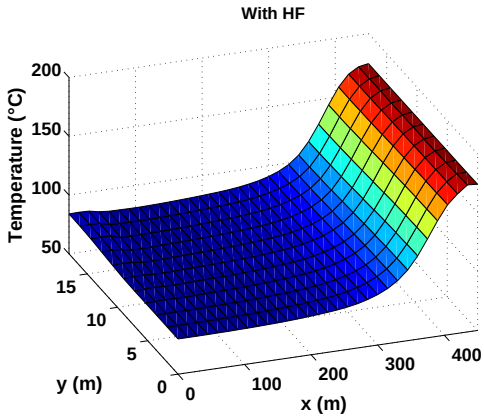

(d) Temperature contour at year 5 with HF

Figure 4.32: Contours of the mixture temperature at two times with/without HF.

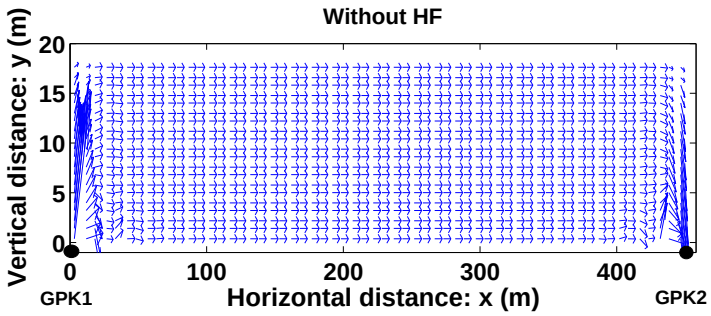

Figure 4.33: Scaled fluid velocity vectors without HF at year 1.

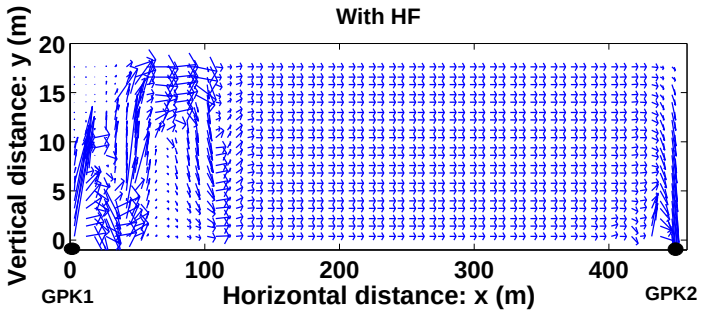

Figure 4.34: Scaled fluid velocity vectors with HF at year 1.

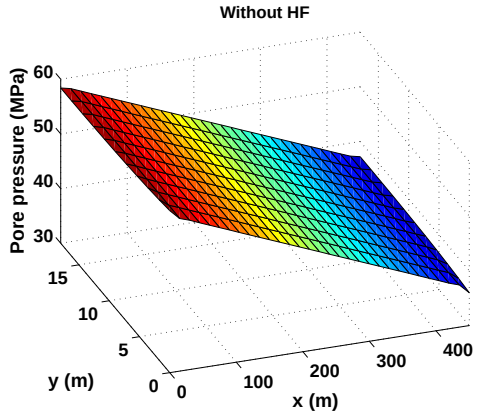

(a) Pressure contour at year 1 without HF

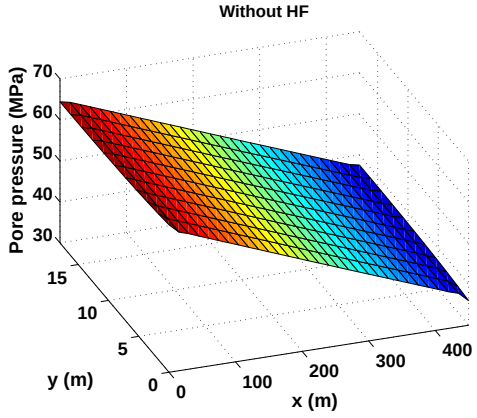

(b) Pressure contour at year 10 without HF

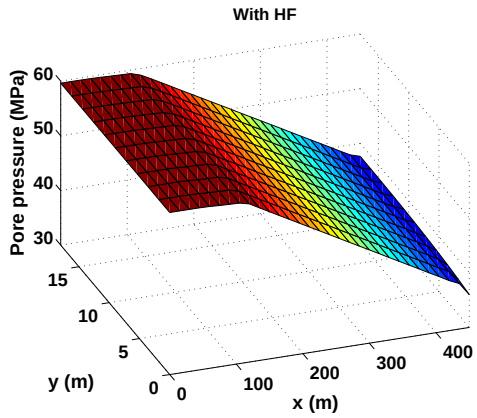

(c) Pressure contour at year 1 with HF

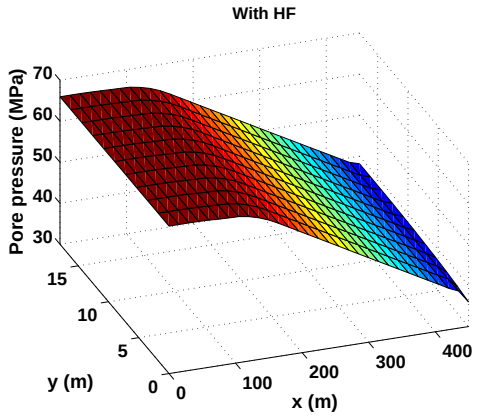

(d) Pressure contour at year 10 with HF

Figure 4.35: Contours of the formation pressure at two times with/without HF.

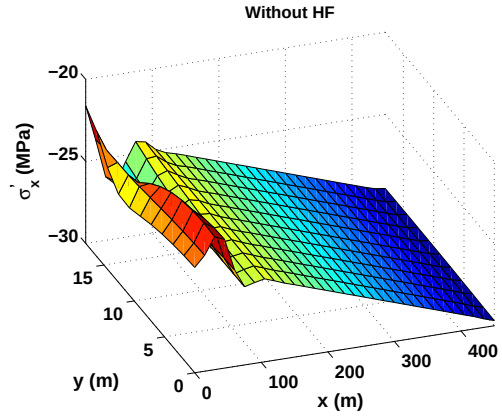

(a) Contour of $\sigma_x^{'}$ at year 1 without HF

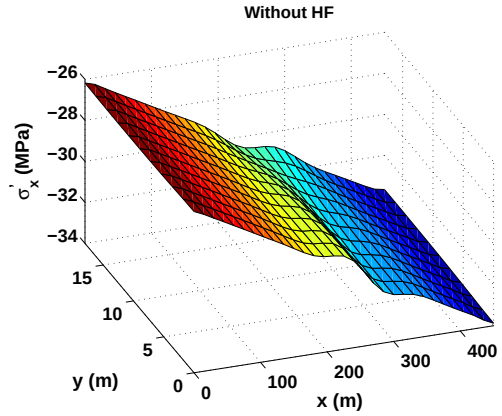

(b) Contour of $\sigma_x^{'}$ at year 5 without HF

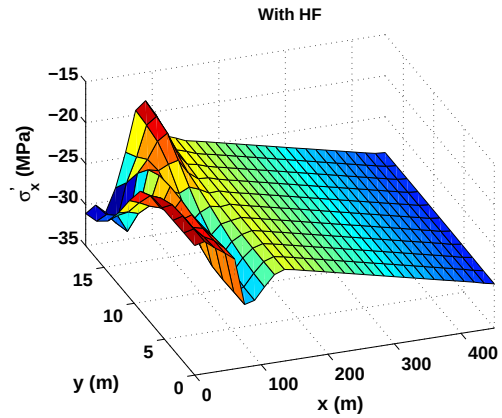

(c) Contour of $\sigma_x^{'}$ at year 1 with HF

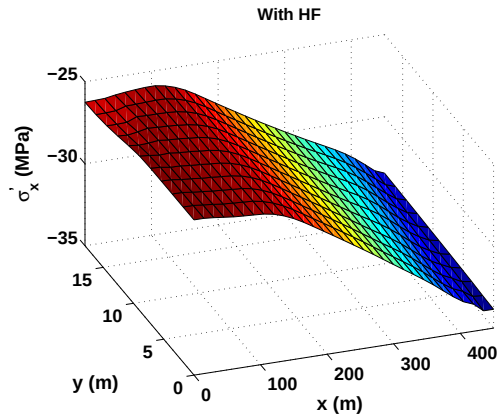

(d) Contour of $\sigma_x^{'}$ at year 5 with HF

Figure 4.36: Contours of longitudinal effective stress $\sigma_x^{'}$ at two times with/without HF.

In the regions where HF is active, formation pressure distribution tends to be uniform in the space before it starts to decline considerably in the regions of low permeability, figures (4.35(c)) and (4.35(d)). This behavior of pressure distribution was also noticed by (Lee and Ghassemi, [2010]) and (Lee and Ghassemi, [2011]). If figure (4.35) is looked at with scrutiny, it is seen that along the line $x = 0$ m, the fluid pressure is about 2 to 2.5 MPa lower in the case when HF is not utilized. This is due to the fact that fluid thermal expansion is much larger than that of the solid. Therefore when cooling, fluid phase will contract more than the solid phase and hence gaps will be formed. Consequently, fluid is to be sucked more strongly in the case of low permeability (without HF) to fill the gaps formed and to reach full saturation which leads to lower pressure values.

The process of HF requires serious pressurization capacities which, along with the permeability

enhancement, cause heat front to travel quite fast in the reservoir by convection, see figures (4.32(c)) and (4.32(d)).

Effective stresses are influenced by the heat front in the very early stages. When heat front moves away, stresses start to adopt the shape of formation pressure distributions, see figures (4.35), (4.36) and (4.37). This behavior of effective stresses was also observed by (Lee and Ghassemi, [2010]) and (Lee and Ghassemi, [2011]).

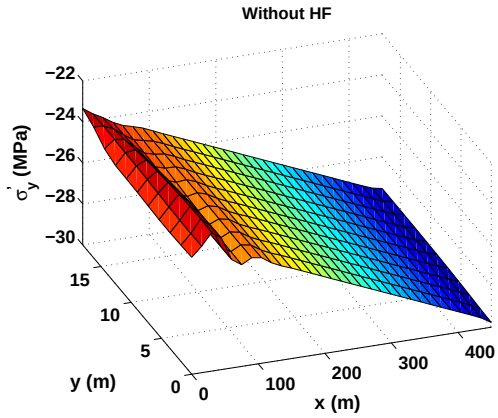

(a) Contour of $\sigma_y^{'}$ at year 1 without HF

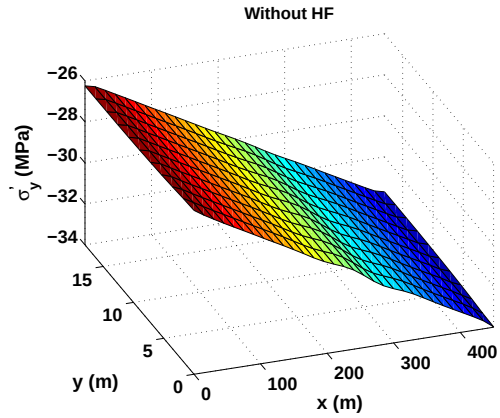

(b) Contour of $\sigma_y^{'}$ at year 5 without HF

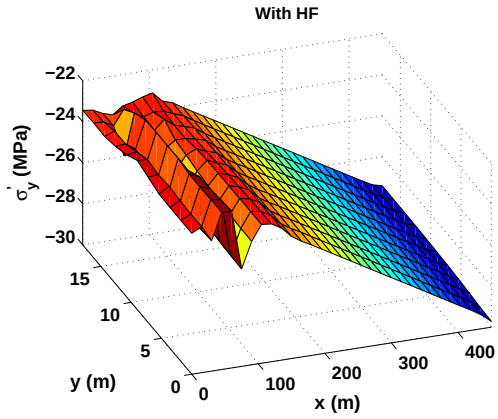

(c) Contour of $\sigma_y^{'}$ at year 1 with HF

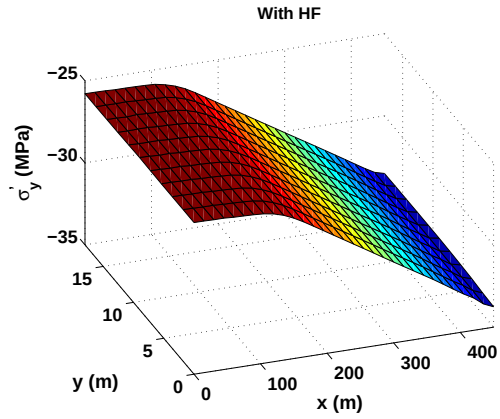

(d) Contour of $\sigma_y^{'}$ at year 5 with HF

Figure 4.37: Contours of transversal effective stress $\sigma_y^{'}$ at two times with/without HF.

Following the results of simulations, it is concluded that:

1. At the early stage of HF both the pressurization capacity as well as heat conduction and/or convection are controlling.

2. Permeability components (k_x and k_y) reach their maximum values at and very close to the injection well where changes are most extreme.

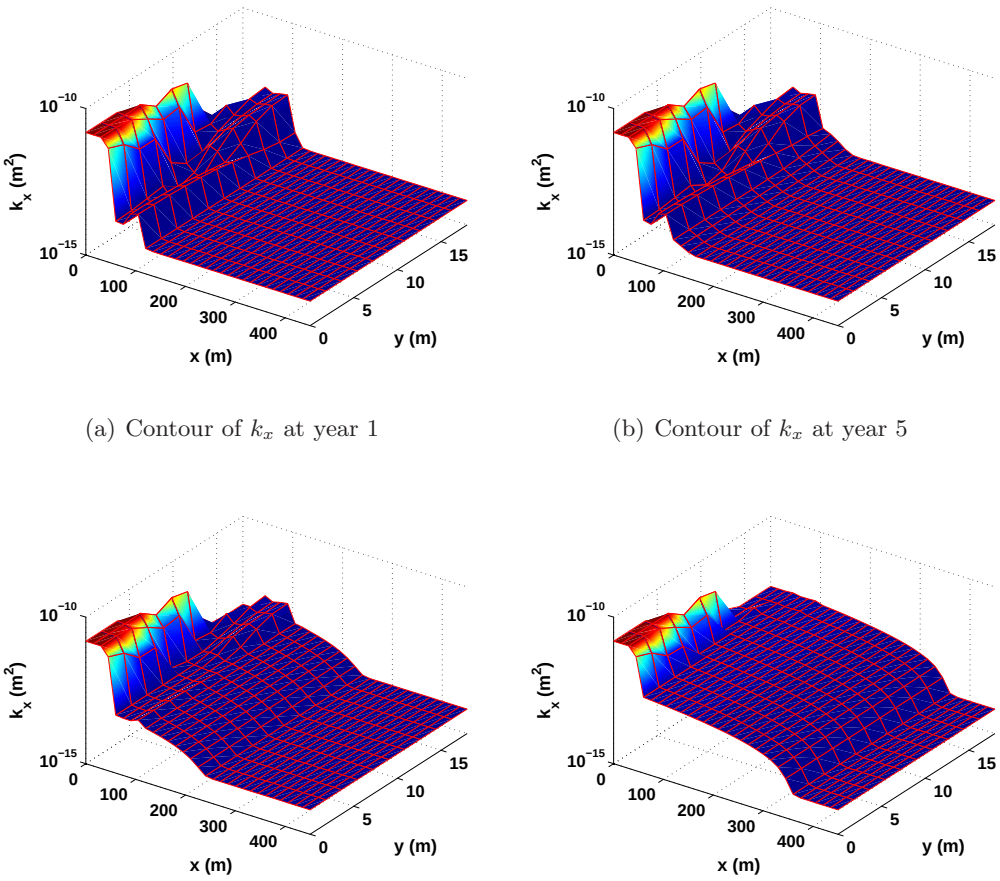

(a) Contour of k_x at year 1

(b) Contour of k_x at year 5

(c) Contour of k_x at year 10

(d) Contour of k_x at year 15

Figure 4.38: Contours of longitudinal permeability component k_x at different times during HF process.

3. High fluid gradients near the injection well, traveling mainly in y–direction, lead cracks to open and the permeability components become considerably large, see figure (4.38(a)) along the symmetry axis $x = 0$ m.

4. After 1 year of pumping, heat effects are still controlling and permeability distribution is following the zig–zag of stress distribution. Permeability components are high in the regions of low effective compressive stresses, see figures (4.36(c)), (4.37(c)) and(4.38(a)).

5. At 5 years of operation, the enhanced hydraulic system along with the high pressurizing capacities lead heat front to reach the end of the reservoir. At this point pressure gradients

are controlling the process of HF, stress surfaces are becoming similar and following the shape of formation pressure distributions.

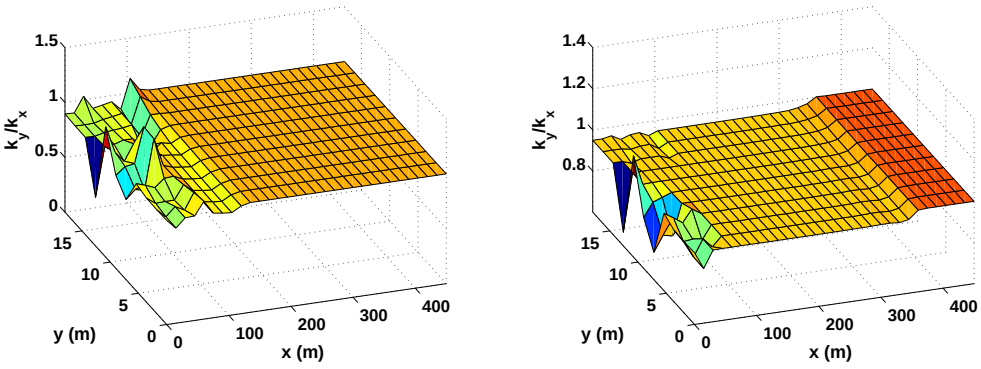

(a) Contour of the ratio k_y/k_x at year 1 (b) Contour of the ratio k_y/k_x at year 15

Figure 4.39: Contours of the ratio k_y/k_x at two times during HF process.

6. Due to the fact that only mode I of fracturing is considered in the aforementioned version of HFM, the previous conclusion wipes off the anisotropy of the permeability tensor and brings k_x to be equal to k_y since the geologic far field stresses are equal[1], see figure (4.39).

7. The only anisotropy observed in the permeability tensor remains close to the injection well and in the projection $x = 0$ m. This is due to the high fluid gradients causing preferential growth of cracks, see figure (4.39(b)).

8. The anisotropy ratio of the permeability tensor components remains in the range [0.4, 2.5] as observed by (Schulze et al., [2001]).

Check appendix (B.1) to understand the role of the fracture toughness K_{Ic} in the process of HF in weak rock formations.

[1]More details about this behavior along with a more sophisticated fracturing model which accounts for mode I and II of crack propagation are presented in chapter (5).

4.6 Stresses around boreholes and borehole stability

This section is consecrated to study the stability of wellbores under shearing effects. The section proceeds as follows; the hollow cylinder model is firstly employed to provide a full solution for the expressions of stress distributions around the borehole. Secondly, Mohr–Coulomb criterion is adopted to express the failure criteria for boreholes under extreme shearing effects.

4.6.1 Stresses around boreholes: The hollow cylinder model

The hollow cylinder model, figure (4.40), is commonly used to describe the stability of boreholes in a stressed formation. This model provides a perception for vertical wells where the horizontal far field stresses are equal.

The hollow cylinder has a full rotational symmetry around its axis and a full translational symmetry along the same axis. The cylinder is loaded with the vertical stress σ_v. The expressions for the stresses in the cylinder are to be derived while it is loaded with internal pressure p_w and external stress σ_h. The external stresses acting on the cylinder are all the time in the direction of the normal to the surface and independent of angular position θ and vertical location z.

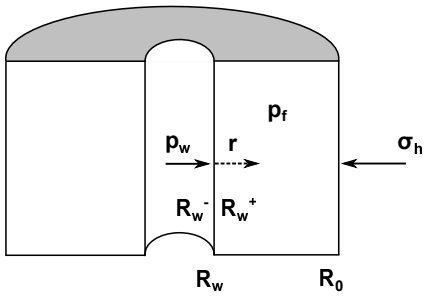

Figure 4.40: Section of the hollow cylinder model, p_w is the borehole pressure and p_f is the formation pore pressure. In the presence of a mud cake $p_f(R_w^+) \neq p_w$, meanwhile if well and formation fluids are fully connected $p_f(R_w^+) = p_f(R_w^-) = p_w$ (rigorous assumption).

If the cylinder is sufficiently long, the only significant deformation will be in the radial direction. Thus, the model will be in the horizontal plane in plane–strain. By ignoring the body forces and by applying the well conditions $R_0 >> R_w$, (Fjaer et al., [2008], p. 139) solved the equations of equilibrium while assuming uniform (in space) fluid formation pressure p_f to reach the following system:

$$\begin{aligned} \sigma_r &= \left(1 - \frac{R_w^2}{r^2}\right) \sigma_h - \frac{R_w^2}{r^2} p_w \\ \sigma_\theta &= \left(1 + \frac{R_w^2}{r^2}\right) \sigma_h + \frac{R_w^2}{r^2} p_w \\ \sigma_z &= \text{constant} \end{aligned} \tag{4.49}$$

Figure (4.41) shows the distribution of stresses around a borehole as expected by the hollow cylinder model. It is seen that stresses increase near the borehole (the inhomogeneity) above the far field stress, this phenomenon is called *stress concentration*.

Unless perfectly lined mud cake is achieved, implementing the assumption of uniform formation pressure is erroneous and does not represent the actual situation taking place in the EGS. Indeed pumping cold water in the well will cause poro–thermoelastic changes.

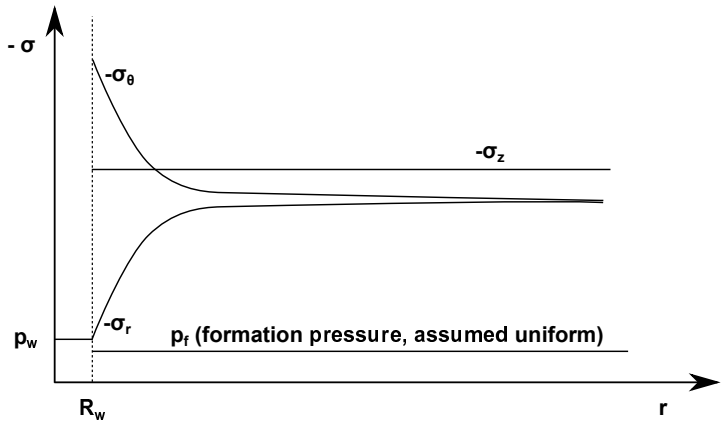

Figure 4.41: Stresses around a borehole in linear elastic formation, compressive stresses are negative. σ_r is always compressive, meanwhile σ_θ could be compressive or tensile depending on p_w.

(Fjaer et al., [2008], p. 141) provided full solution for the expressions of stress distributions around the borehole *while considering varying pore pressure*. In this research we are concerned with stresses on borehole wall ($r = R_w$) as we study the stability of these boreholes. The expressions of stress distributions on the borehole wall of figure (4.40) while assuming varying formation pressure take the form:

$$\begin{aligned} \sigma_r &= -p_w \\ \sigma_\theta &= 2\sigma_h + p_w + 2\varkappa\big(p_{f0} - p_f(R_w^+)\big) - \underbrace{\frac{E\,\alpha_s\,\theta}{3(1-\nu)}}_{\text{Thermal stress part}} \\ \sigma_z &= \sigma_v + 2\varkappa\big(p_{f0} - p_f(R_w^+)\big) - \underbrace{\frac{E\,\alpha_s\,\theta}{3(1-\nu)}}_{\text{Thermal stress part}} \end{aligned} \tag{4.50}$$

$\varkappa$ is the poroelastic stress coefficient defined using Biot's coefficient κ as:

$$\varkappa = \frac{1-2\nu}{2(1-\nu)}\,\kappa \tag{4.51}$$

p_{f0} is the far field formation pressure and $p_f(R_w^+)$ is the formation (reservoir) fluid pressure just at the outer wellbore wall, figure (4.40). If well fluid and the formation fluid are connected, $p_f(R_w^+)$ is equal to p_w. In the presence a mud cake, $p_f(R_w^+)$ is equal to the formation pressure just behind the mud cake.

Equation (4.50) can be explained as follows: if the reservoir pressure is getting increased $p_f(R_w^+) > p_{f0}$, this indicates that water is being pumped into the formation, material is expanding and stresses are increasing in compression. If on the other hand water is being sucked from the formation, formation pressure is decreasing $p_f(R_w^+) < p_{f0}$, material is relaxing and thus stresses are decreasing in compression which normally happens at the production wells. Refer to section (4.2.2.3) to understand the role of the thermal stress part.

4.6.2 Borehole shear failure criteria

The theme of HF process is to cause fractures at the casing shoe of a wellbore to propagate by pumping geothermal fluids with extremely high pressures. Subsequently, HF is synonymous to borehole tensile failure. It is conceivable that with such high pressures at the shoes of wellbores, they are not likely to fail under shearing effects. The research presented below for shear failure of wellbores is highlighted just to provide a full perspective for borehole failure.

The shear failure of a borehole is reached when the deviation of effective stresses around the borehole, due to the change in fluid pressures between the borehole and the formation, exceeds the failure criterion of the rock. Borehole shear failure is demonstrated by rock deformations which are not necessarily dramatic from an operational point of view; borehole shear failure does not mean a lost well, (Fjaer et al., [2008]).

Let us start with a vertical borehole with uniform formation pressure and anisotropic far field stresses. The assumption that the formation pressure is uniform is only reached if the wellbore walls are lined with perfect mud cake. This approach gives an approximation about the range of stress deviation at failure. Nevertheless, a changing formation pressure is to be considered for more realistic research.

As was stated previously, for a linearly elastic material the largest changes in stress states occur at the borehole wall. For uniform formation pressure, the system of equations (4.50) modifies to (Fjaer et al., [2008]):

$$\begin{aligned} \sigma_r &= -p_w \\ \sigma_\theta &= \sigma_H + \sigma_h - 2(\sigma_H - \sigma_h)\cos 2\theta + p_w - \frac{E\,\alpha_s\,\theta}{3(1-\nu)} \\ \sigma_z &= \sigma_v - 2\,\nu(\sigma_H - \sigma_h)\cos 2\theta - \frac{E\,\alpha_s\,\theta}{3(1-\nu)} \end{aligned} \tag{4.52}$$

σ_H is the maximum far field compressive stress, σ_h is the minimum far field compressive stress and θ, as an orientation, is measured relative to the direction of major horizontal stress (σ_H). There are several stress states under which the borehole is expected to fail, yet the most common practical stress states are observed for the principal stress magnitudes corresponding to $-\sigma_\theta > -\sigma_z > -\sigma_r$ and $-\sigma_z > -\sigma_\theta > -\sigma_r$. In the aforementioned two cases $-\sigma_r$ is always the smallest principal stress. Hence, if the formation pressure and temperature change such that $-\sigma_r$ is lowered to a point it becomes the smallest principal stress in the system (4.52), shear failure of the borehole becomes quite possible.

Let us consider the first stress state where $-\sigma_\theta$ is the largest principal stress. According to the failure criterion of Mohr–Coulomb, failure occurs when:

$$-\sigma_\theta^{'} = C_0 - \sigma_r^{'}\,\tan^2(\beta) \tag{4.53}$$

C_0 is the uniaxial compressive strength of the material. β can be defined following the expression shown in equation (4.54):

$$2\beta = \phi + \frac{\pi}{2} \tag{4.54}$$

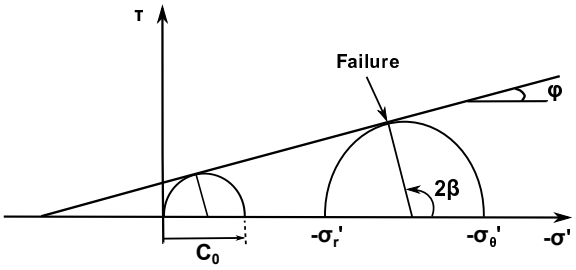

Figure 4.42: Sketch of Mohr-Coulomb criterion, equation (4.53), the angle of the straight line ϕ is "the angle of friction". C_0 is the uniaxial compressive strength of the material. The angle β represents the orientation of failure plane.

β is the angle for which failure criterion is fulfilled, it gives the orientation of the failure plane, see figure (4.42). Since the friction angle ϕ is centered around 30°, β is centered around 60° and thus $\tan^2(\beta) = 3$ generally, (Fjaer et al., [2008], p. 156).

The failure criterion for borehole when $-\sigma_\theta > -\sigma_z > -\sigma_r$ is calculated by substituting the system[1] (4.52) in equation (4.53):

$$p_{w,\min} = p_f + \frac{-3\sigma_H + \sigma_h - 2p_f - C_0}{1 + \tan^2(\beta)} + \frac{E\,\alpha_s\,\theta}{3\left(1 + \tan^2(\beta)\right)(1-\nu)} \tag{4.55}$$

Similarly for the case when $-\sigma_z > -\sigma_\theta > -\sigma_r$, the failure criterion reads:

$$p_{w,\min} = p_f + \frac{-\sigma_v - 2\nu(\sigma_H - \sigma_h) - p_f - C_0}{\tan^2(\beta)} + \frac{E\,\alpha_s\,\theta}{3\,\tan^2(\beta)(1-\nu)} \tag{4.56}$$

Practically, one needs to calculate the value of the minimum borehole pressure using equations (4.55) and (4.56). If the value of p_w applied is lower than the lowest value calculated, shear failure will occur at the borehole wall.

Since the HF process is achieved by increasing borehole pressure p_w to a point where σ'_θ becomes positive (tensile), the borehole is not likely to fail under shear. The failure of the borehole under tension (Hydraulic fracturing, section (4.2.2.1)) is the theme of this research. The value of borehole pressure p_w^f to start HF is calculated using equations (4.8), (4.9), (4.13) or (4.14) whichever applies.

We now apply the conditions addressed in equations (4.55) and (4.56) on the BVP presented in section (4.3) while keeping in mind that for granite, generally, (friction angle $\phi \approx 30°$, failure angle $\beta \approx 60°$, and compressive strength $C_0 \approx 180$ MPa). The vertical burden stress corresponding to 3.7 km depth is $\sigma_v \approx -80$ MPa. Equation (4.55) gives:

$$\begin{aligned} p_{w,\min} = 37 \times 10^6 + \frac{-2 \times -38.9 \times 10^6 - 2 \times 37 \times 10^6 - 180 \times 10^6}{1+3} + \\ + \frac{54 \times 10^9 \times 7.5 \times 10^{-6} \times -90}{3 \times 4 \times 0.75} = -11.1 \text{ MPa}, \end{aligned} \tag{4.57}$$

while equation (4.56) gives:

$$\begin{aligned} p_{w,\min} = 37 \times 10^6 + \frac{80 \times 10^6 - \times 37 \times 10^6 - 180 \times 10^6}{3} + \\ + \frac{54 \times 10^9 \times 7.5 \times 10^{-6} \times -90}{3 \times 3 \times 0.75} = -14.07 \text{ MPa} \end{aligned} \tag{4.58}$$

[1] The most critical cases defined previously, i.e. $\sigma_{\theta,\max}$ and $\sigma_{v,\max}$ are to be considered.

Conditions of borehole shear failure give $p_{w,\min} < 0.0$. As expected, based on the boundary and initial conditions addressed in figure (4.31), the borehole (GPK1) is not likely to fail in shear but rather in tension due to the process of HF and as p_w gets closer to 65 MPa, see section (4.3).

4. SIMULATIONS OF HEAT EXTRACTION FROM NATURAL AND ENHANCED HDR RESERVOIRS BY HYDRAULIC FRACTURING

Chapter 5

Designing HDR reservoirs: Impedance, efficiency, fracturing modes and life–time

Chapter (4) provided a general view about simulations of heat extraction from geothermal reservoirs with and/or without considering permeability enhancement using the process of HF. The fracturing model presented in section (4.3) has been worked such that an anisotropic permeability tensor is calculated at each Gauss' point and at each step of time discretization. This fracturing model accounted only for mode I of fracturing and was integrated in the simulations of the HDR reservoir presented in section (4.1). The last section of chapter (4) addressed the stability of boreholes against shear failure.

More sophisticated numerical studies, in terms of boundary and initial conditions, are presented in this chapter. Field data from several references are also collected to validate the numerical simulations. Designing parameters of an efficient HDR reservoir are addressed along with the usefulness of the process of HF in terms of creating a worthy reservoir. Brines commonly used in running geothermal reservoirs are studied with the possibility of viscosity–temperature change. A brief insight into using carbon dioxide (CO_2) as a geothermal fluid is simply presented following the studies of (Ueda et al., [2005]), (Pruess, [2006]) and (Pruess, [2008]).

A spot of light is shed on improving the fracturing model of section (4.3) to account for a combination of mode I and mode II of fracturing. The new fracturing model is inserted in our FE code where results of different simulations, for the same reservoir, are systematically compared for the cases when HF is/is not accounted for.

While this work is devoted to hydro–mechanical improvements of permeability through HF, the last section of this chapter gives a brief discussion about the chemical enhancement of geothermal reservoirs: a potential alternative or conjugate tool to establish an acceptable fluid flow through HDR reservoirs.

5.1 Designing and modelling of a prototype HDR reservoir

A key criterion in designing HDR projects is the definition of boreholes locations. The location of boreholes is a problem of optimization as it must balance two opposing effects. Low hydraulic impedances and fluid losses could be easily achieved when boreholes are not very far from each other. On the other hand, large reservoir areas mean long thermal operating life and hence improved economical performance, (Bruel, [1995]).

5.1.1 Well testing and hydraulic parameters

EGS are always run under high pressure values where it is almost impossible to assume constant permeability and porosity of the formation. Permeability of EGS is actually pressure dependent often varying by several order of magnitudes from the depressurized situation.

5.1.1.1 Reservoir impedance

An important operational parameter of a geothermal reservoir is the *flow impedance* Z, defined as the pressure (Pa) needed to cause a unit flow rate (m^3/s) through the reservoir. It can be calculated as the difference between the injection and the production wellhead pressures divided by the produced flow rate. The impedance should be smaller than, say $Z < 1000$ MPa s/m^3, if the power required to pump water through the reservoir is not to exceed a substantial fraction of the power produced by the reservoir, (Murphy et al., [1999]).

Figure (5.1) shows a schematic diagram of an HDR reservoir power generating system. As defined in the figure, the impedance of HDR power generating system includes that of both wellbores in addition to that of the reservoir. The impedance of wellbores is comprised of two parts; 1) the frictional resistance to flow in order of 0.004 MPa s/m^3 for injection and production at 10 l/s in 0.2 m diameter wells at 3 km deep, and 2) impedance resulting from the thermo–siphon derived by the deep column of cold dense water in the injection well and hot light water in the production well. This thermo–siphon helps gaining some pressure head. Yet, this gain is usually less than 1 MPa meanwhile the pressure loss in the reservoir is usually several times greater, (Murphy et al., [1999]).

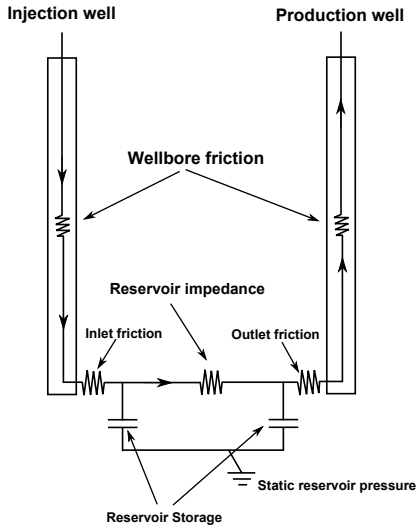

Figure 5.1: Schematic diagram of HDR power generating system, (Murphy et al., [1999]).

In fact, the major part of the reservoir impedance stems from the reservoir itself. The turbulent flow in the reservoir fractures leads to pressure–dependent fracture dilation which normally results in non–linear relation between pressure and flow, (Grecksch et al., [2003]). At the Fenton Hill HDR reservoir the impedance decreased with an increasing level of reservoir pressurization, i.e. at higher flow rates, (Murphy et al., [1999]).

Following figure (5.1), the impedance of an HDR reservoir is to be thought of as having three components. The inlet impedance near the injection well where streamlines concentrate leading to high fluid velocities which result in very turbulent flow. This turbulent flow results in high pressure losses. However, since injection wells normally operate at considerable high pressures, the fracture dilation will lead to some hydraulic connection which offsets the high pressure loss by steering the flow in the direction of fracture evolution. The second component is referred to as reservoir major impedance: at this point streamlines have diverged and fluid velocity becomes almost homogeneous and small, therefore pressure losses may be surprisingly small despite the longer flowpath lengths in the main reservoir. The third component is the outlet impedance near the production well: streamlines converge at this point giving high fluid velocities and extremely turbulent flow. Pressure losses at the production well are serious and greater than those at the injection well. These losses stem from maintaining the production well at lower pressure which result in tightly closed fractures in its vicinity. It turns out that most of the reservoir impedance emits from the production well. Consequently, greater heat production can be garnered from larger reservoirs with greater spacing between injection and production wells without suffering significant impedance increase, (Bruel, [1995]).

Though it seems very complicated to control the impedance of an engineered geothermal reservoir, almost all of the reservoirs created to date have values of $Z < 1000$ MPa s/m^3. Not to forget that reservoirs can be hydraulically manipulated and stimulated to provide the impedance that the operator desires. The ambitious goal of $Z < 100$ MPa s/m^3 is yet to be achieved on a consistent basis, (Murphy et al., [1999]).

(Murphy et al., [1999]) have shown that with time the engineered reservoir flow paths become more diffuse with the longer residence–time paths taking progressively more of the total flow. In addition, field experiments have proven that as the inlet region is progressively cooled, additional flow paths open up and manifold with the previous less-accessible paths (effects of thermal strains, see section (4.2.2.3)).

5.1.1.2 Reservoir water loss

Water loss is an important factor when stimulating EGS. Water losses could be a serious factor where there exists a risk of provoking a damaging earthquake by elevated pore pressure. Other than this risk, water loss is not a serious problem except for the regions where fresh water is not available. It is not recommended to pump ocean/salt water to avoid uncontrolled geochemical reactions.

(Murphy et al., [1999]) have stated three principal components for water losses in an engineered geothermal reservoir. Not all these components are operational for all reservoirs, nor for all times during development and subsequent operations of a particular reservoir. Nevertheless, they help in understanding water loss behavior:

1. Water loss from the periphery of a pressurized reservoir by pressure diffusion through the rock surrounding the pressure dilated reservoir region.

2. Apparent water loss due to water storage in an expanding engineered reservoir. A large part of this stored water could be recovered ultimately when the reservoir is depressurized.

3. Water loss due to flowing into geological faults and fractures which intersect or are intersected by the engineered reservoir.

Operational techniques should compromise between raising pressure and therefore reducing impedance or lowering pressure and hence low water loss. Operating conditions depend upon the site conditions; if water is plentiful, the operator may decide to increase the pressure thus reducing impedance and energy production. If water is scarce, an operator may reduce the pressure thus reducing water loss and accepting higher impedance and lower energy production rate.

5.1.2 Modelling approaches for HDR reservoirs

The presence of natural fractures and faults of various lengths renders HDR reservoirs very heterogeneous. As a result, the choice of a representative volume to model the HDR reservoir is a difficult task and information about every individual fracture is required to reach the so called *near field* models. Generally HDR reservoirs are modeled using two approaches (Bruel, [1995]):

1. HDR reservoirs are assumed to be formed of spherical connected permeable zones. Thermal recovery is calculated using dimensionless parameters via Maxwell analogy, see (Elsworth, [1989]) for more details. This is an averaging approach which may not be valid if the fractures are not fully connected or if they are not evenly distributed in space, which is certainly the case in real HDR reservoirs.

2. Models emerging from the statistics describing the pre–existing fractured system. Such approaches include discrete fracture models which include the major structures governing the flow. However, detailed data sets and relevant parameters are quite difficult to extract from the field.

The second approach is the model adopted so far in simulating thermal recovery from HDR reservoirs. Unless stated, this approach will be used all along this research as well.

The distance between HDR reservoir wellbores is to be estimated considering that the reservoir is to meet the required thermal performance objectives. These thermal objectives were defined in the work of (Jupe et al., [1995]) by thermal performance of 10% thermal drawdown, or less, during 10–year circulation at 15 l/s production. Thermal drawdown $\mathcal{T}_{\mathcal{D}}$ is defined as the relative difference between initial temperature of the reservoir T_0 and production temperature T:

$$\mathcal{T}_{\mathcal{D}} = \frac{T_0 - T}{T_0} \tag{5.1}$$

5.1.2.1 Reservoir design parameters

Having determined performance criteria of an HDR, the objectives of the design are firstly to define the reservoir parameters (e.g. reservoir temperature) needed to achieve this performance, and secondly, to inspect the engineering operations (e.g. wellbores drilling) needed to achieve the design and to manipulate the reservoir performance.

(Jupe et al., [1995]) have divided the modelling studies of an HDR into three components, Table (5.1): the drilling and the completion of injection and production boreholes, the stimulation of the reservoir using high flowrates, and the behavior during long term circulation of the system.

Table 5.1: Key reservoir design parameters, (Jupe et al., [1995]).

Component	Reservoir parameter	Engineering control
Borehole configuration	Reservoir temperature Fracture intersection-frequency and orientation Reservoir volume	Depth Separation Trajectory Number of boreholes Open–hole length
Stimulation	Reservoir volume Growth direction Permeability enhancement Near wellbore impedance	Stimulation flow rate Fluid volume Fluid viscosity Proppants
Circulation	Heat exchange surface area Heat extraction volume Impedance Water loss Thermal drawdown	Circulation direction Flow rate Production well pressure Downhole pump deployment

Many of the reservoir parameters such as: reservoir volume, heat exchange area and growth direction are mainly dependent on the existing fracture networks and their interaction with the *in situ* stress state. A sophisticated model which is capable of implementing complex coupled processes is therefore needed to encompass all aspects of reservoir creation and circulation.

5.1.2.2 Exploitation of large scale hydraulic features

Experimental investigations at Soultz–Sous–Forêts HDR reservoir site have emphasized the existence of large scale fractured zones (>100 m) at depths 2850 to 3500 m. These fractured zones are characterized by their high storage capacity[1] but low productivity, (Jupe et al., [1995]). These natural conductive zones can play a very significant role in exploiting HDR reservoirs considering that a relatively little permeability enhancement is required to achieve low impedance and good productivity of the system. Figure (5.2) shows a schematic representation for the thermal exploitation of isolated large scale conductive fractured zone.

The general fracture pattern at Soultz–Sous–Forêts consists of two main strike directions at N10–E20 and N170.

[1]Storage capacity of a fracture can be defined as how much volume a fracture can provide to store fluid.

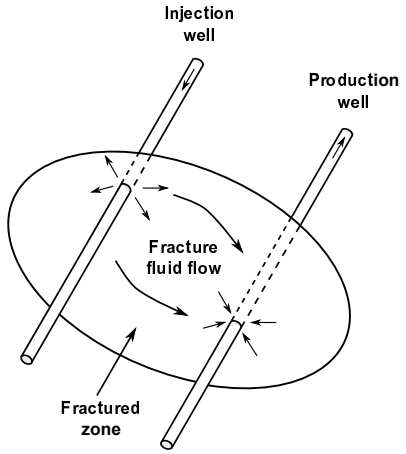

Figure 5.2: Schematic representation of an HDR reservoir design, based on the exploitation of isolated large scale conductive fractured zones.

In situ stress measurements have indicated that stress amplitudes (MPa) for depths (2000–3500 m) can be estimated by the following linear relationships, z (m) is the depth, see (Bruel, [1995]):

$$\begin{array}{lrcl} \text{Minimum horizontal stress:} & -\sigma_h & = & 48.0 + 0.014(z - 3600) \\ \text{Maximum horizontal stress:} & -\sigma_H & = & 0.026z \\ \text{Vertical stress:} & -\sigma_v & = & 0.026z \end{array} \tag{5.2}$$

Stress amplitudes given by the system of equations (5.2) are almost the same as shown for Soultz–Sous–Forêts HDR reservoir in (Evans et al., [2009], p. 37–44). Experimental evidences have proven that the maximum horizontal stress σ_H is oriented in the N170 direction (which is the direction of the fracture pattern).

5.2 Stimulation tests of Soultz–Sous–Forêts HDR reservoir: Phase 1 injection test at GPK1

This section is devoted to study and imitate the phase 1 injection test at GPK1 well of Soultz–Sous–Forêts HDR reservoir. This injection test included pumping high pressurized fluid which led to permeability enhancement as well as a microseismic record. The works of (Bruel, [1995]) and (Jupe et al., [1995]) have fairly addressed this stimulation test and shall be used as a guiding reference for our simulations. This section proceeds as follows; the flow logging at well GPK1 during phase 1 injection test and for 17 days is first simulated using our FE code with the HFM of section (4.3). The time of the simulations is then extended to study the permeability enhancement of the whole reservoir using the process of HF.

5.2.1 Phase 1 injection test at GPK1 well, 1993: Simulating the flow history

In 1993 a stimulation test of GPK1 well, between 2800 m and 3500 m, at Soultz–Sous–Forêts HDR reservoir was conducted. Pressurized fluid led to fracture evolution which in–return generated seismic energy. The spatial distribution of the induced seismic events can be related to the propagation of the fluid pressure front. Roughly, seismic networks can delineate and constrain good estimates of the rock volume affected by the pressurized fluid.

The general shape of the recorded microseismic events at Soultz–Sous–Forêts HDR reservoir shows a dense cloud at 2850 m depth in the horizontal plane. The microseismic cloud extends mainly in the direction of the maximum far field horizontal stress σ_H i.e. N170, see figure (5.3), (Bruel, [1995], p. 442).

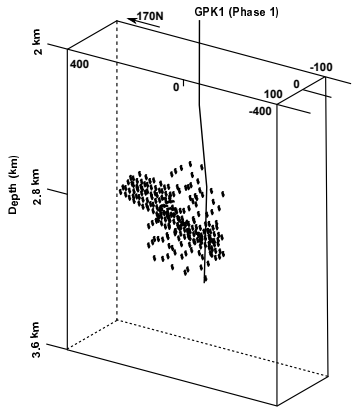

Figure 5.3: Summary of microseismic event locations from the 1993 phase 1 stimulation test, (Bruel, [1995]).

5.2.1.1 The transient BVP: Geometry, material properties and FEM mesh

Based on the seismic event locations presented in (Bruel, [1995], Fig. 2) and based on the study given by (Baumgärtner et al., [2000], p. 268), the fractured zone to be stimulated lies at a depth of 2.8 to 2.9 km and has dimensions of 1 km and 400 m around the well GPK1 with N170 Azimuth and W70 Dip.

The second well GPK2 is drilled 400–500 m away from GPK1 and in the direction of fracture evolution (seismic events), see (Baumgärtner et al., [2000], Fig. 1). The fractured zone to be stimulated is shown in figure (5.4).

The values of *in situ* stresses were calculated using the system of equations (5.2) for $z = 2.8$ km. The initial pressure p_0 and the initial temperature T_0 also correspond to a typical depth

of 2.8 km, (Evans et al., [2009]) and (Bruel, [1995]). A temperature of $T = 50$ °C is applied at the injection well, the temperature at the outlet production well GPK2, 500 m away, is sought. All the other boundaries are thermally insulated, i.e. no thermal fluxes are permitted with the surroundings.

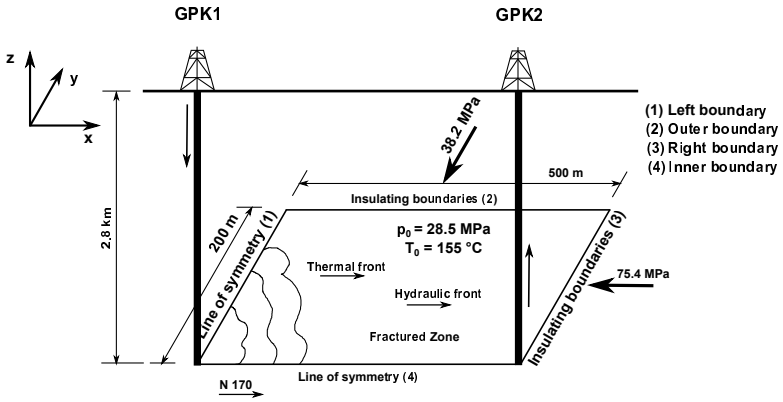

Figure 5.4: Geometric layout of the fractured zone to be stimulated at the HDR reservoir of Soultz–Sous–Forêts. GPK2 is drilled in the direction of fracture evolution. Only quarter of the problem is to be studied due to symmetry.

Production pressure is fixed to $p_0 - 1$ MPa, injection pressure/flux is to be applied corresponding to the purpose of intended simulation, other boundaries are hydraulically insulated from the surroundings. The mechanical boundary conditions are defined by the *in situ* stresses applied at the outer and right boundaries, the inner boundary is constrained in y-direction, meanwhile the left boundary is constrained in x-direction (roller displacement), see figure (5.5).

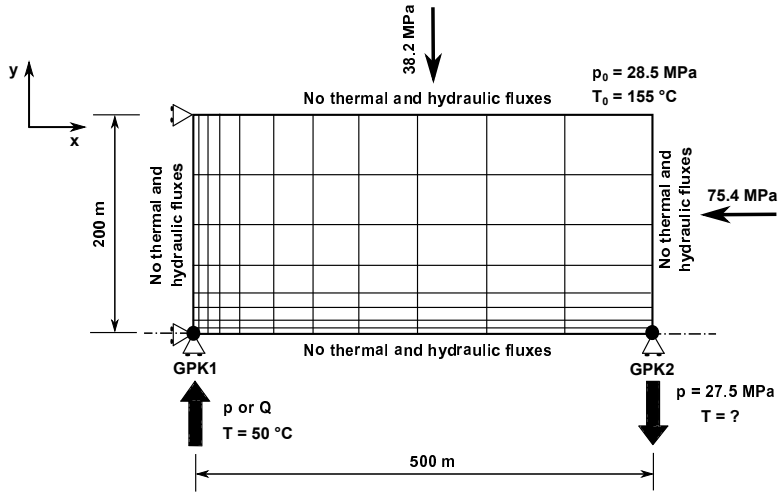

Figure 5.5: Modeling of the phase 1 injection test at Soultz–Sous–Forêts: simulating the flow logging at GPK1, figure is not to scale.

These *in situ* stresses are applied at $t = 0^-$ and allowed to equilibrate with the initial pore pressure of 28.5 MPa. The effective stresses over the geologic times give an *in situ* permeability

of $k_0 = 2.85 \times 10^{-14}$ m^2, (Bruel, [1995], Fig. 5)[1]. Table (5.2) summarizes all the boundary conditions used in the stimulation process.

Table 5.2: Boundary conditions used for the stimulation test at Soultz–Sous–Forêts. l=left, r=right, o=outer, and i=inner boundaries of figure (5.5).

Type	Boundary	Condition
Displacements	l	No horizontal displacement
	i	No vertical displacement
	r and o	Calculated based on the stresses applied
Fluid flow	l, i, r and o	Impermeable
	Injection well	Pore fluid pressure or fluid fluxes
	Production well	Pore fluid pressure ($p = p_0 - 1$ MPa)
Heat flow	l, i, r and o	Thermally insulated
	Injection well	$T = 50$ °C
	Production well	Temperature is sought

The material properties of Soultz–Sous–Forêts reservoir are shown in Table (5.3). These thermo–poroelastic properties are typical for Soultz–Sous–Forêts reservoir rock as shown by (Evans et al., [2009]).

Table 5.3: Material properties of Soultz–Sous–Forêts reservoir.

Property	Value
Drained Young's modulus E	54×10^9 (Pa)
Drained Poisson's ratio ν	0.25
Bulk modulus of solid grains K_s	50×10^9 (Pa)
Bulk modulus of fluid K_f	2.2×10^9 (Pa)
Dynamic viscosity of the fluid μ	3×10^{-4} (Pa.s)
Porosity ϕ	0.1003
Initial permeability k_0	2.85×10^{-14} (m^2)
Solid thermal conductivity χ_s	2.49 (W/m°C)
Fluid thermal conductivity χ_f	0.6 (W/m°C)
Solid heat capacity at constant volume c_{vs}	1000 (J/kg °C)
Fluid heat capacity at constant volume c_{vf}	4200 (J/kg °C)
Density of solid ρ_s	2910.2 (kg/m^3)
Unit weight of water γ_f	9800 (N/m^3)
Volumetric thermal expansion of the solid α_s	7.5×10^{-6} (1/°C)
Volumetric thermal expansion of the fluid α_f	1×10^{-3} (1/°C)

A mesh of 800 elements, 40 elements in $x-$direction and 20 elements in $y-$direction, is used to perform the stimulation. The mesh is refined in $x-$ and $y-$directions near the injection well to track the extreme abrupt changes at this point, see figure (5.5). Material properties for the

[1]The value of the initial permeability k_0 has been back–calculated from (Bruel, [1995], fig. 5) by considering that the enhanced permeability of the reservoir has an order of $\sim 10^{-11}$ m^2, (Evans et al., [2009]).

process of HF are shown in Table (5.4).

Table 5.4: Parameters used in the application of stimulation/ HF process: 1.(Shao et al., [2005]), 2.(Atkinson, [1991], p. 245), 3.(Evans et al., [2009]) and 4.(Bruel, [1995]).

	Parameter	Value	Reference
Damage parameters	Initial radius of cracks r_0 (cm)	25.0	3
	Final radius of cracks r_f (cm)	80.0	3
	Initial aperture of cracks w_0 (cm)	3.084×10^{-3}	Section (2.5.1.1)
	Material tensile strength T_c (MPa)	22.8	Calculated
	Material compressive strength C_0 (MPa)	228	3
	Material toughness parameter K_{Ic} (MPa$\sqrt{\text{m}}$)	1.87	2
	Model parameter η	0.2	Parameterized
	Number of cracks N per unit volume ($\Omega = 1$ m^3)	1×10^6	4
Hydraulic connectivity parameters	t_1	0.0001	1
	t_2	1.0	1
	Initial permeability k_0 (m^2)	2.85×10^{-14}	4

The over all rock tensile strength T_c, in Table (5.4), is taken as 10% of rock compressive strength $C_0 = 228$ MPa. The initial crack radius r_0 is determined based on the study of (Evans et al., [2009], p. 35) assuming homogeneous orientational distribution of cracks in the space. The final crack radius r_f is equal to [3-4] r_0, and the initial average aperture w_0 is calculated based on the study presented in section (2.5.1.1). The fracture physical characteristics in Table (5.4) correspond to large scale geothermal reservoirs. These characteristics are much larger than those in Tables (2.1) and (4.2) for scale laboratory tests.
This combination of crack dimensional properties, Table (5.4), will give permeability components with maximum magnitude order around 10^{-11} m^2 as shown in (Evans et al., [2009], p. 79) for the enhanced reservoir.

The reservoir is initially fully permeable $k_0 > 10^{-18}$ m^2, section (4.2.2.1). The excess formation pressure needed to start the HF for a temperature change of $\theta = -105$ °C is calculated using equation (4.14):

$$p_w^f = -\Big[(1-0.25)\times(3\times -38.2\times 10^6 + 75.4\times 10^6) + (1-2\times 0.25)\times 28.5\times 10^6 - 54000\times 10^6 \times 2.5\times 10^{-6}\times -105 - (1-0.25)\times 22.8\times 10^6\Big] \approx 18 \text{ MPa} \tag{5.3}$$

The casing shoe pressure at the injection well GPK1 should be around $(28.5 + 118 = 46.5)$ MPa to start the hydraulic fracturing. This magnitude is close to the values (around 40 MPa)

implemented at Soultz–sous–Forêts to start HF during phase 1 injection test at a depth of 2.8 km, (Bruel, [1995], Fig. 1). The threshold of HF is chosen to be as in the field $p_w^f = 39$ MPa. The model parameter η is now determined by knowing the threshold of HF.

The conditions addressed in equations (4.55) and (4.56) are to be applied on the BVP presented in figure (5.4) to check the shear stability of borehole GPK1. For granite, generally, (friction angle $\phi \approx 30°$, failure angle $\beta \approx 60°$, and compressive strength $C_0 = 228$ MPa). The vertical burden stress corresponding to 2.8 km depth is $\sigma_v = \sigma_H = -75.4$ MPa. The minimum value of borehole pressure required to cause shear failure by equation (4.55) is:

$$p_{w,\min} = 28.5 \times 10^6 + \frac{-3 \times -75.4 \times 10^6 - 38.2 \times 10^6 - 2 \times 28.5 \times 10^6 - 228 \times 10^6}{1+3} + \\ + \frac{54 \times 10^9 \times 7.5 \times 10^{-6} \times -105}{3 \times 4 \times 0.75} = -0.48 \text{ MPa}, \tag{5.4}$$

while the minimum value of shear failure pressure by equation (4.56) is:

$$p_{w,\min} = 28.5 \times 10^6 + \frac{75.4 \times 10^6 - 0.5(-75.4 \times 10^6 + 38.2 \times 10^6) - 28.5 \times 10^6 - 228 \times 10^6}{3} + \\ + \frac{54 \times 10^9 \times 7.5 \times 10^{-6} \times -105}{3 \times 3 \times 0.75} = -31.97 \text{ MPa} \tag{5.5}$$

The conditions addressed above give $p_{w,\min} < 0.0$. It becomes clear that based on the boundary and initial conditions, addressed in figure (5.4), the borehole (GPK1) is not likely to fail in shear but rather in tension due to the process of HF and as p_w gets closer to 39 MPa.

5.2.1.2 Time scales of the BVP to be stimulated

The time scales associated with the foregoing particular BVP, for lengths $L = 200$ m and $L = 500$ m, were calculated as shown in section (2.1.3), such that:

- For $L = 200$ m,
  - for thermal diffusion $t_\theta = 1676.21$ years,
  - for hydraulic diffusion $t_p = 0.08$ day.
- For $L = 500$ m,
  - for thermal diffusion $t_\theta = 10476.34$ years,
  - for hydraulic diffusion $t_p = 0.47$ day.

The calculated time for the thermal diffusion of heat front is to be reduced several orders of magnitude if the convection of heat is accounted for. For instance, later in section (5.2.2.2), figure (5.10), the average convective velocity over the volume of the reservoir is about $||\boldsymbol{v}_{\text{con}}|| = 5.57 \times 10^{-6}$ m/s. The characteristic time associated with convection of heat is calculated as follows:

$$t_{\text{conv}} = \frac{L\,(= 500\,\text{m})}{||\boldsymbol{v}_{\text{con}}||} = 2.85 \quad \text{years} \tag{5.6}$$

5.2.1.3 Flow history at GPK1 well: Simulations and correlations

The model described in figure (5.5) is to be stimulated by the Hydraulic Fracturing Model (HFM) of section (4.3). The results of simulations of the HF process are to be correlated with the flow logging injection tests performed at GPK1 well of Soultz–Sous–Forêts HDR reservoir in September 1993. The most important level of the stimulation process is located at 2.85 km of GPK1 and absorbs about 60% of the injected fluid, (Bruel, [1995]).

Phase 1 injection test was implemented by pumping water into GPK1 well gradually until a total flow rate of 40 l/s was reached at day 17. The experimental pressure curve at the injection well showed non–linear relation with injected flow announcing the existence of turbulent flow, (Grecksch et al., [2003]). Our simulations for the HF process will be performed by following the schemes presented in Table (5.5).

Table 5.5: Simulation schemes of the HF process at GPK1 for phase 1 injection test.

Scheme	BC † at GPK1	Condition at outer and right boundaries
First scheme	Linear flow rate (in 17 days) (from 0.13 l/s to $\sim$ 20 l/s)	Impermeable boundaries
Second scheme	Linear flow rate (in 17 days) (from 0.13 l/s to $\sim$ 20 l/s)	Permeable boundaries ($p = p_0 = 28.5$ MPa)

†: Boundary Condition(s)

Figure (5.6) shows the applied flow rate history at GPK1 well as suggested by the experimental work of (Bruel, [1995]) and as applied in our simulations. Figure (5.7) correlates between the numerical response obtained by our HFM, first and second schemes in Table (5.5), and the experimental data obtained from (Bruel, [1995], Fig. 1) for a period of 17 days.

When the reservoir is assumed impermeable at the outer and right boundaries (first scheme), the geothermal system reaches a pressure of 137 MPa at a flow rate $\sim$20 l/s ($\sim$ 60% of 40 l/s) with a plateau announcing the presence of extreme turbulent flow near GPK1, see figure (5.7(a)).

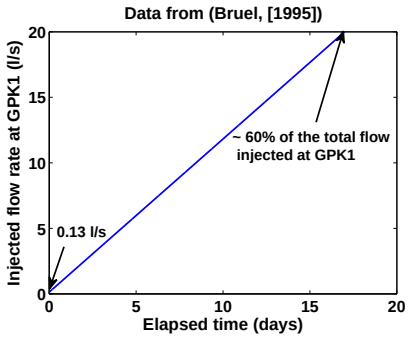

Figure 5.6: Applied flow history at GPK1 during the 1993 phase 1 injection test at Soultz–Sous–Forêts.

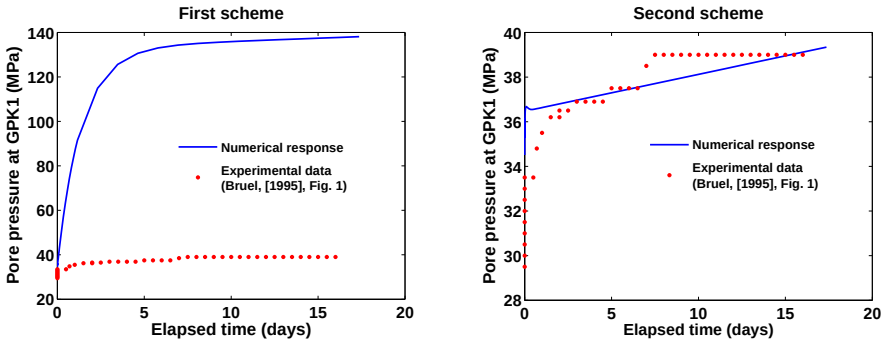

(a) Impermeable boundaries (b) Permeable boundaries

Figure 5.7: Injection pressure at GPK1 during the 1993 phase 1 injection test at Soultz–Sous–Forêts. Comparison between experimental data and the numerical response of our HFM for schemes shown in Table (5.5).

This pressure value of 137 MPa is 3.5 times higher than the HF pressure (39 MPa) obtained experimentally by (Bruel, [1995]). However, when the outer and right boundaries of the reservoir are assumed permeable (second scheme), the geothermal system reaches the pressure of HF at a flow rate of ∼20 l/s *almost* as applied experimentally (∼ 60% of 40 l/s). The numerical response in figure (5.7(b)) is no longer showing an asymptotic plateau as the fluid turbulence is greatly eliminated when the outer and right boundaries are assumed permeable, i.e. smoother flow is achieved within the reservoir.

The previous conclusion can be illustrated by the fact that HF is more effective when the reservoir is impermeable at the boundaries; trapped water helps increasing the pressure of pore fluid. Strong HF process is equivalent to more obvious crack evolution and/or dilation which evidently means more turbulent flow.

5.2.2 Phase 1 injection test at GPK1 well, 1993: Permeability enhancement of the reservoir

The time of the simulations presented in the previous section is to be extended in this part so that the permeability enhancement along the reservoir can be tracked. The BVP as described in figure (5.4) is to be simulated for the cases when HF is/is not accounted for. The effects of HF process on the reservoir impedance and thermal recovery is also addressed.

5.2.2.1 The transient BVP: Geometry, material properties and FEM mesh

The model suggested to start the simulation of HF process of the reservoir is shown in figure (5.8). A homogeneous finite element mesh of 800 elements, 40 elements in $x-$direction and 20 elements in $y-$direction, is used to perform the stimulation. Poroelastic and thermoelastic material properties are exactly as shown in Table (5.3) based on the study of (Evans et al., [2009]). Material properties for the process of HF are shown in Table (5.4).

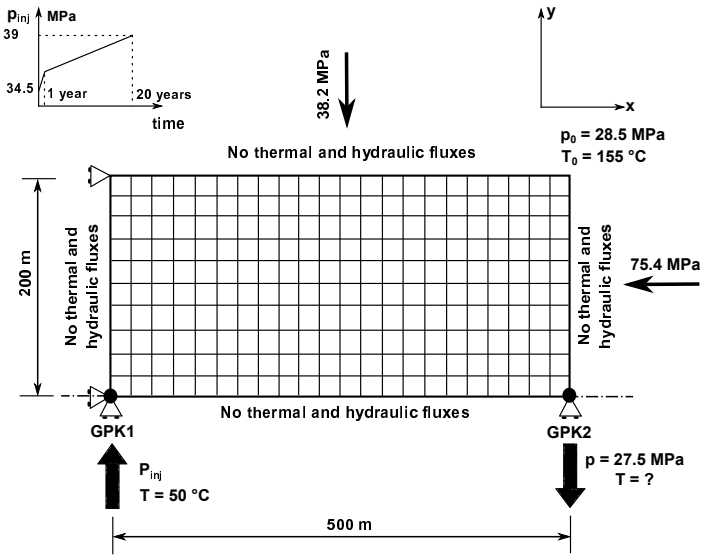

Figure 5.8: Modeling of the phase 1 injection test at Soultz–Sous–Forêts: permeability enhancement of the reservoir. All boundary and initial conditions are shown on the graph, figure is not to scale.

Casing shoe pressure at the injection well GPK1 to start HF has been calculated as in equation (5.3) and should be around 39 MPa. The stability of the borehole GPK1 against shear failure has been also assured as in equations (5.4) and (5.5). Injection pressure is increasing at GPK1 linearly; pumping starts with 34.5 MPa and reaches 35.9 MPa at year 1. Thereafter, it continues to increase also linearly but with a smoother rate to reach a value of 39 MPa after 20 years of injection.

5.2.2.2 Simulations of the HDR reservoir without HF

The results of the simulations for time periods of 5 and 10 years are shown in the following discussion.

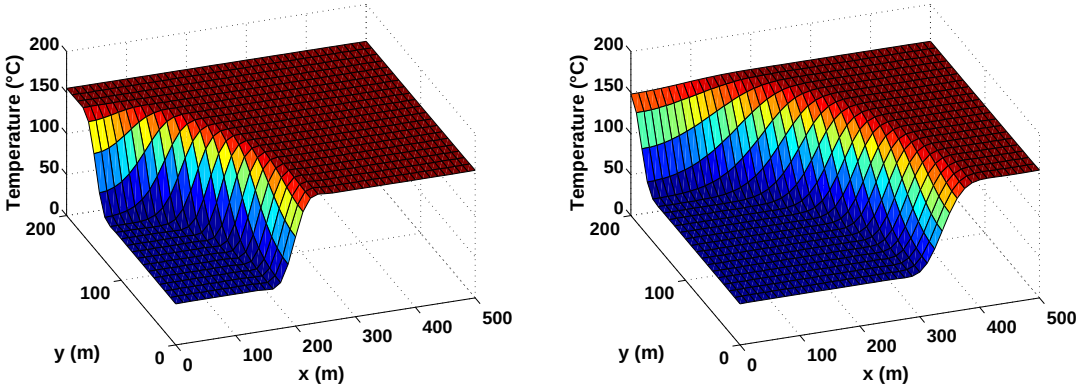

(a) Temperature contour at year 5

(b) Temperature contour at year 10

Figure 5.9: Contours of the mixture temperature at two times, convection of heat is accounted for.

Fracture zone cools in $x-$ and $y-$directions due to the high fluid gradients spreading all over the volume of the reservoir. These large fluid gradients, near the injection well, help opening the cracks along with the reduction in the compressive stresses due to thermal tensile stresses resulting from cooling, see figure (5.10).

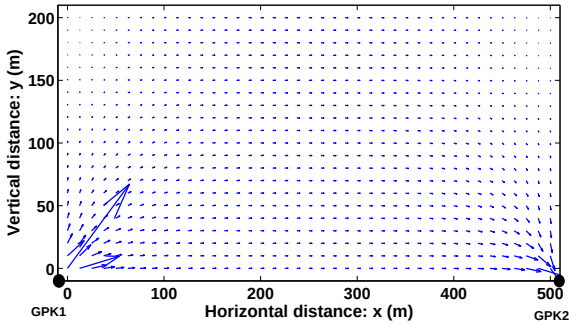

Figure 5.10: Scaled fluid velocity vectors for the defined injection state at well GPK1 and extraction pressure of $p_0 - 1$ MPa at GPK2. The velocity field is not homogeneous at the neighbors of the wells. However, the average velocity of the formation fluid is about $||\boldsymbol{v}|| = 5.57 \times 10^{-6}$ m/s.

The homogeneous mesh, figure (5.8), is composed of 800 elements of size $h_x \times h_y = 12.5$ m $\times$ 10 m. Grid Péclet number ($\mathrm{Pe_g}$) is calculated with an average fluid velocity of $||\boldsymbol{v}|| = 5.57 \times 10^{-6}$ m/s and thermal diffusivity $\psi = \chi/\rho c_v = 7.56 \times 10^{-7}$ m^2/s, see table (5.3).

$$\mathrm{Pe_{g,x}} = \frac{h_x \, ||\boldsymbol{v}||}{2\psi} = 46.05 \tag{5.7}$$

$$\mathrm{Pe}_{\mathrm{g,y}} = \frac{h_y \, ||\boldsymbol{v}||}{2\psi} = 36.84 \tag{5.8}$$

For fluid flow, either in $x-$direction or in $y-$direction, Péclet number is much larger than 1, which indicates that the convection of heat is quite significant and should be accounted for when performing the simulations.

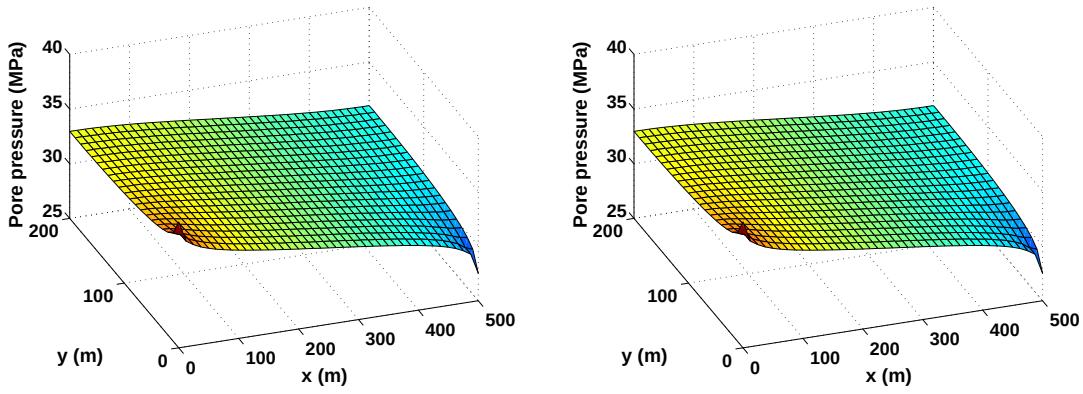

(a) Pore pressure contour at year 5

(b) Pore pressure contour at year 10

Figure 5.11: Contours of the mixture pore pressure at two times, convection of heat is accounted for.

The contours of fluid pore pressure are not showing any considerable changes during the time of simulations. The fast diffusion of pressure front, time scale of 0.48 day, makes the motion of pressure front almost instantaneous at the time scale we are interested in here.

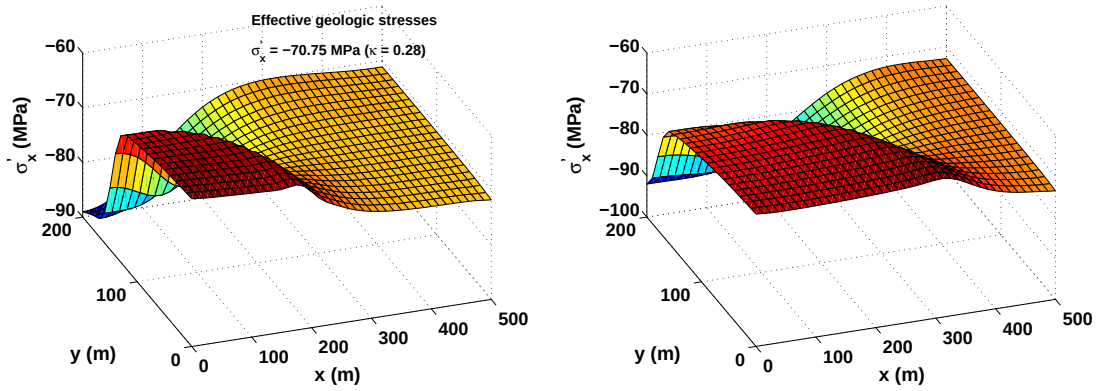

(a) Contour of $\sigma_x^{'}$ at year 5

(b) Contour of $\sigma_x^{'}$ at year 10

Figure 5.12: Contours of longitudinal effective stress $\sigma_x^{'}$ at two times, convection of heat is accounted for.

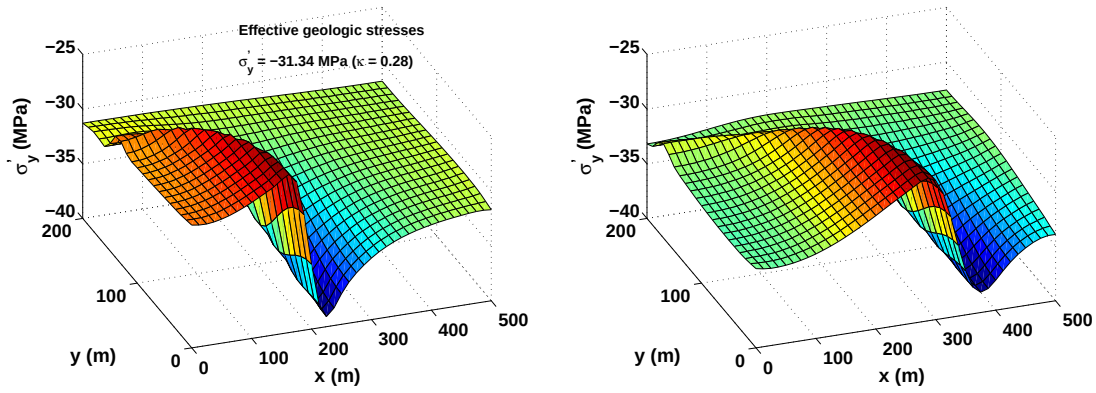

(a) Contour of $\sigma_y^{'}$ at year 5

(b) Contour of $\sigma_y^{'}$ at year 10

Figure 5.13: Contours of transversal effective stress $\sigma_y^{'}$ at two times, convection of heat is accounted for.

The contours of effective stresses are following the diffusion of heat front showing considerable reduction in compressive stresses near the injection well, and in the cooled regions due to the thermal tensile stresses created by cooling. Following figures (5.12(b)) and (5.13(b)), the reservoir is relaxing faster in $y-$direction than in $x-$direction: this effect is due to the geologic far field stress state which imposes much smaller stresses on the outer boundary of the reservoir. Indeed, HF is going to enhance the permeability of the HDR reservoir following the direction of maximum far field stress.

(Bruel, [1995], p. 447) suggested planarity and persistency of the fault crossed by GPK1 at 2.8 km: thus the vertical section of the well GPK2 over which flow is taking place is approximately 550 m extending to about 3.3 km. The radius of operating well GPK2 at such a depth is 15 cm, (Baumgärtner et al., [2000]).

Figure (5.14) shows the relation between injection fluid pressure at the well GPK1 and the magnitude of fluid flux at the same well. The linear relation between them indicates smooth flow without any created and/or improved connections.

The impedance Z of the unenhanced reservoir is shown in figure (5.15). It is calculated as shown in equation (5.9):

$$Z = \frac{P_{\text{inj}} - P_{\text{pro}}}{Q} \tag{5.9}$$

P_{inj} and P_{pro} are the injection and production wellhead pressures respectively, Q is the injected/produced flow rate since there is no leak off. The impedance of the unenhanced reservoir is greater than 1000 MPa s/m^3 at any time, which means an inefficient operation where the power pumped through the reservoir will most probably exceed a substantial fraction of the power produced by the reservoir, (Murphy et al., [1999]).

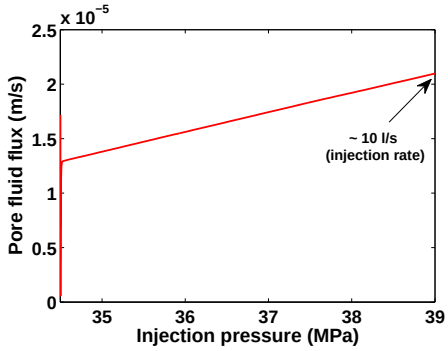

Figure 5.14: Relation between injected pore fluid pressure and the magnitude of created fluid flux at the injection well GPK1 of unenhanced HDR reservoir at Soultz–Sous–Forêts.

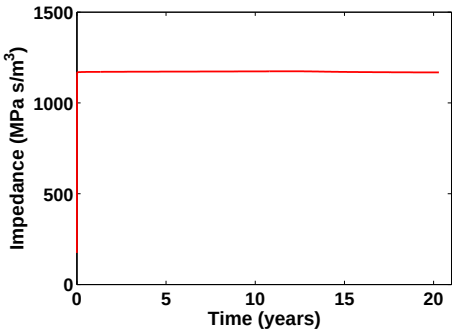

Figure 5.15: Impedance profile of unenhanced HDR reservoir at Soultz–Sous–Forêts.

5.2.2.3 Simulation of the HDR reservoir with HF

If HF is activated in our FE code, after 1 year of pumping at GPK1, casing shoe pressure will reach a value of 35.9 MPa and permeability contours for the enhanced HDR reservoir are shown in figure (5.16).

Cracks are evolving in the direction of maximum far field stress (right boundary) leading longitudinal permeability to reach its maximum value up to distances of ($\simeq$80 m in $y-$direction and $\simeq$240 m in $x-$direction). The results of this simulation are in good agreement with the microseismic events diagram presented in (Bruel, [1995], fig. 2) announcing the propagation of

hydraulic front and fracture coalescence.

Preferential cooling following the new paths of the enhanced permeability is thus expected. The HDR reservoir is no longer cooling, almost equally, in both $x-$ and $y-$ directions; heat diffusion is dominant in the direction of the far field stress (direction of crack evolution), see figure (5.17). The oscillations in temperature contours near the production well are related to the convection of heat as fluid fluxes converge leading to high pore fluid velocity.

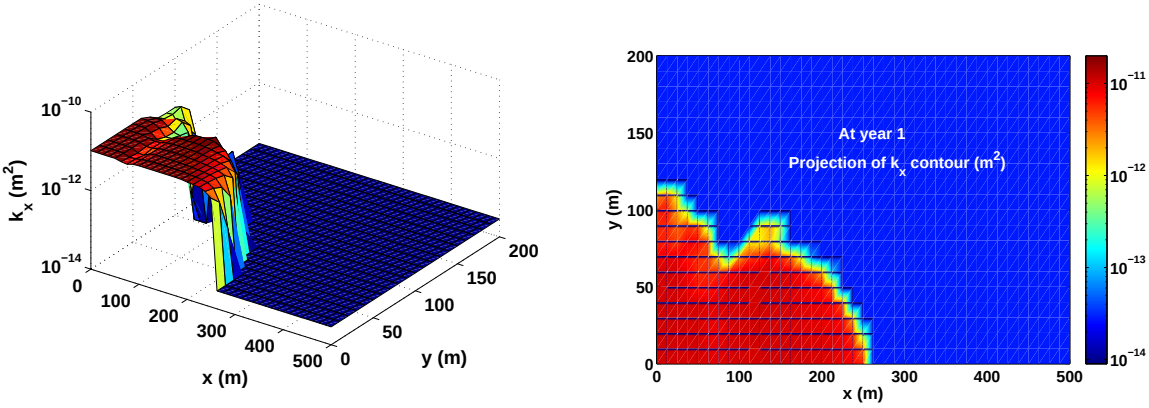

(a) Contour of k_x at year 1

(b) Projection of k_x contour in the $x-y$ plane

Figure 5.16: (a) The contour of longitudinal permeability component k_x at year 1, (b) The projection of k_x contour in $x-y$ plane.

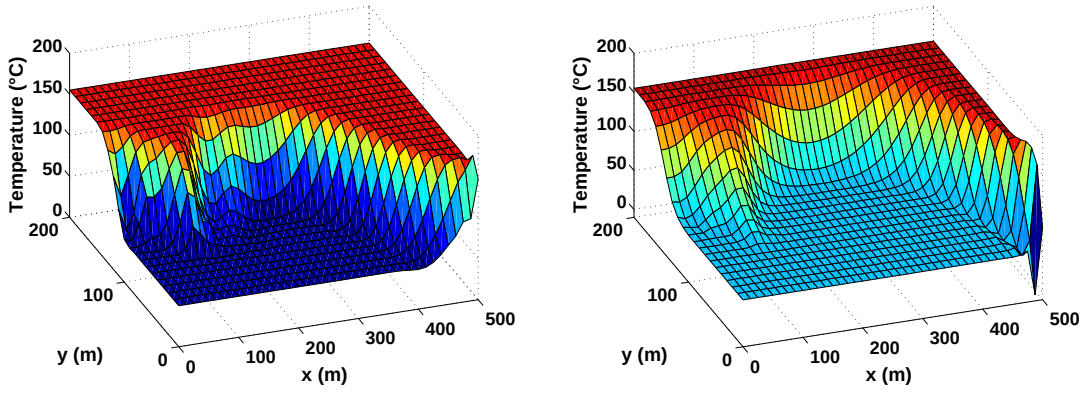

(a) Temperature contour at year 5, with HF

(b) Temperature contour at year 10, with HF

Figure 5.17: Contours of the mixture temperature at two times with HF, convection of heat is accounted for.

These oscillations are purely numerical and stem from the difficulty of modeling heat waves striking stiff boundaries. The phenomenon of forced heat convection will be highlighted with several approaches to heal/mitigate the oscillations in the hyperbolic solutions of the approxi-

mated finite element approach in chapter(6).

Velocity field at year 1, figure (5.18), shows superior pore fluid velocity, $\sim 2.75 \times 10^{-5}$ m/s, in the zone of active HF. The average pore fluid velocity in other regions is around $\sim 6.20 \times 10^{-6}$ m/s.

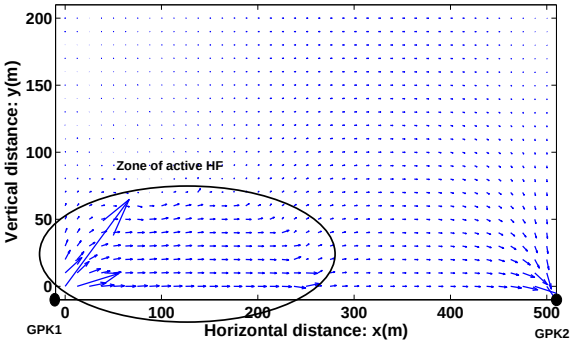

Figure 5.18: Scaled fluid velocity vectors for the defined injection state at well GPK1 and extraction pressure of $p_0 - 1$ MPa at GPK2 when activating HF. The velocity field is not homogeneous at the neighbors of the wells, the average velocity of the formation fluid in the zone of active HF is $||\boldsymbol{v}|| = 2.75 \times 10^{-5}$ m/s while in the other zones it is about $||\boldsymbol{v}|| = 6.20 \times 10^{-6}$ m/s.

Contours of pore fluid pressure at years 5 and 10 are shown in figure (5.19). The changes in pore fluid pressure contours are no longer significant in the zone of active HF. Darcy's law indicates that the gradient of fluid pressure is proportionally related to the inverse of permeability tensor $\boldsymbol{\nabla} p \propto \boldsymbol{k}^{-1}$. The tremendous fast increase in the components of permeability tensor in the zone of active HF makes the changes in pore fluid pressure quite small if compared to the situation of unenhanced HDR reservoir.

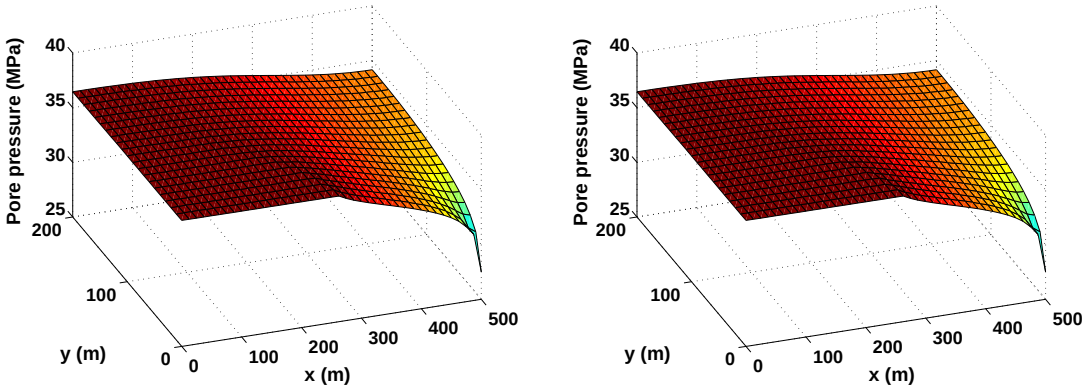

(a) Pore pressure contour at year 5

(b) Pore pressure contour at year 10

Figure 5.19: Contours of the mixture pore pressure at two times with HF, convection of heat is accounted for.

Contours of effective stresses, whether longitudinal or transversal figures (5.20) and (5.21), are following the preferential cooling derived by the process of HF.

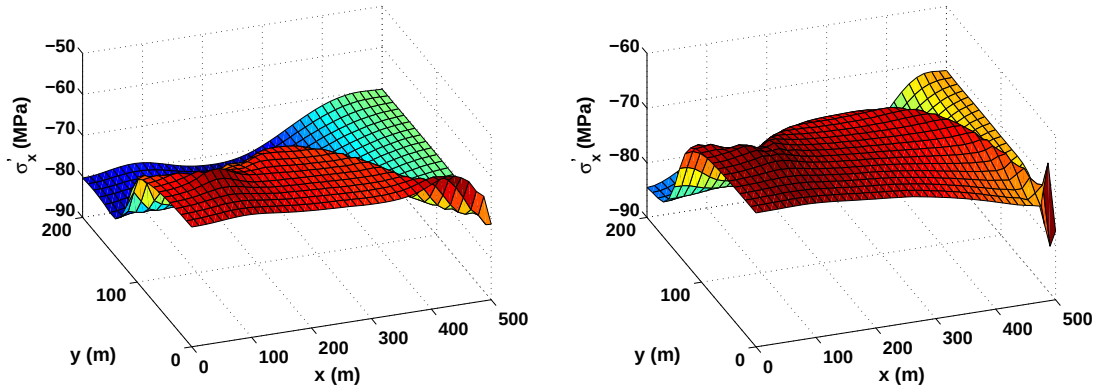

(a) Contour of $\sigma_x^{'}$ at year 5

(b) Contour of $\sigma_x^{'}$ at year 10

Figure 5.20: Contours of longitudinal effective stress $\sigma_x^{'}$ at two times with HF, convection of heat is accounted for.

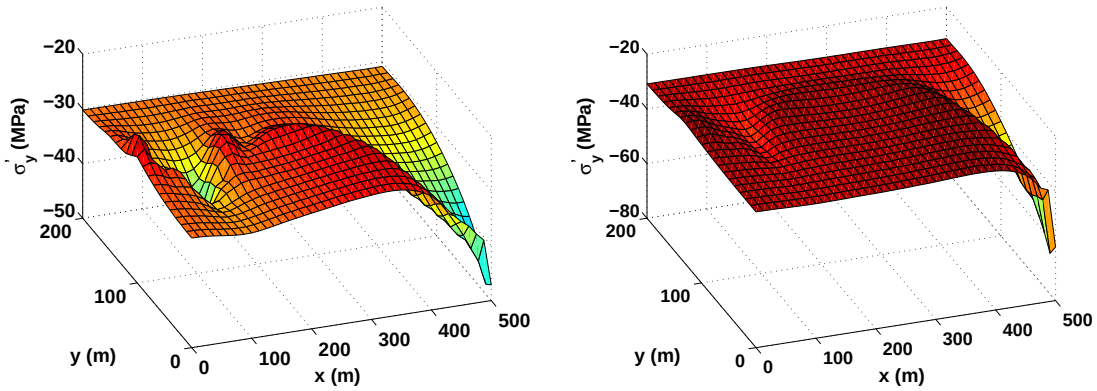

(a) Contour of $\sigma_y^{'}$ at year 5

(b) Contour of $\sigma_y^{'}$ at year 10

Figure 5.21: Contours of transversal effective stress $\sigma_y^{'}$ at two times with HF, convection of heat is accounted for.

Stresses are dawdled in compression in the cooled regions as the reservoir is constrained to some degree on the boundaries of symmetry. The created new highly–permeable paths take most of the fluid gradients directly in the direction of maximum far field stress causing stresses to augment in compression near the outer boundary of the HDR reservoir. Thus at the outer boundary cracks are most likely closing and permeability is thus decreasing, unless shear dilatation might cope for the reduction in their apertures, (Chen et al., [2007]).

Figure (5.22) shows the relation between injected pore fluid pressure and the magnitude of created fluid flux at the injection well GPK1. A non–linear relation is found during the first year of simulation while HF process is active. The non–linearity of the pressure record versus flow record tells us that improved connections are created around the borehole GPK1. It also describes the dependence of hydraulic conductivity on the effective stress (Bruel, [1995]).

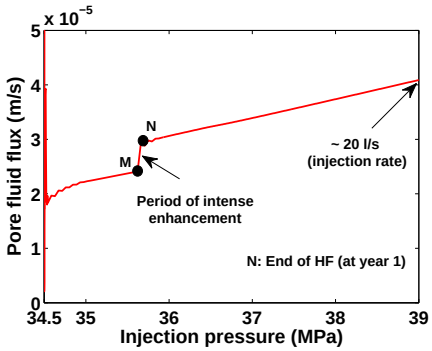

Figure 5.22: Relation between injected pore fluid pressure and the magnitude of created fluid flux at the injection well GPK1. Non–linear relation is clear while HF process is active announcing the creation of improved connections, (Bruel, [1995]).

The statement of *end of HF* in figure (5.22) may sound puzzling. Actually, the experimental work of (Papanastasiou, [1999]) have proven that for every geothermal system there exists an optimum injection schedule (injection pressure and duration). Any further increases in stimulation effort, i.e. stimulation time for a given stimulation pressure, does not provide additional permeability enhancement. Our injection pressure schedule defined in figure (5.8) was sufficient to enhance the reservoir permeability as shown in figure (5.16(a)) up to year 1. The subsequent increases in stimulation pressure and time did not enhance the reservoir permeability any more. Therefore, *end of HF* means the time and pressure values at which the enhancement of the reservoir is final.

The jump between the two points M and N in figure (5.22) can be understood by studying the permeability history at the injection well GPK1, figure (5.23).

Following figure (5.23), it is noticed that permeability evolution at the injection well happens very rapidly. This is due to modeling hydraulic fracturing while considering only mode I of fracture propagation. It is also seen that the period of intense permeability enhancement is taking place earlier at the injection well which is expected due to harsh thermo–poroelastic changes at this point. However, if permeability histories at all the Gauss' points in figure (5.8) are averaged, the period of intense permeability enhancement in the averaged curve will correspond to the jump (M–N) in figure (5.22).

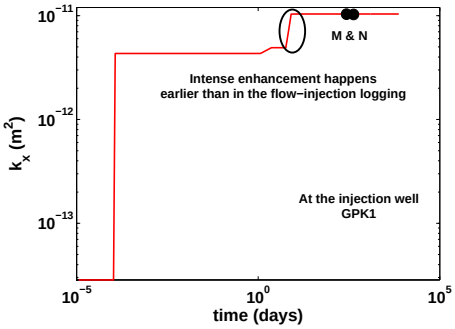

Figure 5.23: Longitudinal permeability k_x history at the injection well GPK1. Points M and N correspond to the period of intense permeability enhancement in figure (5.22). Intense permeability enhancement happens earlier than in the flow–injection logging, figure (5.22).

Process of HF, for only one year, has reduced the flow impedance of the HDR reservoir from ~ 1200 MPa s/m^3 to ~ 600 MPa s/m^3 reducing the power required to pump water through the reservoir and enhancing its efficiency by 50%, see figure (5.24) and equation (5.9).

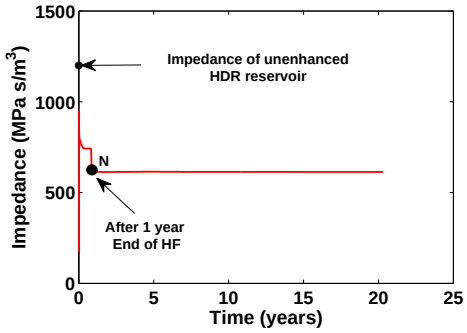

Figure 5.24: Impedance profile of the enhanced HDR reservoir at Soultz–Sous–Forêts.

Figure (5.25(a)) shows the profiles of produced fluid temperatures with HF ($T_{\rm hf}$) and without HF ($T_{\rm whf}$). Figure (5.25(b)) shows the profile of the ratio $T_{\rm whf}/T_{\rm hf}$. In most geothermal systems, the produced fluid is efficiently used as long as its temperature does not drop below 80 °C, (Lund, [2007]).

The standard mean production temperature curve, shown in figure (5.25(a)), is based on the analytical solution provided by (Kolditz, [1995], fig. 5) for one–dimensional matrix heat diffusion and for 15 l/s injection flow rate. Kolditz standard solution shows a thermal drawdown of approximately 29% in 10 years, meanwhile the enhanced reservoir shows a thermal thrawdown of 45%, see figure (5.26). In both cases, thermal drawdown exceeds the limits required by (Jupe et al., [1995]), i.e. 1% thermal drawdown per year. This could be due to the rigorous assumption of neglecting the three–dimensional heat diffusion, (Kolditz, [1995]).

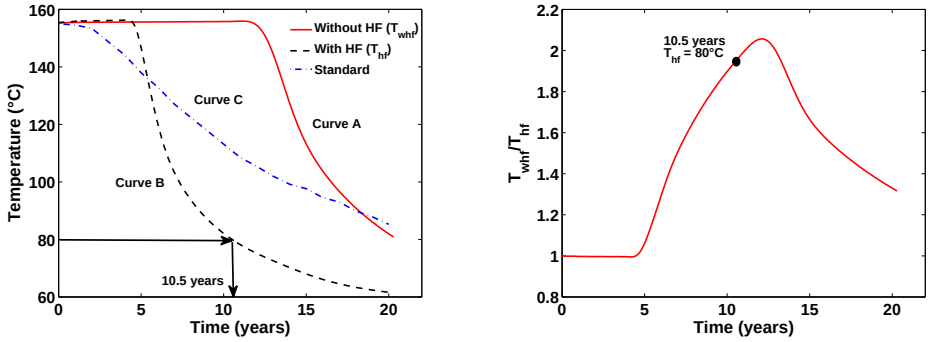

(a) Profiles of produced fluid temperature

(b) Profile of $T_{\mathrm{whf}}/T_{\mathrm{hf}}$

Figure 5.25: (a) Profiles of produced fluid temperature with HF (T_{hf}) and without HF (T_{whf}). (b) Profile of the ratio $T_{\mathrm{whf}}/T_{\mathrm{hf}}$ (temperatures are measured in °C).

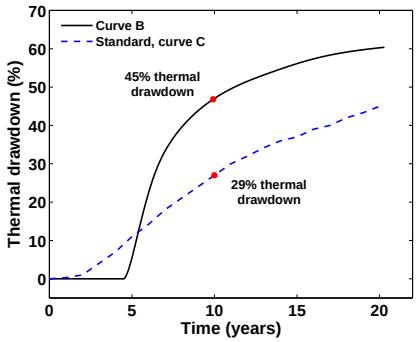

Figure 5.26: Thermal drawdown, equation (5.1), of the mean production temperature for the enhanced HDR reservoir curve B, and the standard production temperature as suggested by (Kolditz, [1995]) curve C.

If the process of HF is utilized in the simulations, the HDR reservoir is exhausted in 10.5, see figure (5.25(a)). However, if HF is not activated the HDR reservoir may last to 20 years. The efficiency of utilizing HF becomes quite clear in terms of the energy used to pump water through the reservoir, see figure (5.24), and in terms of the produced flow rate, see figure (5.27).

After 1 year of the process of HF, the produced flow rate from the HDR reservoir is 2 times higher than if the reservoir was not hydraulically stimulated, see figure (5.27(b)). Considering that the stimulated reservoir will operate efficiently till 10.5 years and that the unenhanced reservoir will efficiently operate till 20 years; the volume of the produced fluid can be calculated by numerically integrating the curves, in figure (5.27(a)), for the case of active HF and the case of inactive HF till the points A and B respectively.

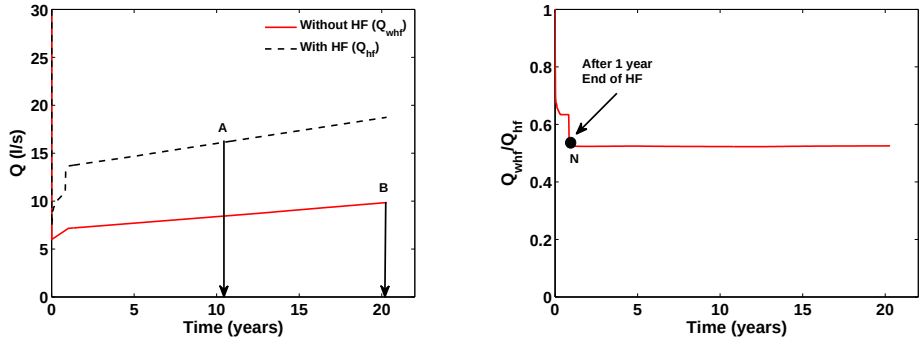

(a) Profiles of produced flow rate (Q)

(b) Profile of $Q_{\mathrm{whf}}/Q_{\mathrm{hf}}$

Figure 5.27: (a) Profiles of produced flow rate with HF (Q_{hf}) and without HF (Q_{whf}). (b) Profile of the ratio $Q_{\mathrm{whf}}/Q_{\mathrm{hf}}$.

- The volume of efficient fluid produced from the stimulated HDR reservoir over a period of 10.5 years is 4.922 Million m^3,
- while the volume of efficient fluid produced from the unenhanced HDR reservoir over a period of 20 years is 5.364 Million m^3.

These huge amounts of water used are not utterly lost; one should keep in mind that the geothermal fluids are recirculated over the volumes of the HDR reservoirs over and over again. It becomes clear now that HF process has increased the efficiency of the HDR reservoir up to 50% according to figure (5.24). Yet by the calculations of efficient fluid volume, only 7 to 8% of the total efficient fluid to be produced is lost over the entire effective age of the reservoir.

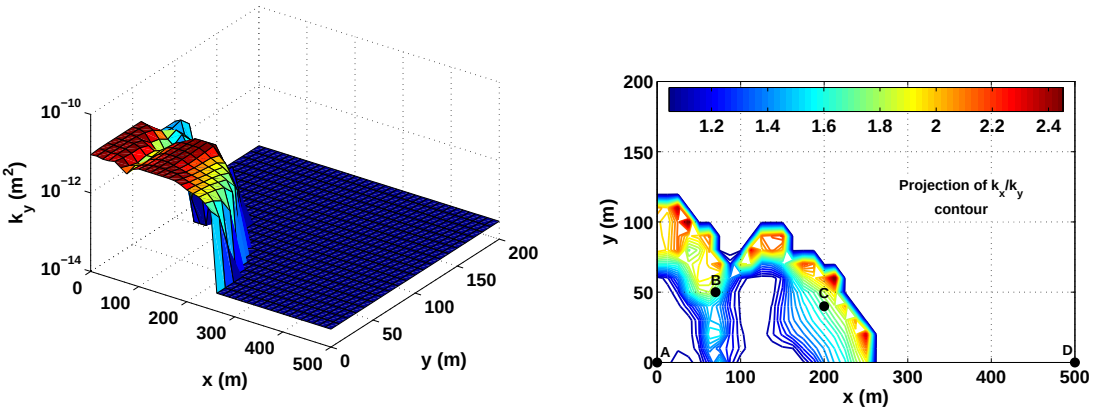

(a) Contour of k_y at year 1

(b) Projection of k_x/k_y contour in the $x-y$ plane

Figure 5.28: (a) The contour of transversal permeability component k_y at year 1. (b) The projection of k_x/k_y contour in $x-y$ plane at year 1.

Figure (5.28(a)) shows the contour of transversal permeability k_y of the enhanced HDR reservoir after 1 year of HF. Figure (5.28(b)) shows the projection of the contour of k_x/k_y in $x-y$ plane with some points where the evolution of fracture radii is to be studied.

The anisotropy of the permeability tensor components remains in the range [0.4, 2.5] as suggested by (Schulze et al., [2001]). Since the longitudinal stress component σ_x is arranged in the position ($\sigma_x = \sigma_{11}$) in the stress tensor used in our FE code, longitudinal fractures lie exactly at the position $\theta = 90°$ and transversal fractures at the position $\theta = 0°$, see figure (5.29) and chapter (4).

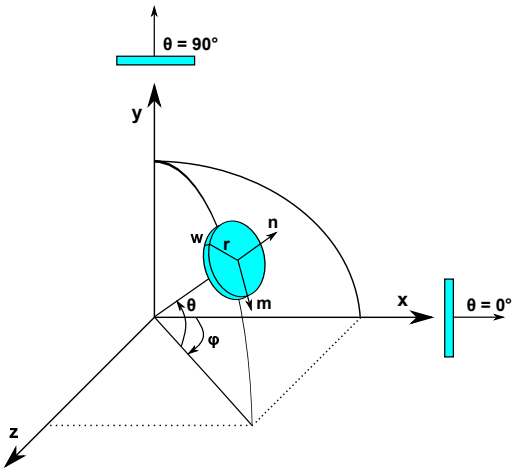

Figure 5.29: θ–ϕ position of a crack of radius $r(\boldsymbol{n})$.

Figure (5.30) shows the directional evolution of fracture radius at the end of the process of HF at points A and D, see figure (5.28(b)).

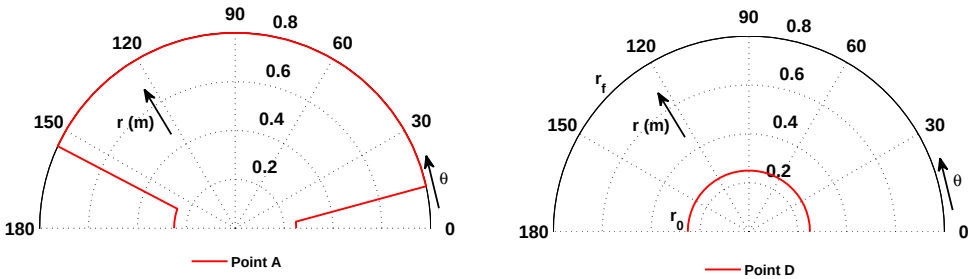

Figure 5.30: Directional evolution of fracture radii at points A and D at year 1 (the end of HF).

Point A represents a position very close to the injection well where the components of permeability tensor increase rapidly and almost equally, nevertheless, with a preference in the direction of far field longitudinal stress $\theta = 90°$, $k_x/k_y = 1.05$. Point D is far away from the region of

active HF and no change to fracture radius is recorded, $r = r_0 = 25$ cm.

Figure (5.31) shows the directional evolution of fracture radii at the end of the process of HF at points B and C, see figure (5.28(b)). At point C, fractures evolve strongly in the longitudinal direction and slightly in the transversal direction $k_x/k_y = 1.7$. Meanwhile, a slighter evolution of fractures in the longitudinal direction is observed at point B which gives $k_x/k_y = 1.6$.

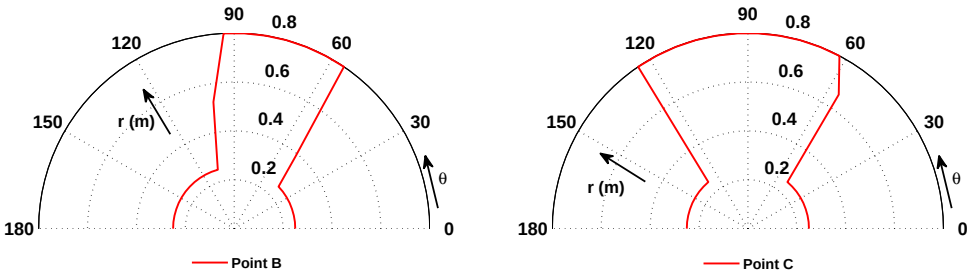

Figure 5.31: Directional evolution of fracture radii at points B and C at year 1 (the end of HF).

5.3 Working fluids of geothermal systems: Characteristics and alternatives

The purpose of this section is to study the effect of geothermal systems conditions, namely pressure and temperature, on the dynamic viscosities of the working fluids. A brief discussion is first presented about the temperature–viscosity change of water substance. Geothermal brines temperature–viscosity change is later addressed and compared to that of the water substance. The simulations of the phase 1 injection test section (5.2.2) are repeated while accounting for temperature–viscosity change of the brine used. Finally, an alternative for geothermal brines, punctually using carbon dioxide CO_2 as a working fluid, is briefly studied.

5.3.1 Thermophysical properties of water substance

The permeability tensor which has been introduced in the equation of balance of the fluid mass section (2.1.2.2), as well as in the matrix formulation section (3.2.3.2), represents an intrinsic characteristic of the porous medium which has been enhanced by causing cracks to evolve and intersect, i.e. improving hydraulic connection. Generally pumping cold water into fractured HDR reservoirs causes considerable changes in temperature field and, possibly, pressure field if HF is utilized to enhance the productivity of HDR reservoirs.

Such considerable changes in the temperature and pressure fields are expected to change the dynamic viscosity of the injected fluid which appears in the explicit form of the equation of balance of the fluid mass section (2.1.2.2), see (Burger et al., [1985]) and (Likhachev, [2003]). The easiness with which a fluid can move through pore spaces or fractures is described by hydraulic conductivity K_H. Hydraulic conductivity depends on the intrinsic permeability of the porous medium, on the degree of saturation[1], and on the density and viscosity of the fluid.

$$K_H = k \frac{\rho g}{\mu}, \tag{5.10}$$

where K_H is the hydraulic conductivity (m/s), k is the intrinsic permeability of the porous medium (m^2), μ is the dynamic viscosity of the fluid (Pa.s), ρ is the density of the fluid (kg/m^3) and g is the acceleration due to gravity (m/s^2).

The circulating fluid used while utilizing and/or enhancing HDR reservoirs is brine water with certain types and amounts of dissolved salts. These dissolved salts are expected to improve the performance of such reservoirs in terms of hydraulic conductivity and preventing mineral precipitation, see (Du et al., [2005]), (Taron et al., [2009]) and (Evans et al., [2009]).

If, conservatively, the geothermal brines are assumed to have the same, or close, thermodynamical characteristics as the water substance, the phase diagram shown in figure (5.32) is assumed to be applicable.

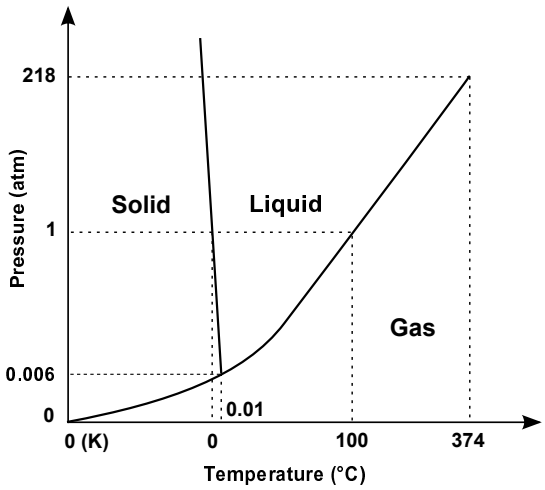

Figure 5.32: Phase diagram of water substance at different temperature and pressure values.

The simulation and/or stimulation of HDR reservoirs is mostly done with temperature values expected in the range 50 to 200 °C and pore fluid pressure of 30 to 50 MPa i.e. 300 to 500 atm.

[1] Assumed equal to 1 all along this research.

According to water phase diagram, figure (5.32), no phase changes of the water substance are expected in such ranges and the water shall be liquid at any time.

5.3.2 Dynamic viscosities of working fluids as a function of temperature and pressure

Dynamic viscosity of a fluid describes its resistance to gradual deformation, and hence flow. It can be thought of as a measure of fluid friction. Water viscosity is independent of fluid pressure except for very high values larger than 80 MPa, yet it is strongly dependent on temperature, (Likhachev, [2003]). Viscosity of liquid water at different temperatures up to the normal boiling point is listed in Table (5.6)[1].

Table 5.6: Dynamic viscosity of water substance (1 cP(centipoise)= 10^{-3} Pa.s).

Temperature T (°C)	Dynamic viscosity μ (cP)
10	1.308
20	1.002
30	0.7978
40	0.6531
50	0.5471
60	0.4658
70	0.4044
80	0.3350
90	0.3150
100	0.2822

(Burger et al., [1985]) have indicated that the variation of water substance viscosity in temperature range of 0 °C to 370 °C can be approximated by equation (5.11), T in Kelvin, with accuracy of 97.5%.

$$\mu = 2.414 \times 10^{-5} \times 10^{\left(\frac{247.8}{T-140}\right)} \qquad \text{(Pa.s)} \tag{5.11}$$

Figure (5.33) shows a quite good agreement between the experimental record of Table (5.6) and the analytical expression of (Burger et al., [1985]) for the temperature range of 10 °C to 100 °C.

[1] www.engineeringtoolbox.com

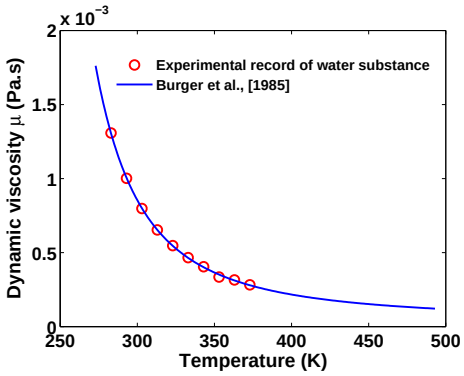

Figure 5.33: Correlation between the experimental record of the water substance shown in Table (5.6) and the analytical expression of (Burger et al., [1985]).

Fluids usually used in geothermal systems are brines with the dominance of Cl and Na ions over a wide range of salinity relevant for geothermal applications. Geothermal fluids are frequently modeled as aqueous NaCl solutions, (Francke and Thorade, [2010]). In most of the geothermal systems, as in Groß Schönebeck 50 km north of Berlin, the total of dissolved solids sums up to 265 g/l with dominant sodium chloride mass fraction of 0.225 kg_{NaCl}/kg_{H_2O} corresponding to a molality of 4.968 mol_{NaCl}/kg_{H_2O}, (Francke and Thorade, [2010]) and (Battistelli et al., [1997]).

(Francke and Thorade, [2010]) collected experimental data from several studies to provide three models, Table (5.7), for brine viscosity calculations.

Table 5.7: Applicability range of various models for calculating brine viscosity, (Francke and Thorade, [2010]).

Study	T (°C)	p (MPa)	Electrolytes	Concentration ($mol.kg^{-1}$)
Model 1	10–350	0.1–50	NaCl	0–5
Model 2	20–150	0.1–35	NaCl	0–6
Model 3	0–350	0.1–100	NaCl, KCl, LiCl	0–6

- Model 1 is based on a study where the ratio of solution viscosity to water substance viscosity is calculated using four coefficients.
- Model 2 is based mainly on experimental studies.
- Model 3 is based on a study where ten parameters were used to calculate the ratio of solution viscosity to water substance viscosity.

The different models, in their respective application range shown Table (5.7), result in very consistent values of brine viscosity (μ_b) with average deviation of 0.3% and maximum deviation of 0.9%. Figure (5.34) shows the viscosity of 0.225 $kg_{NaCl}/kg_{Solution}$ brine for different values of temperature at constant pressure of 1.5 MPa. The values of brine viscosity (μ_b) are the average of the three models listed in Table (5.7). An exponent function of the form $\mu_b = 9.15\times10^7\, T^{-4.37}$, with T being temperature in Kelvin and (μ_b) in Pa.s, is chosen to represent averaged models data with determination coefficient of $R^2 = 0.9957$.

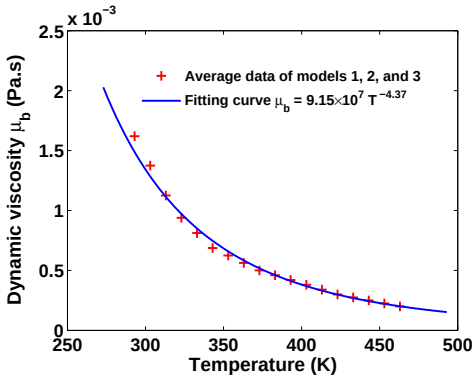

Figure 5.34: Brine viscosity as a function of temperature while pressure and NaCl mass fraction are held constant to 1.5 MPa and 0.225 $kg_{NaCl}/kg_{Solution}$ respectively. Solid line represents the fitting curve of the scattered data with determination coefficient of $R^2 = 0.9957$.

(Francke and Thorade, [2010]) have also employed the models of Table (5.7) to study the effect of NaCl mass fraction on the viscosity of the brine. Brine viscosity has been proven to increase almost linearly by 76% for an NaCl mass fraction change of 0 kg_{NaCl}/kg_{H_2O} to 0.25 kg_{NaCl}/kg_{H_2O} at a temperature of 150 °C and pressure of 1.5 MPa. It has been also found that the effect of fluid pressure is quite insignificant on the brine viscosity at a temperature of 150 °C and pressure values in the range of 0.01 MPa to 50 MPa, see also (Likhachev, [2003]).

Figure (5.35) shows the percent of viscosity increase as result of using sodium chloride NaCl in a concentration of 0.225 kg_{NaCl}/kg_{H_2O} as function of temperature. The curve extends over a temperature range of 0°C to 220°C and is built up using the analytical expression of (Burger et al., [1985]), equation (5.11), to get water substance viscosity (μ) and our fitting curve, figure (5.34), to get brine viscosity (μ_b).

The point highlighted in figure (5.35) indicates 65% of viscosity increase as result of using sodium chloride to a concentration of 0.225 kg_{NaCl}/kg_{H_2O} at temperature of 150 °C. This result matches quite well the work of (Francke and Thorade, [2010], fig. 7).

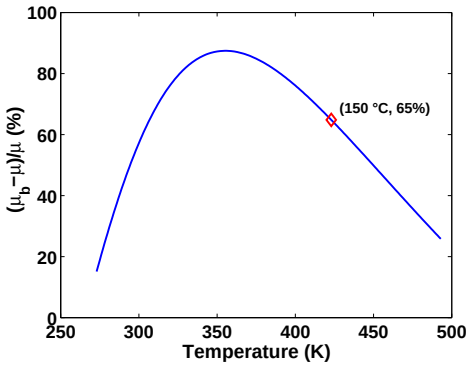

Figure 5.35: Percent of viscosity increase as result of using sodium chloride NaCl in a concentration of 0.225 kg_{NaCl}/kg_{H_2O}, fluid pressure is held at 1.5 MPa.

5.3.3 Phase 1 injection test at GPK1 well, 1993: Permeability enhancement of the reservoir with viscosity–temperature change

The fitting curve presented in figure (5.34) is used to update brine viscosity at each Gauss' point in our FE code with possible viscosity–temperature changes. Assuming brine working fluid, the value of pore fluid viscosity used in all the simulations presented in section (5.2) corresponds to a temperature of 152 °C, see also Table (5.3) and figure (5.34). Injecting cold brine with 50 °C temperature is expected to increase brine viscosity (μ_b) by a threefold, see figure (5.34).

The simulations are to be presented in two manners; firstly with deactivating HF, secondly with activating HF. This shall give us a general view about the effect of increasing brine viscosity as result of cooling on all the simulations presented in section (5.2).

5.3.3.1 Deactivating HF process: Viscosity–temperature change is accounted for

Increasing pore fluid viscosity will definitely decrease the hydraulic conductivity of the porous medium, see equation (5.10). This will in turn decrease the rate by which the hydraulic front is moving. Figure (5.36) shows pore fluid pressure profiles along the plane $y = 0$ m, solid lines account for the simulation when viscosity is updated with temperature, meanwhile dashed lines represent the case of constant brine viscosity $\mu_b = 0.3$ cP.

Following figure (5.36), it is quite clear that increasing the viscosity of the brine as result of cooling slows down the propagation the hydraulic front. The depression in pore pressure values when brine viscosity is increased can be illustrated following Darcy's law. Darcy's law indicates that the change of pore fluid pressure is proportionally related to the negative of the dynamic viscosity, i.e. $\boldsymbol{\nabla} p \propto -\mu$. Increasing dynamic viscosity will increase the change of pore fluid

pressure (in negative) and thus it will reduce the value of pore pressure calculated at a given Gauss' point. The reduction in pore fluid pressure as result of increasing brine viscosity shall definitely hinder the process of HF.

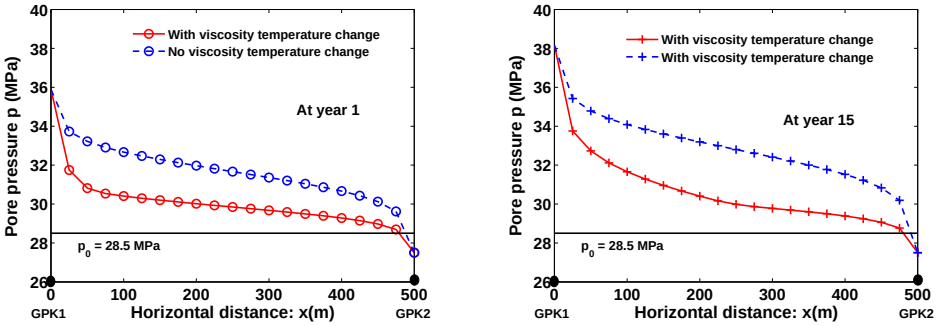

(a) At year 1 (b) At year 15

Figure 5.36: Pore pressure profiles at the plane $y = 0$ m, for the times of 1 and 15 years. Solid lines account for the simulation when viscosity is updated with temperature, meanwhile dashed lines represent the case of constant brine viscosity $\mu_b = 3 \times 10^{-4}$ Pa.s.

Figure (5.37) shows the relation between injection fluid pressure at the well GPK1 and the magnitude of fluid flux at the same well.

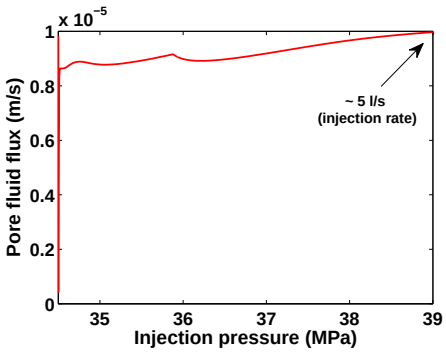

Figure 5.37: Relation between injected pore fluid pressure and the magnitude of created fluid flux at the injection well GPK1, viscosity–temperature change is accounted for.

The relation is no longer linear yet no improved hydraulic connections are created by HF and less fluid flux is obtained, compare with figure (5.14). This non–linear relation, due to viscosity increase, announces more turbulent flow near the injection well equivalent to improving hydraulic connections, compare with figure (5.22).

Figure (5.38) shows the impedance Z of the unenhanced reservoir for a period of 20 years. Clearly, increasing brine viscosity as result of cooling decreases tremendously the efficiency of the HDR reservoir. The impedance continues to increase while the reservoir is becoming more

and more cold announcing less produced volume of fluid and less efficiency of the reservoir, (Murphy et al., [1999]).

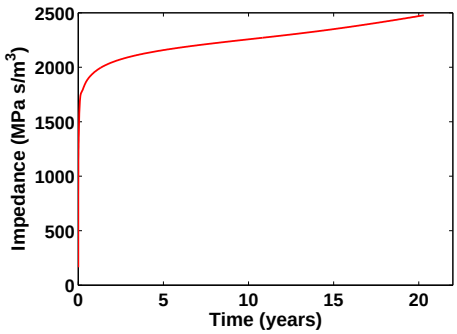

Figure 5.38: Impedance profile of unenhanced HDR reservoir at Soultz–Sous–Forêts, viscosity–temperature change is accounted for.

Increasing brine viscosity also hinders the rate by which heat front is traveling through the reservoir: more viscous fluid is expected to move at lower convective velocity and hence reduced heat convection rate, see figure (5.39) and compare with figure (5.9).

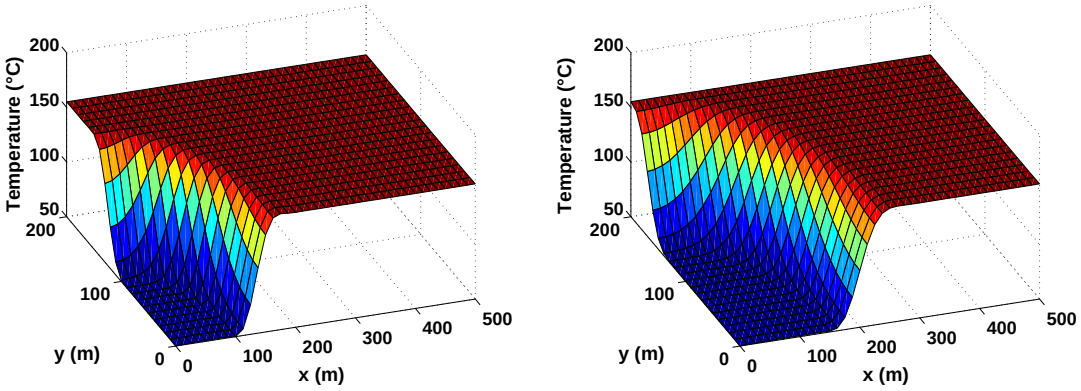

(a) Temperature contour at year 5

(b) Temperature contour at year 10

Figure 5.39: Contours of the mixture temperature at two times, convection of heat and viscosity–temperature change are accounted for.

5.3.3.2 Activating HF process: Viscosity–temperature change is accounted for

As stated previously, increasing pore fluid viscosity hinders the process of HF as it reduces pore fluid pressure. The contours of reservoir permeability at years 1 and 5 are shown in figure (5.40).

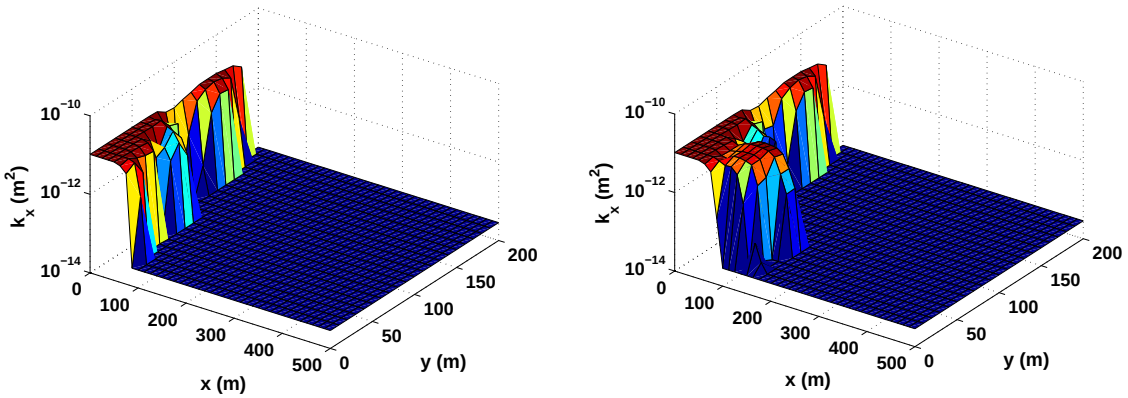

(a) Contour of k_x at year 1

(b) Contour of k_x at year 5

Figure 5.40: Contours of longitudinal permeability component k_x at two times, viscosity–temperature change is accounted for.

Unlike the case when constant brine viscosity was assumed, increasing viscosity by cooling tends to create high fluid gradients near the injection well traveling strongly in $y-$direction and leading fractures to evolve and intersect, see figure (5.40(a)). The lag in heat front, as result of increasing viscosity, renders injection pressure schedule shown in figure (5.8) active[1] till year 5. Cracks continue to evolve following the direction of maximum far field stress (x-direction) leading reservoir permeability to get enhanced up to a distance of 170 m in $x-$direction in 5 years, see figure (5.41).

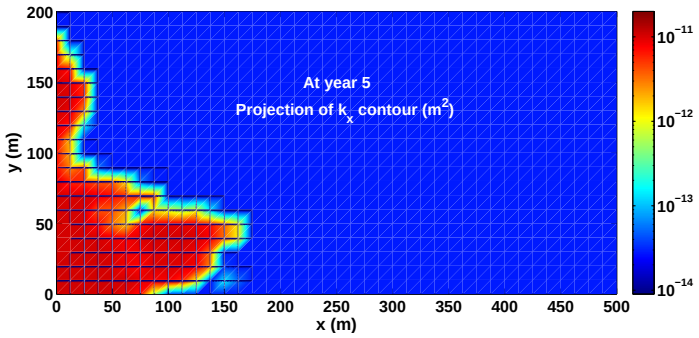

Figure 5.41: Projection of k_x contour in the $x-y$ plane at year 5, viscosity–temperature change is accounted for. Injection pressure schedule shown in figure (5.8) is active till year 5.

The reason why injection pressure schedule of figure (5.8) remains active till year 5 when viscosity–temperature change is accounted for can be explained by the following argument: unlike the case of constant brine viscosity, increasing viscosity by cooling hinders the propagation of the heat wave. The slow propagation of the heat front gives rise to slower movement of thermal

[1]Compare with figure (5.16) where maximum permeability enhancement was obtained at year 1 for the same injection pressure profile.

tensile stresses, which along with the fluid pressure keep on mitigating the geologic compressive stresses and hence helping cracks to evolve.

Figure (5.42) shows the contours of mixture temperature when HF is activated and while accounting for viscosity increase due to brine cooling. Preferential cooling following the new paths of the enhanced permeability is clear. Heat front is traveling mainly in the direction of maximum far field stress following the direction of crack evolution.

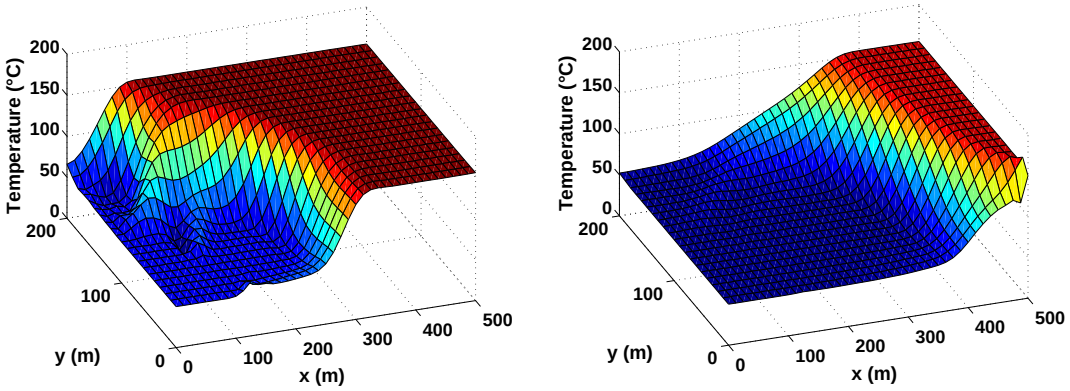

(a) Temperature contour at year 5

(b) Temperature contour at year 10

Figure 5.42: Contours of the mixture temperature at two times with HF, convection of heat and viscosity-temperature change are accounted for.

Following figure (5.43), it is seen that the changes in pore fluid pressure contour are not significant in the regions of enhanced permeability.

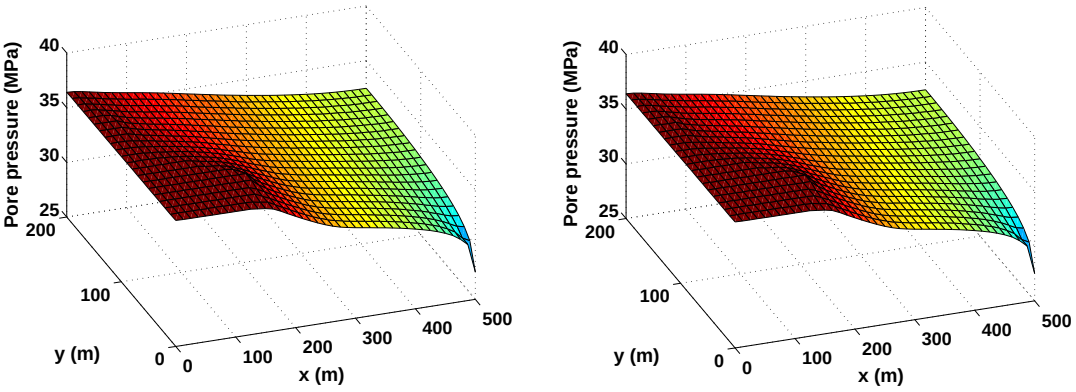

(a) Pore pressure contour at year 5

(b) Pore pressure contour at year 10

Figure 5.43: Contours of the mixture pore pressure at two times with HF, convection of heat and viscosity-temperature change are accounted for.

Figure (5.44) shows the relation between injected pore fluid pressure and the magnitude of

created fluid flux at the injection well GPK1. During the first 5 years, while HF process is active, the produced fluid volume is obviously increasing though the viscosity of the brine fluid is increasing as result of cooling. In fact, permeability enhancement due to HF counteracts the hindrance due to viscosity increase: an approximative linear relation is observed during this period of active HF, compare with figure (5.22). After 5 years, HF process stops which eliminates the part counteracting the hindrance of viscosity increase, thus the produced fluid volume starts to decline considerably.

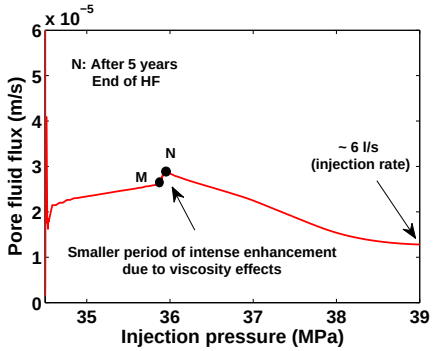

Figure 5.44: Relation between injected pore fluid pressure and the magnitude of created fluid flux at the injection well GPK1, viscosity–temperature change is accounted for.

HF process reduces flow impedance of the HDR reservoir from about 1700 MPa s/m^3 (see figure (5.38) when HF is not activated) to about 700 MPa s/m^3, which should render the operation of the HDR reservoir efficient to a period of about 8.5 years, see figure (5.45). After 8.5 years, flow impedance becomes higher than 1000 MPa s/m^3 and the utilization of the reservoir becomes inefficient. This means that injection pressure must increase to a point HF continues to work such that it counteracts the dragging effects of increased viscosity.

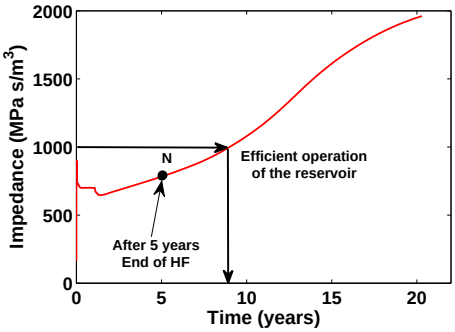

Figure 5.45: Impedance profile of enhanced HDR reservoir at Soultz–Sous–Forêts, viscosity–temperature change is accounted for.

Figure (5.46) proves that an HDR reservoir is going to last longer if the change of geothermal fluid viscosity with temperature is considered, compare with figure (5.25(a)). However this

extended operational life is not of any importance as the impedance exceeds the limits of economic operation from the start in the case of not activated HF and after 8.5 years when HF is activated. The only solution is to increase injection pressure to a point HF continues to work such that it counteracts the dragging effects of increased viscosity.

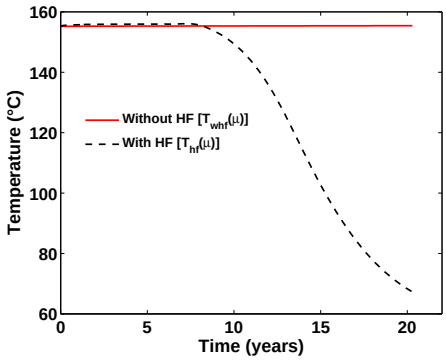

Figure 5.46: Profiles of produced fluid temperature with active HF ($T_{\mathrm{hf}}(\mu)$) and without active HF ($T_{\mathrm{whf}}(\mu)$), convection of heat and viscosity-temperature change are accounted for.

This depressive behavior, as it seems, that stems from changing viscosity with temperature is a direct result of assuming Newtonian geothermal fluids. Authors like (Santoyo et al., [2001]) and (Gutiérrez et al., [2005]) have studied the behavior of eleven Non–Newtonian geothermal fluids: they observed that the temperature changes associated with Non–Newtonian fluids are not as large as we have observed here. In other words, the Non-Newtonian character of the drilling fluids counteracts the thermal dependence of the dynamic viscosity. This statement clearly calls that future studies take into consideration both thermal effects and Non–Newtonian fluids. Possibly their effects may, in some circumstances, be cooperating rather than counteracting.

Other thermophysical properties which include density, specific heat and thermal conductivity do not vary significantly with temperature (less than 15%) for the geothermal drilling fluids. They can be assumed constant and can be approximated by the corresponding values for water substance without remorses, (Gutiérrez et al., [2005]).

5.3.4 EGS using carbon dioxide (CO_2) as working fluid

Evidently, brines used as geothermal working fluids pose a number of concerns. Aside from considerably increasing viscosity due to cooling, brines work as a powerful solvent for many rock minerals especially at elevated temperatures. Dissolution and precipitation effects, if not well considered, clog fracture aperture and hence reduce the permeability and render the EGS reservoir inefficient (in terms of productivity).

However, recent geothermal system applications have been using dissolving brines to enhance the permeability of the reservoirs chemically, see section (5.5). One should keep in mind that, especial and very careful treatment and modeling must be considered when brines are used in running the geothermal systems:

- Modeling brines as Non–Newtonian fluids should be accounted for to counteract the dragging effect of viscosity change.
- Brines salinity must be well recorded so that no excess dissolution and precipitation take place.
- Proppants must be added to the brines so that clogging of fracture aperture due to excessive precipitation may not be encountered.

Since 2000, carbon dioxide (CO_2) as a heat transmission fluid in EGS has triggered a significant research. The idea is appealing: besides capitalizing on the physical advantages of CO2 over water/brines as a working fluid, the technique would, as an ancillary benefit, contribute to storing this heat trapping gas. Indeed, CO_2 has several physical and chemical properties which would render it advantageous as a geothermal working fluid (Pruess, [2006]):

- Reduced power consumption as result of the provided buoyancy force that stems from large density differences[1] between the cold CO_2 in the injection well and the hot CO_2 in the production well.
- CO_2 viscosity is much lower than that of water substance which will develop larger flow velocities for a given pressure gradient which, in turn, reduces the impedance of the EGS reservoir.
- CO_2 is much less effective solvent if compared to water which means mitigating or eliminating clogging problems, such as silica dissolution or precipitation in water based EGS.

5.3.4.1 Thermophysical properties of CO_2

Figure (5.47) shows the phase diagram of CO_2 for different temperature and pressure values, the critical point of CO_2 is shown on the graph corresponding to $T_c = 31.04\ ^\circ\text{C}$ and $p_c = 7.328$ MPa. At lower (subcritical) temperatures and pressures CO_2 can be found in two different phases (liquid or gaseous) as well as two–phase mixtures of these states (on the line of saturation). Supercritical CO_2 forms a strange unique phase that is neither liquid nor gas and can change continuously into either gaseous or liquid CO_2 with no phase boundaries.

[1] Density differences result from CO_2 large thermal expansivity which is, generally, 30 times larger than that of water substance.

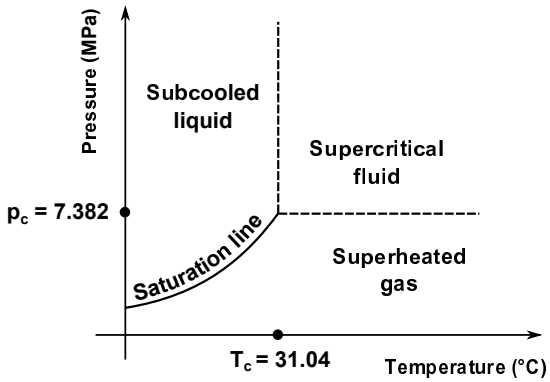

Figure 5.47: Phase diagram of carbon dioxide (CO_2). Dashed lines are only drawn to identify regions with different customary naming conventions. They do not signify phase transitions, as all fluid properties vary smoothly and continuously across these lines, (Pruess, [2006]).

A very important thermophysical property which controls fluid mass flow for a given driving force is called mobility (m) defined as the ratio of density to viscosity of the fluid $m = \rho/\mu$ (inverse of kinematic viscosity s/m^2). CO_2 mobility is generally larger than that of water substance. It also shows a significant dependence on pressure and temperature if compared to water substance.

Interestingly, CO_2 mobility variations are such that they attain maximum values in the regions of intermediate temperatures and pressures extending beyond the saturation line figure (5.47). Mobility becomes smaller for liquid–like CO_2 (low T, high p) and for gas–like CO_2 (high T, low p). For temperature and pressure conditions relevant to geothermal reservoirs operations, CO_2 mobility can be larger than that of water by a factor of 10, see (Pruess, [2008], fig. 2).

5.3.4.2 EGS reservoir heat extraction using CO_2: Benefits and concerns

Recent studies that tried to implement CO_2 as a geothermal working fluid, have come out with several benefits which sound very interesting and promising, (Pruess, [2006]), (Pruess, [2008]) and (Ganzer et al., [2013]):

- For EGS running on CO_2 as a geothermal fluid, heat extraction rates are seen, from simulations and laboratory tests, to be approximately 50% larger than that of water. This indicates a very significant acceleration of energy recovery, i.e. similar to implementing HF process.

- For general EGS working conditions, lower temperature in the vicinity of the injection well increases considerably the viscosity of water if compared to CO_2. This gives CO_2 additional advantage for the flow in the vicinity of the injection well.

- The previous conclusion makes clear that stronger pressure gradients will be developed near the injection well for the case of CO_2. These strong hydraulic gradients mean large drop of pressure available between injection and production wells and hence improved fluid circulation. Figure (5.36) shows how increased viscosity of geothermal brine near the injection well reduces considerably pressure gradients.

- Owing to its large compressibility and expansivity as compared to water, supercritical CO_2 will give rise to strong buoyancy forces between injection and production wells. This will provide an improved fluid circulation, an improved production rate and hence reduced impedance (power consumption) to run the reservoir.

- Using CO_2 as a geothermal fluid will help getting rid, in a matter of geologic storing, of one of the most toxic gases in our planet. Geologic storage of CO_2 will be shown in the form of lost flow mass which depends on the site permeability, porosity and mineralogy of the EGS reservoir.

The very important question about CO_2–based EGS would be always about how to create them. Water–based EGS would include hydraulic and/or chemical enhancement of the existing natural fracture system, and most possibly generating new fractures. CO_2–based EGS would require the additional step of sequestering supercritical CO_2 at the core of the EGS.
(Ueda et al., [2005]) showed a general scheme for CO_2 sequestration into geothermal fields, figure (5.48).

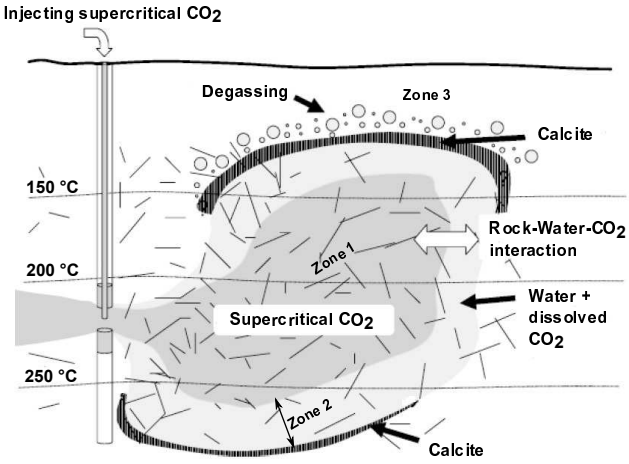

Figure 5.48: General scheme of CO_2 sequestration into geothermal fields, adjusted from (Ueda et al., [2005]).

Supercritical CO_2 is injected down the borehole at high temperature. At the migrating opening of the borehole, CO_2 is dissolved in groundwater where the resulting CO_2–saturated water

reacts with the surrounding rocks and forms calcite assemblages. Such mineral assemblages result in occlusion of the porosity and hence the formation of impermeable layers which can act as a cap rock that traps the supercritical CO_2 fluid.

(Pruess, [2006]) has indicated that a CO_2–based EGS is expected to comprise three reservoir zones:

Zone 1 The core (main volume) of the reservoir from which thermal energy is extracted by pumping CO_2. This volume contains only a single supercritical CO_2 phase and has been created by removing all water by dissolution into the flowing CO_2 stream[1].

Zone 2 Intermediate zone which embodies the main volume and consists of a two–phase mixture of CO_2 and aqueous fluid. Rock–water–CO_2 interactions happen in this zone which result in calcite and clay minerals like kaolinite (Ueda et al., [2005]).

Zone 3 The external zone which is still mainly controlled by the EGS activities. The fluid is a single aqueous phase with dissolved and chemically active CO_2.

Each zone is expected to be different especially for chemical interactions. In zone 1, the long–term exposure to supercritical CO_2 is supposed to cause dehydration of rock minerals which will reduce their molar volume and will increase porosity and permeability of the formations (it is an advantage here).

The chemically active CO_2 in the zone 2 along with the elevated temperatures will render fluid–mineral reactions quite fast. These reactions provide very suitable conditions for sequestering CO_2 in the form of solid minerals. Dissolution and precipitation effects could impact the growth and longevity of the EGS reservoir rendering long–term behavior unclear regarding energy recovery and estimating CO_2 loss rate, see calcite assemblages in figure (5.48), (Pruess, [2006]).

As was cited in the outermost zone, aqueous solutions can be very corrosive and can dissolve several minerals in the rock material aside from attacking steel liners and casings used in the construction of the injection borehole. Yet, sequestration of CO_2 at the core of the EGS reservoir happens quite fast causing aqueous fluids to be quickly removed to reach a single phase of supercritical CO_2. The continuous operation of the CO_2–based EGS reservoir will result in a stream of dry CO_2 that is expected to no longer cause any corrosive effects to the production well, (Pruess, [2006]).

[1]To understand the chemistry of CO_2 solubility in water and brine under reservoir conditions, the reader is advised to check the work of (Enick and Klara, [1990])

5.4 Improving the HFM to stand for shear sliding: Mode I and mode II fracturing model (HFM2)

There are three different approaches to simulate fluid flow in naturally fractured rocks; single continuum, dual continuum and discrete fracture approach. Single continuum approach uses a homogeneous system with a specific permeability tensor to describe the fractured medium. This is the approach that has been and will be used along this research. In dual continuum approach the domain is divided into two interacting parts; 1) the rock matrix where conduction of heat is most dominant and permeability is quite small, 2) the fractures, assumed having regular patterns in most cases, where convection of heat is most dominant and permeability is large, see works of (Gelet et al., [2012]). Finally the discrete fracture approach where fractures are explicitly discretized in the domain, see works of (Bruel, [1995]).

The HFM (Hydraulic Fracturing Model), presented in section (4.3), has been developed to stand for fracture evolution which results from increasing fracture pressure to a point the minimum principal stress becomes tensile and exceeds the tensile strength of the material, and consequently normal separation of fracture surfaces (mode I) occurs. Since fractures in all spatial orientations are considered in the model, shear displacement is expected during fracture opening by mode I, see figure (5.49):

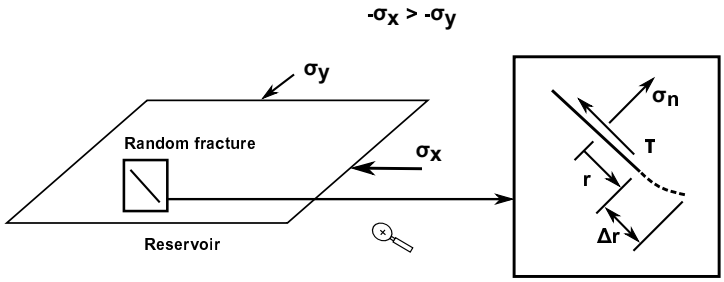

Figure 5.49: Shear slippage of inclined fractures, wing fracture evolution.

5.4.1 From continuum mechanics to fracture mechanics: HFM2

A vertical borehole with a group of vertical cracks with average radius r and arbitrary normal direction $\boldsymbol{n}$ is presented in figure (5.50). This schematic diagram is to be used to define the new Hydraulic Fracturing Model (HFM2) which accounts for opening and shearing of cracks. σ_v is the out–of–plane burden stress.

The same assumptions, as in section (4.3.1), are adopted here. Cracks in the field are relaxed to the initial geophysical conditions which include; the burden and far field stresses, pore fluid pressure and the temperature of the solid and fluid phases.

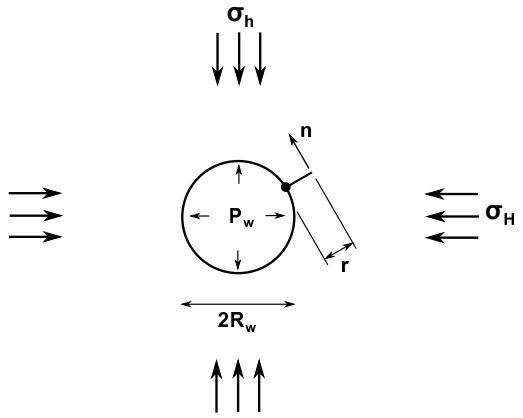

Figure 5.50: Vertical borehole with vertical fracture of average radius r and arbitrary direction $\boldsymbol{n}$.

The Directionally Distributed Fracture Model (DDFM), that was presented and tested experimentally in chapter (2), works for compression and tensile dominated stresses and stands for opening and shearing of cracks, see (Shao et al., [2005]).

If the borehole pressure is gradually increased to a point where the combination of effective normal stress $\sigma_n^{'}$ along with the normal projection of the deviatoric effective stress tensor $\sigma_n^{'d}$ exceeds material toughness, the group of cracks start to propagate and consequently the average aperture of cracks increases. Following section (2.3.2), the model suggested to track the evolution of average radius r of a group of cracks in direction $\boldsymbol{n}$ takes the form:

$$F(\boldsymbol{\sigma}^{'}, r, \boldsymbol{n}) = \sqrt{r}\left[\sigma_n^{'} + f(r)\tilde{q}(\boldsymbol{n})\right] - C_{rc} \leq 0 \tag{5.12}$$

$$\sigma_n^{'} = \boldsymbol{n}.\boldsymbol{\sigma}^{'}.\boldsymbol{n}, \quad \boldsymbol{\sigma}^{'\boldsymbol{d}} = \boldsymbol{\sigma}^{'} - \Big(\frac{\mathrm{tr}\,\boldsymbol{\sigma}^{'}}{3}\Big)\boldsymbol{\delta}, \quad \sigma_n^{'d} = \boldsymbol{n}.\boldsymbol{\sigma}^{'\boldsymbol{d}}.\boldsymbol{n}, \quad \tilde{q}(\boldsymbol{n}) = 3\left\langle\sigma_n^{'d}\right\rangle \tag{5.13}$$

where C_{rc} is the material toughness for mode I and mode II of fracturing. It is worth noting here that the term $[f_{c,t}/(f_{c,t} + \langle -\sigma_n^{'}\rangle)]^m$ is always equal to 1 due to the definition of HF, i.e. $\sigma_n^{'} > 0$ and hence $\langle -\sigma_n^{'}\rangle = 0$.

The function $f(r)$ has the same definition as illustrated in section (2.3.2) and is given by:

$$f(r) = \begin{cases} \xi\left(\dfrac{r_f}{r}\right), & r < r_f \\ \xi, & r \geq r_f \end{cases} \tag{5.14}$$

r_f denotes the critical crack radius for unstable coalescence of cracks, ξ is the model parameter which has the same definition as η[1]. The function $f(r)$ in equation (5.14) has been chosen

[1]The name of the parameter has been changed from η to ξ just to distinguish between HFM2 and HFM of section (3.4).

such that a stable crack growth is assured. The continuum mechanics approach, equations (4.8), (4.9), (4.13) or (4.14), has been presented such that the HFM2 equation (5.12) can be parameterized. ξ is to be determined such that the fracturing will begin at a borehole pressure p_w^f corresponding to one of the cases demonstrated in equations (4.8), (4.9), (4.13) or (4.14) whichever applies.

The derivation of the incremental propagation of a group of cracks of average radius r and arbitrary direction $\boldsymbol{n}$ can be obtained following equations (5.12), (5.13) and (5.14) as shown in section (2.3.2).

When $r < r_f$:

$$F = \sqrt{r}\,\sigma_n^{'} + 3\,\xi\,\left(\frac{r_f}{\sqrt{r}}\right)\,\langle\sigma_n^{'d}\rangle - C_{rc} = 0, \tag{5.15}$$

and,

$$\frac{\partial F}{\partial r} = \frac{1}{2\sqrt{r}}\,\sigma_n^{'} - \frac{3}{2}\,\xi\,\left(\frac{r_f}{\sqrt{r^3}}\right)\,\langle\sigma_n^{'d}\rangle \tag{5.16}$$

$$dr = -\frac{1}{\dfrac{\partial F}{\partial r}}\,\left[\Pi(r,\,\sigma_n^{'})\,(\boldsymbol{n}\otimes\boldsymbol{n}) + \Psi(r,\,\sigma_n^{'d})\,\left(\boldsymbol{n}\otimes\boldsymbol{n} - \frac{\boldsymbol{\delta}}{3}\right)\right]\,:\,d\boldsymbol{\sigma}^{'} \tag{5.17}$$

The functions $\Pi(r,\,\sigma_n^{'})$ and $\Psi(r,\,\sigma_n^{'d})$ are defined as follows:

$$\Pi(r,\,\sigma_n^{'}) = \begin{cases} \sqrt{r}, & \text{if } \sigma_n^{'} > 0 \\ 0, & \text{if } \sigma_n^{'} = 0 \end{cases} \tag{5.18}$$

$$\Psi(r,\,\sigma_n^{'d}) = \begin{cases} 3\,\xi\,\left(\dfrac{r_f}{\sqrt{r}}\right), & \text{if } \sigma_n^{'d} > 0 \\ 0, & \text{if } \sigma_n^{'d} \leq 0 \end{cases} \tag{5.19}$$

The overall crack permeability tensor can be calculated, see section (2.3.2), as follows:

$$\boldsymbol{k}_c = \frac{N}{\Omega}\frac{\lambda}{48}\int_S R(\boldsymbol{n})\,w(\boldsymbol{n})^3\,r(\boldsymbol{n})^2\,(\boldsymbol{\delta} - \boldsymbol{n}\otimes\boldsymbol{n})\,dS \tag{5.20}$$

When $r \geq r_f$ the product $f(r)\,\sqrt{r}$ is no longer decreasing and unstable crack growth is obtained, the latter case is not to be addressed in this research.

5.4.2 Testing and calibrating the HFM2 at a Gauss' point

The fracturing model (HFM2), presented above and which stands for opening and shearing of fractures, is to be validated using the study shown in section (2.5.1.1) by (Shao et al., [2005]) and is to be compared with the numerical response of the HFM model of section (4.3.2).

Again a parallelepiped sample of Lac du Bonnet granite is considered. The rock sample is drilled at the middle where pressurized fluid is permitted to flow. While allowing drainage, the sample is subjected to the stress state shown in figure (5.51).

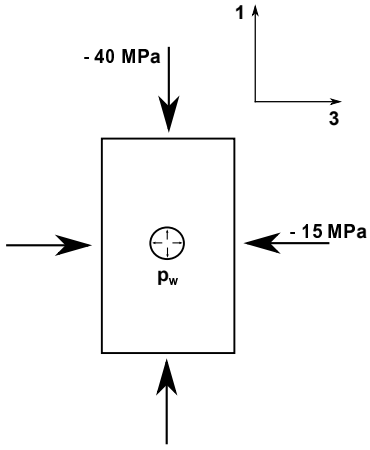

Figure 5.51: parallelepiped sample of Lac du Bonnet granite subjected to the stress state shown and drilled at the middle where fluid is pumped, out of plane stress is equal to -10 MPa.

The parameters used in the simulation are the same as shown in Table (4.2) except for the parameter ξ which replaces η. The value of the model parameter ξ should be determined such that the fractures will start propagating at $p_w^f = 14$ MPa, see section (4.3.2). Let us work equation (5.15) at the threshold of fracture propagation, i.e. $F = 0$:

$$\xi = \frac{C_{rc}\sqrt{r} - r\sigma_n^{'}}{3r_f\langle\sigma_n^{'d}\rangle} \tag{5.21}$$

Following figure (5.51), the first group of cracks to start propagating are those oriented in the direction of maximum principal stress -40 MPa with direction $\boldsymbol{n}$ pointing to the out of plane minimum principal stress -10 MPa. The normal effective stress acting on such a group at the threshold of HF is $\sigma_n^{'} = \sigma_2^{'}$, meanwhile the normal projection of the deviatoric effective stress tensor is calculated for $\boldsymbol{n} = [0,\ 1,\ 0]$ and is equal to $\sigma_n^{'d} = (2\sigma_2^{'} - \sigma_1^{'} - \sigma_3^{'})/3$.

Considering that initial cracks are normally distributed around $r = r_0 = 3$ mm and for a fracturing pressure of $p_w^f = 14$ MPa, the values of $\sigma_n^{'}$ and $\sigma_n^{'d}$ are respectively, 4 MPa and 11.667

MPa. The aforementioned values along with the parameters values presented in Table (4.2) can be substituted in equation (5.21) to get the value of ξ at the pressure threshold of HF (14 MPa):

$$\xi = \frac{C_{rc}\sqrt{r_0} - r_0\,\sigma_n^{'}}{3\,r_f\,\langle\sigma_n^{'d}\rangle} = \frac{1.87\times10^6\times\sqrt{3\times10^{-3}} - 3\times10^{-3}\times4\times10^6}{3\times9\times10^{-3}\times11.667\times10^6} = 0.29 \tag{5.22}$$

The simulation can now be performed and compared with the results of section (4.3.2) as shown below:

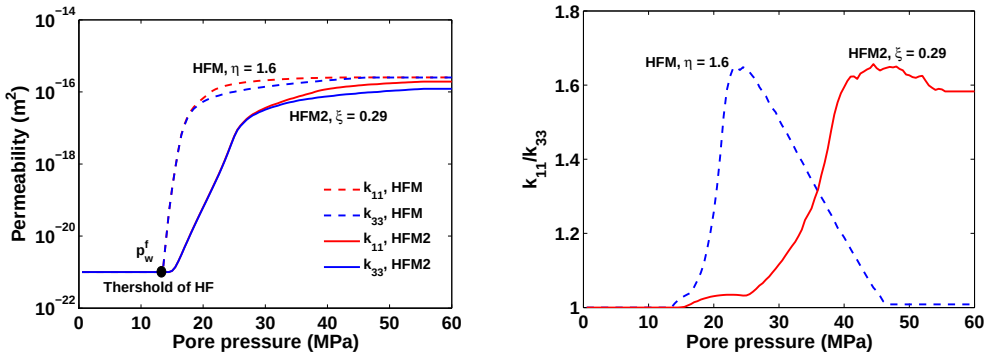

(a) (b)

Figure 5.52: (a) Variation of permeability in the axial and lateral directions while pumping water in a parallelepiped Lac du Bonnet granite sample with a stress state as shown in figure (5.51). (b) The variation of the ratio k_{11}/k_{33} with the formation pressure. Dashed lines describe the simulations of HFM of section (4.3), meanwhile solid lines represent the simulations of the HFM2 discussed above. Colored curves are provided in the digital version.

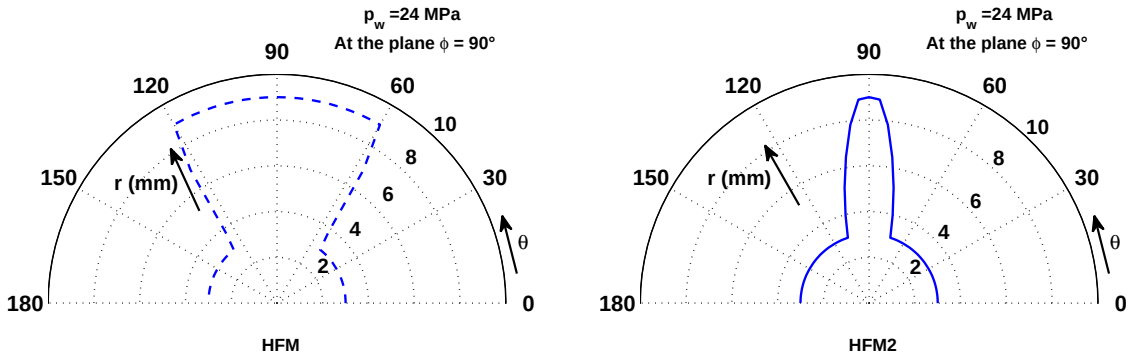

Figure 5.53: Directional evolution of crack radius at $p_w = 24$ MPa and at the plane $\phi = 90°$. The curve with the dashed line represent the simulations using HFM of section (4.3), meanwhile the curve with solid line describe the simulations using HFM2 discussed above.

Following figures (5.52) and (5.53), it is seen that adopting the HFM2 ensures stabler growth of fractures for the same rock, as it accounts for opening and shearing modes of fracturing. The maximum anisotropy of the permeability tensor, as shown in figure (5.52(b)), is about 1.6 for the

two HF models (HFM and HFM2) and remains in the range $[0.4, 2.5]$ as suggested by (Schulze et al., [2001]).

By a glimpse at figure (5.52), the anisotropy ratio k_{11}/k_{33} increases significantly and almost instantly when only mode I (HFM) is considered. However, when modes I and II are adopted (HFM2) the increase in the anisotropy ratio is much smoother due to the shearing effect of fracturing, see also figure (5.53).

At the peaks of the two curves in figure (5.52(b)), most of the cracks pointing to the maximum principal stress -40 MPa and contributing to the component k_{11} are connected ($r = r_f$). Cracks in other orientations continue to grow slowly contributing to the component k_{33}, thus the anisotropy ratio starts to decline after the peaks. When HFM is considered, the increase in the pore fluid pressure will cancel the anisotropy of the permeability tensor, i.e. k_{33} will finally equate k_{11}, which is quite convincing if only opening of fractures is the mode to cause them to evolve. Yet, if HFM2 is adopted, only fractures with certain orientations where $\sigma_n^{'d}$ is positive, i.e. helping shearing fracture plane in equation (5.12), are going to propagate. Other fractures will have negative $\sigma_n^{'d}$ and insufficient $\sigma_n^{'}$ to cause propagating by its own.

The latter case seems to be the most realistic and has been observed by experimental studies, see (Shao et al., [2005]) and (Schulze et al., [2001]). An isotropy ratio of the range $[0.4, 2.5]$ is to be recorded in case of non–hydrostatic loading conditions where wing–crack propagation is the natural phenomenon of fracture evolution.

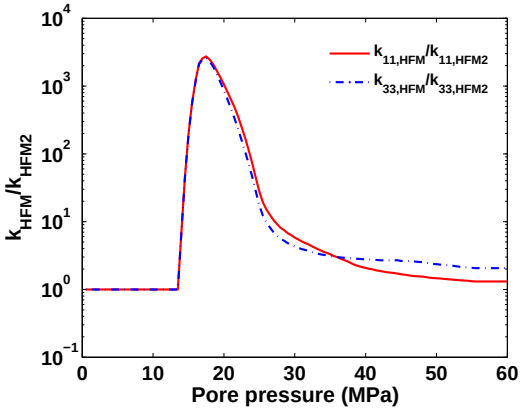

Figure 5.54: Effect of using HFM2 instead of HFM on the order of magnitude for rock permeability. This curve is directly obtained from figure (5.52(a)) by calculating the ratios $k_{11,\mathrm{HFM}}/k_{11,\mathrm{HFM2}}$ and $k_{33,\mathrm{HFM}}/k_{33,\mathrm{HFM2}}$.

Figure (5.54) shows how accounting for mode II of fracture shearing affects considerably the order of magnitude for rock permeability at the beginning of the process of HF. At considerable pore pressure values, the final order of magnitude for axial and lateral permeability components is obtained regardless of the model used to describe HF. Nonetheless, at small pressure values, close to p_w^f, the difference between using HFM or HFM2 can be up to 3 orders of magnitude. This indicates a much smoother evolution of permeability tensor components for HFM2. This is suspected to have significant effects on the process of fluid diffusion.

5.4.3 Phase 1 injection test at GPK1 well, 1993: Permeability enhancement of the reservoir using HFM2

The same boundary and initial conditions as addressed in section (5.2) are considered in the following simulations. Poroelastic and thermoelastic material properties are as in Table (5.3). Material properties for HF are as indicated in Table (5.4) except for the model parameter $\xi = 0.0205$, which is calculated for $p_w^f = 39$ MPa.

Unlike the case when only mode I of fracturing is considered, section (5.2.2), hydraulic fracturing process described by HFM2 requires less energy. For the same pore fluid injection profile, presented in figure (5.8), HF remains active for a period of 2 years meanwhile it was only significant of a period of 1 year when HFM of mode I was considered. After 2 years of stimulation, the reservoir is almost entirely enhanced in the direction of maximum far field stress, i.e. direction of fracture propagation, see figure (5.55).

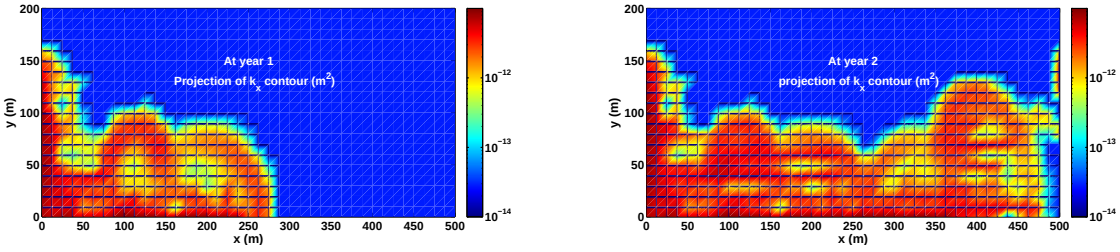

(a) Projection of k_x contour at year 1

(b) Projection of k_x contour at year 2

Figure 5.55: Enhanced longitudinal permeability component k_x depicted as the projection of its contour in the $x-y$ plane. Fracture propagation is in the direction of maximum far field stress. Injection pressure schedule, described in figure (5.8), is sufficient to entirely enhance the HDR reservoir in the longitudinal direction.

Clearly HFM2 provides stabler and smoother evolution of porous block permeability, section (5.4.2), which is translated into slower propagation of the heat front and hence better hydraulic enhancement (in terms of the volume being affected by the process of HF).

The volume of the HDR reservoir enhanced by the process of HF, whether by applying HFM or HFM2, for a period of one year, shows that cracks are evolving in the direction of maximum far field stress (right boundary). This behavior drives longitudinal permeability to get stimulated up to almost the same distances in $x-$ and $y-$ directions for HFM and HFM2 at year 1, compare figures (5.16(b)) and (5.55(a)). The results of these simulations are in good agreement with the microseismic events diagram presented in (Bruel, [1995], fig. 2) for one year of HF, announcing the propagation of hydraulic front and fracture coalescence.

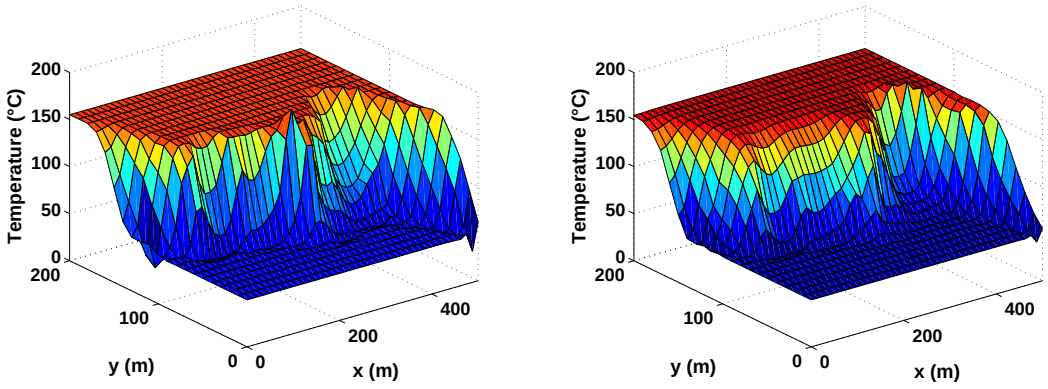

(a) Temperature contour at year 5

(b) Temperature contour at year 10

Figure 5.56: Contours of the mixture temperature at two times with HF by applying HFM2, convection of heat is accounted for.

The preferential cooling following the new paths created by HF is shown in figure (5.56). Heat front diffusion is fast and dominant in the direction of far field stress at which fractures are propagating. The spurious wiggles on the temperature contours come from the shocks that disturb heat front when porous medium permeability is suddenly increased due to HF.

Actually, the sudden increase in the formation permeability leads to significant increase in pore fluid flux and hence pore fluid velocity. The concentration of heat forced convection defined as fluid velocity multiplied by the gradient of mixture temperature $\boldsymbol{v}.\boldsymbol{\nabla}\theta$, see equation (2.19), requires special scrutiny and challenges the numerical methods used generally to solve diffusion–dominated flow problems where convection of heat is not significant. These spurious wiggles will be healed/stabilized by applying the Subgrid Scale (SGS) method, see section (6.4.2).

As observed previously in chapter (4) and section (5.2.2.3), the changes in pore fluid contours are no longer significant in the zones of active HF, see figure (5.57). Since HF simulations by using HFM and/or HFM2 are showing almost the same enhanced volume of the reservoir for a period

of one year, pore pressure contours in figures (5.19(a)) and (5.57(a)) are almost, consequently, the same.

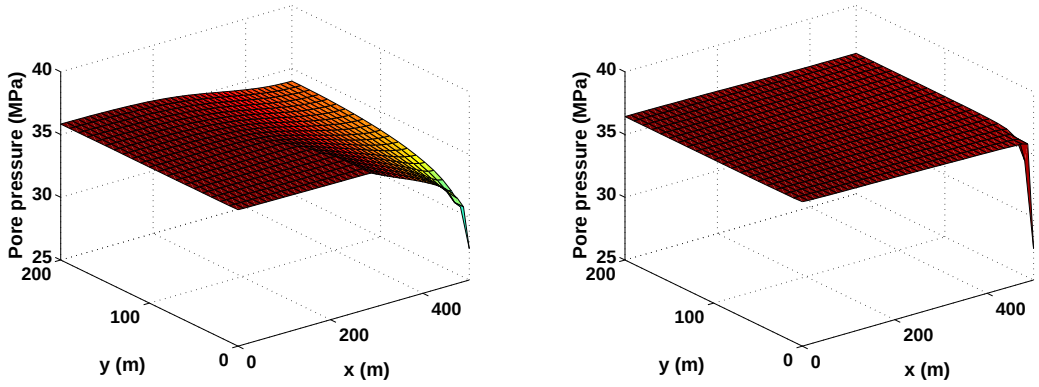

(a) Pore pressure contour at year 1

(b) Pore pressure contour at year 10

Figure 5.57: Contours of the mixture pore pressure at two times with HF by applying HFM2, convection of heat is accounted for.

After 2 years of HF, the HDR reservoir is almost entirely enhanced all over the directions of fracture evolution. The changes in pore pressure contours, over the entire volume of the reservoir, become quite small as the tremendous fast increases in the components of permeability tensor owing to HF become a fact, see figure (5.57(b)).

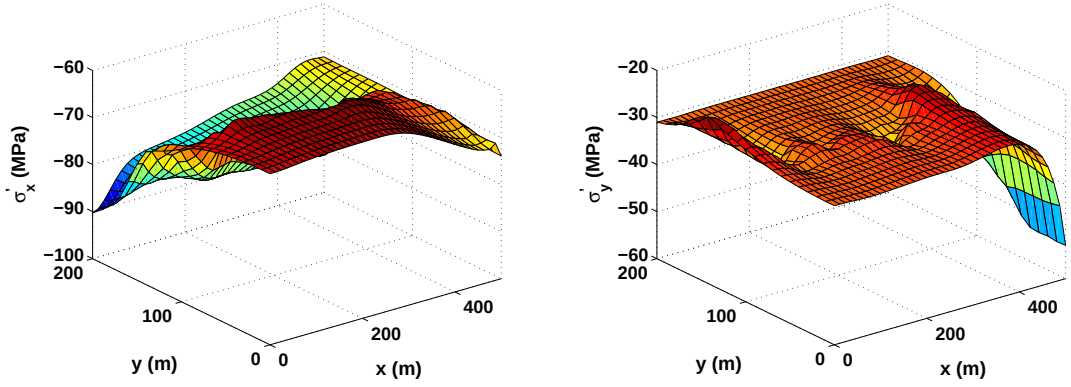

(a) Contour of $\sigma_x^{'}$ at year 10

(b) Contour of $\sigma_y^{'}$ at year 10

Figure 5.58: Contours of longitudinal and transversal effective stresses after 10 years of HF by applying HFM2, convection of heat is accounted for.

Contours of effective stresses, whether longitudinal or transversal, figure (5.58), are following

the preferential cooling derived by the process of HF. Stresses are dawdled in compression in the cooled regions due to tensile thermal stresses. Since the created new highly–permeable paths take most of the fluid gradients directly in the direction of maximum far field stress, effective stresses in such regions decrease in compression as well. However, the deficiency of fluid gradients at other regions, where HF is not working, especially at the outer boundary not far away from the injection well, will cause stresses to increase significantly in compression as it is kept in mind that the reservoir is still hot from the surroundings there. Thus, at the outer boundary, transversal cracks are most likely closing and permeability is possibly decreasing, unless shear dilatation might cope for the reduction in fracture aperture, (Chen et al., [2007]).
Transversal effective stresses are also increasing in compression near the production well and longitudinal cracks are most likely closing causing permeability components to decrease probably.

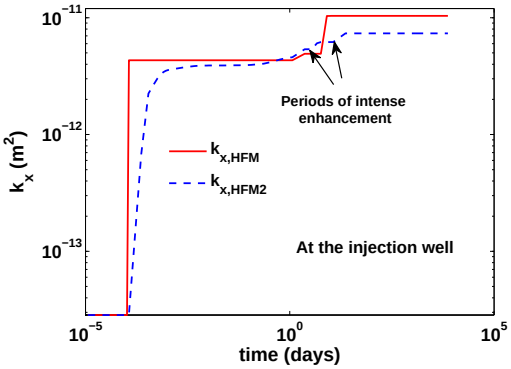

Figure 5.59: Longitudinal permeability k_x history at the injection well: Comparison between the simulations using HFM or HFM2.

As stated in section (5.4.2), HFM2 accounts for mode I and mode II of crack propagation, i.e. cracks are evolving as result of opening and shearing of their planes, and hence a stabler growth of cracks for the same rock. This is clear in figure (5.59) where the curve of longitudinal permeability history is going smoother.

A non–linear relation is found during the first two years of the simulations between injected pore fluid pressure and the magnitude of the induced fluid flux at the injection well GPK1, see figure (5.60(a)). The non–linearity of the pressure record versus flow record tells us that improved connections are created around the borehole GPK1, it also describes the dependence of hydraulic conductivity on the effective stress (Bruel, [1995]), see also figure (5.22).

The jump in the pore fluid pressure–flux record at the end of the process of HF can be explained by considering the curves of permeability history, figure (5.59), and the way pore

fluid flux is calculated. Normal fluid flux over a surface S is calculated by surface integral, see equation (2.11) and section (3.2.1.2), such that: $Q = \iint_S [(-\boldsymbol{k}/\mu).\boldsymbol{\nabla} p]\ \boldsymbol{n}\, dS$.

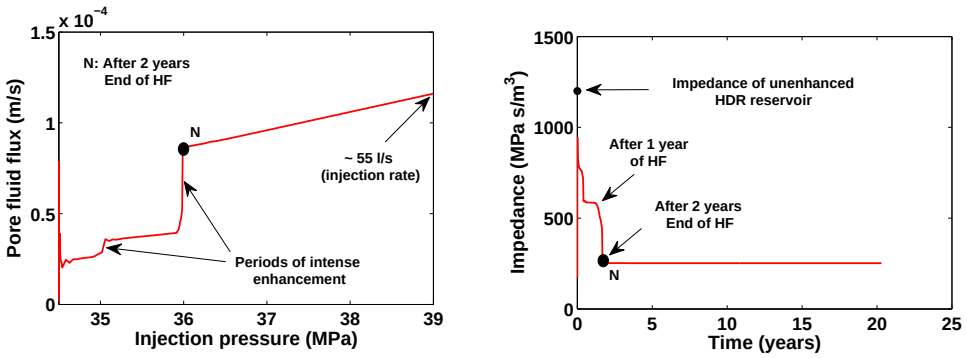

(a) (b)

Figure 5.60: (a) Relation between injected pore fluid pressure and the magnitude of created fluid flux at the injection well GPK1 by HFM2. (b) Impedance profile of the enhanced HDR reservoir at Soultz–Sous–Forêts by HFM2.

For a small change of injection pressure Δp, just before and just after the end of HF, there exists a significant abrupt change in the permeability tensor components averaged all over the volume of the reservoir. This is also clear in figure (5.59) where permeability longitudinal component suddenly jumps to reach the maximum value when cracks coalesce (more clear in the case of HFM of only mode I of fracturing). I think that the jump of the pressure–flux record can be mitigated if the spatial discretization of equation (5.20) is significantly refined, whence a quite small time increment of the simulations is simultaneously considered. Such a suggestion should be exhausting in terms of calculation time and memory storage though.

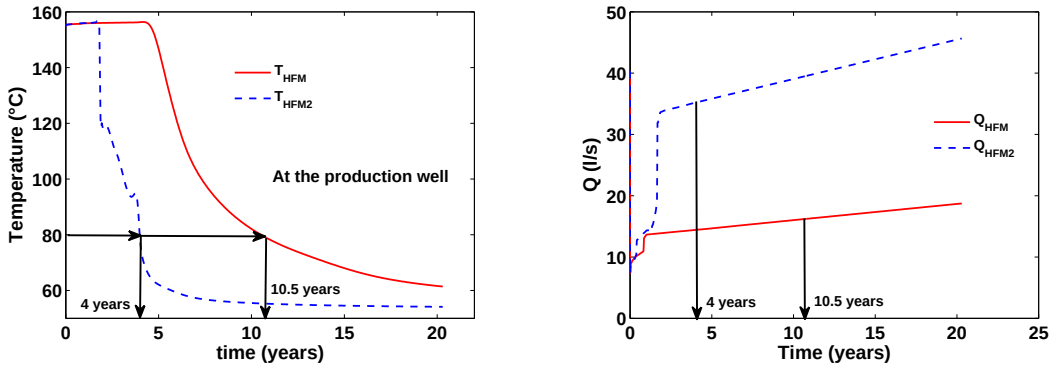

(a) Profiles of produced fluid temperature (b) Profiles of produced flow rate (Q)

Figure 5.61: Comparison between the time profiles of produced (a) temperatures (b) flow rates for HFM and HFM2.

Since HFM2 enhances the permeability of more reservoir volume for the same injection schedule of pore fluid, the reservoir is depleted faster which is well presented in figure (5.61(a)). The produced flow of the HDR reservoir when HFM2 is applied is, by average, 2.5 times higher than that produced if HFM is used in the simulations, figure (5.61(b)). The HDR reservoir will work efficiently for 10.5 years in case of HFM and only 4 years when HFM2 is used. If flow profiles, figure (5.61(b)), are numerically integrated over the efficient age of the HDR reservoir, the useful extracted fluid volume is to be known:

- The volume of efficient fluid produced from the stimulated HDR reservoir by HFM over a period of 10.5 years is 4.922 Million m^3,
- while the volume of efficient fluid produced from the stimulated HDR reservoir by HFM2 over a period of 4 years is 2.681 Million m^3.

These huge amounts of water used are not utterly lost; one should keep in mind that the geothermal fluids are recirculated over the volumes of the HDR reservoirs over and over again. For instance, for the first case of HFM, we need to run the geothermal system on 1280 m^3/day. If there is no fluid lost, this quantity of the geothermal fluid will be pumped and reproduced all along the effective age of 10.5 years.

By the calculations above, about 45.5% of the efficient produced fluid is lost when HFM2 is used in the simulations for the injection schedule presented in figure (5.8). However, using HFM2 has reduced the power needed to operate the HDR reservoir by about 80%, see figure (5.60(b)). The implementation of HF is a matter of compromise; less consumption of energy requires strong HF which, regrettably, means short effective age of the HDR reservoir and hence reduction of the ultimate produced efficient fluid.

(Murphy et al., [1999]) have indicated that the ambitious goal is to enhance HDR reservoirs to a point their impedances become very small, i.e. $Z < 100$ MPa s/m^3 on a consistent basis. This can be achieved numerically by applying HFM2 and choosing such a strong injection schedule where more volume of the reservoir is to be enhanced. Yet, one should keep in mind that such a process will strongly and regrettably reprimand the effective age of the reservoir and thus the amount of the efficient fluid produced.

(Jiang et al., [2013]) have proven that, during heat extraction process, the heat being transferred to the transmissive fluid comes from the reservoir rock matrix directly by convective and conductive heat exchange, with convection of heat being most dominant in most EGS projects

(proven in our work previously). The other part of transferred heat comes indirectly from the rocks enclosing the reservoir mainly by heat conduction into the solid rocks. The contribution from the enclosing rocks is very small compared to the transferred heat coming from the HDR reservoir itself. For the work of (Jiang et al., [2013]), such a contribution did not exceed 6% of the initial reservoir temperature after 25 years of fluid circulation. Thus, assuming that the useful part of the reservoir is properly defined, considering or neglecting the contribution of energy coming from rocks enclosing the reservoir is frivolous. HF process remains a matter of compromise between the energies input to and output from an HDR reservoir.

5.4.4 Beyond HFM and HFM2: Shear slippage under compressive stresses

Neither HFM nor HFM2 accounts for slippage of fracture plane under compressive stresses. Though HFM2 was designed such that mode II of fracturing may occur, the change in fracture aperture was related to the increase of fracture radius under tensile stresses. In fact, as soon as pumping geothermal fluids begins, the geologic stress state acting on the fractures will change. The stress change may create a deviatoric stress condition that can cause shear slippage of some fractures and hence increasing their apertures.

(Bunger et al., [2013]) have developed an analytical approach to simulate the roughness induced opening of fractures in the presence of compressive and shear stresses as well as fluid pressure inside the fracture. They have found that shear slippage takes place along the planes of pre–existing fractures which causes permanent opening of the fracture planes by the fracture asperities (roughness induced opening). Their work has also shown that, this shear slippage before the limit of fracture opening (tensile normal stresses) has a maximum value that can be reached. (Bunger et al., [2013], p. 573) have indicated that this maximum slippage is measured to be of the order of a fraction of a millimeter, meanwhile, fracture aperture that is created by conventional HF is in the order of tens of millimeters.

Consequently, though our research does not stand for fracture slippage before the onset of HF, it is most likely not expected to affect the permeability profiles that were obtained by our simulations.

5.5 Chemical enhancement of geothermal reservoirs: A short review

The permeability of a fractured porous medium is affected by the chemical composition of the injected fluid. Flow is changing corresponding to the paths created and/or closed by dissolution and precipitations of minerals on fracture walls. It is inevitable, in such a case, to consider the fractures as conduits with non–constant apertures which may evolve with time and during the alteration, (Du et al., [2005]).

Considering the chemical enhancement side by side with the process of HF leads to innovative stimulation technologies which take into account a lot of possibilities that were ignored before. Although great breakthroughs have been made in this field, plenty of difficulties are always lying ahead when accounting for the chemical enhancement that include, (Evans et al., [2009]): multiple types of co–existing formation damage, uncertain rock mineralogy, complex chemical reactions between fluids and formation minerals, and fast reaction kinetics at elevated temperatures. Others are: inadequate zonal coverage, limited active penetration of chemicals, rock deconsolidation due to chemical-rock interactions, chemical emulsion and sludge tendencies, corrosion, safety and environmental concerns.

(Taron and Elsworth, [2009]) studied the necessity of coupling between the chemical effects and the geomechanical (mechanical, hydraulic and thermal) processes happening in EGS, as well as quantifying the strength of coupling between the aforementioned processes. They utilized laboratory results of fracture behavior under hydrothermal conditions to describe the aperture changes due to Thermo–Hydro–Mechanical–Chemical (THMC) changes, (Taron and Elsworth, [2009], p. 856). Permeability tensor components have been noticed to be influenced by each geomechanical process separately: a strong influence of mechanical effects in the short–term, the influence of thermal effects in the intermediate–term, and the prolonged and long-term influence of chemical effects.

A strong coupling between chemical and mechanical processes has been observed. Chemical dissolution will affect the aperture (permeability) available for THM responses and the change in the THM responses will affect the flow map, and hence the chemical alteration process.

A method is implemented to introduce the coupling of thermal, hydraulic and chemical precipitation/dissolution processes with the mechanical response in (Taron et al., [2009]). This

article completes the research presented in (Taron and Elsworth, [2009]): it studies the combined influence of stress–driven asperity dissolution, thermal–hydro–mechanical asperity compaction/dilation, and mineral precipitation/dissolution alteration onto the permeability of fractures during thermal, hydraulic, and chemical stimulation. Linear dual–porosity poroelasticity is introduced to mechanically link fractures to the rock matrix. Heterogeneity is accounted for where permeability, porosity, stiffness and chemical composition may spatially differ and evolve with local temperature, effective stress and chemical potential. The approach considers inertial effects in the fracturing process, it has been proven able to represent rapid and undrained response of the fluid–mechanical system to mechanical loading.

Acidizing[1] is the common technique exploited in the process of chemical enhancement. Acidizing has several undesired side effects that include: Clay swelling, fines migration, gel formation/ particle precipitation. These side effects can be mitigated or even avoided by implementing a well designed chemically and physically compatible hydrofluoric[2] acid (FH) stimulation treatment. Care is to be paid when acidizing in the presence of illites, potassium feldspars, sodium feldspars and zeolites, as these compounds can contribute to the formation of matrix–blocking precipitates, (Evans et al., [2009]).

Clay swelling occurs when the acidizing fluids exchange ions with formation minerals: acidizing fluids become more and more brine and thus too weak to prevent clay swelling. Care is to be taken to sustain the salinity of the injected fluid after ion exchange. In details, many water–sensitive clays contain potassium chloride (KCl) and sodium chloride (NaCl) ions that can be exchanged with ions in injected fluids to lower the salinity of the fluid. For example, when a 3% ammonium chloride (NH_4Cl) acidizing fluid flows across a typical ion–exchanging clay, the fluid becomes 3.3% NaCl, a brine too weak to prevent clay swelling, thus requiring a 5% (NH_4Cl) or equivalent solution.

Chemical enhancement has been, for so long, implemented in oil and gas wells: it has been partially adopted in the EGS mainly to remove scaling deposited in the wells after long years of exploitation. However, recently they have been applied to geothermal granitic reservoirs like Fjallbäcka[3] and Beowawe[4] improving fracture network in the host rock, (Evans et al., [2009]).

[1] Well–stimulation method to increase oil production by injecting hydrochloric acid into the oil-bearing formation; the acid dissolves rock to enlarge the porous passages through which the oil must flow.

[2] Hydrofluoric acid (FH) is a solution of hydrogen fluoride in water. Hydrofluoric acid is a highly corrosive acid, capable of dissolving many materials, especially oxides. FH is used as a catalyst to equilibrate the very alkylated formations.

[3] HDR project in Sweden

[4] HDR project in Nevada, USA

In the USA, 90% of the wells chemically enhanced showed two to four fold production increases, (Evans et al., [2009]).

Chemical enhancement was applied to the EGS of Soultz-sous-Forêts: the wells GPK2, GPK3 and GPK4 were subjected to distinct amounts of chemicals and thus the injectivity of each well was altered differently. The chemical treatment at this geothermal site was characterized by high reactivity and slow flow which prevented the penetration of acid to the far field between the wells. Increasing of reactivity is not necessarily the solution; high reactivity involves the creation of "wormholes", i.e. increasing the porosity but not always the permeability of the medium. The compromise could include using high fluid flow that will start HF process, this will result in an enhancement of the fracture network as well as fracture connectivity.

5. DESIGNING HDR RESERVOIRS: IMPEDANCE, EFFICIENCY, FRACTURING MODES AND LIFE–TIME

Chapter 6

Phenomenon of forced heat convection in EGS: Stabilization methods

This chapter sheds a spot of light on the computational difficulties associated with the phenomenon of forced heat convection. The annoying spurious wiggles that appeared on the contours of mixture temperature in the previous research are to be healed and/or mitigated by applying some stabilization methods. The chapter proceeds as follows:

1. The mechanism of forced heat convection is first defined.
2. The Streamline–Upwind/Petrov–Galerkin (SUPG) method, which has been used to stabilize the convection of heat in the previous chapters, is presented.
3. The method of Subgrid Scale (SGS) is studied and integrated into our FE code. The SGS is designed to overcome the defects of the SUPG method especially for early times at the injection well.
4. The simulations of sections (5.2.2) and (5.4.3) are repeated while accounting for the SGS method instead of the SUPG method.
5. Finally, the Discontinuity Capturing Method (DCM) is addressed and integrated into our FE code. The DCM is meant to heal the spurious wiggles of heat convection near the production well at late times.

6.1 Mechanism of forced heat convection

The phenomenon of heat convection, also called advection[1], is defined by the fluid velocity multiplied by the gradient of its temperature, i.e. $\boldsymbol{v}.\boldsymbol{\nabla}\theta$. Heat convection can be well–understood

[1]The term convection and/or advection are synonymous in this research, however, a distinction remains in some disciplines.

by addressing the diffusion and convection of chemicals in a fluid.

Let us assume that we have a solute of concentration $c = c(\boldsymbol{x}, t)$ that is placed in a moving fluid F at position (x_0, y_0) at time $t = 0$. The flow of the fluid F takes place at velocity $\boldsymbol{v} = \boldsymbol{v}(\boldsymbol{x}, t)$ and is assumed uncoupled from external factors like fluid pressure for instance. At time $t = 0^+$, solute will start to diffuse, solute diffusion is homogenized through the space, with velocity $\boldsymbol{v}_s$, figure (6.1).

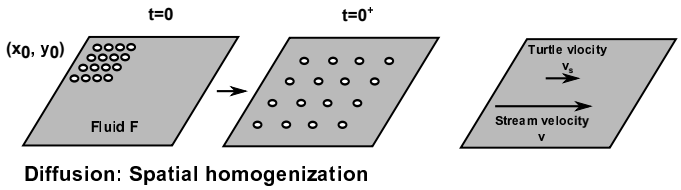

Figure 6.1: Diffusion leads ultimately to a spatially uniform repartition of the solute particles. In a stream, the solute particles with turtle velocity are convected by the flow: their velocity is that of the flow.

Two fluxes are introduced; the absolute flux $\boldsymbol{q}$, and the diffusive flux $\boldsymbol{q}^d$ to highlight that diffusion is relative to the fluid flow:

$$\underbrace{\boldsymbol{q} = c\,\boldsymbol{v}_s}_{\text{absolute flux}}\,, \qquad \underbrace{\boldsymbol{q}^d = c(\boldsymbol{v}_s - \boldsymbol{v})}_{\text{diffusive flux}}, \tag{6.1}$$

where,

$$\boldsymbol{q} = \boldsymbol{q}^d + c\,\boldsymbol{v} \tag{6.2}$$

Diffusion phenomenon is governed by:

- *Fick's law* which relates the diffusive flux $\boldsymbol{q}^d$ to the gradient of solute concentration through the coefficient of molecular diffusion/or the chemical diffusivity D_c, such that:

$$\boldsymbol{q}^d = -D_c\,\boldsymbol{\nabla} c, \quad \text{Fick's law}, \tag{6.3}$$

- and by the balance of mass equation which, in terms of concentration c and absolute flux $\boldsymbol{q}$, writes:

$$\frac{\partial c}{\partial t} + \nabla \boldsymbol{q} = 0 \tag{6.4}$$

By substituting equation (6.2) into equation (6.4) and while assuming constant convective velocity $\boldsymbol{v}$ and constant chemical diffusivity D_c, one writes:

$$\frac{\partial c}{\partial t} + \boldsymbol{v}.\boldsymbol{\nabla} c - D_c\,\nabla^2 c = 0 \tag{6.5}$$

The term $\left[(\partial c/\partial t) + \boldsymbol{v}.\boldsymbol{\nabla} c\right]$ corresponds to a concentration wave propagating at constant velocity $\boldsymbol{v}$.

The aforementioned principle, to describe convection and diffusion of the solute concentration c, is the same as the principle adopted to describe convection and diffusion of heat in a therm–poroelastic framework, see equation (2.19). The difficulty arises when numerically solving the energy balance equation with dominant convection of heat. The Bubnov–Galerkin numerical methods, which are widely and successfully used to describe diffusion–dominated problems, are not as efficient when treating the heat wave $\left[(\partial\theta/\partial t) + \boldsymbol{v}.\boldsymbol{\nabla}\theta\right]$ striking suddenly a stiff boundary. Applying the conventional Bubnov–Galerkin methods will lead to a hyperbolic solution with spurious numerical oscillations presenting the unstable reflexion of the heat wave. Hence, a method is needed to stabilize the spurious numerical oscillations in the hyperbolic solutions of the convection–dominated thermo–poroelastic BVPs.

Several of numerical methods were presented in literature to treat such oscillations, for example: Galerkin/Least Squares method (GLS), the Galerkin/Gradient Least Squares method (GGLS) and the Streamline–Upwind/Petrov–Galerkin (SUPG) method which is widely preferred. The SUPG method does not require an introduction to additional testing functions, it nevertheless adds perturbations to the Galerkin test functions $\boldsymbol{N_\theta}$. This makes this method widely acceptable and easily implemented to the problems of heat convection, not to forget that the SUPG method is clearly described in the available literature.

6.2 Presentation of the SUPG method: Mathematics and FEM formulation

The Streamline–Upwind/Petrov–Galerkin (SUPG) method, is the stabilization method that was used to treat the oscillations of heat convection in all the foregoing research, (Gelet, [2012]). It was sufficient to give smooth numerical solutions except for the following cases:

- Strong pumping near the injection well at early times.
- When HF is activated where strong increase in the permeability tensor components is expected.
- At the production well at late times when the major part of the heat front reaches the stiff boundary there.

6. PHENOMENON OF FORCED HEAT CONVECTION IN EGS: STABILIZATION METHODS

The structure of the SUPG method can be presented by defining the following operators: let $\mathcal{R}$ be the convection–diffusion operator of our generic partial differential equation describing the balance of energy of a thermo–poroelastic transient BVP:

$$\mathcal{R}\,\theta = \dot{\theta} + \boldsymbol{v}.\boldsymbol{\nabla}\theta - \nabla.\left(\psi\,\boldsymbol{\nabla}\theta\right) \quad \text{with} \quad \mathcal{R}_{\text{conv}}\,\theta = \boldsymbol{v}.\boldsymbol{\nabla}\theta, \tag{6.6}$$

$\mathcal{R}$ is the generic differential operator, $\mathcal{R}_{\text{conv}}$ is the convective part of the whole operator $\mathcal{R}$, $\boldsymbol{v}$ is the convective velocity vector (m/s) and ψ is the thermal diffusivity (m^2/s). The transient term of equation (6.6) is integrated in the definition of the differential operator $\mathcal{R}$ as first order derivatives do not only occur in convective terms, but also in time–dependent terms $\partial\theta/\partial t$ of non–stationary problems.

The equation of balance of energy with its source term f can now be expressed by benefiting from the definition of equation (6.6) such that:

$$\mathcal{R}\,\theta - f = 0, \quad \text{with} \quad \mathcal{R}_{\text{conv}}\,\theta = \boldsymbol{v}.\boldsymbol{\nabla}\theta \tag{6.7}$$

The weak form associated with equation (6.7) is defined as:

$$\int_V \delta\theta\,(\mathcal{R}\,\theta - f)\,dV \tag{6.8}$$

$\delta\theta$ is the variation corresponding to the temperature change θ. SUPG method is a Petrov–Galerkin method, thus two different interpolation functions are to be presented to interpolate the unknown temperature change θ and the variation $\delta\theta$:

$$\begin{aligned} \theta &= \boldsymbol{N_\theta}\,\boldsymbol{\theta}^e, \\ \delta\theta &= \boldsymbol{W_\theta}\,\delta\boldsymbol{\theta}^e \end{aligned} \tag{6.9}$$

The SUPG method requires that the standard Bubnov–Galerkin shape functions $\boldsymbol{N_\theta}$ to be modified by a streamline upwind perturbation. The shape function $\boldsymbol{W_\theta}$ is henceforth defined as:

$$\begin{aligned} \boldsymbol{W_\theta} &= \boldsymbol{N_\theta} + \tau\,\mathcal{R}_{\text{conv}}\,\boldsymbol{N_\theta}, \\ &= \boldsymbol{N_\theta} + \tau\,\boldsymbol{v}\,\boldsymbol{\nabla}\boldsymbol{N_\theta} \end{aligned} \tag{6.10}$$

By substituting the definition (6.10) into equation (6.8), the discretized form of the problem is reached:

$$\sum_{e=1}^{N^{el}} [\delta\boldsymbol{\theta}^e]^T \int_{V^e} \boldsymbol{N_\theta^T}\left(\mathcal{R}\,\theta - f\right) dV^e + \underbrace{\sum_{e=1}^{N^{el}} [\delta\boldsymbol{\theta}^e]^T \int_{V^e} \underbrace{\left(\boldsymbol{\nabla}\boldsymbol{N_\theta^T}\,\boldsymbol{v^T}\right)\tau}_{\text{Streamline perturbation}} \left(\mathcal{R}\,\theta - f\right) dV^e}_{\text{Stabilizing part}} = 0 \tag{6.11}$$

τ is the stabilization parameter that weighs the perturbation, it is expressed as:

$$\tau = \frac{h}{2|\boldsymbol{v}|}\left(\coth(\alpha) - \frac{1}{\alpha}\right) \tag{6.12}$$

$\boldsymbol{v}$ is the convective velocity (m/s), h is the typical element length (m) and α is the Péclet number. It is observed that the perturbation term $\tau\,\boldsymbol{v}\,\boldsymbol{\nabla N_\theta}$ is applied to all the terms of the weak form; including those in the residual form f of the differential equation. This ensures that consistency is enforced from the beginning and that the exact solution should fulfill the stabilized weak form.

To overcome the deficiencies of the SUPG method to heal the oscillations in the numerical solutions of transient convection–diffusion problems at early times and when activating the HF process, the Subgrid Scale/Gradient Subgrid Scale SGS/GSGS method is to be presented.

6.3 Presentation of the SGS/GSGS method

As stated previously, the application of the SUPG method is not sufficient to circumvent the spurious oscillations in the numerical solutions especially at small time steps and when activating HF. Actually, the characteristic time that weighs the stabilization of the SUPG method, equation (6.12), can be expressed as in (Yin et al., [2009]):

$$\tau = \frac{1}{\sqrt{\left(\frac{2}{\Delta t}\right)^2 + \left(\frac{2|\boldsymbol{v}|}{h}\right)^2 + 9\left(\frac{4\psi}{h^2}\right)^2}}, \tag{6.13}$$

with Δt being time step (s), $\boldsymbol{v}$ is the convective velocity (m/s), h is the typical element length (m) and ψ is the thermal diffusivity (m^2/s). For quite small time steps ($\Delta t \to 0$), the stabilization coefficient τ becomes inefficient:

$$\lim_{\Delta t \to 0} \tau = 0 \tag{6.14}$$

It is, henceforth, conceivable that the calculation of the stabilization parameter must take into account a time–dependent factor, where the transition between the convection–dominated situation and the diffusion dominated situation in small time steps is indeed natural.

The incorporation of a time–dependent factor into the calculation of the stabilizing parameters was declared in the work of (Harari, [2004]). He suggested that the transient term of a transient diffusion problem can be transformed into a reaction term by first discretizing in time instead of the conventional method of first discretizing in space. This scheme of integration

converts the transient diffusion problem into a steady diffusion–reaction problem. The latter problem is deployed to include the conversion of a transient convection–diffusion problem to a steady convection–diffusion–reaction problem addressed by (SGS/GSGS method).

6.3.1 The mathematics of the SGS/GSGS method

In an explicit form, let $\mathcal{L}$ be the steady state convection–diffusion operator and $\mathcal{L}_*$ its adjoint defined by integration by parts[1]:

$$\begin{aligned} \mathcal{L}\,\varphi &= \boldsymbol{v}.\boldsymbol{\nabla}\varphi - \nabla.\left(\psi\,\boldsymbol{\nabla}\varphi\right) \\ -\mathcal{L}_*\,\varphi &= \boldsymbol{v}.\boldsymbol{\nabla}\varphi + \nabla.\left(\psi\,\boldsymbol{\nabla}\varphi\right) \end{aligned} \tag{6.15}$$

The transient problem is now defined as:

$$\frac{\partial\phi}{\partial t} + \mathcal{L}\,\varphi - f = 0, \quad \text{with appropriate boundary and initial conditions} \tag{6.16}$$

Now the transient convection–diffusion problem (6.16) is to be integrated using a generalized trapezoidal scheme (β method) to find a definition for the reaction term:

$$\frac{\varphi_{n+1} - \varphi_n}{\Delta t} + \left(\mathcal{L}\,\varphi - f\right)_{n+\beta} = 0 \tag{6.17}$$

Applying the notation $a_{n+\beta} = (1-\beta)\,a_n + \beta\,a_{n+1}$, equation (6.17) can be further manipulated:

$$\begin{aligned} \beta\left(\mathcal{L}_{n+1}\,\varphi_{n+1} - f_{n+1}\right) + \frac{\varphi_{n+1}}{\Delta t} &= -(1-\beta)\left(\mathcal{L}_n\,\varphi_n - f_n\right) + \frac{\varphi_n}{\Delta t} \\ \boldsymbol{v}_{n+1}.\boldsymbol{\nabla}\varphi_{n+1} - \nabla.\left(\psi\,\boldsymbol{\nabla}\varphi_{n+1}\right) + \frac{\varphi_{n+1}}{\beta\,\Delta t} &= \frac{-(1-\beta)}{\beta}\,\mathcal{L}_n\,\varphi_n + \frac{f_{n+\beta}}{\beta} + \frac{\varphi_n}{\beta\,\Delta t} \end{aligned} \tag{6.18}$$

Let us redefine the operators $\mathcal{L}$ and $\mathcal{L}_*$ such that all the time–independent parts of equation (6.18) are highlighted in the left hand side:

$$\begin{aligned} \mathcal{N}\,\varphi &= \boldsymbol{v}.\boldsymbol{\nabla}\varphi - \nabla.\left(\psi\,\boldsymbol{\nabla}\varphi\right) - s\,\varphi, \\ -\mathcal{N}_*\,\varphi &= \boldsymbol{v}.\boldsymbol{\nabla}\varphi + \nabla.\left(\psi\,\boldsymbol{\nabla}\varphi\right) + s\,\varphi \end{aligned} \tag{6.19}$$

s is the source parameter $s > 0$ for production and $s < 0$ for dissipation or absorption, the source parameter s is expressed following the formulation:

$$s = \frac{-1}{\beta\,\Delta t} < 0 \tag{6.20}$$

[1] $\int_V \left(\mathcal{L}\,\varphi, \mathcal{E}\right) = \int_{\partial V} \left[\boldsymbol{v}\,\varphi\,\mathcal{E} - (\psi\,\boldsymbol{\nabla}\varphi)\mathcal{E} + \varphi\,\psi\,\boldsymbol{\nabla}\mathcal{E}\right].\boldsymbol{n}\,dS + \int_V \left(\varphi, \mathcal{L}_*\,\mathcal{E}\right)$

The steady convection–diffusion–reaction problem at step $n+1$ is now defined as:

$$\mathcal{N}\,\varphi_{n+1} - F_{n+1} = 0, \tag{6.21}$$

where:

$$F_{n+1} = \frac{-(1-\beta)}{\beta}\,\mathcal{L}_n\,\varphi_n + \frac{f_{n+\beta}}{\beta} + \frac{\varphi_n}{\beta\,\Delta t} \tag{6.22}$$

The weak form of the stabilized equation (6.21) can be reached by discretizing the space Ω into N^{el} non–overlapping generic elements e, where each occupies a volume of Ω^e such that $\Omega = \sum_{e=1}^{N^{el}} \Omega^e$. For a spatial discretization corresponding to a characteristic length h, let $\mathcal{N}^h$ be the associated finite element solution and $\mathcal{V}^h$ be the weighting space. For some variation w^h which belongs to the space $\mathcal{V}^h$, the integral weak form of equation (6.21) is sought such that: let us find $\varphi^h \in \mathcal{N}^h$ for all $w^h \in \mathcal{V}^h$:

$$\begin{aligned}\int_V w^h\Big(\mathcal{N}\,\varphi^h_{n+1} - F_{n+1}\Big)\,dV + \sum_{e=1}^{N^{el}}\int_{V^e}\Big(-\mathcal{N}_*\,w^h_{n+1}\Big)\,\tau^e_{00}\Big(\mathcal{N}\,\varphi^h_{n+1} - F_{n+1}\Big)\,dV^e \\ + \sum_{e=1}^{N^{el}}\int_{V^e}\boldsymbol{\nabla}\Big(-\mathcal{N}_*\,w^h_{n+1}\Big)\,\tau^e_{11}\,\boldsymbol{\nabla}\Big(\mathcal{N}\,\varphi^h_{n+1} - F_{n+1}\Big)\,dV^e = 0,\end{aligned} \tag{6.23}$$

where τ^e_{00} (s) and τ^e_{11} ($\mathrm{m}^2\,\mathrm{s}$) are the stabilization parameters.

(Hauke et al., [2007]) have implemented the one–dimensional nodal exactness to relate the stabilization parameters τ^e_{00} and τ^e_{11} to two dimensionless parameters namely t_{00} and t_{11} respectively:

$$\begin{aligned}\tau^e_{00} &= \frac{h}{|\boldsymbol{v}|}\,t_{00}, \\ \tau^e_{11} &= \frac{h^3}{|\boldsymbol{v}|}\,t_{11}\end{aligned} \tag{6.24}$$

With nodal exactness they could have also defined these dimesionless parameters as:

$$t_{00} = \left(-2\sigma + \frac{\sigma^2\,\sinh(\alpha)}{-\cosh(\alpha) + \cosh(\gamma) + \sigma\,\sinh(\alpha)}\right)^{-1}, \tag{6.25}$$

and:

$$t_{11} = \frac{1}{6\sigma^3}\left(-3 - \sigma^2 + \frac{3\sigma}{\alpha} + \frac{\sigma\Big(3\sigma\cosh(\gamma) + (-3+\sigma^2)\sinh(\alpha)\Big)}{-2\cosh(\alpha) + 2\cosh(\gamma) + \sigma\sinh(\alpha)}\right), \tag{6.26}$$

where:

$$\gamma = \sqrt{\alpha(-2\sigma + \alpha)} \tag{6.27}$$

α and σ are the Péclet and Damköhler numbers respectively, they are defined as following:

$$\begin{aligned} \alpha &= \frac{|\boldsymbol{v}|\, h}{2\psi} = \frac{\text{Advection}}{\text{Diffusion}} \quad \text{Péclet number} \\ \sigma &= \frac{s\, h}{|\boldsymbol{v}|} = \frac{\text{Reaction}}{\text{Advection}} \quad \text{Damköhler number} \end{aligned} \tag{6.28}$$

Figure (6.2) shows the behavior of the parameters t_{00} and t_{11} as functions of α and σ.

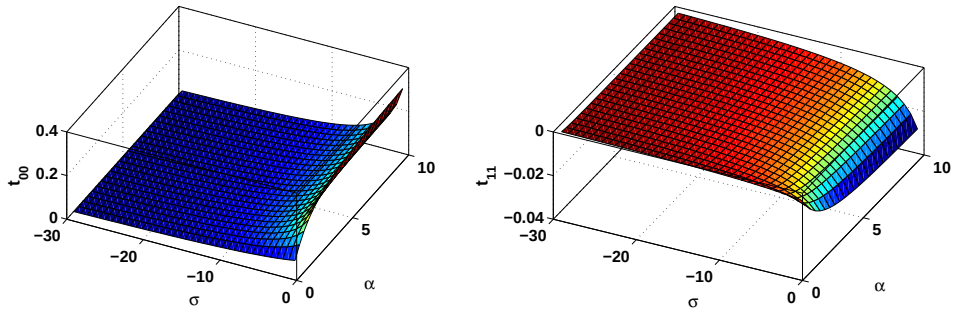

(a) (b)

Figure 6.2: Dimensionless stabilizing parameters (a): t_{00} and (b): t_{11} stemming from one–dimensional nodal exactness of (Hauke et al., [2007]).

Following figure (6.2), it is noted that the first stabilizing parameter t_{00} is always positive, whereas the second one t_{11} is always negative. For linear elements in one–dimensional problems and under convective–diffusive dominant condition ($\sigma \to 0$), the method, equation (6.23), produces the same modification as the SUPG method in absence of the reactive term s:

$$\begin{aligned} &\int_V w^h \left(\mathcal{N}\, \varphi^h_{n+1} - F_{n+1} \right) dV \\ &+ \sum_{e=1}^{N^{el}} \int_{V^e} \left(\boldsymbol{v}.\boldsymbol{\nabla} w^h_{n+1} \right) \tau^e_{\text{ad}} \left(\mathcal{N}\, \varphi^h_{n+1} - F_{n+1} \right) dV^e = 0, \end{aligned} \tag{6.29}$$

where τ^e_{ad} is the standard convective parameter obtained by implementing Taylor expansion of equations (6.25) and (6.27) around ($\sigma = 0$), see (Hauke et al., [2007]) for details[1]:

$$\tau^e_{ad} \xrightarrow{\sigma \to 0} \frac{h}{2|\boldsymbol{v}|} \left(\coth(\alpha) - \frac{1}{\alpha} \right) \tag{6.30}$$

[1]The third term of equation (6.23) disappears as at least for linear elements in one–dimensional problems, the gradient stabilization term $\mathcal{N}_*$ disappears when $\sigma \to 0$ as τ^e_{11} is uniformly bounded to a limit, see figure (6.2(b)), whence $s^2\, \tau^e_{11} \to 0$. The previous remark becomes quite clear if the matrix form of equation (6.23) is derived for one–dimensional problem with linear elements.

(Hauke et al., [2007], p. 309–311) have provided several definitions for the stabilizing parameters τ_{00}^{e} and τ_{11}^{e} depending on the dominant limit: convective–diffusive with no reaction limit, without convection limit, reaction dominated limit and high Péclet number limit. The general expressions of equations (6.25) and (6.26) were implemented in the work of (Yin et al., [2009]) and showed good results. The only case where it is thought that the general expressions could be troublesome is when s is very small, generally less than 10^{-3} (1/s). The latter case is addressed as "convective–diffusive with no reaction limit".

The convective–diffusive with no reaction limit is to be implemented if s is considerably small: as $s \to 0$, $\sigma \to 0^{-}$ as well and the dimensionless stabilizing parameters are to be calculated as follows:

$$\begin{aligned} t_{00} &\rightarrow \frac{1}{2}\left(\coth(\alpha) - \frac{1}{\alpha}\right) \xrightarrow{\alpha \to 0} \frac{\alpha}{6} \\ t_{11} &\rightarrow \frac{-1}{24}\left(\frac{3}{\alpha^3}\big(1 - \alpha\coth(\alpha)\big) + \coth(\alpha)\right) \xrightarrow{\alpha \to 0} -\frac{\alpha}{60} \end{aligned} \tag{6.31}$$

For a single porosity isotropic thermo-poroelastic BVP, the equation of balance of energy of the mixture, section (2.1.2.3), reads:

$$\frac{\partial \theta}{\partial t} + \boldsymbol{v}.\boldsymbol{\nabla}\theta - \nabla.\left(\psi\,\boldsymbol{\nabla}\theta\right) - \underbrace{T_0\left[\frac{\left(\phi_0\,\alpha_f + (\kappa - \phi_0)\alpha_s^{'}\right)}{\rho\, c_v}\frac{\partial p}{\partial t} - \frac{K\,\alpha_s^{'}}{\rho\, c_v}\frac{\partial}{\partial t}\left(\varepsilon_{kk}\right)\right]}_{f} = 0 \tag{6.32}$$

By comparing equation (6.32) and equation (6.16) and while considering the definitions of equation (6.28), the appropriate convection and reaction parameters α and σ read:

$$\alpha \leftarrow \frac{|\boldsymbol{v}|\,h}{2\psi}, \tag{6.33}$$

and:

$$\sigma \leftarrow -\frac{h}{\beta\,\Delta t\,|\boldsymbol{v}|} \tag{6.34}$$

6.3.2 The finite element formulation of the SGS/GSGS method

Let us consider that we have a geothermal BVP on which we desire to apply the SGS/GSGS method. Let us denote the geostatic step by n at which the discretization of time is $t = 0$. At step $n+1$, Δt is recorded, equation (6.32) is discretized in time to get the reaction term $(s\,\theta)$ and the term $\mathcal{N}\theta_{n+1}$ is defined as, see equation (6.19):

$$\mathcal{N}\,\theta_{n+1} = \boldsymbol{v}_{n+1}.\boldsymbol{\nabla}\theta_{n+1} - \nabla.\left(\psi\,\boldsymbol{\nabla}\theta_{n+1}\right) - s\,\theta_{n+1} \tag{6.35}$$

The source term F_{n+1} is more complicated and depends on the trapezoidal time integration of f, equation (6.32), and the term $\mathcal{L}_n\,\theta_n$, equation (6.22):

$$\mathcal{L}_n\,\theta_n = \boldsymbol{v}_n.\boldsymbol{\nabla}\theta_n - \nabla.\left(\psi\,\boldsymbol{\nabla}\theta_n\right), \tag{6.36}$$

Let us define the following two coefficients[1]:

$$a_p = \frac{\left(\phi_0\,\alpha_f + (\kappa - \phi_0)\alpha_s^{'}\right)T_0}{\rho\,c_v}, \tag{6.37}$$

and:

$$a_\varepsilon = -\frac{K\,\alpha_s^{'}\,T_0}{\rho\,c_v} \tag{6.38}$$

The source term f is now defined as:

$$f = a_p\,\frac{\partial p}{\partial t} + a_\varepsilon\,\frac{\partial}{\partial t}(\varepsilon_{kk}), \tag{6.39}$$

and hence:

$$\frac{f_{n+\beta}}{\beta} = \frac{1}{\beta}\Big[(1-\beta)\,f_n + \beta\,f_{n+1}\Big], \tag{6.40}$$

and finally,

$$\frac{f_{n+\beta}}{\beta} = \left(\frac{1}{\beta} - 1\right)\Big[a_p\,\dot{p}^n + a_\varepsilon\,\dot{\varepsilon}_{kk}^n\Big] + a_p\,\dot{p}^{n+1} + a_\varepsilon\,\dot{\varepsilon}_{kk}^{n+1} \tag{6.41}$$

By substituting equations (6.36) and (6.41) into equation (6.22), the following definition of F_{n+1} is obtained:

$$\begin{aligned} F_{n+1} \;&=\; -\left(\frac{1}{\beta} - 1\right)\Big[\boldsymbol{v}_n.\boldsymbol{\nabla}\theta_n - \nabla.\left(\psi\,\boldsymbol{\nabla}\theta_n\right)\Big] + \left(\frac{1}{\beta} - 1\right)\Big[a_p\,\dot{p}^n + a_\varepsilon\,\dot{\varepsilon}_{kk}^n\Big] + a_p\,\dot{p}^{n+1} + a_\varepsilon\,\dot{\varepsilon}_{kk}^{n+1} \\ &-\; s\theta_n \end{aligned} \tag{6.42}$$

By collecting all the previously known terms (of step n) of equation (6.42) in one side, the formulation of a variable $-G_n$ is defined as follows:

$$-\,G_n = \left(1 - \frac{1}{\beta}\right)\Big[\boldsymbol{v}_n.\boldsymbol{\nabla}\theta_n - \nabla.\left(\psi\,\boldsymbol{\nabla}\theta_n\right)\Big] - s\theta_n + \left(\frac{1}{\beta} - 1\right)\Big[a_p\,\dot{p}^n + a_\varepsilon\,\dot{\varepsilon}_{kk}^n\Big] \tag{6.43}$$

[1]Despite being a rigorous assumption, a homogeneous isotropic continuum is assumed

Now F_{n+1} sums to:

$$F_{n+1} = a_p\,\dot{p}^{n+1} + a_\varepsilon\,\dot{\varepsilon}_{kk}^{n+1} - G_n \tag{6.44}$$

Equation (6.35) and equation (6.44) are to be integrated into equation (6.23) along with appropriate definition of interpolation functions to get the matrix form of the weak formulation of equation (6.23). Let $\boldsymbol{N_\theta}$ be the interpolation functions chosen to interpolate the unknown temperature change θ, and $\boldsymbol{W_\theta}$ the interpolation functions to interpolate the variation corresponding to the temperature change $\delta\theta$:

$$\begin{aligned} \theta &= \boldsymbol{N_\theta}\,\boldsymbol{\theta}^e, \\ w^h &= \boldsymbol{W_\theta}\,\delta\boldsymbol{\theta}^e = \boldsymbol{N_\theta}\,\delta\boldsymbol{\theta}^e, \\ \boldsymbol{\nabla}(w^h) &= \boldsymbol{\nabla}\boldsymbol{N_\theta}\,\delta\boldsymbol{\theta}^e \end{aligned} \tag{6.45}$$

Bubnov–Galerkin method is adopted in this study and the weighting functions are chosen equal to the shape functions ($\boldsymbol{W_\theta} = \boldsymbol{N_\theta}$). The matrix form of equation (6.23) is to be obtained working term by term of the Left Hand Side (LHS):

1. First term of the LHS

$$\int_V w^h \Big(\mathcal{N}\,\varphi_{n+1}^h - F_{n+1}\Big)\,dV \tag{6.46}$$

Yet:

$$\mathcal{N}\,\theta_{n+1}^h - F_{n+1} = \underbrace{\boldsymbol{v}_{n+1}.\boldsymbol{\nabla}\theta_{n+1} - \underbrace{\psi\Delta\theta_{n+1}}_{\Delta\theta=\nabla.(\boldsymbol{\nabla}\theta)} - s\,\theta_{n+1}}_{\mathcal{N}\,\theta_{n+1}^h} - a_p\,\dot{p}^{n+1} - a_\varepsilon\,\dot{\varepsilon}_{kk}^{n+1} + G_n \tag{6.47}$$

Integration by parts for the diffusive term ($\psi\Delta\theta_{n+1}$):

$$\int_V w^h\,\psi\Delta\theta_{n+1}\,dV = \int_{\partial V} w^h\,\psi\,\boldsymbol{\nabla}\theta.\boldsymbol{n}\,ds - \int_V \psi\boldsymbol{\nabla}w^h.\boldsymbol{\nabla}\theta\,dV \tag{6.48}$$

The definitions of equation (6.45) are now applied to get the matrix form of equation (6.46):

$$\begin{aligned} &\int_{V^e} w^h\,(\mathcal{N}\,\theta_{n+1})^e\,dV^e = \int_{V^e} w^h\,\mathcal{N}(\boldsymbol{N_\theta}\,\boldsymbol{\theta}_{n+1}^e)\,dV^e \\ &= \sum_{e=1}^{N^{el}} [\delta\boldsymbol{\theta}^e]^T \Bigg[\int_{V^e} \boldsymbol{N_\theta^T}\Big(\boldsymbol{v}_{n+1}^T\,\boldsymbol{\nabla}\boldsymbol{N_\theta} - s\,\boldsymbol{N_\theta}\Big)\,\boldsymbol{\theta}_{n+1}^e + (\boldsymbol{\nabla}\boldsymbol{N_\theta})^T\,\psi\,\boldsymbol{\nabla}\boldsymbol{N_\theta}\,\boldsymbol{\theta}_{n+1}^e\,dV^e \\ &+ \boldsymbol{N_\theta^T}\int_{\partial V^e} \frac{h_{n+1}}{\rho\,c_v}\,ds^e\Bigg], \end{aligned} \tag{6.49}$$

where:

$$\frac{h_{n+1}}{\rho\, c_v} = \frac{-\chi\, \boldsymbol{\nabla}\theta_{n+1}.\boldsymbol{n}}{\rho\, c_v} = \frac{\text{Normal heat flux}}{\text{volumetric specific heat}}, \quad \chi \text{ is the thermal conductivity} \tag{6.50}$$

Before getting the matrix form of the weak formulation $\int_V -w^h\, F_{n+1}\, dV$, let us recall the following definitions from section (3.2.2):

$$\begin{aligned} \boldsymbol{v_s} &= \boldsymbol{N_u}\, \dot{\boldsymbol{u}}^e, \\ \dot{\varepsilon}_{kk} &= \text{tr}(\boldsymbol{B_u})\, \dot{\boldsymbol{u}}^e, \\ \dot{p} &= \boldsymbol{N_p}\, \dot{\boldsymbol{p}}^e \end{aligned} \tag{6.51}$$

The quantity $-G_n$, of equation (6.44), is to be treated as an influence working at the interior of the generic elements; hence no integration by parts is needed for the diffusive term $\psi\, \nabla.(\boldsymbol{\nabla}\theta_n)$. Let us define the coefficient a_β such that:

$$a_\beta = \left(1 - \frac{1}{\beta}\right) \tag{6.52}$$

$$\begin{aligned} &\int_{V^e} -w^h\, F^e_{n+1}\, dV^e \\ &= \sum_{e=1}^{N^{el}} [\delta\boldsymbol{\theta}^e]^T \int_{V^e} \boldsymbol{N}^{\boldsymbol{T}}_{\boldsymbol{\theta}} \Big[- a_p\, \boldsymbol{N_p}\, \dot{\boldsymbol{p}}^e_{n+1} - a_\varepsilon\, \text{tr}(\boldsymbol{B_u})\, \dot{\boldsymbol{u}}^e_{n+1} - a_\beta \Big[\boldsymbol{v}_n^T\, \boldsymbol{\nabla} \boldsymbol{N_\theta} - \psi\, \boldsymbol{\Delta} \boldsymbol{N_\theta} \Big] \boldsymbol{\theta}^e_n \\ &+ s\, \boldsymbol{N_\theta}\, \boldsymbol{\theta}^e_n + a_\beta \Big[a_p\, \boldsymbol{N_p}\, \dot{\boldsymbol{p}}^e_n + a_\varepsilon\, \text{tr}(\boldsymbol{B_u})\, \dot{\boldsymbol{u}}^e_n \Big] \Big] dV^e \end{aligned} \tag{6.53}$$

The elemental vector $\boldsymbol{G^e_n}$ is now defined as:

$$\boldsymbol{G^e_n} = \boldsymbol{N}^{\boldsymbol{T}}_{\boldsymbol{\theta}} \left(-a_\beta \Big[\boldsymbol{v}_n^T\, \boldsymbol{\nabla} \boldsymbol{N_\theta} - \psi\, \boldsymbol{\Delta} \boldsymbol{N_\theta} \Big] \boldsymbol{\theta}^e_n + s\, \boldsymbol{N_\theta}\, \boldsymbol{\theta}^e_n + a_\beta \Big[a_p\, \boldsymbol{N_p}\, \dot{\boldsymbol{p}}^e_n + a_\varepsilon\, \text{tr}(\boldsymbol{B_u})\, \dot{\boldsymbol{u}}^e_n \Big] \right) \tag{6.54}$$

Let us now consider the following definitions for four elemental vectors namely, $\boldsymbol{C^e_{1\theta}}$, $\boldsymbol{C^e_{1u}}$, $\boldsymbol{C^e_{1p}}$ and $\tilde{\boldsymbol{C}}^{\boldsymbol{e}}_{\boldsymbol{1\theta}}$:

$$\boldsymbol{C^e_{1\theta}} = \boldsymbol{N}^{\boldsymbol{T}}_{\boldsymbol{\theta}}\, \boldsymbol{v}^T_{n+1}\, \boldsymbol{\nabla} \boldsymbol{N_\theta} + \psi\, (\boldsymbol{\nabla} \boldsymbol{N_\theta})^T\, \boldsymbol{\nabla} \boldsymbol{N_\theta} - s\, \boldsymbol{N}^{\boldsymbol{T}}_{\boldsymbol{\theta}}\, \boldsymbol{N_\theta}, \tag{6.55}$$

$$\boldsymbol{C^e_{1u}} = -a_\varepsilon \, \boldsymbol{N^T_\theta} \, \mathrm{tr}(\boldsymbol{B_u}), \tag{6.56}$$

$$\boldsymbol{C^e_{1p}} = -a_p \, \boldsymbol{N^T_\theta} \, \boldsymbol{N_p}, \tag{6.57}$$

and finally:

$$\boldsymbol{\tilde{C}^e_{1\theta}} = -a_\beta \, \boldsymbol{N^T_\theta} \, \boldsymbol{v}_n^T \, \boldsymbol{\nabla N_\theta} + a_\beta \, \psi \, \boldsymbol{N^T_\theta} \, \boldsymbol{\Delta N_\theta} + s \, \boldsymbol{N^T_\theta} \, \boldsymbol{N_\theta} \tag{6.58}$$

The elemental vector $\boldsymbol{G^e_n}$ becomes:

$$\boldsymbol{G^e_n} = \boldsymbol{\tilde{C}^e_{1\theta}} \, \boldsymbol{\theta}^e_n - a_\beta \, \boldsymbol{C^e_{1p}} \, \dot{\boldsymbol{p}}^e_n - a_\beta \, \boldsymbol{C^e_{1u}} \, \dot{\boldsymbol{u}}^e_n \tag{6.59}$$

(Finite element matrices $\boldsymbol{\tilde{C}^e_{1\theta}}$, $\boldsymbol{C^e_{1p}}$ and $\boldsymbol{C^e_{1u}}$ are estimated at time n)

The matrix form of equation (6.46) finally sums to:

$$\begin{aligned} &\int_{V^e} \; w^h \Big((\mathcal{N}\,\theta_{n+1})^e - F^e_{n+1} \Big) \, dV^e \\ = \;& \sum_{e=1}^{N^{el}} [\delta\boldsymbol{\theta}^e]^T \Bigg[\int_{V^e} \boldsymbol{C^e_{1\theta}} \, \boldsymbol{\theta}^e_{n+1} + \boldsymbol{C^e_{1u}} \, \dot{\boldsymbol{u}}^e_{n+1} + \boldsymbol{C^e_{1p}} \, \dot{\boldsymbol{p}}^e_{n+1} \, dV^e + \int_{V^e} \boldsymbol{G^e_n} \, dV^e \\ + \;& \int_{\partial V^e} \boldsymbol{N^T_\theta} \, \frac{h_{n+1}}{\rho \, c_v} \, ds^e \Bigg] \end{aligned} \tag{6.60}$$

2. Second term of the LHS

$$\sum_{e=1}^{N^{el}} \int_{V^e} \Big(-\mathcal{N}_* \, w^h_{n+1} \Big)^e \, \tau^e_{00} \underbrace{\Big((\mathcal{N}\,\theta_{n+1})^e - F^e_{n+1} \Big)}_{\text{Worked in equation (6.46)}} \, dV^e \tag{6.61}$$

$$\Big(-\mathcal{N}_* \, w^h_{n+1} \Big)^e = -\mathcal{N}_* (\boldsymbol{N_\theta} \, \delta\boldsymbol{\theta}^e) = \boldsymbol{v}^T_{n+1} \, \boldsymbol{\nabla N_\theta} \, \delta\boldsymbol{\theta}^e + \psi \, \boldsymbol{\Delta N_\theta} \, \delta\boldsymbol{\theta}^e + s \, \boldsymbol{N_\theta} \, \delta\boldsymbol{\theta}^e \tag{6.62}$$

$$\sum_{e=1}^{N^{el}} \int_{V^e} \Big(-\mathcal{N}_* \, w^h_{n+1} \Big)^e \, dV^e = \sum_{e=1}^{N^{el}} [\delta\boldsymbol{\theta}^e]^T \int_{V^e} (\boldsymbol{\nabla N_\theta})^T \, \boldsymbol{v}_{n+1} + \psi \, (\boldsymbol{\Delta N_\theta})^T + s \, \boldsymbol{N^T_\theta} \, dV^e \tag{6.63}$$

The boundary terms of the thermal diffusivity in equation (6.61) vanish by considering the stabilization contribution only on the element's interior.

$$(\mathcal{N}\,\theta_{n+1})^e = \mathcal{N}(\boldsymbol{N_\theta}\,\boldsymbol{\theta}^e_{n+1}) = \left[\boldsymbol{v}^T_{n+1}\,\boldsymbol{\nabla N_\theta} - \psi\,\boldsymbol{\Delta N_\theta} - s\,\boldsymbol{N_\theta}\right]\,\boldsymbol{\theta}^e_{n+1} \tag{6.64}$$

$$\begin{aligned} -F^e_{n+1} &= -a_p\,\boldsymbol{N_p}\,\dot{\boldsymbol{p}}^e_{n+1} - a_\varepsilon\,\mathrm{tr}(\boldsymbol{B_u})\,\dot{\boldsymbol{u}}^e_{n+1} - a_\beta\left[\boldsymbol{v}^T_n\,\boldsymbol{\nabla N_\theta} - \psi\,\boldsymbol{\Delta N_\theta}\right]\boldsymbol{\theta}^e_n + s\,\boldsymbol{N_\theta}\,\boldsymbol{\theta}^e_n \\ &+ a_\beta\left[a_p\,\boldsymbol{N_p}\,\dot{\boldsymbol{p}}^e_n + a_\varepsilon\,\mathrm{tr}(\boldsymbol{B_u})\,\dot{\boldsymbol{u}}^e_n\right] \end{aligned} \tag{6.65}$$

Let us define the following elemental vectors:

$$\boldsymbol{C^{eT}_{2\theta}} = (\boldsymbol{\nabla N_\theta})^T\,\boldsymbol{v}_{n+1} + \psi\,(\boldsymbol{\Delta N_\theta})^T + s\,\boldsymbol{N^T_\theta}, \tag{6.66}$$

$$\boldsymbol{C^e_{2\theta}} = \boldsymbol{v}^T_{n+1}\,\boldsymbol{\nabla N_\theta} + \psi\,\boldsymbol{\Delta N_\theta} + s\,\boldsymbol{N_\theta}, \tag{6.67}$$

$$\boldsymbol{C^e_{3\theta}} = \boldsymbol{v}^T_{n+1}\,\boldsymbol{\nabla N_\theta} - \psi\,\boldsymbol{\Delta N_\theta} - s\,\boldsymbol{N_\theta}, \tag{6.68}$$

$$\boldsymbol{C^e_{2u}} = -a_\varepsilon\,\mathrm{tr}(\boldsymbol{B_u}), \tag{6.69}$$

$$\boldsymbol{C^e_{2p}} = -a_p\,\boldsymbol{N_p}, \tag{6.70}$$

$$\boldsymbol{\tilde{C}^{eT}_{2\theta}} = -a_\beta\,\boldsymbol{v}^T_n\,\boldsymbol{\nabla N_\theta} + a_\beta\,\psi\,\boldsymbol{\Delta N_\theta} + s\,\boldsymbol{N_\theta} \tag{6.71}$$

and finally:

$$\boldsymbol{M^e_n} = \boldsymbol{\tilde{C}^e_{2\theta}}\,\boldsymbol{\theta}^e_n - a_\beta\,\boldsymbol{C^e_{2p}}\,\dot{\boldsymbol{p}}^e_n - a_\beta\,\boldsymbol{C^e_{2u}}\,\dot{\boldsymbol{u}}^e_n \tag{6.72}$$

(Finite element matrices $\boldsymbol{\tilde{C}^e_{2\theta}}$, $\boldsymbol{C^e_{2p}}$ and $\boldsymbol{C^e_{2u}}$ are estimated at time n)

Finally the matrix form of equation (6.62) is expressed as:

$$\begin{aligned} &\sum_{e=1}^{N^{el}} \int_{V^e}\left(-\mathcal{N}_*\,w^h_{n+1}\right)^e \tau^e_{00}\left((\mathcal{N}\,\theta_{n+1})^e - F^e_{n+1}\right)dV^e \\ &= \sum_{e=1}^{N^{el}}[\delta\boldsymbol{\theta}^e]^T\int_{V^e}\boldsymbol{C^{eT}_{2\theta}}\,\tau^e_{00}\left[\boldsymbol{C^e_{3\theta}}\,\boldsymbol{\theta}^e_{n+1} + \boldsymbol{C^e_{2u}}\,\dot{\boldsymbol{u}}^e_{n+1} + \boldsymbol{C^e_{2p}}\,\dot{\boldsymbol{p}}^e_{n+1} + \boldsymbol{M^e_n}\right]dV^e \end{aligned} \tag{6.73}$$

3. Third term of the LHS

Before proceeding in getting the matrix form of the third term of the LHS of equation (6.23), let us keep in mind the following definitions[1]:

$$\boldsymbol{\nabla}(-\mathcal{N}_*\,\varphi) = \boldsymbol{v}.\boldsymbol{\nabla^2}\varphi + \boldsymbol{\nabla v}\,\boldsymbol{\nabla}\varphi + \boldsymbol{\nabla}\Big(\nabla.\,(\psi\,\boldsymbol{\nabla}\varphi)\Big) + s\,\boldsymbol{\nabla}\varphi, \tag{6.74}$$

$$\boldsymbol{\nabla}(\mathcal{N}\,\varphi) = \boldsymbol{v}.\boldsymbol{\nabla^2}\varphi + \boldsymbol{\nabla v}\,\boldsymbol{\nabla}\varphi - \boldsymbol{\nabla}\Big(\nabla.\,(\psi\,\boldsymbol{\nabla}\varphi)\Big) - s\,\boldsymbol{\nabla}\varphi, \tag{6.75}$$

and,

$$\boldsymbol{\nabla}(\mathcal{L}\,\varphi) = \boldsymbol{v}.\boldsymbol{\nabla^2}\varphi + \boldsymbol{\nabla v}\,\boldsymbol{\nabla}\varphi - \boldsymbol{\nabla}\Big(\nabla.\,(\psi\,\boldsymbol{\nabla}\varphi)\Big) \tag{6.76}$$

It is henceforth concluded:

$$\begin{aligned}\boldsymbol{\nabla}\Big(-\mathcal{N}_*\,w^h_{n+1}\Big)^e &= \boldsymbol{\nabla}\Big(-\mathcal{N}_*(\boldsymbol{N_\theta}\,\delta\boldsymbol{\theta}^e)\Big)\\ &= \boldsymbol{v}^T_{n+1}\,\boldsymbol{\nabla^2 N_\theta}\,\delta\boldsymbol{\theta}^e + (\boldsymbol{\nabla v}_{n+1})^T\,\boldsymbol{\nabla N_\theta}\,\delta\boldsymbol{\theta}^e + \psi\,\boldsymbol{\nabla}(\boldsymbol{\Delta N_\theta})\,\delta\boldsymbol{\theta}^e\\ &+ s\,\boldsymbol{\nabla N_\theta}\,\delta\boldsymbol{\theta}^e\end{aligned} \tag{6.77}$$

$$\begin{aligned}&\sum_{e=1}^{N^{el}}\ \int_{V^e}\boldsymbol{\nabla}\Big(-\mathcal{N}_*\,w^h_{n+1}\Big)^e\,dV^e\\ =\ &\sum_{e=1}^{N^{el}}\ [\delta\boldsymbol{\theta}^e]^T\int_{V^e}(\boldsymbol{\nabla^2 N_\theta})^T\,\boldsymbol{v}_{n+1} + (\boldsymbol{\nabla N_\theta})^T\,\boldsymbol{\nabla v}_{n+1} + \psi\,\Big(\boldsymbol{\nabla}(\boldsymbol{\Delta N_\theta})\Big)^T + s\,(\boldsymbol{\nabla N_\theta})^T\,dV^e\end{aligned} \tag{6.78}$$

The boundary terms of the thermal diffusivity vanish by considering the stabilization contribution only on the element's interior.

$$\begin{aligned}\boldsymbol{\nabla}(\mathcal{N}\,\theta_{n+1})^e &= \boldsymbol{\nabla}\Big(\mathcal{N}(\boldsymbol{N_\theta}\,\boldsymbol{\theta}^e_{n+1})\Big)\\ &= \Big[\boldsymbol{v}^T_{n+1}\,\boldsymbol{\nabla^2 N_\theta} + (\boldsymbol{\nabla v}_{n+1})^T\,\boldsymbol{\nabla N_\theta} - \psi\,\boldsymbol{\nabla}(\boldsymbol{\Delta N_\theta}) - s\,\boldsymbol{\nabla N_\theta}\Big]\,\boldsymbol{\theta}^e_{n+1}\end{aligned} \tag{6.79}$$

$$\begin{aligned}\boldsymbol{\nabla}(-F^e_{n+1}) &= -a_p\,\boldsymbol{\nabla N_p}\,\dot{\boldsymbol{p}}^e_{n+1} - a_\varepsilon\,\boldsymbol{\nabla}\mathrm{tr}(\boldsymbol{B_u})\,\dot{\boldsymbol{u}}^e_{n+1} - a_\beta\Big[\boldsymbol{v}^T_n\,\boldsymbol{\nabla^2 N_\theta} + (\boldsymbol{\nabla v}_n)^T\,\boldsymbol{\nabla N_\theta}\\ &- \psi\,\boldsymbol{\nabla}(\boldsymbol{\Delta N_\theta})\Big]\,\boldsymbol{\theta}^e_n + s\,\boldsymbol{\nabla N_\theta}\,\boldsymbol{\theta}^e_n + a_\beta\Big[a_p\,\boldsymbol{\nabla N_p}\,\dot{\boldsymbol{p}}^e_n + a_\varepsilon\,\boldsymbol{\nabla}\mathrm{tr}(\boldsymbol{B_u})\,\dot{\boldsymbol{u}}^e_n\Big]\end{aligned} \tag{6.80}$$

[1] $\boldsymbol{\nabla}(\boldsymbol{v}.\boldsymbol{\nabla}\varphi) = \dfrac{\partial}{\partial x_i}\left(v_k\dfrac{\partial\varphi}{\partial x_k}\right) = v_k\,\dfrac{\partial^2\varphi}{\partial x_i\partial x_k} + \dfrac{\partial v_k}{\partial x_i}\,\dfrac{\partial\varphi}{\partial x_k}$

Let us define the following elemental vectors:

$$\boldsymbol{\nabla C^{eT}_{2\theta}} = (\boldsymbol{\nabla^2 N_\theta})^T \boldsymbol{v}_{n+1} + (\boldsymbol{\nabla N_\theta})^T \boldsymbol{\nabla v}_{n+1} + \psi \left(\boldsymbol{\nabla(\Delta N_\theta)}\right)^T + s\,(\boldsymbol{\nabla N_\theta})^T, \tag{6.81}$$

$$\boldsymbol{\nabla C^{e}_{2\theta}} = \boldsymbol{v}^T_{n+1} \boldsymbol{\nabla^2 N_\theta} + (\boldsymbol{\nabla v}_{n+1})^T \boldsymbol{\nabla N_\theta} + \psi \left(\boldsymbol{\nabla(\Delta N_\theta)}\right) + s\,\boldsymbol{\nabla N_\theta}, \tag{6.82}$$

$$\boldsymbol{\nabla C^{e}_{3\theta}} = \boldsymbol{v}^T_{n+1} \boldsymbol{\nabla^2 N_\theta} + (\boldsymbol{\nabla v}_{n+1})^T \boldsymbol{\nabla N_\theta} - \psi\,\boldsymbol{\nabla(\Delta N_\theta)} - s\,\boldsymbol{\nabla N_\theta}, \tag{6.83}$$

$$\boldsymbol{\nabla C^{e}_{2u}} = -a_\varepsilon\,\boldsymbol{\nabla}\mathrm{tr}(\boldsymbol{B_u}), \tag{6.84}$$

$$\boldsymbol{\nabla C^{e}_{2p}} = -a_p\,\boldsymbol{\nabla N_p}, \tag{6.85}$$

$$\boldsymbol{\nabla \tilde{C}^{eT}_{2\theta}} = -a_\beta\,\boldsymbol{v}^T_n \boldsymbol{\nabla^2 N_\theta} - a_\beta\,(\boldsymbol{\nabla v}_n)^T \boldsymbol{\nabla N_\theta} + a_\beta\,\psi \left(\boldsymbol{\nabla(\Delta N_\theta)}\right) + s\,\boldsymbol{\nabla N_\theta}, \tag{6.86}$$

and finally:

$$\boldsymbol{\nabla M^{e}_{n}} = \boldsymbol{\nabla \tilde{C}^{e}_{2\theta}}\,\boldsymbol{\theta}^e_n - a_\beta\,\boldsymbol{\nabla C^{e}_{p}}\,\dot{\boldsymbol{p}}^e_n - a_\beta\,\boldsymbol{\nabla C^{e}_{2u}}\,\dot{\boldsymbol{u}}^e_n \tag{6.87}$$

(Finite element matrices $\boldsymbol{\nabla \tilde{C}^{e}_{2\theta}}$, $\boldsymbol{\nabla C^{e}_{2p}}$ and $\boldsymbol{\nabla C^{e}_{2u}}$ are estimated at time n)

The matrix form is now expressed as:

$$\begin{aligned} &\sum_{e=1}^{N^{el}} \int_{V^e} \boldsymbol{\nabla}\left(-\mathcal{N}_*\,w^h_{n+1}\right)^e \tau^e_{11}\,\boldsymbol{\nabla}\left((\mathcal{N}\,\theta_{n+1})^e - F^e_{n+1}\right) dV^e \\ &= \sum_{e=1}^{N^{el}} [\delta\boldsymbol{\theta}^e]^T \int_{V^e} \boldsymbol{\nabla C^{eT}_{2\theta}}\,\tau^e_{11}\left[\boldsymbol{\nabla C^{e}_{3\theta}}\,\boldsymbol{\theta}^e_{n+1} + \boldsymbol{\nabla C^{e}_{2u}}\,\dot{\boldsymbol{u}}^e_{n+1} + \boldsymbol{\nabla C^{e}_{2p}}\,\dot{\boldsymbol{p}}^e_{n+1} + \boldsymbol{\nabla M^{e}_{n}}\right] dV^e \end{aligned} \tag{6.88}$$

The matrix forms of equations (6.60), (6.73) and (6.88) are to be combined to get the entire behavior of the steady advective–diffusive–reaction BVP expressed in equation (6.23). Let us define the following conclusive elemental vectors:

$$
\begin{aligned}
\boldsymbol{C}^{\boldsymbol{e}}_{\boldsymbol{\theta}} &= \boldsymbol{C}^{\boldsymbol{e}}_{\boldsymbol{1\theta}} + \tau^{e}_{00}\,\boldsymbol{C}^{\boldsymbol{eT}}_{\boldsymbol{2\theta}}\,\boldsymbol{C}^{\boldsymbol{e}}_{\boldsymbol{3\theta}} + \tau^{e}_{11}\,\boldsymbol{\nabla C}^{\boldsymbol{eT}}_{\boldsymbol{2\theta}}\,\boldsymbol{\nabla C}^{\boldsymbol{e}}_{\boldsymbol{3\theta}},\\
\boldsymbol{C}^{\boldsymbol{e}}_{\boldsymbol{u}} &= \boldsymbol{C}^{\boldsymbol{e}}_{\boldsymbol{1u}} + \tau^{e}_{00}\,\boldsymbol{C}^{\boldsymbol{eT}}_{\boldsymbol{2\theta}}\,\boldsymbol{C}^{\boldsymbol{e}}_{\boldsymbol{2u}} + \tau^{e}_{11}\,\boldsymbol{\nabla C}^{\boldsymbol{eT}}_{\boldsymbol{2\theta}}\,\boldsymbol{\nabla C}^{\boldsymbol{e}}_{\boldsymbol{2u}},\\
\boldsymbol{C}^{\boldsymbol{e}}_{\boldsymbol{p}} &= \boldsymbol{C}^{\boldsymbol{e}}_{\boldsymbol{1p}} + \tau^{e}_{00}\,\boldsymbol{C}^{\boldsymbol{eT}}_{\boldsymbol{2\theta}}\,\boldsymbol{C}^{\boldsymbol{e}}_{\boldsymbol{2p}} + \tau^{e}_{11}\,\boldsymbol{\nabla C}^{\boldsymbol{eT}}_{\boldsymbol{2\theta}}\,\boldsymbol{\nabla C}^{\boldsymbol{e}}_{\boldsymbol{2p}},\\
\boldsymbol{F}^{\boldsymbol{e}}_{\boldsymbol{cn}} &= \boldsymbol{G}^{\boldsymbol{e}}_{\boldsymbol{n}} + \tau^{e}_{00}\,\boldsymbol{C}^{\boldsymbol{eT}}_{\boldsymbol{2\theta}}\,\boldsymbol{M}^{\boldsymbol{e}}_{\boldsymbol{n}} + \tau^{e}_{11}\,\boldsymbol{\nabla C}^{\boldsymbol{eT}}_{\boldsymbol{2\theta}}\,\boldsymbol{\nabla M}^{\boldsymbol{e}}_{\boldsymbol{n}}
\end{aligned}
\tag{6.89}
$$

And finally:

$$
\begin{aligned}
&\sum_{e=1}^{N^{el}}\begin{bmatrix}\delta\dot{\boldsymbol{u}}^{e} & \delta\dot{\boldsymbol{p}}^{e} & \delta\dot{\boldsymbol{\theta}}^{e}\end{bmatrix}^{T}
\left(\int_{V^e}\begin{bmatrix}---&---&---\\---&---&---\\---&---&\boldsymbol{C}^{\boldsymbol{e}}_{\boldsymbol{\theta}}\end{bmatrix}\begin{bmatrix}\boldsymbol{u}^{e}_{n+1}\\ \boldsymbol{p}^{e}_{n+1}\\ \boldsymbol{\theta}^{e}_{n+1}\end{bmatrix}dV^{e}\right.\\
&\qquad\left.+\int_{V^e}\begin{bmatrix}---&---&---\\---&---&---\\\boldsymbol{C}^{\boldsymbol{e}}_{\boldsymbol{u}}&\boldsymbol{C}^{\boldsymbol{e}}_{\boldsymbol{p}}&---\end{bmatrix}\begin{bmatrix}\dot{\boldsymbol{u}}^{e}_{n+1}\\ \dot{\boldsymbol{p}}^{e}_{n+1}\\ \dot{\boldsymbol{\theta}}^{e}_{n+1}\end{bmatrix}dV^{e}\right)\\
&+\sum_{e=1}^{N^{el}}\begin{bmatrix}\delta\dot{\boldsymbol{u}}^{e} & \delta\dot{\boldsymbol{p}}^{e} & \delta\dot{\boldsymbol{\theta}}^{e}\end{bmatrix}^{T}
\left(\int_{\partial V^e}\begin{bmatrix}---\\---\\\boldsymbol{N}^{\boldsymbol{T}}_{\boldsymbol{\theta}}\,\dfrac{h_{n+1}}{\rho\,c_v}\end{bmatrix}ds^{e}+\int_{V^e}\begin{bmatrix}---\\---\\\boldsymbol{F}^{\boldsymbol{e}}_{\boldsymbol{cn}}\end{bmatrix}dV^{e}\right)=\begin{bmatrix}---\\---\\\boldsymbol{0}\end{bmatrix}
\end{aligned}
\tag{6.90}
$$

If the stabilizing parameters τ^{e}_{00} and τ^{e}_{11} are set to zero in the system of equations (6.89), the conventional matrix form of the equation of balance of energy in a thermo–poroelastic frame work is retrieved provided that, the first trapezoidal integration of time is accounted for.

6.3.3 First, second and third order gradients of the shape functions of the four–node bilinear quadrilateral elements (Q4)

Two–dimensional four–node isoparametric elements are used to represent the spatial discretization of the geothermal BVPs being considered in this research. The shape functions at a given node are equal to one at this node and to zero at the other nodes. The shape functions of a reference (parent) four-node bilinear quadrilateral element are shown in figure (6.3).

Let us assume that we have two vectors namely $\boldsymbol{x}^{\boldsymbol{e}}$ and $\boldsymbol{y}^{\boldsymbol{e}}$ that collect the physical coordinates of the nodes of an arbitrary element running counter–clockwise[1]:

$$
[\boldsymbol{x}^{\boldsymbol{e}}]^{T}=[x^{e}_{1}\;\;x^{e}_{2}\;\;x^{e}_{3}\;\;x^{e}_{4}],\quad [\boldsymbol{y}^{\boldsymbol{e}}]^{T}=[y^{e}_{1}\;\;y^{e}_{2}\;\;y^{e}_{3}\;\;y^{e}_{4}]
\tag{6.91}
$$

[1]The collection of the coordinates should follow the same scheme as for the parent elements in $\zeta-\eta$ system of figure (6.3).

$$N^1 = \tfrac{1}{4}(1-\zeta)(1-\eta)$$
$$N^2 = \tfrac{1}{4}(1+\zeta)(1-\eta)$$
$$N^3 = \tfrac{1}{4}(1+\zeta)(1+\eta)$$
$$N^4 = \tfrac{1}{4}(1-\zeta)(1+\eta)$$

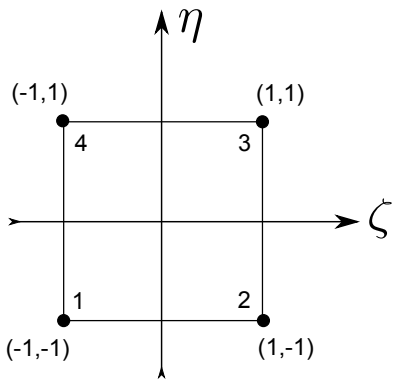

Figure 6.3: Shape functions for a four-node bilinear quadrilateral reference element. Nodal points are labeled in ascending order in counter-clockwise direction.

Let us define the following geometrical vectors and their corresponding parameters:

$$\boldsymbol{I}^T = [1\ \ 1\ \ 1\ \ 1], \quad \boldsymbol{\zeta}^T = [-1\ \ 1\ \ 1\ \ -1], \quad \boldsymbol{\eta}^T = [-1\ \ -1\ \ 1\ \ 1], \quad \boldsymbol{h}^T = [1\ \ -1\ \ 1\ \ -1] \tag{6.92}$$

$$\begin{aligned} \alpha_0 &= \frac{1}{4}\,\boldsymbol{I}^T\,\boldsymbol{x^e}, \quad \alpha_1 = \frac{1}{4}\,\boldsymbol{\zeta}^T\,\boldsymbol{x^e}, \quad \alpha_2 = \frac{1}{4}\,\boldsymbol{\eta}^T\,\boldsymbol{x^e}, \quad \alpha_3 = \frac{1}{4}\,\boldsymbol{h}^T\,\boldsymbol{x^e}, \\ \beta_0 &= \frac{1}{4}\,\boldsymbol{I}^T\,\boldsymbol{y^e}, \quad \beta_1 = \frac{1}{4}\,\boldsymbol{\zeta}^T\,\boldsymbol{y^e}, \quad \beta_2 = \frac{1}{4}\,\boldsymbol{\eta}^T\,\boldsymbol{y^e}, \quad \beta_3 = \frac{1}{4}\,\boldsymbol{h}^T\,\boldsymbol{y^e} \end{aligned} \tag{6.93}$$

The physical coordinates of an arbitrary element can thus be obtained from the parent coordinates $\zeta - \eta$ of figure (6.3) by implementing the following isoparametric interpolation:

$$\begin{aligned} x &= \alpha_0 + \alpha_1\,\zeta + \alpha_2\,\eta + \alpha_3\,\zeta\,\eta, \\ y &= \beta_0 + \beta_1\,\zeta + \beta_2\,\eta + \beta_3\,\zeta\,\eta \end{aligned} \tag{6.94}$$

Let us define the following notation:

$$\begin{aligned} A_{13} &= \alpha_1 + \alpha_3\,\eta, \qquad A_{23} = \alpha_2 + \alpha_3\,\zeta, \qquad B_{13} = \beta_1 + \beta_3\,\eta, \\ B_{23} &= \beta_2 + \beta_3\,\zeta, \\ \Delta_0 &= \alpha_1\,\beta_2 - \alpha_2\,\beta_1, \qquad X = \alpha_1\,\beta_3 - \alpha_3\,\beta_1, \quad H = \alpha_3\,\beta_2 - \alpha_2\,\beta_3, \\ \Delta &= \Delta_0 + X\,\zeta + H\,\eta \end{aligned} \tag{6.95}$$

and:

$$a_i = \frac{1}{4}\,(1+\eta_i\,\eta)\,\zeta_i, \quad b_i = \frac{1}{4}\,\zeta_i\,\eta_i, \quad c_i = \frac{1}{4}\,(1+\zeta_i\,\zeta)\,\eta_i, \quad i \in [1,\ 4] \tag{6.96}$$

Now the first, the second and the third gradients of the parent coordinates are expressed as follows:

- First order gradients of the parent coordinates

$$\begin{aligned} \frac{\partial \zeta}{\partial x} &= \frac{B_{23}}{\Delta}, & \frac{\partial \zeta}{\partial y} &= -\frac{A_{23}}{\Delta}, \\ \frac{\partial \eta}{\partial x} &= -\frac{B_{13}}{\Delta}, & \frac{\partial \eta}{\partial y} &= \frac{A_{13}}{\Delta} \end{aligned} \tag{6.97}$$

- Second order gradients of the parent coordinates

$$\begin{aligned} \frac{1}{H}\frac{\partial^2 \zeta}{\partial x \partial x} &= \frac{1}{X}\frac{\partial^2 \eta}{\partial x \partial x} = 2\,\frac{B_{13}+B_{23}}{\Delta^3}, \\ \frac{1}{H}\frac{\partial^2 \zeta}{\partial x \partial y} &= \frac{1}{X}\frac{\partial^2 \eta}{\partial x \partial y} = -\frac{A_{23}\,B_{13}+A_{13}\,B_{23}}{\Delta^3}, \\ \frac{1}{H}\frac{\partial^2 \zeta}{\partial y \partial y} &= \frac{1}{X}\frac{\partial^2 \eta}{\partial y \partial y} = 2\,\frac{A_{13}\,A_{23}}{\Delta^3} \end{aligned} \tag{6.98}$$

- Third order gradients of the parent coordinates[1]

$$\begin{aligned} \frac{1}{H}\frac{\partial^3 \zeta}{\partial x^3} &= \frac{1}{X}\frac{\partial^3 \eta}{\partial x^3} = 3 \times \frac{1}{H}\frac{\partial^2 \zeta}{\partial x \partial x}\frac{B_{13}\,H - B_{23}\,X}{\Delta^2}, \\ \frac{1}{H}\frac{\partial^3 \zeta}{\partial x^2 \partial y} &= \frac{1}{X}\frac{\partial^3 \eta}{\partial x^2 \partial y} = 3 \times \frac{1}{H}\frac{\partial^2 \zeta}{\partial x \partial y}\frac{B_{13}\,H - B_{23}\,X}{\Delta^2} - \frac{\beta_3}{\Delta^3}, \\ \frac{1}{H}\frac{\partial^3 \zeta}{\partial y^2 \partial x} &= \frac{1}{X}\frac{\partial^3 \eta}{\partial y^2 \partial x} = 3 \times \frac{1}{H}\frac{\partial^2 \zeta}{\partial x \partial y}\frac{A_{23}\,X - A_{13}\,H}{\Delta^2} - \frac{\alpha_3}{\Delta^3}, \\ \frac{1}{H}\frac{\partial^3 \zeta}{\partial y^3} &= \frac{1}{X}\frac{\partial^3 \eta}{\partial y^3} = 3 \times \frac{1}{H}\frac{\partial^2 \zeta}{\partial y \partial y}\frac{A_{23}\,X - A_{13}\,H}{\Delta^2} \end{aligned} \tag{6.99}$$

The first, the second and the third gradients of the shape functions $N_i = \frac{1}{4}(1+\zeta_i\,\zeta)(1+\eta_i\,\eta), \quad i \in [1,\ 4]$ are expressed as follows:

- First order gradients of the shape functions

$$\begin{aligned} \frac{\partial N_i}{\partial x} &= a_i\,\frac{\partial \zeta}{\partial x} + c_i\,\frac{\partial \eta}{\partial x}, \\ \frac{\partial N_i}{\partial y} &= a_i\,\frac{\partial \zeta}{\partial y} + c_i\,\frac{\partial \eta}{\partial y} \end{aligned} \tag{6.100}$$

- Second order gradients of the shape functions

$$\begin{aligned} \frac{\partial^2 N_i}{\partial x \partial x} &= a_i\,\frac{\partial^2 \zeta}{\partial x \partial x} + 2\,b_i\,\frac{\partial \zeta}{\partial x}\frac{\partial \eta}{\partial x} + c_i\,\frac{\partial^2 \eta}{\partial x \partial x}, \\ \frac{\partial^2 N_i}{\partial x \partial y} &= a_i\,\frac{\partial^2 \zeta}{\partial x \partial y} + b_i\left(\frac{\partial \zeta}{\partial x}\frac{\partial \eta}{\partial y} + \frac{\partial \zeta}{\partial y}\frac{\partial \eta}{\partial x}\right) + c_i\,\frac{\partial^2 \eta}{\partial x \partial y}, \\ \frac{\partial^2 N_i}{\partial y \partial y} &= a_i\,\frac{\partial^2 \zeta}{\partial y \partial y} + 2\,b_i\,\frac{\partial \zeta}{\partial y}\frac{\partial \eta}{\partial y} + c_i\,\frac{\partial^2 \eta}{\partial y \partial y} \end{aligned} \tag{6.101}$$

[1] There are several equivalent ways of expressing these derivatives.

- Third order gradients of the shape functions

$$
\begin{aligned}
\frac{\partial^3 N_i}{\partial x^3} &= a_i \frac{\partial^3 \zeta}{\partial x^3} + 3b_i \left(\frac{\partial^2 \zeta}{\partial x^2} \frac{\partial \eta}{\partial x} + \frac{\partial \zeta}{\partial x} \frac{\partial^2 \eta}{\partial x^2} \right) \\
&+ c_i \frac{\partial^3 \eta}{\partial x^3}, \\
\frac{\partial^3 N_i}{\partial x^2 \partial y} &= a_i \frac{\partial^3 \zeta}{\partial x^2 \partial y} + b_i \left(\frac{\partial \zeta}{\partial y} \frac{\partial^2 \eta}{\partial x^2} + \frac{\partial \eta}{\partial y} \frac{\partial^2 \zeta}{\partial x^2} + 2 \frac{\partial^2 \zeta}{\partial x \partial y} \frac{\partial \eta}{\partial x} + 2 \frac{\partial^2 \eta}{\partial x \partial y} \frac{\partial \zeta}{\partial x} \right) \\
&+ c_i \frac{\partial^3 \eta}{\partial x^2 \partial y}, \\
\frac{\partial^3 N_i}{\partial x \partial y^2} &= a_i \frac{\partial^3 \zeta}{\partial x \partial y^2} + b_i \left(\frac{\partial \zeta}{\partial x} \frac{\partial^2 \eta}{\partial y^2} + \frac{\partial \eta}{\partial x} \frac{\partial^2 \zeta}{\partial y^2} + 2 \frac{\partial^2 \zeta}{\partial x \partial y} \frac{\partial \eta}{\partial y} + 2 \frac{\partial^2 \eta}{\partial x \partial y} \frac{\partial \zeta}{\partial y} \right) \\
&+ c_i \frac{\partial^3 \eta}{\partial x \partial y^2}, \\
\frac{\partial^3 N_i}{\partial y^3} &= a_i \frac{\partial^3 \zeta}{\partial y^3} + 3b_i \left(\frac{\partial^2 \zeta}{\partial y^2} \frac{\partial \eta}{\partial y} + \frac{\partial \zeta}{\partial y} \frac{\partial^2 \eta}{\partial y^2} \right) \\
&+ c_i \frac{\partial^3 \eta}{\partial y^3}
\end{aligned}
\tag{6.102}
$$

6.4 Implementation of the SGS/GSGS method: Results and simulations

Since the SGS method requires to first integrate in time instead of space, a special treatment should be accounted for when the method is implemented in the time integration scheme of section (3.2.4). The time scheme adopted so far works as follows: the Newton direction $\Delta \mathbb{V}$ is obtained by solving the system $\mathbb{C}^* (\alpha \Delta \mathbb{V}) = \mathbb{R}^i_{n+\alpha}$ where the tangent matrix $\mathbb{C}^*$ and the residual $\mathbb{R}^i_{n+\alpha}$ are accurately calculated at each iteration of the predictor multi–corrector method. The calculated Newton direction $\Delta \mathbb{V}$ is then used to obtain the new vector of the primary unknowns $\mathbb{X}^{i+1}_{n+1}$.

Integration in time at first step means that the vector of the primary unknowns $\mathbb{X}^{i+1}_{n+1}$ is already solved for. It also necessarily requires that the convective velocity field $\boldsymbol{v}^{i+1}_{n+1}$ to be used in forming the tangent matrix $\mathbb{C}^*$, see equation (6.90). All of this is reprimanding a direct implementation of the SGS method in our integration time scheme, the following approach is adopted to overcome this obstacle:

1. The convective velocity field of the previous integration step $\boldsymbol{v}^{i}_{n+1}$ is to be used in forming the convective terms of the tangent matrix $\mathbb{C}^*$ as the field $\boldsymbol{v}^{i+1}_{n+1}$ is not yet known.

2. Only the components of the positions ($\boldsymbol{K}^e_{j3}$ and $\boldsymbol{D}^e_{j3}$, $j = 1$, 2, and 3) of the stiffness and diffusion matrices $\mathbb{K}$ and $\mathbb{D}$, are not consistent with the time integration scheme as they are to be multiplied by the unknowns $\boldsymbol{\theta}^{e,\,i+1}_{n+1}$ and $\dot{\boldsymbol{\theta}}^{e,\,i+1}_{n+1}$, see equation (6.90).

3. By recalling the definitions of $\boldsymbol{\theta}^{e,\,i+1}_{n+1}$ and $\dot{\boldsymbol{\theta}}^{e,\,i+1}_{n+1}$ of section (3.2.4):

$$\begin{aligned} \boldsymbol{\theta}^{e,\,i+1}_{n+1} &= \tilde{\boldsymbol{\theta}}^{e,\,i}_{n+1} + \beta\,\Delta t\,\Delta\boldsymbol{\theta}^e \\ \dot{\boldsymbol{\theta}}^{e,\,i+1}_{n+1} &= \dot{\boldsymbol{\theta}}^{e,\,i}_{n+1} + \Delta\boldsymbol{\theta}^e \end{aligned} \tag{6.103}$$

4. The multiplication of the third column components of the matrices $\mathbb{K}$ and $\mathbb{D}$ by the unknowns $\boldsymbol{\theta}^{e,\,i+1}_{n+1}$ and $\dot{\boldsymbol{\theta}}^{e,\,i+1}_{n+1}$ becomes:

$$\boldsymbol{K}^e_{j3}\,\boldsymbol{\theta}^{e,\,i+1}_{n+1} + \boldsymbol{D}^e_{j3}\,\dot{\boldsymbol{\theta}}^{e,\,i+1}_{n+1} = \boldsymbol{R}^i_{n+\beta}(\theta), \tag{6.104}$$

$$\boldsymbol{K}^e_{j3}\,(\tilde{\boldsymbol{\theta}}^{e,\,i}_{n+1} + \beta\,\Delta t\,\Delta\boldsymbol{\theta}^e) + \boldsymbol{D}^e_{j3}\,(\dot{\boldsymbol{\theta}}^{e,\,i}_{n+1} + \Delta\boldsymbol{\theta}^e) = \boldsymbol{R}^i_{n+\beta}(\theta), \tag{6.105}$$

and:

$$\underbrace{(\boldsymbol{K}^e_{j3}\,\beta\,\Delta t + \boldsymbol{D}^e_{j3})}_{\boldsymbol{C}^*(\theta)}\,\beta\,\Delta\boldsymbol{\theta}^e = \underbrace{\beta\,\boldsymbol{R}^i_{n+\beta}(\theta) - \beta\,\boldsymbol{K}^e_{j3}\,\tilde{\boldsymbol{\theta}}^{e,\,i}_{n+1} - \beta\,\boldsymbol{D}^e_{j3}\,\dot{\boldsymbol{\theta}}^{e,\,i}_{n+1}}_{\text{Adjusted RHS}} \tag{6.106}$$

β is the integration coefficient of the trapezoidal rule (1/2 or 2/3 generally).

The foregoing presentation of the SGS method has been implemented to our FE code to study its stabilizing effects on the oscillations in the hyperbolic solutions of the convection-diffusion problems. The same BVP as described in section (5.2.2) is considered, results of simulations for heat extraction as well as HF using HFM2 are to be presented.

6.4.1 Phase 1 injection test at GPK1 well, 1993: Heat extraction simulations, convection of heat is treated by the SGS method

The same homogeneous finite element mesh, as in section (5.2.2), is used to perform heat extraction simulations. Poroelastic and thermoelastic material properties are exactly as shown in Table (5.3) based on the study of (Evans et al., [2009]).

Figure (6.4) compares the profiles of temperature and pressure, along the line of symmetry $y = 0$ m, for the SGS and the SUPG methods at different times of 10 days, 6 months and at years 1, 2, 5 and 10. It is obvious that the implementation of the SGS method heals quite satisfactorily the oscillations of the SUPG method even at quite small time interval of 10 days.

The profiles of pore fluid pressure do not differ between the SGS and the SUPG methods since hydraulic diffusion happens very rapidly. The jump in the pressure profiles at the injection well between the time intervals of 10 days and 6 months is due to the pumping schedule, see figure (5.8).

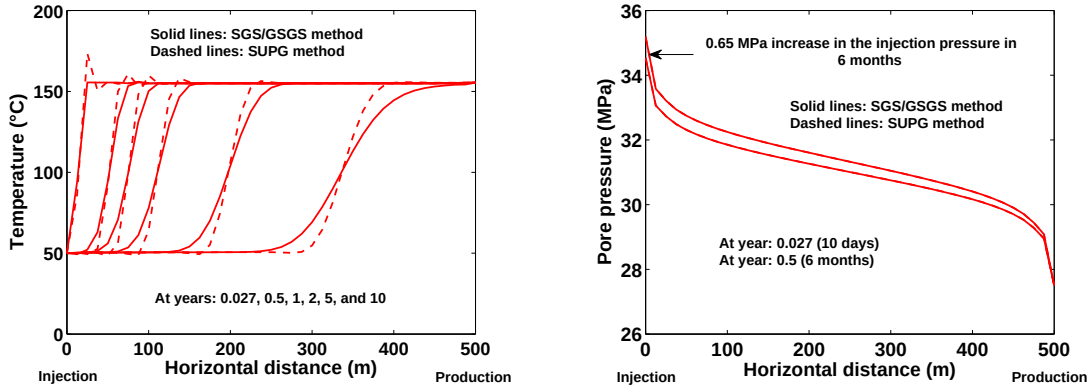

(a) Temperature profiles

(b) Pore pressure profiles

Figure 6.4: Temperature and pore pressure profiles along the line of symmetry $y = 0$ m: (a) Heat convection oscillations near the injection well are well stabilized when the SGS method is applied. (b) Pore fluid pressure profiles are not affected by the SGS method since hydraulic diffusion is very fast.

Though the SGS method was wonderfully capable of circumventing the heat convection oscillations at very short and intermediate time intervals, its capacity deteriorates with time.

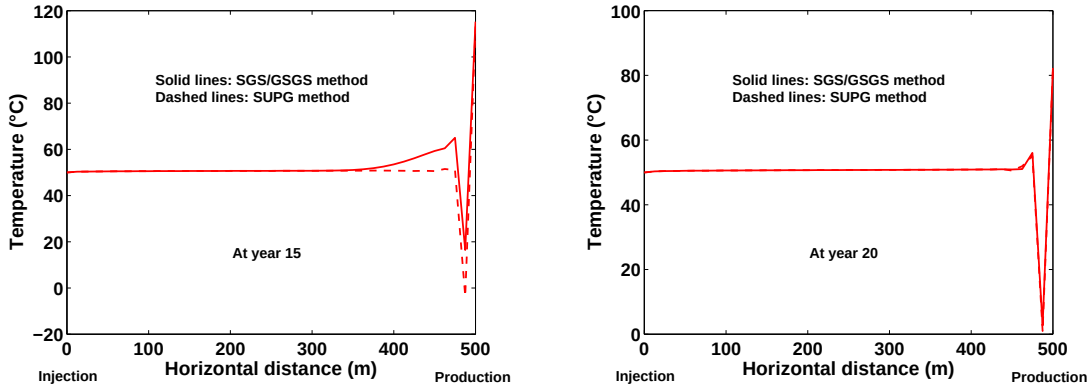

(a) Temperature profiles at year 15

(b) Temperature profiles at year 20

Figure 6.5: Temperature profiles along the line of symmetry $y = 0$ m: (a) Heat convection oscillations are mitigated at the production well but far from being healed. (b) The capacity of the SGS method is lost; SUPG and SGS methods are almost the same.

At year 15 and despite mitigating the wiggles at the production well, the SGS method still

leaves serious temperature oscillations, see figure (6.5(a)).

At quite large time intervals near the production well, the source term becomes negligible ($s \to 0$) meanwhile the convective velocity is considerably large. This causes the Damköhler number to disappear ($\sigma \to 0$), therefore the capacity of the SGS method is lost as a convection–dominated situation appears and the stabilizing method produces the same modification as the SUPG method, see figure (6.5(b)).

6.4.2 Phase 1 injection test at GPK1 well, 1993: Permeability enhancement by HFM2, convection of heat is treated by the SGS method

The same BVP as in sections (5.2.2) and (5.4.3) is to be stimulated/enhanced using the HFM2 and while implementing the SGS method. The purpose of this section is to use the SGS method to heal the annoying convection oscillations which appear in figure (5.56), and to study its effects on the stimulation (permeability contours) of the HDR reservoir.

Figure (6.6) shows the contours of reservoir temperature during the process of stimulation at times of 5 and 10 years. The application of the SGS method cures almost all of heat convection oscillations, compare for instance with figure (5.56).

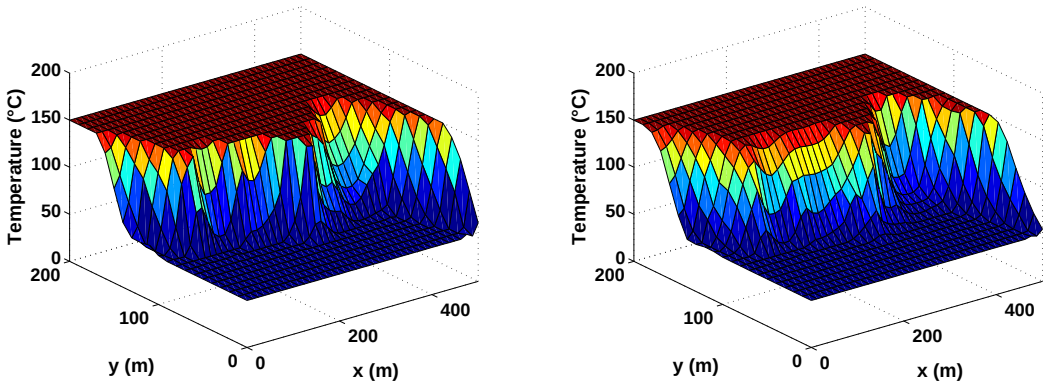

(a) Temperature contour at year 5

(b) Temperature contour at year 10

Figure 6.6: Contours of the mixture temperature at different times with HF by applying HFM2, convection of heat is treated by the SGS method.

The contours of the enhanced permeability of the HDR reservoir are about 0.96 times smaller when the SGS method is implemented. This is conceivable by following figure (6.4) where the mixture temperature at a definite location is a little bit smaller for the case of the SGS method.

It seems like SGS method is more stabilizing/more diffusive than the SUPG method for the same conditions, see figure (6.7) and compare with figure (5.55) of SUPG method.

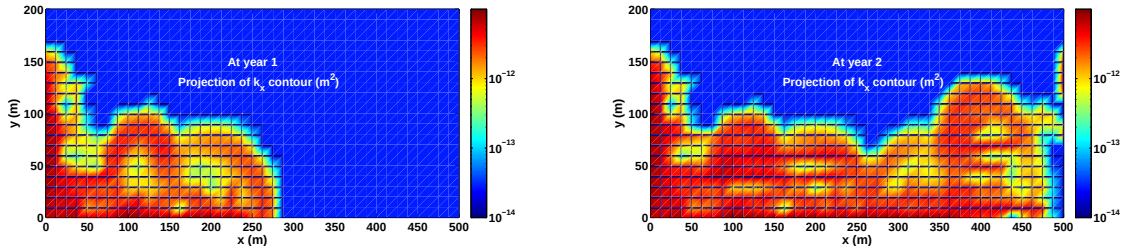

(a) Projection of k_x contour at year 1 with SGS (b) Projection of k_x contour at year 2 with SGS

Figure 6.7: Enhanced longitudinal permeability component k_x depicted as the projection of its contour in the $x-y$ plane. Fracture propagation is in the direction of maximum far field stress. Injection pressure schedule, described in figure (5.8), is sufficient to entirely enhance the HDR reservoir in the longitudinal direction.

The previous conclusion becomes more evident when the history of the enhanced permeability is plotted at some point, see figure (6.8). It is clear that the evolution of the longitudinal permeability is smoother in the case of the SGS method as it provides more stabilization. Nonetheless, the same general evolution behavior is more or less obtained for the SGS and the SUPG methods.

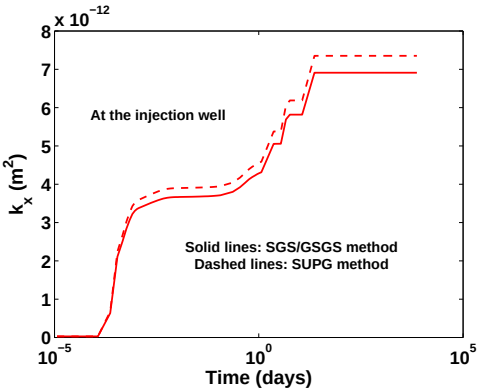

Figure 6.8: Longitudinal permeability k_x history at the injection well; comparison between the simulations when implementing the SGS method (solid lines) and the SUPG method (dashed lines).

The advantages and disadvantages of the SGS/GSGS method can finally be summed up:

1. The SGS method has been proven capable of efficiently healing the heat convection oscillations at very short and intermediate time intervals.

2. The SGS method is also efficient to cure the stubborn heat convection oscillations even while tremendously enhancing the HDR reservoir permeability by the process of HF.

3. The implementation of SGS method slightly affects the values of the enhanced permeability of the HDR reservoir which can be neglected without remorses.

4. At quite large time intervals and if convection–dominated situations are present, SGS method loses its efficiency and SUPG method is retrieved. In other words, SGS provides results similar to the SUPG.

6.5 Beyond the SGS and the SUPG methods

Neither the SGS method nor the SUPG method was capable of healing the numerical noises resulting from the heating wave striking the stiff boundary at the production well. Yet, such noises were a bit mitigated in the case of the SGS method for moderately long periods, see figure (6.5(a)). (John and Knobloch, [2007]) have defined an interesting modification to the SUPG method such that it may become capable of treating the spurious numerical wiggles at long periods, their approach is called Discontinuity Capturing Method (DCM) in the literature.

6.5.1 The Discontinuity Capturing Method (DCM)

The DCM is developed to smoothly treat the sharp shock oscillations which result from heat waves suddenly striking stiff boundaries at long times of the simulations, see (John and Knobloch, [2007]) and (Hughes, [2000], chapter 9). The DCM can be resumed by the following strategy:

The DCM suggests the following shape function for the variation in the temperature change $\delta\theta$:

$$\boldsymbol{W_\theta} = \boldsymbol{N_\theta} + \tau_1\, \boldsymbol{v}\, \boldsymbol{\nabla N_\theta} + \tau_2\, \boldsymbol{v}_{||}\, \boldsymbol{\nabla N_\theta} \tag{6.107}$$

$\boldsymbol{v}_{||}$ is the projection of $\boldsymbol{v}$ on $\boldsymbol{\nabla}\theta$, defined as:

$$\boldsymbol{v}_{||} = \begin{cases} \dfrac{\boldsymbol{v}.\boldsymbol{\nabla}\theta}{||\boldsymbol{\nabla}\theta||^2}\, \boldsymbol{\nabla}\theta, & \text{if } \boldsymbol{\nabla}\theta \neq \boldsymbol{0} \\ \boldsymbol{0}, & \text{if } \boldsymbol{\nabla}\theta = \boldsymbol{0} \end{cases} \tag{6.108}$$

By substituting the definition (6.107) in equation (6.8), the discretized form for the DCM is obtained:

$$\sum_{e=1}^{N} [\delta\boldsymbol{\theta}^e]^T \int_{V^e} \boldsymbol{W_\theta^T} \left(\mathcal{R}\,\theta - f \right) dV^e = 0 \tag{6.109}$$

Gradient of temperature change $\boldsymbol{\nabla}\theta$ is obtained through the discretization[1] $\boldsymbol{\nabla N_\theta}\, \boldsymbol{\theta}^e$. $||\boldsymbol{x}||$ is the Euclidean norm of the vector $\boldsymbol{x}$. The interaction of the shape function $\boldsymbol{W_\theta^T}$ with the convection term $\boldsymbol{v}.\boldsymbol{\nabla\theta}$ in equation (6.109) leads to:

[1] This is a non–linear stabilizing method as $\boldsymbol{v}_{||} = \boldsymbol{v}_{||}(\boldsymbol{\theta}^e)$.

$$\begin{aligned} \boldsymbol{W}_{\boldsymbol{\theta}}^{\boldsymbol{T}}\,\boldsymbol{v}.\boldsymbol{\nabla\theta} &= \boldsymbol{N}_{\boldsymbol{\theta}}^{\boldsymbol{T}}\,\boldsymbol{v}.\boldsymbol{\nabla\theta} + \boldsymbol{\nabla N}_{\boldsymbol{\theta}}^{\boldsymbol{T}}\,\tau_1\,\boldsymbol{v}^{\boldsymbol{T}}\,\boldsymbol{v}.\boldsymbol{\nabla\theta} + \boldsymbol{\nabla N}_{\boldsymbol{\theta}}^{\boldsymbol{T}}\,\tau_2\,\boldsymbol{v}_{||}^{\boldsymbol{T}}\,\boldsymbol{v}.\boldsymbol{\nabla\theta}, \\ &= \boldsymbol{N}_{\boldsymbol{\theta}}^{\boldsymbol{T}}\,\boldsymbol{v}.\boldsymbol{\nabla\theta} + \boldsymbol{\nabla N}_{\boldsymbol{\theta}}^{\boldsymbol{T}}\,\tau_1\,\boldsymbol{v}^{\boldsymbol{T}}\,\boldsymbol{v}.\boldsymbol{\nabla\theta} + \boldsymbol{\nabla N}_{\boldsymbol{\theta}}^{\boldsymbol{T}}\,\tau_2\,\boldsymbol{v}_{||}^{\boldsymbol{T}}\,\boldsymbol{v}_{||}.\boldsymbol{\nabla\theta}, \end{aligned} \tag{6.110}$$

due to the fact that $\boldsymbol{v}.\boldsymbol{\nabla\theta} = \boldsymbol{v}_{||}.\boldsymbol{\nabla\theta}$ by equation (6.108), one writes:

$$\boldsymbol{W}_{\boldsymbol{\theta}}^{\boldsymbol{T}}\,\boldsymbol{v}.\boldsymbol{\nabla\theta} = \boldsymbol{N}_{\boldsymbol{\theta}}^{\boldsymbol{T}}\,\boldsymbol{v}.\boldsymbol{\nabla\theta} + \underbrace{\boldsymbol{\nabla N}_{\boldsymbol{\theta}}^{\boldsymbol{T}}\,\tau_1\,\boldsymbol{v}^{\boldsymbol{T}}\,\boldsymbol{v}.\boldsymbol{\nabla\theta}}_{\text{Streamline operator}} + \underbrace{\boldsymbol{\nabla N}_{\boldsymbol{\theta}}^{\boldsymbol{T}}\,\tau_2\,\boldsymbol{v}_{||}^{\boldsymbol{T}}\,\boldsymbol{v}_{||}.\boldsymbol{\nabla\theta}}_{\text{DCM operator}} \tag{6.111}$$

The stream line matrix $\boldsymbol{v}^{\boldsymbol{T}}\,\boldsymbol{v}$ is a first–order positive semidefinite matrix acting only in the streamline direction. While the discontinuity capturing matrix $\boldsymbol{v}_{||}^{\boldsymbol{T}}\,\boldsymbol{v}_{||}$ is also a first–order positive semidefinite matrix yet acting only in the direction of the discrete solution temperature gradient.

The stabilizing parameters τ_1 and τ_2 are defined such that:

$$\tau_1 = \tau \quad \text{(of the SUPG method)} \quad \text{and} \quad \tau_2 = \tau_{||}, \tag{6.112}$$

$\tau_{||}$ is deduced using the same strategy to calculate τ, equation (6.12), but using the parallel velocity $\boldsymbol{v}_{||}$. If $\boldsymbol{v} = \boldsymbol{v}_{||}$ the doubling of the stabilizing parameter τ is engaged. At this point the SUPG method alone is sufficient to do the required stabilization and the component $\tau\,\boldsymbol{v}^{\boldsymbol{T}}\,\boldsymbol{v}$ in the direction $\boldsymbol{\nabla}\theta$ must be removed. The stabilizing parameters are to be calculated following this scheme:

$$\tau_1 = \tau \quad \text{and} \quad \tau_2 = \max[0, (\tau_{||} - \tau)] \tag{6.113}$$

6.5.2 Phase 1 injection test at GPK1 well, 1993: Heat extraction simulations, convection of heat is treated by the DCM method

The afore–presented DCM has been integrated into the Fortran 90 FE code, where the simulations of section (6.4.1) were redone for the same initial BVP for long periods. Figure (6.9) shows that the DCM is capable of almost entirely healing the numerical noises at the production well resulting from heating waves hitting the stiff boundary the that position.

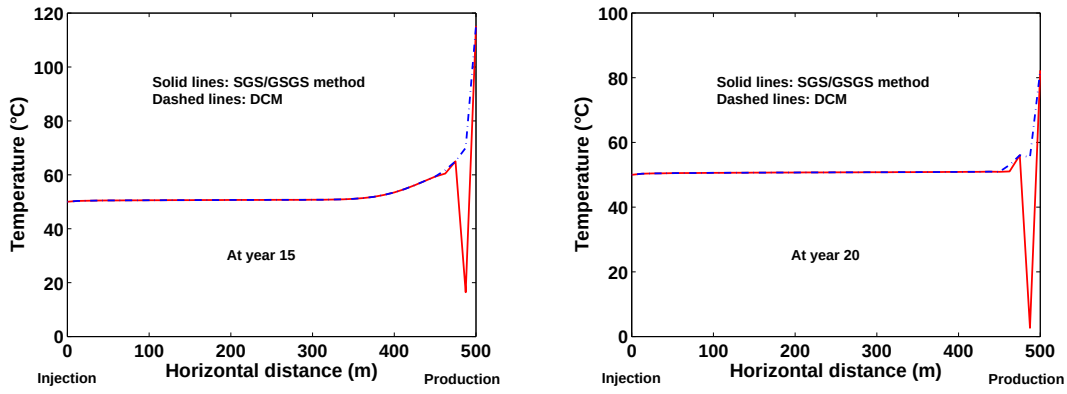

(a) Temperature profiles at year 15

(b) Temperature profiles at year 20

Figure 6.9: Temperature profiles along the line of symmetry $y = 0$ m. DCM is capable of treating the most stubborn numerical noises at the production well where both the SGS and SUPG methods were proven inefficient.

6. PHENOMENON OF FORCED HEAT CONVECTION IN EGS: STABILIZATION METHODS

Reflections and perspectives

The main objective of this research was to develop a constitutive model to describe the permeability enhancement of a fractured medium in a fully coupled thermo–poroelastic analysis. The following main achievements may be listed:

1. general view about Enhanced Geothermal Systems (EGS),
2. formulation of the governing equations for a fully coupled thermo–poroelastic analysis in homogeneous single–porosity media,
3. fracturing models to track the crack evolution in all possible spatial orientations,
4. implementation of the thermo–poroelastic governing equations in a domestic finite element (FE) code using a time marching scheme in a non–linear context,
5. integration of the fracturing models in the FE code to couple permeability stimulation with the thermo–poroelastic analysis to study transient heat extraction from enhanced geothermal systems,
6. presentation of several stabilization methods to heal the oscillations in the hyperbolic solutions due to forced heat convection.

The following points are worth of further research:

1. A model emerging from the statistics describing the pre–existing geothermal fractured systems has been used all along this research in simulating thermal recovery. This model included discrete fracture patterns which formed the major structures governing the flow (the reservoir). The direction of the flow and the generation of the new hydraulically created fracture networks were assumed to happen within the reservoir volume. Such models require accurate stochastically generated realizations of the site on the geophysical and mechanical aspects. The key points for an improved model include:

(a) investigating large scale heterogeneities of the geothermal site:
The characteristics of the explored faults should be well recorded. Fault zones are usually irregular, branched, anastomosed, and curved rather than simple and planar. The dip angle of such zones, as well as their interaction with the surroundings control the direction of the flow and the amount of water lost while operating the geothermal systems. Once all these factors are taken into consideration, the small scale heterogeneities, at the reservoir scale, must be also deemed.

(b) quantifying small scale heterogeneities:
- fracture properties: fracture distribution, density, average radius and average aperture,
- natural fluid production and its contribution to the mass balance,
- the influence of heterogeneity on the hydraulic conductivity and storage capacity,
- the influence of heterogeneity on the mechanical properties,
- the influence of heterogeneity on the fracture properties.

2. The fracturing models, which were developed to describe HF, did not stand at all for fracture slippage and permeability reduction under compressive stresses. Actually, the natural directional enhancement of EGS leaves regions of the reservoir with very large compressive stresses where aperture reduction and/or slippage is expected. We call future research on developing our models so as they could track permeability change due to fracture aperture reduction and/or increase under compressive stresses.

3. Experimental tests providing pore pressure and temperature variations in igneous rocks with forced convection in the context of thermal recovery from enhanced geothermal reservoirs would be welcome. The experimental data are to be correlated to the numerical responses where the models of fracturing and thermo–poroelasticity can be calibrated.

4. The impact of temperature change on the viscosity of Non-Newtonian geothermal fluids should be assessed. The Non-Newtonian character of the drilling fluids was proven to counteract the thermal dependence of their dynamic viscosity. This statement clearly calls that future studies take into consideration both thermal effects and Non–Newtonian fluids. Possibly their effects may, in some circumstances, be cooperating rather than counteracting.

5. For very high velocities in porous media, inertial effects become significant. Non–Darcian flow should be considered to account for such inertial effects which lead to non–linear dependence of pressure gradient on the velocity of the fluid.

6. EGS require large volumes of circulating water to generate electricity, and a considerable amount of this water is lost during production. Donald Brown of Los Alamos National Laboratory proposition of substituting CO_2 for water in EGS production systems is not an environmentalist's fairytale. We call for further research on CO_2–based EGS as they might be that last truffula seed that we can pass on to our posterity.

Appendices

Appendix A

A.1 Macroscopic free enthalpy of a fractured medium

Consider a Representative Elementary Volume (REV) Ω of a brittle material which is initially isotropic and homogeneous, including an array of mesocracks. Each mesocrack i or set of quasi–oriented mesocracks is characterized by its surface S^i, orientation $\boldsymbol{n}^i$ and its crack displacement discontinuity $\boldsymbol{b}^i$. The expression of the global strain on the REV considering the contribution of all the cracks is:

$$\boldsymbol{\varepsilon} = \boldsymbol{S}^0 : \boldsymbol{\sigma} + \frac{1}{2\Omega} \sum_i \int_{S^i} \left(\boldsymbol{b}^i \otimes \boldsymbol{n}^i + \boldsymbol{n}^i \otimes \boldsymbol{b}^i \right) S^i \tag{A.1}$$

Here, $\boldsymbol{S}^0$ is the initial compliance fourth–order tensor. If $\boldsymbol{n}^i$ remains constant over the cracks (flat cracks) and if the cracks are quasi–circular (with radius a^i), equation (A.1) becomes:

$$\boldsymbol{\varepsilon} = \boldsymbol{S}^0 : \boldsymbol{\sigma} + \frac{1}{2\Omega} \sum_i \left(\boldsymbol{b}^i_{avg} \otimes \boldsymbol{n}^i + \boldsymbol{n}^i \otimes \boldsymbol{b}^i_{avg} \right) S^i, \tag{A.2}$$

where $\boldsymbol{b}^i_{avg}$ is $\boldsymbol{b}^i$ averaged over the mesocrack set i. Following the sense of equation (A.2), the global strain is composed of two terms: the first represents the matrix strain without damage, the second includes the contribution of the mesocracks. The macroscopic free enthalpy of the fractured medium can be expressed as:

$$W_c = \frac{1}{2} \boldsymbol{\sigma} : \boldsymbol{S}^0 : \boldsymbol{\sigma} + \frac{1}{2\Omega} \sum_i \boldsymbol{n}^i . \boldsymbol{\sigma} . \boldsymbol{b}^i_{avg} \, S^i \tag{A.3}$$

(Kachanov, [1992]) gives the form of $\boldsymbol{b}^i_{avg}$ in a three–dimensional case of crack embedded in an infinite body with stress $\boldsymbol{\sigma}$ at infinity. In the general case, where mesocracks are allowed to open, $\boldsymbol{b}^i_{avg}$ comprises normal and shear components:

$$\boldsymbol{b}^i_{avg} = \underbrace{\frac{16(1-\nu_0^2)}{3\pi}\frac{a^i}{E_0}(\boldsymbol{n}^i.\boldsymbol{\sigma}.\boldsymbol{n}^i)\boldsymbol{n}^i}_{\text{Shear component}} + \underbrace{\frac{16(1-\nu_0^2)}{3\pi(1-\nu_0/2)}\frac{a^i}{E_0}\left[\boldsymbol{n}^i.\boldsymbol{\sigma} - (\boldsymbol{n}^i.\boldsymbol{\sigma}.\boldsymbol{n}^i)\boldsymbol{n}^i\right]}_{\text{Normal component}} \tag{A.4}$$

Let us define the elastic compliance h of a crack as:

$$h = \frac{16(1-\nu_0^2)}{3E_0(2-\nu_0)} \tag{A.5}$$

Substituting equation (A.4) in equation (A.3) and manipulating the result, one obtains:

$$\begin{aligned} W_c \;=\; \frac{h}{\Omega}\Bigg[\sum_i \frac{a^i}{\pi}\left(1-\frac{\nu_0}{2}\right)\boldsymbol{\sigma}.\boldsymbol{n}^i(\boldsymbol{n}^i.\boldsymbol{\sigma}.\boldsymbol{n}^i)\boldsymbol{n}^i\, S^i \;+\; \sum_i \frac{a^i}{\pi}\Big((\boldsymbol{\sigma}.\boldsymbol{\sigma}) : (\boldsymbol{n}^i\otimes\boldsymbol{n}^i) \\ -\; \boldsymbol{\sigma} : (\boldsymbol{n}^i\otimes\boldsymbol{n}^i\otimes\boldsymbol{n}^i\otimes\boldsymbol{n}^i) : \boldsymbol{\sigma}\Big)\, S^i\Bigg] \end{aligned} \tag{A.6}$$

In our model of damage, equation (2.44), effective stresses are directly used in the free enthalpy relation. This means that poroelastic parameters and thermoelastic parameters used in calculating the effective stresses, i.e. Biot's coefficient (κ) and the thermal expansion of the solid phase (α_s) are not assumed to deteriorate with damage (rigorous assumption), see (Lu et al., [2010]) for details.

A.2 Derivation of the Directionally Distributed Fracture Model (DDFM) to describe damage and permeability evolution: Equation (2.63)

Following the crack propagation criterion given by equations (2.49), (2.50) and (2.51), we can derive the evolution of crack propagation as a function of the crack radius, the normal effective stress, and the deviatoric effective stress for the case $r < r_f$.

$$F = \sqrt{r}\,\sigma_n^{'}\left(\frac{f_{c,t}}{f_{c,t}+\langle-\sigma_n^{'}\rangle}\right)^m + 3\,\eta\left(\frac{r_f}{\sqrt{r}}\right)\langle\sigma_n^{'d}\rangle - C_{rc} \tag{A.7}$$

When $F(r,\, \sigma_n^{'},\, \sigma_n^{'d},\, \boldsymbol{n}) = 0$ cracks start to propagate:

$$dF = \frac{\partial F}{\partial r}\,dr + \frac{\partial F}{\partial \boldsymbol{\sigma}^{'}} \,:\, d\boldsymbol{\sigma}^{'}, \tag{A.8}$$

which leads to the following equation:

$$dF = \frac{\partial F}{\partial r}\,dr + \left[\frac{\partial F}{\partial \sigma_n^{'}}\frac{\partial \sigma_n^{'}}{\partial \boldsymbol{\sigma}^{'}} + \frac{\partial F}{\partial \sigma_n^{'d}}\frac{\partial \sigma_n^{'d}}{\partial \boldsymbol{\sigma}^{'}}\right] \,:\, d\boldsymbol{\sigma}^{'}, \tag{A.9}$$

and considering the definitions mentioned in equation (2.50), we conclude:

$$\begin{aligned}
\sigma_n^{'} &= \boldsymbol{n}.\boldsymbol{\sigma}^{'}.\boldsymbol{n} \\
\sigma_n^{'d} &= \boldsymbol{n}.\boldsymbol{\sigma}^{'}.\boldsymbol{n} - \boldsymbol{n}.\left[\left(\frac{\boldsymbol{\sigma}^{'}}{3}\right)\boldsymbol{\delta}\right].\boldsymbol{n} \\
\frac{\partial \sigma_n^{'}}{\partial \boldsymbol{\sigma}^{'}} &= \boldsymbol{n}\otimes\boldsymbol{n} \\
\frac{\partial \sigma_n^{'d}}{\partial \boldsymbol{\sigma}^{'}} &= \boldsymbol{n}\otimes\boldsymbol{n} - \frac{\boldsymbol{\delta}}{3}(\boldsymbol{n}\,\boldsymbol{n})
\end{aligned} \tag{A.10}$$

The evolution of damage can be expressed as:

$$dr = -\frac{1}{\dfrac{\partial F}{\partial r}}\left[\frac{\partial F}{\partial \sigma_n^{'}}\frac{\partial \sigma_n^{'}}{\partial \boldsymbol{\sigma}^{'}} + \frac{\partial F}{\partial \sigma_n^{'d}}\frac{\partial \sigma_n^{'d}}{\partial \boldsymbol{\sigma}^{'}}\right] : d\boldsymbol{\sigma}^{'}, \tag{A.11}$$

$$\frac{\partial F}{\partial r} = \frac{1}{2\sqrt{r}}\,\sigma_n^{'}\left(\frac{f_{c,t}}{f_{c,t}+\langle -\sigma_n^{'}\rangle}\right)^m - \frac{3}{2}\,\eta\left(\frac{r_f}{\sqrt{r^3}}\right)\langle \sigma_n^{'d}\rangle \tag{A.12}$$

Let us assume that $\sigma_n^{'} > 0$ and whether $\sigma_n^{'d}$ is positive or negative, $\partial F/\partial \sigma_n^{'}$ will take the following form:

$$\frac{\partial F}{\partial \sigma_n^{'}} = \sqrt{r}, \tag{A.13}$$

when $\sigma_n^{'} < 0$ and whether $\sigma_n^{'d}$ is positive or negative,

$$F = \sqrt{r}\,\sigma_n^{'}\left(\frac{f_{c,t}}{f_{c,t}-\sigma_n^{'}}\right)^m + 3\,\eta\left(\frac{r_f}{\sqrt{r}}\right)\langle \sigma_n^{'d}\rangle - C_{rc}, \tag{A.14}$$

$$\frac{\partial F}{\partial \sigma_n^{'}} = \sqrt{r}\,\sigma_n^{'}\frac{m\,f_{c,t}^m}{(f_{c,t}-\sigma_n^{'})^{m+1}} + \sqrt{r}\left(\frac{f_{c,t}}{f_{c,t}-\sigma_n^{'}}\right)^m, \tag{A.15}$$

when $\sigma_n^{'d} > 0$ and whether $\sigma_n^{'}$ is positive or negative,

$$F = \sqrt{r}\,\sigma_n^{'}\left(\frac{f_{c,t}}{f_{c,t}+\langle -\sigma_n^{'}\rangle}\right)^m + 3\,\eta\left(\frac{r_f}{\sqrt{r}}\right)\sigma_n^{'d} - C_{rc}, \tag{A.16}$$

$$\frac{\partial F}{\partial \sigma_n^{'d}} = 3\,\eta\left(\frac{r_f}{\sqrt{r}}\right), \tag{A.17}$$

when $\sigma_n^{'d} < 0$ and whether $\sigma_n^{'}$ is positive or negative,

$$\frac{\partial F}{\partial \sigma_n^{'d}} = 0 \tag{A.18}$$

Finally, the evolution of the average radius of the set of cracks in direction $\boldsymbol{n}$ takes the following form:

$$dr = -\frac{1}{\dfrac{\partial F}{\partial r}}\left[\Pi(r,\,\sigma_n^{'})\,(\boldsymbol{n}\otimes\boldsymbol{n}) + \Psi(r,\,\sigma_n^{'d})\,\left(\boldsymbol{n}\otimes\boldsymbol{n} - \frac{\boldsymbol{\delta}}{3}\right)\right] : d\boldsymbol{\sigma}^{'} \tag{A.19}$$

The functions $\Pi(r,\,\sigma_n^{'})$ and $\Psi(r,\,\sigma_n^{'d})$ can be defined as follows:

$$\Pi(r,\,\sigma_n^{'}) = \begin{cases} \sqrt{r}, & \text{if } \sigma_n^{'} > 0 \\ \sqrt{r}\,\sigma_n^{'}\,\dfrac{m\,f_{c,t}^{m}}{(f_{c,t}-\sigma_n^{'})^{m+1}} + \sqrt{r}\,\left(\dfrac{f_{c,t}}{f_{c,t}-\sigma_n^{'}}\right)^{m}, & \text{if } \sigma_n^{'} < 0 \\ 0, & \text{if } \sigma_n^{'} = 0 \end{cases} \tag{A.20}$$

$$\Psi(r,\,\sigma_n^{'d}) = \begin{cases} 3\,\eta\,\left(\dfrac{r_f}{\sqrt{r}}\right), & \text{if } \sigma_n^{'d} > 0 \\ 0, & \text{if } \sigma_n^{'d} \leq 0 \end{cases} \tag{A.21}$$

When $r \geq r_f$: this indicates that cracks start to coalesce to form macroscopic fractures which will finally lead the sample to failure, equation (A.7) is expressed as:

$$F = \sqrt{r}\,\sigma_n^{'}\,\left(\frac{f_{c,t}}{f_{c,t}+\langle-\sigma_n^{'}\rangle}\right)^{m} + 3\,\eta\,\sqrt{r_f}\,\langle\sigma_n^{'d}\rangle - C_{rc} \tag{A.22}$$

Following the same procedures as above, one can write:

$$\frac{\partial F}{\partial r} = \frac{1}{2\sqrt{r}}\,\sigma_n^{'}\,\left(\frac{f_{c,t}}{f_{c,t}+\langle-\sigma_n^{'}\rangle}\right)^{m} \tag{A.23}$$

$$dr = -\frac{1}{\dfrac{\partial F}{\partial r}}\left[\Pi(r,\,\sigma_n^{'})\,(\boldsymbol{n}\otimes\boldsymbol{n}) + \Psi(r,\,\sigma_n^{'d})\,\left(\boldsymbol{n}\otimes\boldsymbol{n} - \frac{\boldsymbol{\delta}}{3}\right)\right] : d\boldsymbol{\sigma}^{'} \tag{A.24}$$

The functions $\Pi(r,\,\sigma_n^{'})$ and $\Psi(r,\,\sigma_n^{'d})$ can be defined as follows:

$$\Pi(r,\,\sigma_n^{'}) = \begin{cases} \sqrt{r}, & \text{if } \sigma_n^{'} > 0 \\ \sqrt{r}\,\sigma_n^{'}\,\dfrac{m\,f_{c,t}^{m}}{(f_{c,t}-\sigma_n^{'})^{m+1}} + \sqrt{r}\,\left(\dfrac{f_{c,t}}{f_{c,t}-\sigma_n^{'}}\right)^{m}, & \text{if } \sigma_n^{'} < 0 \\ 0, & \text{if } \sigma_n^{'} = 0 \end{cases} \tag{A.25}$$

$$\Psi(r,\,\sigma_n^{'d}) = \begin{cases} 3\,\eta\,\sqrt{r_f}, & \text{if } \sigma_n^{'d} > 0 \\ 0, & \text{if } \sigma_n^{'d} \leq 0 \end{cases} \tag{A.26}$$

Though the unstable crack evolution, when $r \geq r_f$, is derived as above, it will not be used in this research unless crack healing is accounted for, see (Atkinson, [1991], chapter 4).

Appendix B

B.1 The effective fracture toughness in Hydraulic Fracturing (HF): HF in weak formations

(Papanastasiou, [1999]) had the problem of a hydraulically–driven fracture addressed by studying the numerous contributions since early fifties. It was found that classical HF simulators that are based on linear elasticity often underestimate the down–hole pressures which are measured in field operations. It has been also noted that the difference in pressures encountered in field and predicted by conventional HF become higher in weak formations. This discrepancy was explained using several hypotheses among which the most consistent with practical observations are:

- Rock dilation: the observed high pressure, encountered in the field, is related to huge fluid–pressure drop and the existence of dry regions near crack tip. Rock dilation has been proposed as the source of sharp pressure drop near crack tip, rock dilation beyond the advancing fracture will constrain the opening which may lead to high pressure gradients. Elasticity does not account for rock dilation and thus it can not provide the required high pressure drop to match field encountered values.

- Effective fracture toughness: the values of fracture toughness measured in laboratories underestimate *in situ* values. Estimations based on HF field data showed that typical fracture toughness values are two or three times higher than the values calculated from conventional laboratory tests. Studies presented in the available literature attributed these increases of field fracture toughness to scale effects, to the influence of confining stresses and plasticity in the process zone near the crack tip.

It has been noted that plastic yielding results in shorter but wider fractures if compared with elastic fracturing, the shorter wider fractures developed by elasto–plastic fracturing models are

expected to result in smaller fluid lag regions, henceforth better predicting field HF pressure, (Papanastasiou, [1999]). To account for plastic yielding and the increase of effective fracture toughness it incites, an elasto–plastic HF model based on finite element analysis has been used by the study of (Papanastasiou, [1999]).

Inelastic deformation has an extent which depends strongly on rock properties and loading stresses. Plastic deformation is expected to take place in weak rocks, such as clayey rocks or poorly consolidated sandstones, in areas close to the crack tip due to huge stress concentrations. Inelastic deformation near the crack tip produces a plastic yielding zone, if the plastic zone size is small compared to the radius of the evolving crack, the assumption of linear elastic fracture mechanics holds correct and can be used to describe the fracturing process. However, in soft rocks plastic zones are not likely to be small enough to a point the assumption of linear elasticity would hold sufficient, in such a case the application of plasticity theory will be necessary to analyze properly the irreversible strains due to excessive shear stresses around the fracture tip, see section (2.2.1).

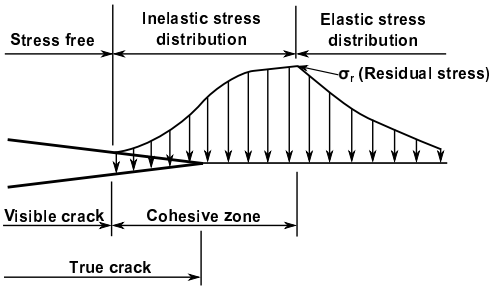

Figure B.1: Representation of the elasto–plastic fracturing process of rocks.

In a stationary crack, the plastic zone will develop near the crack tip and depending on the stress concentration and material properties, the fracture will deform either elastically or plastically. If rock was soft and the stress concentration was sufficient to create a plastic zone significantly large, plastic yielding will take place and fracture will deform plastically and the plastic zone shall unload elastically behind the advancing crack, the new area near the current tip will deform later plastically, see figure (B.1).

(Papanastasiou, [1999]) has shown that the rock mass remote from the fracture may deform elastically, whereas the area near the body of the fracture is initially elastic then deforms plastically and finally unloads elastically after the fracture has advanced. The main processes which govern hydraulic fracturing in a weak formation are:

- Viscous fluid flow in the fracture, see section (5.3).

- Elasto–plastic deformation caused by stress concentration incited by the state of *in situ* stresses as well as the action of fluid pressure.
- Fracture propagation into the rock formation.

The elasto–perfectly plastic model, which was adopted by (Papanastasiou, [1999]), was capable of dealing with nonproportioanl loading in order to track the plastic yielding–elastic unloading of the plastic zone at the crack tip. The model has proven that during fracture propagation the size of the plastic zone increases before it reaches a constant size eventually. Effective fracture toughness was found to develop following the size of the plastic zone; it starts with rock fracture toughness K_c, which dictates the energy required for propagating elastic fractures, and increases to reach an asymptotic value when the plastic zone is fully developed. Higher energy is needed for propagating elasto–plastic fractures as the plastic yielding softens the material surrounding the crack tip and creates an effective shielding in which the level of stress in the direction of propagation is reduced.

(Papanastasiou, [1999]) has found that the size of the plastic zone, along with the corresponding effective fracture toughness, increase with the contrast of several factors that include; the magnitude of the *in situ* stresses, the strength of the rock, the elastic modulus and the pumping parameters that include fluid viscosity and flow rate. Elastic analyses were later performed using the values of the effective fracture toughness, calculated by the elasto–plastic model, to estimate whether plasticity effect in HF can be embedded in the notion of effective fracture toughness while doing elastic fracturing. It has been demonstrated that, in terms of pressure and fracture profiles, an elastic model using the concept of effective fracture toughness matches the results of plasticity quite well.

Appendix C

C.1 Sub–matrices of the weak formulation of therm–poroelasticity: Chapters (3) and (6)

First, for displacement:

$$\boldsymbol{u} = \begin{bmatrix} u_x \\ u_y \end{bmatrix} = \boldsymbol{N_u}\, \boldsymbol{u^e},$$

$$[\boldsymbol{u^e}]^T = \begin{bmatrix} u_x^1 & u_y^1 & u_x^2 & u_y^2 & u_x^3 & u_y^3 & u_x^4 & u_y^4 \end{bmatrix},$$

$$\boldsymbol{N_u} = \begin{bmatrix} N_u^1 & 0 & N_u^2 & 0 & N_u^3 & 0 & N_u^4 & 0 \\ 0 & N_u^1 & 0 & N_u^2 & 0 & N_u^3 & 0 & N_u^4 \end{bmatrix},$$

$$\boldsymbol{B_u} = \begin{bmatrix} N_{u,x}^1 & 0 & N_{u,x}^2 & 0 & N_{u,x}^3 & 0 & N_{u,x}^4 & 0 \\ 0 & N_{u,y}^1 & 0 & N_{u,y}^2 & 0 & N_{u,y}^3 & 0 & N_{u,y}^4 \\ N_{u,y}^1 & N_{u,x}^1 & N_{u,y}^2 & N_{u,x}^2 & N_{u,y}^3 & N_{u,x}^3 & N_{u,y}^4 & N_{u,x}^4 \end{bmatrix},$$

$$\mathrm{tr}(\boldsymbol{B_u}) = \begin{bmatrix} N_{u,x}^1 & N_{u,y}^1 & N_{u,x}^2 & N_{u,y}^2 & N_{u,x}^3 & N_{u,y}^3 & N_{u,x}^4 & N_{u,y}^4 \end{bmatrix},$$

$$\boldsymbol{\nabla}(\mathrm{tr}(\boldsymbol{B_u})) = \begin{bmatrix} N_{u,xx}^1 & N_{u,yx}^1 & N_{u,xx}^2 & N_{u,yx}^2 & N_{u,xx}^3 & N_{u,yx}^3 & N_{u,xx}^4 & N_{u,yx}^4 \\ N_{u,xy}^1 & N_{u,yy}^1 & N_{u,xy}^2 & N_{u,yy}^2 & N_{u,xy}^3 & N_{u,yy}^3 & N_{u,xy}^4 & N_{u,yy}^4 \end{bmatrix},$$

$$\boldsymbol{v} = \begin{bmatrix} v_x \\ v_y \end{bmatrix},$$

$$\boldsymbol{\nabla v} = \begin{bmatrix} v_{x,x} & v_{x,y} \\ v_{y,x} & v_{y,y} \end{bmatrix}$$

Second, for pore fluid pressure:

$$p = \boldsymbol{N_p}\, \boldsymbol{p^e},$$

$$[\boldsymbol{p^e}]^T = \begin{bmatrix} p^1 & p^2 & p^3 & p^4 \end{bmatrix},$$

$$\boldsymbol{N_p} = \begin{bmatrix} N_p^1 & N_p^2 & N_p^3 & N_p^4 \end{bmatrix},$$

$$\boldsymbol{\nabla N_p} = \begin{bmatrix} N_{p,x}^1 & N_{p,x}^2 & N_{p,x}^3 & N_{p,x}^4 \\ N_{p,y}^1 & N_{p,y}^2 & N_{p,y}^3 & N_{p,y}^4 \end{bmatrix}$$

Third, for mixture temperature:

$$\theta = \boldsymbol{N_\theta}\, \boldsymbol{\theta^e},$$

$$[\boldsymbol{\theta^e}]^T = \begin{bmatrix} \theta^1 & \theta^2 & \theta^3 & \theta^4 \end{bmatrix},$$

$$\boldsymbol{N_\theta} = \begin{bmatrix} N_\theta^1 & N_\theta^2 & N_\theta^3 & N_\theta^4 \end{bmatrix},$$

$$\boldsymbol{\nabla N_\theta} = \begin{bmatrix} N_{\theta,x}^1 & N_{\theta,x}^2 & N_{\theta,x}^3 & N_{\theta,x}^4 \\ N_{\theta,y}^1 & N_{\theta,y}^2 & N_{\theta,y}^3 & N_{\theta,y}^4 \end{bmatrix},$$

$$\boldsymbol{\Delta N_\theta} = \begin{bmatrix} N_{\theta,xx}^1 + N_{\theta,yy}^1 & N_{\theta,xx}^2 + N_{\theta,yy}^2 & N_{\theta,xx}^3 + N_{\theta,yy}^3 & N_{\theta,xx}^4 + N_{\theta,yy}^4 \end{bmatrix},$$

$$\boldsymbol{v}^T\, \boldsymbol{\nabla^2 N_\theta} = \begin{bmatrix} v_x\, N_{\theta,xx}^1 + v_y\, N_{\theta,xy}^1 & v_x\, N_{\theta,xx}^2 + v_y\, N_{\theta,xy}^2 & v_x\, N_{\theta,xx}^3 + v_y\, N_{\theta,xy}^3 & v_x\, N_{\theta,xx}^4 + v_y\, N_{\theta,xy}^4 \\ v_x\, N_{\theta,yx}^1 + v_y\, N_{\theta,yy}^1 & v_x\, N_{\theta,yx}^2 + v_y\, N_{\theta,yy}^2 & v_x\, N_{\theta,yx}^3 + v_y\, N_{\theta,yy}^3 & v_x\, N_{\theta,yx}^4 + v_y\, N_{\theta,yy}^4 \end{bmatrix},$$

$$\boldsymbol{\nabla v}\, \boldsymbol{\nabla N_\theta} = \begin{bmatrix} v_{x,x}\, N_{\theta,x}^1 + v_{y,x}\, N_{\theta,y}^1 & v_{x,x}\, N_{\theta,x}^2 + v_{y,x}\, N_{\theta,y}^2 & v_{x,x}\, N_{\theta,x}^3 + v_{y,x}\, N_{\theta,y}^3 & v_{x,x}\, N_{\theta,x}^4 + v_{y,x}\, N_{\theta,y}^4 \\ v_{x,y}\, N_{\theta,x}^1 + v_{y,y}\, N_{\theta,y}^1 & v_{x,y}\, N_{\theta,x}^2 + v_{y,y}\, N_{\theta,y}^2 & v_{x,y}\, N_{\theta,x}^3 + v_{y,y}\, N_{\theta,y}^3 & v_{x,y}\, N_{\theta,x}^4 + v_{y,y}\, N_{\theta,y}^4 \end{bmatrix},$$

$$\boldsymbol{\nabla(\Delta N_\theta)} = \begin{bmatrix} N_{\theta,xxx}^1 + N_{\theta,yyx}^1 & N_{\theta,xxx}^2 + N_{\theta,yyx}^2 & N_{\theta,xxx}^3 + N_{\theta,yyx}^3 & N_{\theta,xxx}^4 + N_{\theta,yyx}^4 \\ N_{\theta,xxy}^1 + N_{\theta,yyy}^1 & N_{\theta,xxy}^2 + N_{\theta,yyy}^2 & N_{\theta,xxy}^3 + N_{\theta,yyy}^3 & N_{\theta,xxy}^4 + N_{\theta,yyy}^4 \end{bmatrix}$$

References

[1] Abousleiman Y., Bai M., Cui L., and Zhang J. **Dual–porosity poroelastic modeling of generalized plane strain**. *International Journal of Rock Mechanics and Mining Sciences*, **36**:1087–1094, 1999.

[2] Abousleiman Y. and Ekbote S. **Solutions for the inclined borehole in a porothermoelastic transversely isotropic medium.** *Journal of Applied Mechanics*, **72**(1):102–114, 2005.

[3] Abousleiman Y. and Nguyen V. **Geomechanical coupled poromechanics solutions while drilling in naturally fractured shale formations with field case applications.** In *SPE ATCE*, New Orleans, Louisiana, 4-7 October 2009. Society of Petroleum Engineers.

[4] Amos G. *MATLAB An introduction with applications*. John Wiley & Sons, Inc., second edition, 2005.

[5] Anderson D. N. and Lund J. W. **Direct utilization of geothermal energy: A technical handbook**. Geothermal Resources Council, Davis, CA (USA); Oregon Institute of Technology, Klamath Falls (USA), 1979.

[6] Asanuma H., Baria R., Dyer B., Garnish J., Jung R., Michelet S., Nicholls .J, Sanjuan B., Soma N., and Tischner T. **Creation of an HDR reservoir at 5000m depth at the European HDR project.** In *Proceedings of the 31st Workshop on Geothermal Reservoir Engineering*, Stanford University, Stanford, California, 30-February 2006.

[7] Atkinson B. K. *Fracture mechanics of rock*. Academic Press Limited, London, Great Britain, second printing edition, 1991.

[8] Baghbanan A. and Jing L. **Stress effects on permeability in a fractured rock mass with correlated fracture length and aperture**. *International Journal of Rock Mechanics and Mining Sciences*, **45**:1320–1334, 2008.

[9] Bai M. and Abousleiman Y. **Thermo–poroelastic coupling with application to consolidation**. *International Journal for Numerical and Analytical methods in Geomechanics*, **21**:121–132, 1997.

[10] Bandis S. C. and Barton N. R. **Application of a new numerical model of joint behavior to rock mechanics problems**. In *Proceedings of International Symposium on Fund Rock Joints*, pages 345–456, Bjorkliden, Sweden, 1985.

[11] Bandis S. C., Lumsden A. C., and Barton N. R. **Fundamentals of rock joint deformation**. *International Journal of Rock Mechanics, Mining Sciences and Geomechanics Abstracts*, **20**(6):249–268, 1983.

[12] Baria R., Baumgärtner J., Gérard A., Jung R., and Weidler R. **Hydraulic and microseismic results of a massive stimulation tests at 5 km depth at the European Hot–Dry–Rock test site Soultz, France.** In *Proceedings of The 27th Workshop on Geothermal Reservoir Engineering*, Stanford University, Stanford, California, 2002.

[13] Baria R., Baumgärtner J., Gérard A., and Garnish J. **The European HDR program: Main targets and results of the deepening of the well GPK2 to 5000 m.** In *Proceedings of the World Geothermal Congress 2000*, Kyushu, Tohoku, Japan, 28-May - 10-June 2000.

[14] Battistelli A., Calore C., and Pruess K. **The simulator TOUGH2/EWASG for modelling geothermal reservoirs with brines and non–condensible gas**. *Geothermics*, **26**(4):437–464, 1997.

[15] Baumgärtner J., Gérard A., Baria R., and Garnish J. **Progress at the European HDR project at Soultz–Sous–Forêts: Preliminary results from the deepening of the well GPK2 to 5000 m**. In *Proceedings of The 25th Workshop on Geothermal Reservoir Engineering*, Stanford University, Stanford, California, 22–24 January 2000.

[16] Baumgärtner J., Jung R., Gérard A., Baria R., and Garnish J. **The European HDR project at Soultz–Sous–Forêts: Simulation of the second deep well and first circulation experiments**. In *Proceedings of The 21st Workshop on Geothermal Reservoir Engineering*, Stanford University, Stanford, California, 22–24 January 1996.

[17] Bazant Z. P. and Oh B. H. **Efficient numerical integration on the surface of a sphere**. *Zeitschrift fur Angewandte Mathematik und Mechanik*, **66**(1):37–49, 1986.

[18] Beardsmore G. **The burgeoning Australian geothermal energy industry**. *Geo–Heat Center Quarterly Bulletin*, **28**(3):20–26, 2007.

[19] Bebout D. G., Gavenda V. J., and Gregory A. R. **Geothermal Resources, Wilcox Group, Texas Gulf Coast**. In *Geothermal Technologies Legacy Collection*, U.S. Department of Energy, 1–January 1978.

[20] Bertani R. **World geothermal generation in 2007**. *Geo–Heat Center Quarterly Bulletin*, **28**(3):8–19, 2007.

[21] Bezner H. C. *Fortran 77*. Prentice-Hall, Inc, United States, 1989.

[22] Bieniawski Z.T. **Mechanism of brittle fracture of rock: Part I-theory of the fracture process**. *International Journal of Rock Mechanics and Mining Sciences and Geomechanics Abstracts*, **4**(4):395–404, 1967.

[23] Blaisonneau A., Peter-Borie M., and Gentier S. *Rock Mechanics for Resources, Energy and Environment*. Taylor & Francis Group, Wroclaw, Pologne, 2013.

[24] Blond E., Schmitt N., and Hild F. **Response of saturated porous media to cyclic thermal loading**. *International Journal for Numerical and Analytical Methods in Geomechanics*, **27**:883–904, 2003.

[25] Brown S. R. **Fluid flow through rock joints: The effect of surface roughness.** *Journal of Geophysical Research*, **92**(B2):1337–1347, 1987.

[26] Brown D. and Duchane D. **Hot Dry Rock (HDR) geothermal energy research and development at Fenton Hill**. *Geothermal Heat Center Bulletin*, 2002.

[27] Bruel D. **Using the migration of the induced seismicity as a constraint for fractured hot dry rock reservoir modelling.** *International Journal of Rock Mechanics and Mining Sciences*, **44**:1106–1117, 2007.

[28] Bruel D. **Impact of induced thermal stresses during circulation tests in an engineered fractured geothermal reservoir.** *Oil and Gas Science and Technology*, **57**(5):459–470, 2002.

[29] Bruel D. **Heat extraction modelling from forced fluid flow through stimulated fractured rock masses: Application to the Rosemanowes hot dry reservoir**. *Geothermics*, **24**(3):361–374, 1995.

[30] Bruel D. **Modelling heat extraction from forced fluid flow through simulated fractured rock masses: Evaluation of the Soultz–Sous–Forêts site potential**. *Geothermics*, **24**(3):439–450, 1995.

[31] Bruno M. S. and Nakagawa F. M. **Pore pressure influence on tensile fracture propagation in sedimentary rock.** *International Journal of Rock Mechanics, Mining Sciences and Geomechanics Abstracts*, **28**(4):261–273, 1991.

[32] Bunger A. P., McLennan J., and Jeffrey R. *Effective and sustainable hydraulic fracturing.* InTech, Janeza Trdine 9, 51000 Rijeka, Croatia, first edition, 2013.

[33] Burger J., Sourieau P., and Combarnous M. *Thermal methods of oil recovery.* Editions Technip, 45800 Saint–Jean–de–Braye, 1985.

[34] Cataldi R. **Review of the historiographic aspects of geothermal energy in the Mediterranean and Mesoamerican areas prior to the modern age.** *Geo–Heat Center Quarterly Bulletin*, **15**(1):13–16, 1993.

[35] Chen Y., Zhou C., and Sheng Y. **Formulation of strain–dependent hydraulic conductivity for a fractured rock mass.** *International Journal of Rock Mechanics and Mining Sciences*, **44**(7):981–996, 2007.

[36] Cheng A. H.-D. and Ghassemi A. **Effect of fluid leak-off on heat extraction from a fracture in hot dry rock.** *Geothermal Resources*, **25**:217–220, 2001.

[37] Cheng A. H.-D., Ghassemi A., and Detournay E. **Integral equation solution of heat extraction from a fracture in hot dry rock.** *International Journal for Numerical and Analytical Methods in Geomechanics*, **25**:1327–1338, 2001.

[38] Ching H. L. and Ian F. *Fluid flow in discontinuous rocks.* Champon & Hall, 2–6 Boundary Row, London, Great Britain, first edition, 1993.

[39] Curtis R., Hellström G., Lund J., Rybach L., and Sanner B. **Geothermal (ground–source) heat pumps: A world overview.** *Geothermal Heat Center Bulletin*, 2004.

[40] Detournay E. and Cheng A. H.-D. **Plane strain analysis of a stationary hydraulic fracture in a poroelastic medium.** *International Journal of Solids and Structures*, **37**:1645–1662, 1991.

[41] Detournay E. and Cheng A. H.-D. **Poroelastic response of a borehole in a non-hydrostatic stress field.** *International Journal of Solids and Structures*, **25**(3):171–182, 1988.

[42] Dezayes Ch., Gentier S., and Genter A. **Deep geothermal energy in western Europe: The Soultz project**. In *proceedings of BRGM/RP–54227–FR, 48 p., 7 fig*, Orléans, France, October 2005.

[43] Dickson M. H. and Fanelli M. **What is geothermal energy?** Technical report, Istituto di Geoscienze e Georisorse, CNRS, Pisa, Italy, 2004.

[44] Du J., Liu C., Fu B., Ninomiya Y., Zhang Y., Wang C., Wang H., and Sun Z. **Variations of geothermometry and chemical-isotopic compositions of hot spring fluids in the Rehai geothermal field, southwestern China**. *Journal of Volcanology and Geothermal Research*, **142**:243–261, 2005.

[45] Duchane D. and Brown D. **Hot Dry Rock (HDR) geothermal energy research and development at Fenton Hill, New Mexico**. *Geothermal Heat Center Bulletin*, 2002.

[46] Elsworth D. **Theory of thermal recovery from a spherically stimulated Hot Dry Rock reservoir**. *Journal of Geophysical Research*, **94**(B2):1927–1934, 1989.

[47] Enick M. R. and Klara S. M. **CO_2 solubility in water and brine under reservoir conditions.** *Chemical Engineering Communications*, **90**(1):23–33, 1990.

[48] Evans K., Valley B., Häring M., Hopkirk R., Baujard C., Kohl T., Mégel T., André L., Portier S., and Vuataz F. **Studies and support for the EGS reservoirs at Soultz–sous–Forêts.** Technical report, Centre for Geothermal Research – CREGE, c/o CHYN, University of Neuchâtel, 2009.

[49] Fabre D., Mazerolle F., and Raynaud S. **X-ray density tomography: a tool to characterize pores and cracks in rocks**. In *Proceedings of the ISRM International Symposium*, Pau, France, 30 August to 2 September 1989.

[50] Fjaer E., Holt R. M., Horsrud P., Raaen A. M., and Risnes R. *Petroleum related rock mechanics.* Elsevier B.V., Radarweg 29, 1000 AE Amsterdam, The Netherlands, second edition, 2008.

[51] Francke H. and Thorade M. **Density and viscosity of brine: An overview from a process engineers perspective**. *Chemie der Erde*, **70**(S3):23–32, 2010.

[52] Ganzer L., Reitenbach V., Pudlo D., Albrecht D., Singhe A. T., Awemo K. N., Wienand J., and Gaupp R. **Experimental and numerical investigations on CO_2 injection and enhanced gas recovery effects in Altmark gas field (Central Germany)**. *Acta Geotechnica*, **DOI 10.1007/s11440–013–0226–7**, 2013.

[53] Ghassemi A. and Zhou X. X. **A three-dimensional thermo-poroelastic model for fracture response to injection/extraction in enhanced geothermal systems.** *Geothermics*, **40**:39–49, 2011.

[54] Ghassemi A., Nyrgen A., and Cheng A. **Effects of heat extraction on fracture aperture: A poro-thermoelastic analysis.** *Geothermics*, **37**:525–539, 2008.

[55] Ghassemi A., Tarasovs S., and Cheng A. H.-D. **Integral equation solution of heat extraction induced thermal stress in enhanced geothermal reservoir.** *International Journal for Numerical and Analytical Methods in Geomechanics*, **29**:829–844, 2005.

[56] Gelet R. *Thermo–hydro–mechanics of deformable porous media with double porosity and local thermal non–equilibrium.* Thesis, École Doctorale: Ingénierie–Matériaux Mécanique Energétique Environnement Procédés Production, September 2012.

[57] Gelet R., Loret B., and Khalili N. **Borehole stability analysis in a thermoporoelastic dual-porosity medium.** *International Journal of Rock Mechanics and Mining Sciences*, **50**:65–76, 2012.

[58] Gelet R., Loret B., and Khalili N. **Thermal recovery from a fractured medium in local thermal non-equilibrium.** *International Journal for Numerical and Analytical Methods in Geomechanics*, **37**(15):2471–2501, 2012.

[59] Gelet R., Loret B., and Khalili N. **A thermo-hydro-mechanical coupled model in local thermal non-equilibrium for fractured HDR reservoir with double porosity.** *Journal of Geophysical Research: Solid Earth*, **117**:B07205, 2012.

[60] Gidely J. L. *Recent advances in hydraulic fracturing.* Richardson, TX (USA), Society of Petroleum Engineers, 1989.

[61] Grecksch G., Jung R., Tischner T., and Weidler R. **Hydraulic fracturing at the European HDR/HFR test site Soultz–Sous–Forêts (France) – a conceptual model**. In *Proceedings of the European Geothermal Conference*, Leibniz Institute for Applied Geosciences GGA, Germany, 2003.

[62] Griffith A. A. **The phenomena of rupture and flow in solids.** *Philosophical Transactions of the Royal Society of London*, **A221**:163–198, 1921.

[63] Gutiérrez A. G., Paredes G. E., and Espejo G. A. **Effect of variable rheological properties of drilling muds and cements on the temperature distribution in geothermal wells.** In *Proceedings of World Geothermal Congress 2005*, Antalya, Turkey, 24–29 April 2005.

[64] Halm D. and Dragon A. **A model of anisotropic damage by mesocrack growth; unilateral effect.** *International Journal of Damage Mechanics*, **5**:384–402, 1996.

[65] Harari I. **Stability of semidiscrete formulations for parabolic problems at small time steps.** *Computer Methods in Applied Mechanics and Engineering*, **193**:1491–1516, 2004.

[66] Hauke G., Sangalli G., and Doweidar M. **Combining adjoint stabilized methods for the advection–diffusion–reaction problem.** *Mathematical Models and Methods in Applied Sciences.*, **17**(2):305–326, 2007.

[67] Hayashi K., Willis-Richards J., Hopkirk R. J., and Niibori Y. **Numerical models of HDR geothermal reservoirs — a review of current thinking and progress.** *Geomechanics*, **28**:507–518, 1999.

[68] Hughes T. J. R. *The finite element method; linear static and dynamic finite element analysis.* Dover Publications Inc., Mineola, New York, second edition, 2000.

[69] He L. W. and Jin Z. H. **A local thermal non-equilibrium poroelastic theory for fluid saturated porous medium.** *Journal of Thermal Stresses*, **33**(8):799–813, 2010.

[70] Irwin G. **Analysis of stresses and strains near the end of a crack traversing a plate.** *Journal of Applied Mechanics*, **24**:361–364, 1957.

[71] Jiang F., Luo L., and Chen J. **A novel three–dimensional transient model for subsurface heat exchange in enhanced geothermal systems**. *International Communications in Heat and Mass Transfer*, **41**:57–62, 2013.

[72] John V. and Knobloch P. **On spurious oscillations at layers diminishing (SOLD) methods for convection-diffusion equations: Part I - A review**. *Computer Methods in Applied Mechanics and Engineering*, **196**(17–20):2197–2215, 2007.

[73] Jupe A. J., Bruel D., Hicks T., Hopkirk R., Kappelmeyer O., Kohl T., Kolditz O., Rodrigues N., Smolka K., Willis-Richards J., Wallroth T., and Xu S. **Modelling of a European prototype HDR reservoir**. *Geothermics*, **24**(3):403–419, 1995.

[74] Kachanov M. **Effective elastic properties of cracked solids: Critical review of some basic concepts**. *Applied Mechanics Review*, **45**(8):304–335, 1992.

[75] Kagel A., Bates D., and Gawell K. **A guide to geothermal energy and the environment, geothermal energy association**. Pennsylvania Avenue SE, Washington, D.C., 22–April 2005.

[76] Kanj M. and Abousleiman Y. **Porothermoelastic analyses of anisotropic hollow cylinders with applications**. *International Journal for Numerical and Analytical Methods in Geomechanics*, **29**(2):103–126, 2005.

[77] Klimczak C., Schultz R. A., Parashar R., and Reeves D. M. **Cubic law with aperture-length correlation: Implications for network scale fluid flow.** *Hydrogeology Journal*, **18**(4):851–862, 2010.

[78] Kohl T. and Mégel T. **Predictive modeling of reservoir response to hydraulic stimulations at the European EGS site Soultz-sous-Forêts.** *International Journal of Rock Mechanics and Mining Sciences*, **44**:1118–1131, 2007.

[79] Kohl T., Evans K. F., Hopkirk R. J., Jung R., and Rybach L. **Observation and simulation of non–Darcian flow transients in fractured rocks**. *Water Resources Research*, **33**(3):407–418, 1997.

[80] Kohl T., Evans K. F., Hopkirk R. J., and Rybach L. **Coupled hydraulic, thermal and mechanical considerations for the simulation of hot dry rock reservoirs.** *Geothermics*, **24**(3):345–359, 1995.

[81] Kolditz O. **Modelling flow and heat transfer in fractured rocks: Dimensional effect of matrix heat diffusion.** *Geothermics*, **24**(3):421–437, 1995.

[82] Kranz R. L., Frankel A. D., Engelder T., and Scholz C. H. **The permeability of whole and jointed barre granite.** *International Journal of Rock Mechanics and Mining Sciences and Geomechanics Abstracts*, **16**(4):225–234, 1979.

[83] Lee S. H. and Ghassemi A. **Three-dimensional thermo-poro-mechanical modeling of reservoir stimulation and induced microseismicity in geothermal reservoir.** In *Proceedings of the Thirty Sixth Workshop on Geothermal Reservoir Engineering*, Stanford University, Stanford, California, 31–January - 3–February 2011.

[84] Lee S. H. and Ghassemi A. **Thermo-poroelastic analysis of injection–induced rock deformation and damage evolution.** In *Proceedings of the Thirty-Fifth Workshop on Geothermal Reservoir Engineering*, Stanford University, Stanford, California, 1–3 February 2010.

[85] Likhachev E. R. **Dependence of water viscosity on temperature and pressure**. *Technical Physics*, **48**(4):514–515, 2003.

[86] Lu F. Y., Wu X. X., and Shao F. J. **Anisotropic damage coupled modeling of saturated porous rock**. *Science China Technological Sciences*, **53**(10):2681–2690, 2010.

[87] Lubarda V. A., Krajcinovic D., and Mastilovic S. **Damage model for brittle elastic solids with unequal tensile and compressive strengths**. *Engineering Fracture Mechanics*, **49**(5):681–697, 1994.

[88] Lund J. W. **Characteristics, development, and utilization of geothermal resources.** *Geothermal Heat Center Bulletin*, 2007.

[89] Mary H., Dickson F., and Mario F. *What is Geothermal Energy?* Istituto di Geoscienze e Georisorse, CNR , Pisa, Italy, 2004.

[90] Metcalf M. and Reid J. *Fortran 90/95 explained.* Oxford University Press Inc., New York, USA, 1996.

[91] McTigue D. F. **Thermoelastic response of fluid-saturated porous rock.** *Journal of Geophysical Research*, **91**:9533–9542, 1986.

[92] Mogilevskaya S. G., Rothenburg L., and Dusseault M. B. **Growth of pressure induced fracture in the vicinity of a wellbore**. *International Journal of Fracture*, **104**(4):23–30, 2000.

[93] Murphy H., Brown D., Jung R., Matsunaga I., and Parker R. **Hydraulics and well testing of engineered geothermal reservoirs**. *Geothermics*, **28**:491–506, 1999.

[94] Noorishad J., Tsang C. F., and Witherspoon P. A. **Theoretical and field studies of coupled hydromechanical behavior of fractured rocks: Development and verification of a numerical simulator.** *International Journal of Rock Mechanics, Mining Sciences and Geomechanics Abstracts*, **29**(4):401–409, 1992.

[95] Oda M., Takemura T., and Aoki T. **Damage growth and permeability change in triaxial compression tests of Inada granite.** *Mechanics of Materials*, **34**:313–331, 2002.

[96] Papanastasiou P. **The effective fracture toughness in hydraulic fracturing.** *International Journal of Fracture*, **96**:127–147, 1999.

[97] Papanastasiou P. and Thiercelin M. **Influence of inelastic rock behavior in hydraulic fracturing.** *International Journal of Rock Mechanics, Mining Sciences and Geomechanics Abstracts*, **30**:1241–1247, 1993.

[98] Paterson M. S. and Wong T. F. *Experimental rock deformation–the brittle field.* Springer–Verlag, Heidelberg, Berlin, second edition, 2005.

[99] Pensée V., Kondo D., and Dormieux L. **Micromechanical analysis of anisotropic damage in brittle materials.** *Journal of Engineering Mechanics*, **128**(8):889–897, 2002.

[100] Pruess K. **Role of fluid pressure in the production behavior of enhanced geothermal systems with CO_2 as working fluid**. *Lawrence Berkeley National Laboratory*, pages 1–8, 2008.

[101] Pruess K. **Enhanced geothermal systems (EGS) using CO_2 as working fluid–A novel approach for generating renewable energy with simultaneous sequestration of carbon.** *Geothermics*, **35**:351–367, 2006.

[102] Rahman M. M. *Effect of natural fracture on hydraulic fracture propagation in poroelastic formation: fully coupled numerical model to investigate the interaction between induced and natural fracture.* Thesis, School of Petroleum Engineering, Sydney, NSW, Australia, September 2010.

[103] Raven K. G. and Gale J. E. **Water flow in a natural rock fracture as a function of stress and sample size.** *International Journal of Rock Mechanics and Mining Sciences and Geomechanics Abstracts*, **22**(4):251–261, 1985.

[104] Rejeb A. and Bruel D. **Hydromechanical effects of shaft sinking at the Sellafield site**. *International Journal of Rock Mechanics and Mining Sciences*, **38**(1):17–29, 2001.

[105] Rice J. R. and Cleary M. P. **Some basic stress–diffusion solutions for fluid-saturated elastic porous media with compressible constituents.** *Reviews of Geophysics*, **14**:227–241, 1976.

[106] Santoyo E., Gutiérrez S. S., Gracía A., Espinosa G., and Moya S. L. **Rheological property measurement of drilling fluids used in geothermal wells.** *Applied Thermal Engineering*, **21**:283–302, 2001.

[107] Savitski A. A. and Detournay E. **Propagation of a penny-shaped fluid-driven fracture in an impermeable rock: Asymptotic solutions.** *International Journal of Solids and Structures*, **39**:6311–6337, 2002.

[108] Selvadurai A. P. S. and Suvorov A. P. **THM processes in a fluid–saturated poroelastic geomaterial: Comparison of analytical results and computational estimates.** In *Proceedings of the 3rd CANUS Rock Mechanics Symposium*, McGill University, Montreal, Canada, May 2009.

[109] Selvadurai A. P. S. Mahyari A. T. and. **Computational modelling of steady crack extension in poroelastic media.** *International Journal of Solids and Structures*, **35**(34–35):4869–4885, 1998.

[110] Schulze O., Popp T., and Kern H. **Development of damage and permeability in deforming rock salt.** *Engineering Geology*, **61**:163–180, 2001.

[111] Shao F. J., Zhou H., and Chau K. T. **Coupling between anisotropic damage and permeability variation in brittle rocks.** *International Journal for Numerical and Analytical Methods in Geomechanics*, **29**:1231–1247, 2005.

[112] Shao F. J., Hoxha D., Bart M., Homand F., Duveau G., Souley M., and Hoteit N. **Modeling of induced anisotropic damage in granites.** *International Journal of Rock Mechanics and Mining Sciences*, **36**(8):1001–1012, 1999.

[113] Shibuya Y., Sekine H., Takahashi Y., and Abé H. **Multiple artificial geothermal reservoir cracks in a hot dry rock mass for extraction of heat.** *Journal of Energy Resources Technology*, **107**(2):274–279, 1985.

[114] Simpson G. and Guéguen Y. **Permeability enhancement due to microcrack dilatancy in the damage regime.** *Journal of Geophysical Research*, **106**(B3):3999–4016, 2001.

[115] Souley M., Homand F., Pepa S., and Hoxha D. **Damage-induced permeability changes in granite: A case example at the URL in Canada.** *International Journal of Rock Mechanics and Mining Sciences*, **38**(2):297–310, 2001.

[116] Spencer A. J. M. *Continuum mechanics.* Dover Publications Inc., Mineola, New York, 2004.

[117] Takahashi H. and Watanabe K. **Parametric study of the energy extraction from hot dry rock based on fractal fracture network model.** *Geomechanics*, **24**(2):223–236, 1995.

[118] Taron J. and Elsworth D. **Coupled mechanical and chemical processes in engineered geothermal reservoirs with dynamic permeability**. *International Journal of Rock Mechanics and Mining Sciences*, **47**:1339–1348, 2010.

[119] Taron J. and Elsworth D. **Thermal-hydrologic-mechanical-chemical processes in the evolution of engineered geothermal reservoirs**. *International Journal of Rock Mechanics and Mining Sciences*, **46**:855–864, 2009.

[120] Taron J., Elsworth D., and Min K. B. **Numerical simulation of thermal–hydrologic–mechanical–chemical processes in deformable, fractured porous media.** *International Journal of Rock Mechanics and Mining Sciences*, **46**:842–854, 2009.

[121] Tenzer H. **Development of hot dry rock technology.** *Geo-Heat Center Quarterly Bulletin*, **22**(2):14–22, 2001.

[122] Turcotte D. L. and Schubert G. *Geodynamics.* Cambridge University Press, Cambridge, England, UK, second edition, 2002.

[123] Ueda A., Kato K., Ohsumi T., Yajima T., Ito H., Kaieda H., Metcalfe R., and Takase H. **Experimental studies of CO_2–rock interaction at elevated temperatures under hydrothermal conditions.** *Geochemical Journal*, **39**:417–425, 2005.

[124] Vandamme L. and Curran J. H. **A three-dimensional hydraulic fracturing simulator.** *International Journal for Numerical Methods in Engineering*, **28**(4):909–927, 1989.

[125] Van Den Hoek P. J., Van Den Berg J. T. M., and Shlyapobersky J. **Theoretical and experimental investigation of rock dilatancy near the tip of a propagating hydraulic fracture.** *International Journal of Rock Mechanics, Mining Sciences and Geomechanics Abstracts*, **30**(7):1261–1264, 1993.

[126] Walsh J. B. and Grosenbaugh M. A. **A new model for analyzing the effects of fractures on compressibility.** *Journal of Geophysical Research*, **84**:3532–3536, 1979.

[127] Wang Y. and Dusseault M. B. **A coupled conductive-convective thermo-poroelastic solution and implications for wellbore stability.** *Journal of Petroleum Science and Engineering*, **38**:187–198, 2003.

[128] White E. D. and Williams L. D. **Assessment of geothermal resources of the United States–1975**. *Geological Survey Circular 726*, 1975.

[129] White E. D., Buffler L. J. P., and Truesdell A. H. **Vapor-dominated hydrothermal systems compared with hot-water systems.** *Economic Geology*, **66**:75–97, 1971.

[130] Williams L. D. and Menard W. H. *Assessment of geothermal resources of the United States.* Library of Congress, Utah, USA, 1978.

[131] Wright M. **Nature of geothermal resources in geothermal direct–use engineering and design guidebook.** *Geo–Heat Center Quarterly Bulletin*, **11**(3):27–69, 1989.

[132] Yin S., Dusseault M. B., and Rothenburg L. **Thermal reservoir modeling of petroleum geomechanics.** *International Journal for Numerical and Analytical Methods in Geomechanics*, **33**:449–485, 2009.

[133] Zangerl C., Evans K. F., Eberhardt E., and Loew S. **Normal stiffness of fractures in granitic rocks: A compilation of laboratory and in situ experiments.** *International Journal of Rock Mechanics and Mining Sciences*, **45**:1500–1507, 2008.

[134] Zhou X. X., Ghassemi A., and Cheng A. H.-D. **A three-dimensional integral equation model for calculating poro-and thermoelastic stresses induced by cold water injection into a geothermal reservoir.** *International Journal for Numerical and Analytical Methods in Geomechanics*, **33**:1613–1640, 2009.

[135] Zimmerman R. W. and Bodvarsson G. S. **Hydraulic conductivity of rock fractures.** *Transport in Porous Media*, **23**:1–30, 1996.

[136] Zoback M. D. and Byerlee J. D. **The effect of microcrack dilatancy on the permeability of Westerly granite.** *Journal of Geophysical Research*, **80**(5):752–755, 1975.

[137] Zoggy M. and Techn S. C. **History of heat pumps swiss contributions and international milestones.** In *9th International IEA Heat Pump Conference*, Zürich, Switzerland, May 2008.